

University of Warwick institutional repository: <http://go.warwick.ac.uk/wrap>

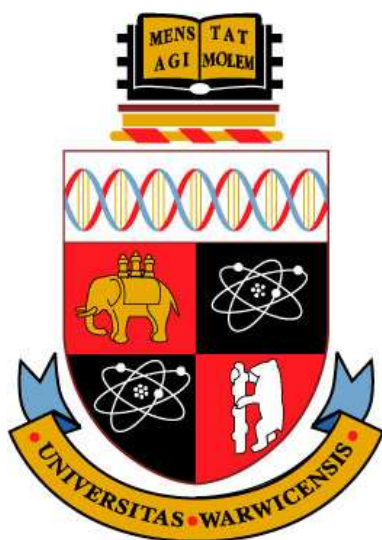
A Thesis Submitted for the Degree of PhD at the University of Warwick

<http://go.warwick.ac.uk/wrap/55616>

This thesis is made available online and is protected by original copyright.

Please scroll down to view the document itself.

Please refer to the repository record for this item for information to help you to cite it. Our policy information is available from the repository home page.



New approaches to protein crystallization

by

Barry R. Silver

Thesis

Submitted to the University of Warwick

for the degree of

Doctor of Philosophy

THE UNIVERSITY OF
WARWICK

Table of Contents

List of Figures and Tables	v
Acknowledgements.	xxi
Declarations	xxii
Abbreviations	xxiii
Abstract	xxiv
1. Introduction.....	1
1.A Historical aspects of protein crystallization.	1
1.B Basic protein structure and biochemistry.	3
1.C Protein solubility.....	5
1.D Metastability, metastable zone width and crystal nucleation.....	12
1.E Protein crystal nucleation requires an alternative to CNT.....	16
1.F Protein crystal growth.....	20
1.G Protein phase diagrams and protein crystallization.....	23
1.H Commonly used practical methods for protein crystallization	29
1.I The microbatch method – an ‘accidental’ example of protein crystallization at the oil/water interface.....	35
1.J An introduction to the oil-water interface.....	37
1.K Lysozyme adsorption to oil-water and air-water interfaces	41
1.L An introduction to the electrified oil/water interface.....	47
1.M The ideally polarisable liquid interface	49
1.N Experimental arrangements for electrochemical work at the oil/water interface	51
1.O General electrochemical basics.....	52
1.P Mass transport.....	60
1.Q Confocal Laser Scanning Microscopy (CLSM)	63
1.R Reference.....	66

2. Electrochemically-assisted growth of lysozyme crystals.....	73
2.A Previous work	73
2.A.1 Experimental arrangements used in previous studies	74
2.B Experimental	89
2.C Results.....	92
2.C.1 The “one well” arrangement.....	92
2.C.2 The “multi-well” arrangement.....	98
2.D Discussion	103
2.D.1 An interpretation of the results via electrochemically-induced shifts in solution conditions at the electrode surface	103
2.D.2 Toward a simple semi-quantitative description of the “electrochemically-induced solution shifts” interpretation.....	111
2.D.3 An alternative interpretation of the results based on protein crystallization at electrode surfaces via electrophoretic effects and the effect of the protein film.....	119
2.E Suggestions and Recommendations	124
2.E.1 The extent of the pH gradient at various heights above the anode	125
2.E.2 The measurement of the proposed temporal evolution of chloride concentration at various heights above the anode.	127
2.E.3 Protein film structure and thickness and different electrode materials	128
2.E.4 The dynamic phase diagram	129
2.E.5 New experimental arrangements	129
2.E.6 X-ray diffraction quality of crystals produced on electrode surfaces	131
2.E.7 Alternative protein/precipitant systems for future work	133
2.E.8 In-situ systems for fundamental study	139
2.E.9 Large protein crystals for neutron crystallography applications ?	140
2.F References	141

3. Protein crystallization at the oil/water interface	145
3.A Experimental	145
3.B Results	148
3.C Discussion.....	154
3.C.1. Increases and decreases in the extent of protein crystallization on ‘active’ and ‘inactive’ oil/water interfaces. Towards a plausible explanation of the results presented within this chapter. ...	160
3.C.1.1. The protein hydration shell	160
3.C.1.2. Protein hydration and the location of hydration waters	166
3.C.1.3. Entropy gains and losses may be a major driving force in the protein crystallization process.	167
3.C.1.4. Towards a possible mechanism to help rationalise the results.	170
3.C.1.5. No organic solvent was found bound to lysozyme and the location of lysozyme hydration water was similar to that found within protein databanks.	171
3.C.1.6. The difference in the extent of crystallization between air/water and oil/water interfaces	173
3.C.1.7. Lysozyme exhibits different surface activities at different oil/water interfaces	174
3.C.1.8. The aqueous-ionic liquid (BMIM-PF6) interface and its effect on lysozyme crystallization	176
3.D Appendix I	181
3.D.1. Pendant drop shape analysis for the measurement of dynamic interfacial surface tension.	181
3.D.2. X-Ray Diffraction Patterns and Refined protein structure	184
3.E References.....	187
 4. The electrified oil/water interface – a new approach to lysozyme crystallization ...	191
4.A Experimental.....	191
4.B Results.....	194
4.C Discussion	199
4.D Appendix I.....	205
4.D.1 An introduction to liquid – liquid electrochemistry.	205
(Compiled from ref. ^{1, 6, 13})	205
4.D.2 The standard Gibbs energy of transfer	208
4.D.3 Gibbs energy of transfer for single ions	210
4.E References.....	212

5. Large potential-induced changes in interfacial tension between two immiscible electrolyte solutions (ITIES) by the probable electroadsorption/ desorption of proteins.	213
.....	
5.A Introduction	214
5.B Experimental	218
5.C Results and Discussion	222
5.C.1. The blank. Cell 1 containing no protein or buffer. Aqueous phase contained 3% (w/v) NaCl only.	222
5.C.2. Lysozyme	224
5.C.3. Catalase	230
5.C.3.1. Catalase 0.05 mg/ml at pH 4.5 and pH 9	230
5.C.3.2. Catalase 1 mg/ml to 30 mg/ml at pH 3 and 1 mg/ml at pH 9	238
5.C.4. Myoglobin	245
.....	245
5.C.5. Cytochrome C	248
5.C.6. Dodecylbenzenesulfonic acid sodium salt	251
5.C.7. Gold nanoparticles	252
5.D References	260
 6. The rapid crystallization of tetrabutylammonium tetrphenylborate (TBATPB) at the ITIES.	263
.....	
6.A Introduction	264
6.B Experimental	265
6.C Results and Discussion	268
6.D References	292
 7. Conclusions	294
7.A Chapter 2	294
7.B. Chapter 3	296
7.C Chapter 4	298
7.D Summary Chapters 2, 3 and 4	299
7.E Chapter 5	299
7.F Chapter 6	300

List of figures and tables

Chapter 1

<i>Figure 1.1 Two different cartoon representations of the lysozyme molecule. The figure left is a ribbon representation of lysozyme, with alpha helices shown in red and beta strands in blue. Irregular loops are shown by grey rope. The figure right represents the solvent accessible surface area of lysozyme¹⁵, the surface is coloured in accordance with the electrostatic potential of the surface (at unknown pH), where positively charged residues are drawn in blue and negatively charged residues in red. Illustrations left and right are taken from 1HEL from the RCSB PDB ref. 16</i>	<i>4</i>
<i>Figure 1.2 The effect of pH on the solubility of β-lactoglobulin. The isoelectric point of this protein, located at the solubility minimum, is approximately 5.4. Figure taken and adapted from ref. ¹⁸</i>	<i>6</i>
<i>Figure 1.3 Typical 'salting in' and 'salting out' behaviour of a protein illustrated by changes in protein solubility with respect to the ionic strength of various electrolyte solutions. At low ionic strength, protein solubility increases, and begins to fall rapidly at higher ionic strengths. The protein used here was enolase (a metalloenzyme) and the figure was taken from ref.¹⁹</i>	<i>7</i>
<i>Figure 1.4 Three states of an arbitrary crystallizing solution. (a) Refers to a solution which is termed stable (b) represent an unstable solution and (c) represents a solution which is metastable. Figure is adapted from ref. 18.</i>	<i>12</i>
<i>Figure 1.5 Surface and volume contributions to the overall Gibbs energy of cluster formation. Figure adapted from ref. 25. If the overall Gibbs energy is negative clusters will form and grow.</i>	<i>13</i>
<i>Figure 1.6 Clusters of various sizes. The edge length of each cluster is depicted. Figure adapted from ref.25</i>	<i>15</i>
<i>Figure 1.7 Alternative pathways leading from solution to solid crystal: (a) supersaturated solution; (b) ordered subcritical cluster of solute molecules, proposed by classical nucleation theory; (c) liquid-like cluster of solute molecules, dense precursor proposed by two-step nucleation theory; (d) ordered crystalline nuclei; (e) solid crystal. Figure taken from ref.24</i>	<i>19</i>
<i>Figure 1.8 A cartoon representation of a developing crystal face which shows the positions of the kink, the ledge and the terraces as described by the TLK model of crystal growth. Growth units will find more energetically favourable attachment at kink sites than any other position on the crystal surface. Figure taken from ref. 40</i>	<i>21</i>
<i>Figure 1.9 A cartoon representation of top left: spiral dislocation growth, top right: two dimensional nucleation growth and bottom middle: a surface making a transition from the two dimensional mode of growth to three dimensional mode of growth. Figure adapted from ref.43.....</i>	<i>22</i>

<i>Figure 1.10 The Miers diagram indicating three main zones on the temperature/protein phase diagram. Figure from ref. 18.....</i>	<i>24</i>
<i>Figure 1.11 Generic phase diagram proposed by Muschol²² and co-workers. Panel (a) indicates a phase diagram for proteins with conventional solubility behaviour. Panel (b) indicates phase diagram for proteins with retrograde solubility. Solution conditions above the solubility curve in (a) and below the solubility curve in (b) are metastable with respect to crystallization. Zone II indicates an area of liquid-liquid phase separation. Gelation is common in Zone III and indicative of very high protein concentrations. Cross hatched area on the border between Zone I and Zone III is an area of amorphous precipitate formation. The best position for protein crystallization is in Zone I, just outside the cross hatched area and near Zone II^{19, 28}. Figure taken from ref.22</i>	<i>25</i>
<i>Figure 1.12 The lysozyme/NaCl phase diagram at pH 4.5 taken from Iwai and co-workers⁴⁴. An arbitrary solution starting condition is indicated by a red-dot on the diagram. Figure taken and adapted from ref.44.....</i>	<i>26</i>
<i>Figure 1.13 A lysozyme-NaCl diagram compiled at pH 4.2 and 20 degrees Celsius, with a temporal element. The figure has been taken from ref. 45. Lines A and B refer to 'paths' taken across the diagram via dialysis and vapour diffusion crystallization experiments respectively. Times to lysozyme crystallization at various lysozyme-NaCl compositions are indicated on the phase diagram.</i>	<i>28</i>
<i>Figure 1.14 The sitting drop (left) and the hanging drop (right) vapour diffusion techniques for screening and optimization of protein crystallization trials. "[ppt]" in diagram refers to the concentration of precipitant and is sometimes half that of the reservoir. Figures taken from ref.48.....</i>	<i>30</i>
<i>Figure 1.15 The sandwich drop vapour diffusion crystallization technique. The protein solution is sandwiched between a coverslip and water is drawn via vapour diffusion from the droplet by the reservoir. Figure taken from ref.48.....</i>	<i>31</i>
<i>Figure 1.16 Lysozyme/NaCl phase diagram taken from Iwai⁴⁴ and co-workers. A typical path taken across the phase diagram by a successful vapour diffusion experiment is shown by the series of black arrows. At position 1, the solution is undersaturated and is taken to position 2 where nucleation occurs. Due to crystal nucleation, the local protein concentration decreases and the solution is taken to position 3 which is conducive to good crystal growth. Figure adapted from ref. 44</i>	<i>31</i>
<i>Figure 1.17 An example of a free-interface diffusion set-up. A narrow pore capillary is filled with both protein and precipitant solution and diffusion is allowed to occur. Figure taken from ref.48.</i>	<i>32</i>
<i>Figure 1.18 The microbatch method showing an oil droplet underneath a layer of oil. The green lines (bottom) indicate water diffusing out of the droplet. Figures taken from ref. 48.</i>	<i>33</i>
<i>Figure 1.19 A microdialysis arrangement showing a sample within a dialysis button sealed with dialysis membrane. Water and some precipitant are allowed to exchange between the button and the reservoir across the membrane. Figures taken from ref. 48</i>	<i>34</i>
<i>Figure 1.20 Varied contact angles for a particle at an oil/water interface. Figure from ref. 11.....</i>	<i>40</i>
<i>Figure 1.21 The three stage protein adsorption regime prevalent at low protein concentration. Regime I is absent at high protein concentration. Cartoon has been taken from ref. 23.</i>	<i>42</i>

<i>Figure 1.22 A cyclic voltammogram indicating the transfer of ions (Li^+, Cl^-, TBA^+, TPB^-) between two liquid phases (water and nitrobenzene) as a function of applied potential. Figure from ref. 4.....</i>	<i>50</i>
<i>Figure 1.23 A simple voltaic cell consisting of zinc and copper metallic strips (acting as electrodes) immersed in a solution of ammonium chloride and connected by some wire. Figure taken from ref. 108...</i>	<i>52</i>
<i>Figure 1.24 Diagram illustrates the existence of an activation energy barrier (ΔG^\ddagger) which must be overcome in order to get from substrate A to product B. Figure taken from ref.105</i>	<i>56</i>
<i>Figure 1.25 The difference in activation energy in order to achieve the oxidised state (O) from an initially reduced state (R) and vice versa. Figure adapted from ref.105</i>	<i>57</i>
<i>Figure 1.26 The activation energy shows a dependence on the applied potential. Figure taken and adapted from ref. 105.....</i>	<i>58</i>
<i>Figure 1.27 A cartoon schematic showing the major components of a modern CLSM. Picture taken from ref. 111</i>	<i>63</i>
<i>Figure 1.28 The molecular structure of fluorescein (see references 113-114).....</i>	<i>65</i>
<i>Table 1.1 Practical methods for creating the supersaturated condition. Table adapted from ref.19.....</i>	<i>11</i>

Chapter 2

<i>Figure 2.1 A schematic of the galvanostatic experimental arrangement used in the Mirkin study. Protein solutions are within capillaries and precipitant was in the gel. Figure taken from ref. 2.....</i>	<i>75</i>
<i>Figure 2.2 Experimental arrangement used within both the Moreno and Sasaki⁴ and Sasaki³ et al. studies. Figure taken from ref. 3.....</i>	<i>76</i>
<i>Figure 2.3 Micrographs of lysozyme crystals obtained using apparatus indicated in Figure 2.2 at a supersaturation ratio of $\beta=3.0$. Distance between electrodes was 0.5 cm. (a) Experiment in solution without current, (b) with current, (c) growth in gels without current, and (d) growth in gels in the presence of a constant current. The cathode is on the right and the anode is on the left. Current applied was $2\mu\text{A}$. Figure from ref. 4.</i>	<i>77</i>
<i>Figure 2.4 Crystals formed on the surface of electrodes at different values of supersaturation with an applied DC current ($2\mu\text{A}$). Panel (a) $\beta=1.0$, (b) $\beta=2.0$, (c) $\beta=3.0$ and (d) $\beta=5.0$. Distance between electrodes was maintained constant at 0.5 cm. Crystal growth was performed using a gelled media. Cathode is on the right and anode is on the left. Figure from ref. 4.....</i>	<i>78</i>

- Figure 2.5 Different cell geometries used by Nieto-Mendoza⁶. Cell (A) was used exclusively for experiments under potentiostatic control. Cell B and Cell C refer to other cell geometry arrangements. The sharp linear objects are electrodes which are placed within different cell geometries. Figure from ref. 6.80
- Figure 2.6 Plot of the average size of lysozyme crystals obtained under controlled potential conditions⁶. Cell geometry used is type A, which contains 30 mg/ml lysozyme in 200mM acetate buffer (pH 4.5) and NaCl 40 mg/ml, after 24 h at 15 °C. Figure taken from ref. 6.81
- Figure 2.7 Micrographs of the HOPG working electrode at (a) 0, (b) 20, (c) 40, (d) 60, (e) 80 and (f) 100 min from the beginning of the experiment. Control experiment without any applied potential. Figure taken from ref. 5.83
- Figure 2.8 Micrographs of the HOPG working electrode at (a) 0, (b) 20, (c) 40, (d) 60, (e) 80 and (f) 100 min from the beginning of the experiment. Potential were cycled between -0.95 V to 0.5 V at a rate 40 mV/s for 1 ½ hours. Figure from ref. 5.83
- Figure 2.9 Experimental arrangement used for the Hammadi⁷ et al (2007) study84
- Figure 2.10 BPTI crystallization under an applied potential of 0.785 V. Note localization of BPTI crystals at the anode. Panel (a) indicates the start of the experiment. Panels from left to right, (b) to (d), indicate 7, 11, and 20 hours at the applied potential. Polarity of the electrode is indicated. Figure adapted from ref. 7.85
- Figure 2.11 Lysozyme crystals were found to be located on the cathode in the Hammadi⁷ et al study. Lysozyme crystallizing solution contained 25 mg/ml lysozyme in 0.7 M NaCl and 80 mM sodium acetate buffer at pH 4.5. A potential of 0.9 V was applied for (a) 0 and (b) 12 hours. Polarities of electrodes are as indicated. Panel (c) shows higher magnification view of panel (b), the presence of gel and mass nucleation are notable. Figure from ref. 7.85
- Figure 2.12 Quartz DLS cell with platinum electrodes used by Perez¹² et al. Figure from ref. 11.86
- Figure 2.13 The crystallization of cytochrome c in a DLS modified cell at 10 °C reported by Perez et al. (a) After 3 days of experiment. (b) After 5 days of crystal growth. (c) Cytochrome c needle-like crystals after 8 days of experiment. (d and e) Close-up of the needles shown in (c). There is a typo in the original graphic from the literature and the 'second (d)' should read 'e'. Figure from ref. 11.87
- Figure 2.14 The extent of BPTI (20 mg/ml - NaCl 1.6M) nucleation in the vicinity of the tip in 0.5% agarose gel (0.8 V - 0.74 μ A) as reported by Hammadi⁸ et al. The experiment was conducted over 12 hours. W-electrode wires shown are 125 μ m in diameter. Figure from ref. 8.88

Figure 2.15 “Nucleation waves” created by Hammad⁸ et al. in a BPTI (20 mg/ml, NaCl 1.6 M, pH 4.6) solution at 20 °C with DC voltage. The anode had been coated with wax, leaving the electrode tip exposed. The W wire electrode was 125 µm in diameter. Initially, nucleation occurred at the wax-coated anode (panels (a) and (b)) after 2 hours at 0.8 V (0.74 µA). The voltage was subsequently increased to 0.9 V (0.73 µA), a second nucleation wave was reported by the authors after 1 hour (panel c). The voltage was again increased to 1 V (1.40 µA), and a third nucleation wave was recorded within 1 hour of the voltage increase (panel d). Figure from ref. 8.....88

Figure 2.16 Lysozyme crystals formed at an electrode surface after 2 h. From left to right: 5 µA applied current; no current (Control A); and no current with solution pH of 3.5 (Control B). Scale bar shown is 350 µm. The crystals were viewed in-situ via optical microscopy.....92

Figure 2.17 In situ laser scanning confocal micrograph of the electrode interface and the surrounding layer of insulating Bakelite after 45 min of applied current. The blue line indicates the interface between the electrode and the surrounding insulating material. Dark circles within the blue line are oxygen bubbles formed via electrolysis.....93

Figure 2.18 Fluorescence intensity map perpendicular to the 2 mm diameter platinum disc electrode (5 µA applied). White areas indicate a pH ≥ 6.5 whilst darker areas are pH < 5. Elongated white areas on the electrode surface are lysozyme crystals which have incorporated fluorophore during growth. The scale bar is indicated. The blue cross has horizontal arms of 500 µm in length either side of the centre-point (giving a total of 1 µm in horizontal distance). The base of the blue cross is located over the approximate centre of the electrode.....94

Figure 2.19 Time dependence of fluorescence intensity at the electrode surface as a result of growth and dissolution of fluorescently labelled lysozyme crystals. From 0–1777 s, 5 µA current was applied. The current was then switched to 12 µA from 1777–1924 s and dissolution was seen. From 1924–2649 s 5 µA was again applied and growth resumed. For 2649 s onwards a current of 20 µA was applied and rapid dissolution resulted. In situ CLSM images at several times are shown (not background subtracted, area shown 550 µm × 550 µm).96

Figure 2.20 The rise in potential for a crystallizing solution (‘one-well’ arrangement) containing 37.5 mg/ml lysozyme and 4% (w/v) NaCl under galvanostatic control (2 A/m²). The working electrode was 2 mm diameter Pt disc electrode and counter electrode was platinum gauze. Note that potentials were well over 1.4 V for most of the time and no clear transition time is evident.....97

Figure 2.21 Initial solution conditions 37.5 mg/ml lysozyme and 3.5 % (w/v) NaCl (pH circa 6.5). Numbers on panels indicate applied anodic current densities in A/m². Micrographs taken after 2 hours. 750 µm diameter Pt electrodes. Gas bubbles from electrolysis are evident in panel “1.8”.98

Figure 2.22 Initial solution conditions 45 mg/ml lysozyme and 3.5 % (w/v) NaCl (pH circa 6.5). Numbers on panels indicate applied anodic current densities in A/m². Micrographs taken after 2 hours. 750 µm diameter platinum electrodes.98

Figure 2.23 Initial solution conditions 37.5 mg/ml lysozyme and 4 % (w/v) NaCl (pH circa 6.5). Numbers on panels indicate applied anodic current densities in A/m^2 . Micrographs taken after 2 hours. 750 μm diameter platinum electrodes. Micrograph panel 0 was taken at a magnification different from other panels.99

Figure 2.24 Initial solution conditions 45 mg/ml lysozyme and 4 % (w/v) NaCl (pH circa 6.5). Numbers on panels indicate applied anodic current densities in A/m^2 . Micrographs taken after 2 hours. 750 μm diameter platinum electrodes.99

Figure 2.25 Initial solution conditions 30 mg/ml lysozyme and 4.5 % (w/v) NaCl (pH circa 6.5). Numbers on panels indicate applied anodic current densities in A/m^2 . Micrographs taken after 2 hours. 750 μm diameter platinum electrodes.100

Figure 2.26 Initial solution conditions 37.5 mg/ml lysozyme and 4.5 % (w/v) NaCl (pH circa 6.5). Numbers on panels indicate applied anodic current densities in A/m^2 . Micrographs taken after 2 hours. 750 μm diameter platinum electrodes.100

Figure 2.27 Initial solution conditions 45 mg/ml lysozyme and 4.5 % (w/v) NaCl (pH circa 6.5). Numbers on panels indicate applied anodic current densities in A/m^2 . Micrographs taken after 2 hours. 750 μm diameter platinum electrodes.101

Figure 2.28 Protein film is evident on the surface of one of the electrodes in the 'multi-well' arrangement. Note two dimensional islands on the surface of growing crystals indicative of crystal growth at high levels of supersaturation. The well contained 37.5 mg/ml lysozyme and 4% (w/v) NaCl and a current density of 0.9 A/m^2 was used. The platinum electrode was 750 μm in diameter.101

Figure 2.29 A lysozyme/NaCl phase diagram representing initial solution conditions of all experimental conditions used in conjunction with the 'multi-well' arrangement. Yellow squares represent initial crystallization conditions before applied current. Black wavy arrow (top right) indicates shift direction due to chloride oxidation (vide infra). Small black arrows indicate 'shift' direction of nucleation zone lines due to water oxidation (vide infra). The width of the metastable zone (between a solid and a dashed line of the same colour) and the position of the zone of undersaturation (to the left of solid coloured lines) are also shown to 'shift' with changes in pH. Figure adapted from ref.22.102

Figure 2.30 A proposed experimental arrangement for the direct measurement of pH and chloride ion concentration measurement above the surface of an electrode with feedback control. The computer is able to control both the micropositioner and the potentiostat via feedback from the electrodes.131

Figure 2.31 The solubility of crystalline glucose isomerase in the presence of ammonium sulphate taken at approximately pH 5.5 from work by Chayen⁶¹. Panel (b) same as (a) except that the solubility has been plotted on a log scale. Figures taken from ref. 61134

Figure 2.32 The solubility of glucose isomerase as a function pH from 61.134

Figure 2.33 A phase diagram for the ferritin/ $CdSO_4$ system in 0.2 M sodium acetate buffer (pH 5). Note the very short width of the metastable zone. The solubility curve is the solid line and the dashed lines indicate the beginning of the nucleation zone. Figure taken from ref. 65.137

Figure 2.34 The crystallization of ferritin on a 2mm diameter Pt disc electrode under a 2 A/m² cathodic regime after 2 hours. Black areas are cadmium islands. Crystal morphology is showing signs of becoming dendritic.138

Table 2.1 A table representing hypothetical initial solution conditions (Start) and final hypothetical solution conditions (Finish) of hypothetical lysozyme crystallizing solutions. The path taken to the final solution state (Path) via electrolysis is given. The likely outcome (Result) of that path is also given. U represents an undersaturated solution, M represents a metastable solution and N represents a solution in which nucleation is likely to occur.....109

Table 2.2 Chloride concentrations obtained at the electrode surface after 2 hours of electrolysis at prescribed current densities. The current densities correspond to that used within the 'multi-well' arrangement. The pH attained at the electrode surface is also indicated. 30% of the total current was allotted to chloride oxidation and 70% of the total current was allotted to water electrolysis.....118

Chapter 3

Figure 3.1 Diagram of apparatus used to monitor the oil/water and air/water interfaces optically during crystallization. The insert was slid within the barrel and a lightly greased, glass cover-slip placed on the end of the barrel. The depression within the insert contained either a droplet of oil or aqueous solution depending on which phase was more dense.147

Figure 3.2 The extent of protein crystallization at a variety of 'inactive' oil/water interfaces. Percentages indicated refer to the (w/v) % of NaCl present in the aqueous phase. The aqueous phase contained 37.5 mg/ml lysozyme in all cases. Scale bars indicated are 1 mm in length. PDMS is polydimethylsiloxane (or silicon oil).....148

Figure 3.3 The extent of lysozyme crystallization on the bromoform/aqueous interface at varied aqueous phase salt concentrations. Percentages indicate (w/v) % NaCl in the aqueous phase. 37.5 mg/ml lysozyme was used within the aqueous phase in all cases. Scale bar is 1 mm and applies across all panels.149

Figure 3.4 Optical micrographs illustrating, for comparative purposes, the extent of lysozyme crystallization air/aqueous (left) and bromoform/aqueous (right) interfaces after 24 hours at room temperature. 37.5 mg/ml lysozyme with 3% (w/v) NaCl was used. Large crystals of approximately 500 μ m were seen on the oil/water interface. Scale is 1.5 mm.149

Figure 3.5 A comparison of the extent of lysozyme crystallization on the chloroform/aqueous interface and the corresponding air/aqueous interface at varied salt concentrations. Percentages indicate (w/v) % NaCl in the aqueous phase. Scale bar applies to all panels and is 1 mm in length. 37.5 mg/ml lysozyme was used within the aqueous phase in all cases.150

Figure 3.6 A comparison between the extent of lysozyme crystallization on the 1, 2-dichloroethane/aqueous interface and the corresponding aqueous/air interface. Percentages indicate (w/v) % NaCl in the aqueous phase. 37.5 mg/ml lysozyme was used in the aqueous phase in all cases. The crystals are seen to 'sink' into the oil phase somewhat. Scale bar is 1 mm and applies across all panels.150

Figure 3.7 The extent of lysozyme crystallization on the aqueous/BMIM-PF6 interface. 'Lys' indicates the concentration of lysozyme in mg/ml and NaCl concentration is given in (w/v) %. Scale bar indicated is 1 mm and applies to all small panels. A close up (large panels) of two panels is given bottom right which highlights the morphology of lysozyme crystals formed at this specific ionic liquid/aqueous interface.151

Figure 3.8 Sideways aspect of the extent of lysozyme crystallization on the oil/water interface after 24 hours. Oil/water interfaces were made by filling a small glass vial of approximately 13 mm diameter with equal volumes of aqueous and oil phase. The same volume glass vial is used in all cases. The aqueous phase in all cases contained 37.5 mg/ml and 3.5 % (w/v) NaCl. From top left to right: aqueous /BMIM-PF6 interface, aqueous/ 1:1 chloroform and benzene interface and aqueous/nitrobenzene interface. Middle left to right same as top left to right except the interface is viewed at a higher magnification. Bottom left to right: aqueous/1, 2-dichloroethane, aqueous/haloethane and aqueous/octan-1-ol interfaces. 'W' denotes aqueous phase and 'OIL' denotes the oil phase. Arrow in middle centre panel points toward crystal growth within the oil phase. Spherulites are seen on the 1-octanol interface.152

Figure 3.9 A flaccid pendant droplet (left) containing 30 mg/ml lysozyme and 3% (w/v) NaCl in 1, 2-dichloroethane after 3 hours of immersion. The same droplet (right) after increasing the hydrostatic pressure via the additions of small volumes of aqueous solution (ΔV). The extent of the protein skin is clearly evident and it appears to be thick. Additionally, the protein film displays quite marked mechanical strength under the induced hydrostatic pressure. Note that crystal growth occurred on the aqueous side on the interface.....153

Figure 3.10 Dynamic interfacial tension data from pendant drop analysis. 30 mg/ml lysozyme as the aqueous phase with benzene (blue); 1, 2-dichloroethane (red) and chloroform (black) as the oil phase. Protein free chloroform-water, 1, 2-dichloroethane-water and benzene-water interfacial tensions were approximately 27.1, 28.9 and 24 mN/m respectively (Table 3.1). Aqueous protein solutions contained no precipitant making them 'non-crystallizing' for this analysis.....153

Figure 3.11 A cartoon depicting the proposed water stripping and water retention behaviour propose solvents of different polarity.....171

Figure 3.12 A pendant droplet suspended from a needle point. Three dimensionless first order differential equations used to evaluate the shape factor of the pendant droplet are shown. Vertical and horizontal force components are also shown.....183

<i>Figure 3.13 Diffraction pattern of lysozyme grown on the chloroform/water interface. The resolution rings are at 1.7, 2.2, 3.3 and 6.6 Å.....</i>	<i>184</i>
<i>Figure 3.14 A close-up of diffraction pattern featured in Figure 3.13. The zoom shows that diffraction spots go out to the edge of 1.7 Å.....</i>	<i>185</i>
<i>Figure 3.15 The refined lysozyme structure from previous diffraction patterns.....</i>	<i>186</i>
<i>Table 3.1 Summary of main properties of the oil phases used within this study. ‘Active’ solvents are indicated in bold.....</i>	<i>147</i>

Chapter 4

<i>Figure 4.1 A cartoon representation of the experimental arrangement.....</i>	<i>193</i>
<i>Figure 4.2 Cyclic voltammogram of Cell 1 (4.1) without lysozyme. Initial scan direction was negative. Scan rate 50 mV/s. Polarity was that of the aqueous phase.....</i>	<i>194</i>
<i>Figure 4.3 Cyclic voltammogram of cell given in (4.1) with the addition of 30 mg/ml lysozyme. Initial scan direction negative. Scan rate 50 mV/s. Polarity is that of the aqueous phase.</i>	<i>195</i>
<i>Figure 4.4 The effect of an applied potential on the crystallization of lysozyme at the ITIES. Top left : pendant droplet after 2 hours at +0.2 V, middle top: control experiment no applied potential (open circuit, referred to as 0 V), top right: pendant droplet after 2 hours at -0.2 V. Aqueous phases contained 30 mg/ml and 4% (w/v) NaCl in all cases. Organic phases contained 10 mM TBATPB in all cases. Bottom panels are close-ups of (left) the control and (right) -0.2 V treatment. Scale bars shown are 1.472 mm in length in all cases. Crystals which are seen in the -0.2 V treatment are approximately 430 µm across. Note increased film formation and nucleation on the + 0.2 V treatment (top left). Polarity was of the aqueous phase in all cases.....</i>	<i>196</i>
<i>Figure 4.5 Potential-dependent dynamic interfacial surface tension as a function of applied potential (Cell 1). The aqueous phase contained 30 mg/ml lysozyme and 3% (w/v) NaCl. “0 V” refers to an open circuit condition of no applied potential and all polarities are that of the aqueous phase.</i>	<i>197</i>
<i>Figure 4.6 Dynamic potential-dependent interfacial tension data for an aqueous phase containing 1 mg/ml lysozyme and 3% (w/v) NaCl. Blue dots and circles indicate an applied potential of -0.2 V at pH 3 and pH 9 respectively. Red dots and circles indicate an applied potential of + 0.2 V at pH 3 and pH 9 respectively.....</i>	<i>198</i>
<i>Figure 4.7 Phase diagram by Iwai and co-workers for the lysozyme/NaCl crystallization system at pH 4.5. Initial conditions of 30 mg/ml lysozyme and 4% (w/v) NaCl are indicated. Figure taken and adapted from ref. 15. A decrease in protein concentration around growing crystals will result in a ‘shift’ of solution conditions into the metastable zone.</i>	<i>200</i>

Chapter 5

Figure 5.1 Electrowetting on a dielectric with the Young angle and contact angle indicated (left panel). A potential is applied to the droplet. Dielectric is shown in right panel as the insulating layer (S) which covers a doped Si wafer electrode. Schematics from taken from ref. 2-3.....215

Figure 5.2 Schematic of the experimental set-up. A droplet of aqueous solution is extruded through a stainless steel 'hook' to form a droplet at the hook tip. An Ag/AgCl wire is 'plumbed' into a syringe which contains the aqueous phase. Ag/AgTPB wire is placed within the oil phase. A drop shape analysis system (camera icon) measures dynamic interfacial tension via the pendant drop method when potential is applied between the two electrodes with the aid of a potentiostat. The hook was electrically insulated from both electrodes.221

Figure 5.3 (a) Potential-dependent γ behaviour (scan rate 50 mV s^{-1}) for an aqueous phase (Cell 1) containing no protein or buffer. The first cycle is indicated on both (a) and (b). Figure (b) represents corresponding CV's for (a). Black arrows on (b) indicate the potential scan cycle, which was in a negative direction from 0 V to -0.4 V, then to +0.4V and back to negative again.....222

Figure 5.4 γ data from aqueous pendant droplets containing 1 and 10 mg/ml lysozyme with (bottom panels) and without (top panels) 3% (w/v) NaCl (pH 3). Oil phase was 10 mM TBATPB in 1, 2-DCE. The triangular waveform (-0.4 V to +0.4 V at 50 mV/s) used is illustrated. Key for figure in Table 5-1224

Figure 5.5 γ data for aqueous pendant droplets containing 20 and 30 mg/ml lysozyme with (bottom panels) and without (top panels) 3% (w/v) NaCl (pH 3). Oil phase contained 10 mM TBATPB in 1, 2-DCE. The triangular waveform used (-0.4 V to + 0.4 V at 50 mV/s) is illustrated. Key for panels in Table 5-1.....225

Figure 5.6 Potential-dependent γ data for aqueous pendant droplets containing 1 mg/ml lysozyme and 3% (w/v) NaCl at pH 9. Oil phase contained 10 mM TBATPB in 1, 2-DCE. Key for all panels is blue = CV, black = OCP, red= +0.2 V, green = -0.2 V.....226

Figure 5.7 Shifts in proposed adsorption (Ads) and desorption (Des) potentials with increasing cycle number. Cell 1 containing 10 mg/ml and 3% (w/v) NaCl (pH 3) in the aqueous phase. The dotted lines indicate the directions of the trend in 'Ads' and 'Des'. Scan rate was 50 mV/s. IFT refers to γ227

Figure 5.8 No shift in suggested adsorption and desorption potentials with increasing cycle number for lysozyme at pH 9. Cell 1 with an aqueous phase containing 1 mg/ml lysozyme and 3% (w/v) NaCl (pH 9). The charge on lysozyme at pH 9 would be zero or very close to zero. Lysozyme is shown to display 'desorption', not evident for lysozyme under similar experimental conditions at pH 3. IFT refers to γ229

Figure 5.9 (a) Potential-dependent IFT behaviour (scan rate 50 mV s^{-1}) for an aqueous phase (Cell 1) containing 0.05 mg/ml catalase (buffered at pH 4.5). (b) correspond to CV's for (a). Various stages on the CV are numbered in sequence and are explained in further detail within the text. Blue arrows on (b) indicate the potential scan cycle, which was in a negative direction from 0 V to -0.4 V , then to $+0.4 \text{ V}$ and back to negative again. Colours used in (a) indicate the cycle order which is black, red, green and then yellow (4^{th} cycle).....230

Figure 5.10 (a) Potential-dependent γ behaviour (scan rate 50 mV s^{-1}) for an aqueous phase (Cell 1) containing 0.05 mg/ml catalase (buffered at pH 9). 3(b) corresponds to CV's for 3 (a). Various stages on the CV are numbered in sequence and are explained in further detail within the text. Blue arrows indicate the potential scan cycle, which was in a negative direction from 0 V to -0.4 V , then to $+0.4 \text{ V}$ and back to negative again. Colours used in (a) indicate the cycle order which is black, red, green and then yellow (4^{th} cycle).....232

Figure 5.11 Shifts in postulated adsorption (Ads) and desorption (Des) potentials for 0.05 mg/ml catalase at pH 9. Cell 1 with an aqueous phase containing 0.05 mg/ml catalase and $3\% \text{ (w/v)}$ NaCl ...234

Figure 5.12 Potential/time-dependent γ characteristics for aqueous phases (Cell 1) containing: no protein (black); 0.05 mg/ml catalase at pH 4.5 (red); and 0.05 mg/ml catalase at pH 9 (blue). The data are from Figure 5.3, Figure 5.9 and Figure 5.10. Potential swept between $+0.4 \text{ V}$ and -0.4 V , initially from 0 V to -0.4 V (indicated for catalase pH 9 with the red downward pointing arrows). The dotted, vertical black lines indicate particular potentials. Yellow lines and pink lines superimposed on experimental data (blue line) highlight the magnitude of the γ change for particular 'legs' of each cycle. The red arrows indicate the extent of γ decrease by virtue of protein electroadsorption at negative aqueous potentials. IFT refers to $\gamma \text{ (mN/m)}$235

Figure 5.13 Dynamic interfacial tension data from aqueous pendant drops containing 1 and 10 mg/ml catalase with (top and bottom right panels) and without (top and bottom left panels) $3\% \text{ (w/v)}$ NaCl (pH 3). Oil phase contained 10 mM TBATPB in 1,2-DCE in all cases. Key for panels given in Table 5-2238

Figure 5.14 Dynamic surface tension data from aqueous pendant droplets containing 20 and 30 mg/ml catalase with (bottom panels) and without (top panels) $3\% \text{ (w/v)}$ NaCl (pH 3). Oil phase contained 10 mM TBATPB in 1,2-DCE. Key for all panels given in Table 5-2239

Figure 5.15 An γ/CV diagram with an aqueous phase containing 1 mg catalase and $3\% \text{ (w/v)}$ NaCl (pH 3). The oil phase contained 10 mM TBATPB. Coloured lines indicate different potential sweep cycles with respect to the cyclic voltammogram component inherent in the diagram. The first cycle (in red), changes to the second cycle (navy blue) at -0.4 V . Navy blue changes to light blue and light blue changes to magenta. Arrows indicate cycle direction. Solid black line indicates a conventional cyclic voltammogram for corresponding γ -data. Data has been smoothed using a Savitsky-Golay algorithm for clarity and is not represented by a solid fitting line.240

Figure 5.16 Shifts in postulated adsorption (*Abs*) and desorption (*Des*) potentials with increasing cycle number for catalase at pH 3. Cell 1 with an aqueous phase containing 1 mg/ml catalase with 3% NaCl (at pH 3). The adsorption and desorption potentials trend toward more negative potentials.....242

Figure 5.17 γ -potential diagram with aqueous phase containing 1 mg catalase and 3 % (w/v) NaCl (pH 9). The oil phase contained 10 mM TBATPB. Coloured lines indicate different cycles with respect to the cyclic voltammogram component inherent in the diagram. The first cycle (in black), changes to the second cycle (in red) at -0.4 V. Red changes to green, green changes to dark blue and dark blue changes to light blue. Arrows indicate cycle direction. Solid blue line indicates a conventional cyclic voltammetry curve.243

Figure 5.18 Shifts in apparent adsorption (*Abs*) and desorption (*Des*) potentials with cycle number for catalase at pH 9. Cell 1 with an aqueous phase containing 1 mg/ml catalase and 3% (w/v) NaCl. Note the opposite trending between the *Ads* and the *Des*. The *Abs* trends as expected from the adsorption of negatively charged protein to the interface but the *Des* trends opposite to that which was expected. IFT refers to γ244

Figure 5.19 Dynamic interfacial tension data for aqueous pendant droplets containing 1 and 10 mg/ml myoglobin with (bottom panels) and without (top panels) 3% (w/v) NaCl. Oil phase contained 10 mM TBATPB in 1,2-DCE. Key for panels in Table 5-3.245

Figure 5.20 Dynamic interfacial tension data for aqueous droplets containing 20 and 30 mg/ml myoglobin with (bottom panels) and without (top panels) 3% (w/v) NaCl. Oil phase contained 10 mM TBATPB in 1,2-DCE. Key for all panels in Table 5-3.246

Figure 5.21 An γ /CV diagram for 1 mg myoglobin and 3% (w/v) in the aqueous phase and 10 mM TBATPB (in 1,2-dichloroethane) in the oil phase. Different coloured lines indicate different sweep segments. Due to the reversible nature of protein adsorption indicated within this figure, all segments overlap. Arrows indicate cycle direction. Solid blue line indicates a conventional cyclic voltammetry curve. 1st cycle in black, 2nd cycle in red, 3rd cycle in green and 4th cycle in blue.....247

Figure 5.22 A plot of current and interfacial surface tension against applied potential for an aqueous pendant droplet containing 0.05 mg/ml cytochrome c and 3 % (w/v) NaCl at pH 3. The organic phase was 1, 2-dichloroethane. The potential was cycled between 0.4 and -0.4 V (scan rate was 50 mV/s, starting at 0V, initial direction negative).248

Figure 5.23 A plot of potential and normalised (against maximum) interfacial surface tension against time for an aqueous pendant droplet containing 0.05 mg/ml cytochrome c and 3 % (w/v) NaCl at pH 3. The data is from Figure 5.22. The organic phase was 1, 2-dichloroethane. The potential was cycled between 0.4 and -0.4 V (scan rate was 50 mV/s, starting at 0V, initial scan rate negative). Conditions were the same as that represented in Figure 5.22. Numbers in green indicate different stages of potential dependent surface tension change. Red horizontal lines indicate potentials at which each stage begins. Note the lack of shift in adsorption and desorption potentials. The normalised data (γ) only extends to a value of 1.....249

Figure 5.24 Interfacial surface tension data with aqueous phase containing 20 mM LiCl and 0.125 mM (black), 0.25 mM (green), 0.5 mM (blue) and 1 mM (red) dodecylbenzenesulfonic acid sodium salt. Oil phase contained 10 mM TBATPB in 1,2-DCE. Potential was cycled between 0.4 and -0.4 V at 50 mV/s. Initial scan was negative. Anionic surfactant. The pH of solution was approximately 6.5.251

Figure 5.25 Gold nanoparticles in 20 mM LiCl (aqueous phase). The oil phase consisted of 10 mM TBATPB in 1,2-dichloroethane in all cases. Purple = gold full (no dilution), blue= 0.5, red= 0.25, black = 0.125 (0.875 water + 0.125 gold stock). Potential was cycled between 0.8 and -0.8V at 50 mV/s. Initial scan direction was negative.252

Figure 5.26 Gold nanoparticles (no dilution) with no salt (except 20 mM LiCl-red) and gold nanoparticles with salt (960 mM NaCl-blue). Potential was scanned between 0.8 and -0.8 V at 50 mV/s. Initial scan direction negative from 0V.....253

Figure 5.27 Potential-dependent adsorption of gold nanoparticles (no dilution) and 960 mM NaCl. Potential sweep between -0.8 and 0.8V at 50 mV/s. The initial scan was negative from 0V. Different stages of the reversible adsorption process are featured as coloured lines on the potential versus time curve. Yellow line indicates a decrease in surface tension, accumulation of nanoparticles⁴⁰ and ion transfer¹⁰ (-0.2 V to -0.8 V), blue line and pink line indicates an area within and either side of the potential window which sees a return to γ values at ca. $t=0^{10}$, green line indicates positive potential nanoparticle accumulation and ion transfer¹⁰. IFT refers to γ254

Table 5-1 Key for Figure 5.4 and Figure 5.5225

Table 5-2 Key for figures Figure 5.13 and Figure 5.14239

Table 5-3 Key for figures Figure 5.19 and Figure 5.20246

Table 5-4 Summary of main physical properties of proteins used within this chapter255

Chapter 6

Figure 6.1 Rapid interfacial crystallization promoted by KCl but not NaCl over the experimental time frame. Panels top were a Cell 1 arrangement with 0.1 M KCl (aqueous phase) and 20 mM TBATPB (organic phase). A constant potential of +0.6 V was applied. Individual panels (top) indicate the amount of time after application of the potential. Big panel bottom right: a magnified view of the last panel at top left. Big panel bottom left was the Cell 1 arrangement with 0.1 M NaCl (aqueous phase) and 20 mM TBATPB (organic phase) and demonstrates an absence of interfacial crystals after 30 minutes at a constant potential of +0.7 V. Scale bars indicated are 700 μm . The 'whisker-like' crystals formed as above were observed after about 25 s (after the potential was applied)......268

Figure 6.2 Top panels (left to right): an open-circuit condition with no applied potential (OCP). Bottom panels (left to right): a constant +1 V potential. The oil phase contained 10 mM TBATPB in 1, 2-DCE in all cases. Aqueous phase (droplets) contain from left to right (top and bottom): 3% (w/v) NaCl, 3% (w/v) NaCl + 10% (v/v) NH_4OH (conc.) and 3% (w/v) NaCl + 10 % (v/v) NH_4OH + 15 mM hydrazine. Potential was applied for about 15 minutes in all cases. The black object supporting the pendant droplet was 1.47 mm in diameter. All experiments were conducted within the Cell 2 arrangement. Some light crystallization is evident on the 3% (w/v) NaCl condition.269

Figure 6.3 Top panels (left to right): an open-circuit condition with no applied potential (OCP). Bottom panels (left to right): a constant +1 V potential was applied. The oil phase contained 10 mM TBAPF_6 in 1, 2-DCE in all cases. Aqueous phases contain from left to right: 3% (w/v) NaCl, 3% (w/v) NaCl + 10% (v/v) NH_4OH (conc.) and 3% (w/v) NaCl + 10 % (v/v) NH_4OH + 15 mM hydrazine. Potential was applied for about 15 minutes in all cases. The black object supporting the pendant droplet was 1.471 mm in diameter. All experiments were conducted within the Cell 2 arrangement. No crystallization was evident under any condition over the experimental time frame.....270

Figure 6.4 Needle-like (left) and cube-like (right) crystals grown on the ITIES using pendant droplets with different aqueous and oil phase ion combinations. Left panel: aqueous phase contained 6 % (w/v) KCl and the oil phase contained 10 mM TBATPB (in 1,2-DCE). Potential was applied for 5 minutes at +1 V. Right panel: the aqueous phase contained 6% (w/v) CsCl and the oil phase contained 10 mM TBAPF_6 (in 1,2-DCE). Potential was applied for 10 minutes at +2 V. Small cubes (right) appear to be growing in a chain-like manner. All experiments conducted within the Cell 2 arrangement.270

Figure 6.5 Interfacial crystals resulting from an applied potential of + 1 V using an aqueous phase containing 1 mM AgNO_3 + 10 % (v/v) NH_4OH . The oil phase contained 10 mM TBATPB in 1, 2-DCE. Crystals appeared after approximately 10 minutes. Black region at the bottom of the pendant droplet is 1.47 mm across. Experiments conducted within the Cell 2 arrangement.271

Figure 6.6 Branching “fern” growth with bunches of needle-like crystals which appear to originate and branch from single points. The aqueous phase contained 3% NaCl + 10% (v/v) NH_4OH . A potential of +0.8 V was applied for a few minutes. Blue arrows indicate apparent origin of branching points.

Experiments conducted within the Cell 2 arrangement.272

Figure 6.7 A comparison between the TBATPB morphology straight from the bottle [(a) and (b)] and TBATPB grown on the ITIES via the application of + 1 V potential [(c) and (d)]. For (c) and (d) the Cell 2 arrangement was used and 0.8 M KCl was present in the aqueous phase with 50 mM TBATPB present in the organic phase. Scale bars represent 2 μm in (a) and (c), 200 nm in (b) and 1 μm in (d). Crystals were imaged using SEM. Crystals grown at the ITIES are considerably longer along the c-axis than those from the ‘bottle’. No gold sputtering was used and extensive charging effects are evident.274

Figure 6.8 (a) and (b) Scanning electron micrographs of crystals ‘harvested’ from the interface (Cell 1). (a) Crystals, not gold sputtered, and extensive ‘charging’ is evident. (b) Crystals which were gold sputtered allowing examination at high magnification without deterioration under the electron beam. The geometric cross section and the elongated morphology was typical for crystals produced at oil/water interface (c) Typical SEM-EDAX analysis of the ‘whiskers’, the silicon peak is due to the silicon wafer substrate. (d) ^1H -NMR spectrum of needles harvested from the interface, indicating TBATPB. Scale bar on (a) is 10 μm and scale bar on (b) is 20 μm275

Figure 6.9 SEM micrographs of structures grown using 10% (v/v) NH_4OH (conc) + 1 mM AuCl_3 + 3 % (w/v) NaCl in the aqueous phase and 10 mM TBATPB in 1,2-dichloroethane in the organic phase. The applied potential was +1 V. Top left: typical crystal morphology. Top right: ‘rod-like’ tubular structures. Bottom left: hollow structure with geometric cross section. Bottom right: hollow structure with rectangular cross section. Crystals were formed using the Cell 2 arrangement.276

Figure 6.10 TEM micrograph of crystals of the type shown in Figure 6.9. The tube-like structures are the ‘whiskers’ and the geometric dark patches are electron-dense and could be metal particles.277

Figure 6.11 Optical micrograph of crystals harvested from the interface and spot stained with SnCl_2 . Note the purple stain around the periphery of the ‘whisker’, indicating the presence of gold. The crystals were grown within the Cell 2 arrangement and contained 10% (v/v) NH_4OH (conc) + 1 mM AuCl_3 + 3 % (w/v) NaCl in the aqueous phase and 10 mM TBATPB in 1,2-dichloroethane in the organic phase. Magnification was x 500.278

Figure 6.12 Typical experimental arrangement used for Cell 1. A micropipette of 53 μm inner diameter containing aqueous solution and a Ag/AgCl electrode was immersed into a reservoir containing a conductive organic phase and a Ag/AgTPB electrode. ‘WE’ is the ‘working electrode’, ‘CE’ is the counter-electrode and ‘RE’ is the reference electrode. The reference and counter electrodes were shorted together. The arrangement was viewed optically from a sideways aspect within a Krüss DSA 100 apparatus, as has been done in previous chapters.280

Figure 6.13 Cyclic voltammograms (CVs) (a and b) and corresponding potentiostatic current transients (c and d) for micro-ITIES arrangement (Cell 1). Concentration of electrolyte in aqueous and organic phase are indicated on figures. First potential sweep cycle on (a) and (b) is indicated in black, with the second indicated in red. Coloured lines in (c) and (d) correspond to applied anodic potentials. Scan rates for CV's were (a) = 0.025 V/s and (b) = 0.02 V/s.281

Figure 6.14 Cyclic voltammograms (CV) (a and b) and corresponding potentiostatic current transients (c and d) for the micro-ITIES arrangement (Cell 1). Concentrations in both aqueous and organic phases are indicated on figures. First potential sweep cycle is indicated in black on (a) and (b), with the second indicated in red. Coloured lines in (c) and (d) refer to applied anodic potentials. Scan rates for CV's were (a) = 0.025 V/s and (b) = 0.025 V/s.....282

Figure 6.15 Optical micrograph indicating the extent of crystallization at the mouth of the micropipettes at varied potential. "High" and "Low" KCl refer to an aqueous phase containing 0.8 M KCl and 22 mM respectively which was contained within the micropipette. Low TBATPB refers to an oil phase (outside the pipette) containing 0.1 mM TBATPB. Each micropipette represented in the micrograph was the same micropipette. The micropipette was however used in different experiments. Applied potentials were as indicated and were applied for a period of 400 s using Cell 1. This figure corresponds directly to the end result of potentiostatic current transients in Figure 6.13 (c) and Figure 6.14 (c). The internal diameter of the micropipette was 53 μm283

Figure 6.16 Optical micrograph indicating the extent of crystallization at the mouth of the micropipettes at varied potential. "High" KCl and "Low" KCl refer to an aqueous phase containing 0.8 M KCl and 22 mM KCl respectively (within the pipette). High TBATPB refers to an oil phase containing 50 mM TBATPB (outside the pipette). Each micropipette represented in the micrograph was the same micropipette. The micropipette was however used in different experiments. Applied potentials are as indicated and were applied for a period of 400 s using Cell 1. This figure corresponds directly to the end result of potentiostatic current transients in Figure 6.13 (d) and Figure 6.14 (d). The internal diameter of the micropipette was 53 μm284

Figure 6.17 A cartoon of the suggested TBATPB crystallization mechanism, which may be initiated by the association of K^+ and TPB⁻. Each stage of the process is numbered and we have divided the process into 4 stages.288

Acknowledgements

First and foremost I would like to thank Professor Patrick Unwin for his help, support and supervision over the last 3 years. His insight and experience have proved invaluable in a variety of contexts. A big thank you also goes to Professor Alison Rodger for initiating, maintaining and directing the MOAC DTC. Without Alison none of this would be possible. Her hard work, diligence and impeccable social skills are often emulated but are never quite matched. Thanks also to Professor Vilmös Fülöp, who conducted X-ray crystallography (Chapter 3).

Thanks to the ‘unsung heroes of the workshops’ namely Mr. Lee Butcher, Mr. Marcus Grant and Mr. Kirk Harris from the Mechanical Workshop and Electronics Workshop. Lee and Marcus have fabricated a number of pieces of equipment (Teflon-based and other) used for experiment within this thesis. The equipment was manufactured always to specification and always with a smile. Special thanks to Kirk who helped greatly with galvanostat manufacture (Chapter 2).

Thank you also to Mr. Adam Morgan, Mr. Petr Dudin, Mr Ian Portman, Dr. Richard Walton and Dr. Stefan Bon who helped with the compilation of Chapter 6. In particular Adam provided H-NMR analysis and helped with crystal preparation, Petr provided the SEM images, Ian provided the TEM images and Dr’s Walton and Bon provided useful advice, discussion and manpower when needed.

Declarations

The work contained within this thesis is entirely original and my own work, except where acknowledged in the text. I confirm that this thesis has not been submitted for a degree at another university.

Abbreviations

<i>NAM</i>	<i>N-acetylmuramic acid</i>
<i>NAG</i>	<i>N-acetylglucosamine</i>
<i>CNT</i>	<i>Classical Nucleation theory</i>
<i>AFM</i>	<i>Atomic Force Microscopy</i>
<i>TLK</i>	<i>Terrace-Ledge-Kink</i>
<i>ref.</i>	<i>reference</i>
<i>CLSM</i>	<i>Confocal Laser Scanning Microscopy.</i>
<i>pI</i>	<i>isoelectric point</i>
<i>CV</i>	<i>cyclic voltammetry</i>
<i>DLS</i>	<i>dynamic light scattering</i>
<i>BPTI</i>	<i>bovine pancreatic trypsin inhibitor</i>
<i>Pt</i>	<i>platinum</i>
<i>W</i>	<i>tungsten</i>
<i>QCM</i>	<i>quartz crystal microbalance</i>
<i>approx.</i>	<i>approximately</i>
<i>ITIES</i>	<i>interface between two immiscible electrolyte solutions</i>
<i>TBATPB</i>	<i>tetrabutylammonium tetrphenylborate</i>
<i>DCE</i>	<i>1,2 dichloroethane</i>

Abstract

This thesis was focussed toward providing new approaches to protein crystallization. Herein, we describe three new such approaches.

Firstly, we describe proof-of-concept studies which demonstrate that simple DC electrochemical systems may be used to enhance and/or control the growth of lysozyme protein crystals on the surface of platinum disc electrodes. Secondly, we demonstrate how various oil/water interfaces provide both novel and unique environments for the study and enhancement of protein crystallization studies. In particular, we show how some oil/water interfaces greatly enhance the extent of lysozyme crystallization in comparison to the air/water interface whilst others do not. Thirdly, we show for the first time, that by application of small magnitude potentials to the ITIES, large increases in lysozyme crystal growth can be achieved (on the ITIES) in short time.

Additionally, and unrelated to protein crystallization, we find that large potential-dependent changes in surface tension may be achieved by probable reversible adsorption/desorption of proteins to and from the oil-water interface. The reversible changes in droplet geometry are, in some cases, large and seem controllable. As such, this methodology warrants consideration as means to enhance the performance of alternative liquid/liquid ultra low-voltage and conventional electrowetting systems.

The rapid crystallization of TBATPB at the ITIES is also reported for the first time. This work is of importance to theory and experiment regarding ion-transfer mechanisms at the ITIES. Additionally, this work may point towards a new type of crystallization technology for a variety of molecules grounded in methodology developed for liquid/liquid electrochemical systems.

1.Introduction

1.A Historical aspects of protein crystallization.

Almost one hundred and seventy years have passed since the first protein was accidentally crystallised. McPherson¹ describes how a Professor Hünefeld, who was at the time, studying a sample of blood from the common earthworm (*Lumbricus terrestris*), noticed the formation of flat plate-like crystals in the blood. These 'blood crystals' were found by Hünefeld to form when the blood was pressed between two glass microscope slides and allowed to dry very slowly. The crystals were later identified as haemoglobin, a well known iron-containing oxygen-transport metalloprotein.

After Hünefeld's initial discovery (*circa* 1840), there followed a flurry of research activity with various investigators trying to isolate and crystallize various proteins¹. Biochemical knowledge in 19th century was understandably at a very early stage of development and researchers were forced to work with proteins obtainable in large quantity only. Despite this limiting prerequisite, a modicum of success with regards the crystallization of some proteins was realised. Researchers continued working with what was thought of at the time as a novel means to purify newly isolated proteins.

The belief, that protein crystallization was useful solely as a means to increase protein purity continued into the early 20th century until pioneering work by a group of legendary crystallographers (Astbury, Bernal, Bragg and Perutz)¹. These scientists demonstrated unequivocally that protein crystals could be used as a means to provide important structural information about proteins via the newly emerging discipline of X-ray crystallography.

As the field of protein crystallography began to grow and mature, researchers began to demand higher and higher structural resolution from crystallographic studies¹. Modern radiation sources have largely kept pace with this demand. As today there are numerous world-wide synchrotron radiation facilities which provide highly collimated and bright radiation, capable of probing matter on the sub-atomic length scale. However, the major bottleneck *en route* to the elucidation of high resolution three dimensional protein structures is still the formation and subsequent diffraction quality of the protein crystal itself². The formation and the intrinsic diffraction quality of protein crystals is in turn known to be dependent on a complicated set of interactions between the protein and the solvent (often containing precipitant) in which the protein exists^{1, 3-4}.

Very soon after Hünefeld's initial discovery, researchers began to realise that the problem of protein crystallization needed to be tackled in a systematic and purposeful fashion. Otto Fünke (*circa.* 1851) is attributed with the first series of articles detailing the *in vitro* crystallization of haemoglobins from the blood of human, horse, pig, dog, cat and fish⁵. Since the beginning of Fünke's systematic approach, no 'hard and fast' rules with which one can use to successfully crystallize a newly isolated protein exist. The crystallization problem is tackled nowadays on a trial and error basis with the use of computer controlled robots which enable large amounts of chemical space to be sampled using micro to nanolitre volumes of expensive, concentrated protein solution⁶.

Surprisingly, the same physicochemical techniques used by Hünefeld in his 1840 study, namely controlled evaporation of water from protein solutions, forms the basis of most of the modern day protein crystal growth techniques⁶.

1.B Basic protein structure and biochemistry.

The ‘central dogma’ of molecular biology⁷ states that “DNA makes RNA makes protein”. The sequence of amino acids which constitute any given protein are encoded within the DNA and are translated on the ribosome via a transcribed RNA intermediate⁷. Once translated, a protein will assume a specific three dimensional shape or tertiary structure which is due mostly to the physicochemical nature of the primary sequence from which it is composed⁸. Proteins may thus be viewed as heteropolymeric entities, as they are composed of combinations of many different amino acids bound via amide linkages through a series of condensation reactions⁹. Each amino acid, of which there are 20 which naturally occur, have differing chemical side chains. This property of amino acids is largely responsible for the unique biological function imparted to a protein after translation and correct folding⁹.

Hen egg white lysozyme (Figure 1.1), is considered a model protein for protein crystallization studies¹⁰. This is mostly because of the low cost and high availability of the protein. Lysozyme is an ellipsoidally shaped¹¹, monomeric protein with a mass of approximately 14.3 kDa. It is composed of a series 129 amino acids¹². Lysozymes, in general, are additionally classified as enzymes and are commonly found in hen egg whites, human tears, and other bodily secretions. The main enzymatic function¹³ of lysozyme is to break down gram-positive bacterial cell walls and thus provide a modest degree of protection against bacterial infection.

After correctly folding, lysozyme displays a catalytic cleft on its surface (the active site for this enzyme) which serves to hydrolyze the β - (1-4) - glycosidic bond between residues of N-acetylmuramic acid (NAM) and N-acetylglucosamine (NAG). NAM and NAG are polysaccharides found in the bacterial cell wall of gram-positive bacteria¹². The tertiary structure of lysozyme is stabilised via four pairs of cysteine residues which form disulphide bridges between amino acid positions 6 and 127, 30 and 115, 64 and 80, 76 and 94. Lysozyme has a theoretical isoelectric point of approximately pH 9.6¹⁴ and is thus considered positively charged at pH below approximately 10.

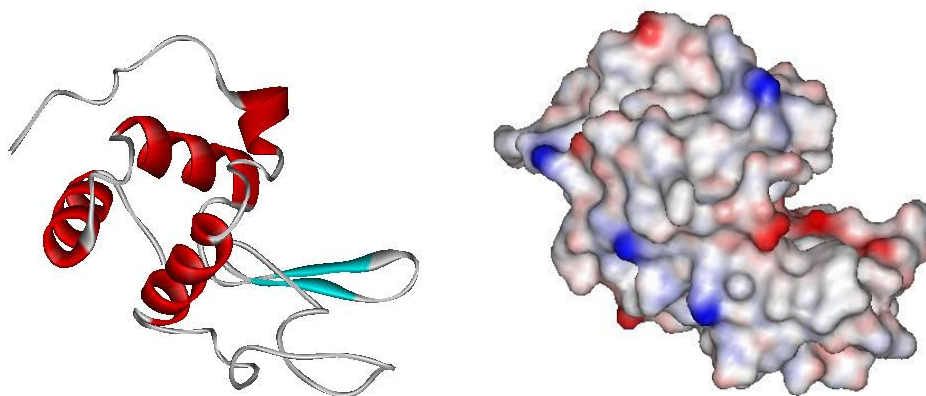


Figure 1.1 Two different cartoon representations of the lysozyme molecule. The figure left is a ribbon representation of lysozyme, with alpha helices shown in red and beta strands in blue. Irregular loops are shown by grey rope. The figure right represents the solvent accessible surface area of lysozyme¹⁵, the surface is coloured in accordance with the electrostatic potential of the surface (at unknown pH), where positively charged residues are drawn in blue and negatively charged residues in red. Illustrations left and right are taken from 1HEL from the RCSB PDB ref. 16

Proteins are by necessity “designed” (via evolution) to exist and function in water based environments, such as that found within the confines of a cell¹⁷. Water, a solvent which is highly polar, enables the solvation and ionization of a wide range of organic and ionic molecules. Since proteins consist of long chains of amino acids which are generally ionisable, the interaction between the solvent accessible surface of a protein (Figure 1.1) and the surrounding aqueous solvent environment is extremely complex.

By altering both the charge of the protein (via changing the solution pH for example) and by adding various ionic and organic precipitants one may induce various protein aggregation processes to occur by altering protein-protein and protein-solvent interactions¹⁸⁻²⁰.

1.C Protein solubility

The solubility of a protein is lowest near its isoelectric point¹⁸. At this pH the protein has a net charge of zero. This solubility behaviour can be explained by Debye-Hückel theory¹⁸ and the solubility of a protein in the presence of ionic precipitant can be given by

$$\ln\left(\frac{S}{S_0}\right) = \frac{Z^2 e^2 N \kappa}{2 \epsilon_r R T (1 + \kappa a)} \quad (1.1)$$

S is the protein solubility when electrolyte is present in solution, S_0 is the protein solubility without any electrolyte. Z is the net charge on the protein. N is Avogadro's number, e is the elementary unit of charge (an electron has therefore $-1e$ charge), κ is the inverse Debye length, ϵ_r is the dielectric constant (or relative static permittivity, a dimensionless number), R is the gas constant, T is absolute temperature and ' a ' is the ionic radius.

By inspection of (1.1) one finds that if $Z = 0$, protein solubility will be at a minimum. Additionally, if one were to assume that protein charge were a linear function of pH near the isoelectric point, then one would expect a typically parabolic relationship between $\ln\left(\frac{S}{S_0}\right)$ and pH (Figure 1.2).

In general, proteins will be net positively charged at pH below the isoelectric point and net negatively charged at pH above the isoelectric point. The example given in Figure 1.2 is for a protein with a mid range isoelectric point. Proteins with high isoelectric points such as lysozyme ($pI \approx 10$) will therefore be positively charged over a wide range of physiologically reasonable pH values (say pH 3 to pH 8 for example).

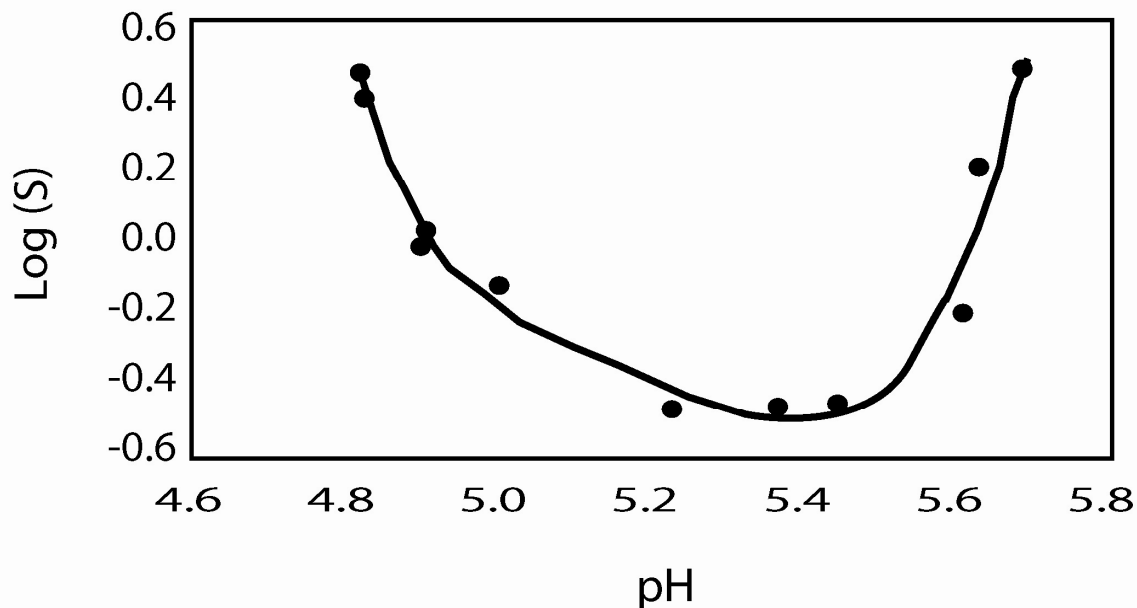


Figure 1.2 The effect of pH on the solubility of β -lactoglobulin. The isoelectric point of this protein, located at the solubility minimum, is approximately 5.4. Figure taken and adapted from ref. ¹⁸

With low concentrations of electrolyte, the solubility of a protein in aqueous solution is usually increased. This phenomenon is termed 'salting in'. In contrast, if one were to increase the concentration of electrolyte, protein solubility will begin to rapidly decline, and the protein will begin to 'salt out' or precipitate. This behaviour, typical for many proteins, is illustrated in Figure 1.3.

‘Salting in’ behaviour can also be explained by Debye-Hückel theory¹⁸. By referring to (1.1), and considering that the inverse Debye length (κ) may be given by

$$\kappa = \sqrt{\frac{8\pi N e^2 I}{1000 \epsilon_r k T}} \quad (1.2)$$

N is Avogadro’s number, e is the charge on an electron, I is the ionic strength, ϵ_r is the dielectric constant, k is the Boltzmann constant and T is absolute temperature.

By inspection of (1.1) and (1.2) one finds that by making additions of electrolyte, increases in the ionic strength (I) will result and therefore κ will also increase. Thus by adding low concentrations of electrolyte, protein solubility will increase (Figure 1.3). At higher ionic strengths, Debye-Hückel theory fails to explain ‘salting-out’ behaviour¹⁸.

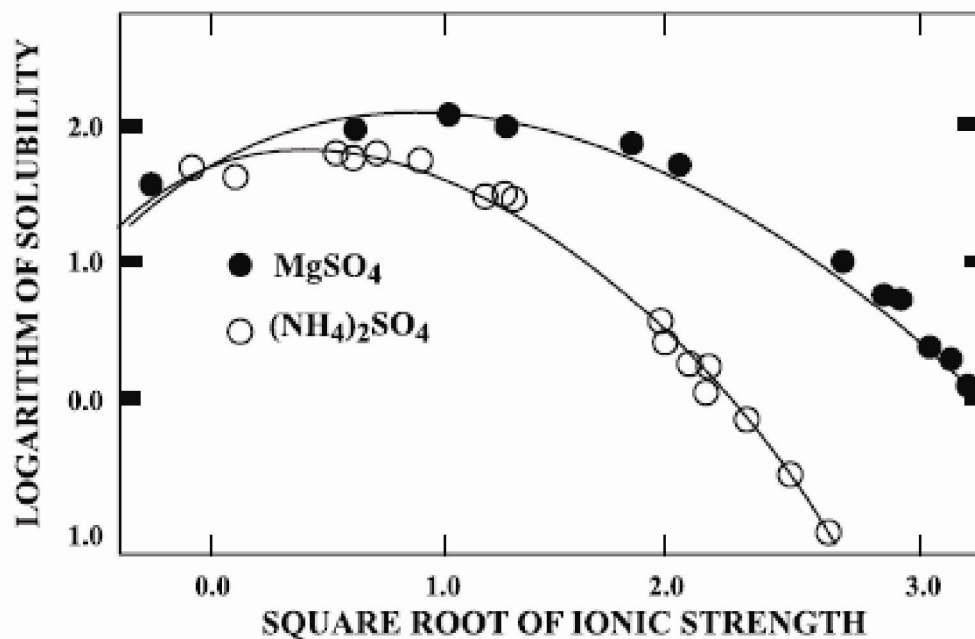


Figure 1.3 Typical ‘salting in’ and ‘salting out’ behaviour of a protein illustrated by changes in protein solubility with respect to the ionic strength of various electrolyte solutions. At low ionic strength, protein solubility increases, and begins to fall rapidly at higher ionic strengths. The protein used here was enolase (a metalloenzyme) and the figure was taken from ref.¹⁹

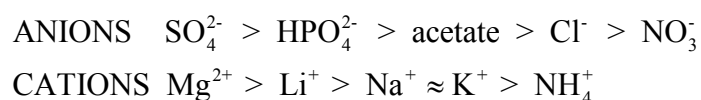
Salting-out behaviour is not well understood¹⁸⁻¹⁹. It is thought that the competition between the protein solute and the electrolyte for solvent molecules (for example, water) to maintain their hydration shells¹⁸ is responsible for this effect. In an 'attempt' to fulfil their electrostatic requirements, protein molecules begin to self-associate or 'salt-out'.

It is found that at higher salt concentrations protein solubility may be better described by the following empirical expression due to Cohn¹⁸ (1.3)

$$\log S = B - KI \quad (1.3)$$

where S is the solubility of the protein, B is a constant referred to as idealised solubility (a function of protein, pH and temperature). K is a salt specific constant (again a function of pH, mixing and salt), and I is the ionic strength.

The effectiveness of various ions to decrease protein solubility, which is of importance to protein crystallization, can be indicated by a Hofmeister series²⁰ and various lists, and groupings of various ions of various types exist within the literature^{18, 20}. The Hofmeister series was originally compiled with respect to the effectiveness of various ions to affect the solubility of egg white proteins¹⁸ and the original series is given by the series immediately below.



It was generally thought that “water structure making” and “breaking” by salts were central to the Hofmeister series²⁰, however recent work has cast doubt on this popular notion²⁰ and lends support to the idea of a direct interaction between the ion and the macromolecule which in turn affects the solubility behaviour.

Recent work²⁰, has highlighted the importance of these Hofmeister effects, mostly due to their relevance to a wide range of fields such as enzyme activity, protein stability and the crystallization of proteins²⁰. Despite the obvious importance of ion-specific Hofmeister effects, a molecular level understanding of the process *is still not available* and much work remains to be done²⁰. The reader is thus referred to comprehensive reviews (such as given in ref.21) of this very large, complicated and interesting topic for further reading.

Within the context of this thesis, the Hofmeister series has importance with respect to protein solubility, which is directly linked to protein crystallization via its effect on the supersaturation of a protein solution. However, a notion of a ‘well-behaved series of ions’ which have predictable effects on protein solubility is erroneous as some proteins display strange and counter-intuitive solubility behaviour.

For example, some protein systems (apoferritin and sickle cell haemoglobin²² for example) exhibit retrograde solubility²², which is marked by a decrease in protein solubility with an increase in temperature²³. Moreover, lysozyme, at high pH, follows an inverse Hofmeister series at low ionic strength but then suddenly reverts to a direct Hofmeister series as the ionic strength is increased²¹.

It may therefore be said that protein solubility, is currently considered a very complicated process which depends on a large variety of solution conditions and interactions between protein, solution and any ions present in solution. It is a very active area of research today and is still not properly understood¹⁸.

At a very basic level, in order for one to form a protein crystal, one has simply to add precipitant (either of an ionic or an organic nature) to a monomerically pure protein solution at the correct pH and protein concentration and wait for a period of time. On the face of it, the task appears deceptively simple. Yet when one considers the possible range of protein-protein, protein-solvent, precipitant-solvent and protein-precipitant interactions available at varied pH and in the presence of various types of precipitant of varied ionic strength, the sheer complexity of 'guessing' the correct crystallization conditions becomes apparent and is daunting. This is particularly true when one does not have any knowledge of the three dimensional structure of the fully folded protein under investigation and hence is 'blind' to a molecular view of the nature of the solvent accessible protein surface. To make matters even worse some proteins are available in such small quantity, that large scale crystallization trials are unfeasible without great expense.

Despite, this and many other technical problems associated with arriving at the correct solution conditions required for protein crystallization, what is known with some degree of certainty at least, is that the first step towards the formation of any crystal, protein or otherwise, is the formation of a stable solid phase from a supersaturated solution.

There are various practical methods for causing the supersaturated condition and some are given in Table 1.1. All of these methods rely on various solution adjustments to minimise protein solubility.

Table 1.1 Practical methods for creating the supersaturated condition. Table adapted from ref.19

1	Direct mixing of solutions to create a supersaturated solution
2	Alter temperature
3	Alter the salt concentration
4	Alter pH
5	Add solubility changing ligand
6	Alter dielectric of medium
7	Direct removal of water
8	Change the protein concentration

1.D Metastability, metastable zone width and crystal nucleation

The driving force behind crystallization is supersaturation¹⁸. A solution in which the solute concentration exceeds the solution equilibrium concentration at a given temperature is termed a supersaturated solution. Supersaturated solutions are by their very nature metastable¹⁸.

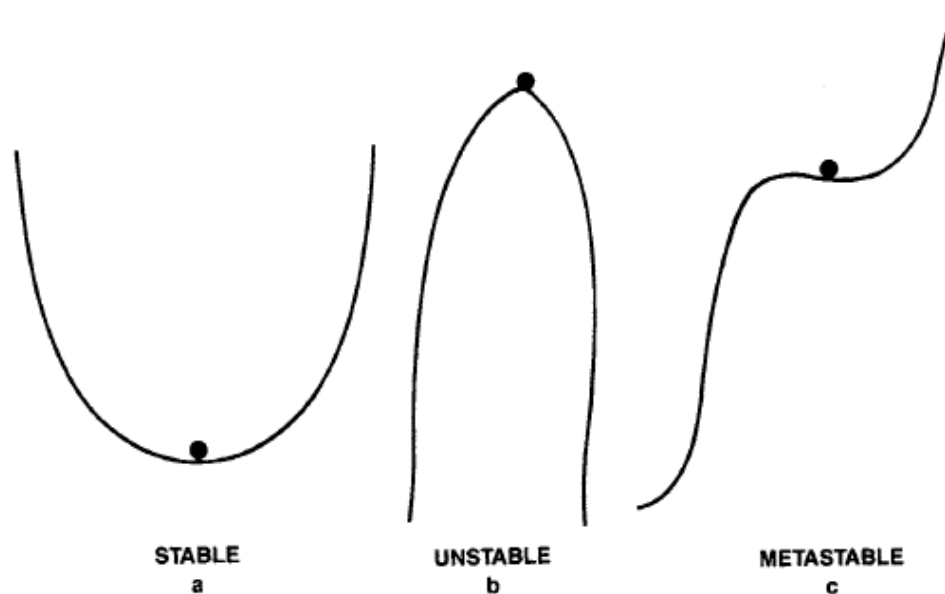


Figure 1.4 Three states of an arbitrary crystallizing solution. (a) Refers to a solution which is termed stable (b) represent an unstable solution and (c) represents a solution which is metastable. Figure is adapted from ref. 18.

By reference to Figure 1.4, one notes a cartoon representation of three arbitrary states of a crystallizing solution. A solution which is properly stable is depicted in Figure 1.4(a). The stable solution is at its lowest energy state and any perturbation will not shift the state of the solution. A solution which is in an unstable state is depicted in Figure 1.4(b). In this case, any small perturbation is able shift the state of the solution easily and hence it is unstable. A solution which is in a metastable state is depicted in Figure 1.4(c). The metastable solution is in a ‘quasi-minimum energy’ state and may be shifted into a lower, more stable energy state by a small but *finite* perturbation.

As all supersaturated solutions are metastable, making a crystallizing solution more supersaturated may not immediately result in crystallization. To explain why a crystallizing solution does not immediately form a crystal one needs to first consider classical nucleation theory.

Classical nucleation theory (CNT) is a simple and widely used description of the nucleation process²⁴. This thermodynamic description of nucleation was first developed by Gibbs at the end of the 19th century. Gibbs defined the Gibbs free energy change required for cluster formation, as the sum of the free energy change required for liquid-solid phase transformation (ΔG_V) and the Gibbs energy change for the formation of a surface (ΔG_S)²⁴.

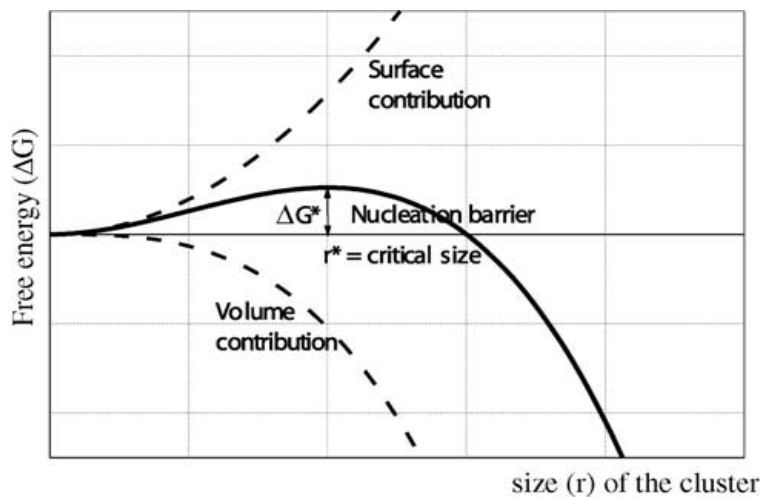


Figure 1.5 Surface and volume contributions to the overall Gibbs energy of cluster formation. Figure adapted from ref. 25. If the overall Gibbs energy is negative, clusters will form and grow.

Since the solid state is more stable than the liquid state, ΔG_V has a negative contribution to the overall Gibbs energy change. The formation of a solid surface involves positive Gibbs energy changes which are proportional to the size of the cluster²⁴. “Competition” between the contributions of ΔG_V and ΔG_S will therefore dictate whether a formed cluster will continue to grow or begin to ‘dissolve’ back into solution (Figure 1.5).

The situation is more easily described with the aid of a simple intuitive example²⁵.

If one were to imagine a protein monomer which has been dissolved within an aqueous solvent and is free to move amongst the solvent molecules. The solution composition is such that a crystallization event is thermodynamically favoured. Imagine also that protein monomers (represented for ease of visualization as balls, *vide infra*), have cubic symmetry (even though they are represented by balls in the diagram) and have 6 bonds which are normal to each face of the cubic growth unit.

Within solution, a number of growth units will collide (inelastically) with one another and hence, on occasion, collisions will result in a 'bonding' event which will form clusters of an arbitrary size. The location of cluster formation is purely random and thus an exact location for the collision event is not given.

One finds that cluster lifetimes are governed by a balance between the cohesive forces between growth units (given by shared bonds between growth units) and the number of bonds shared between the growth units and the solvent itself. The number of shared bounds within the cluster is proportional to the volume (ΔG_v) whilst the number of unshared bonds is proportional to the cluster surface area (ΔG_s).

Hence an energy balance for the simple cubic system, as just described, may be given by

$$\Delta G = -\Delta G_v + \Delta G_s \quad (1.4)$$

ΔG_v and ΔG_s are the volume and surface Gibbs energies as depicted in Figure 1.5.

For cubic systems of edge size 2 (Figure 1.6) which contain 8 growth units and 12 saturated bonds, the surface forces (24 unsaturated bonds) are in excess of the forces holding the cluster together and hence the cluster will fall apart.

At edge sizes of 3 or more, surface forces are less than volume forces and the cluster survives and grows spontaneously. At clusters of edge size of exactly three, both surface and volume forces are equal, and hence a critical nucleus is said to be formed (Figure 1.5).

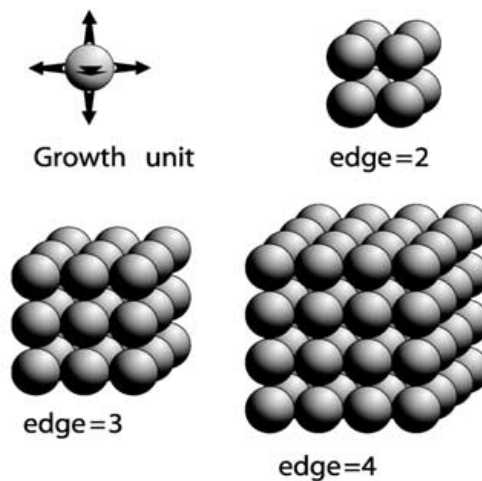


Figure 1.6 Clusters of various sizes. The edge length of each cluster is depicted. Figure adapted from ref.25

The reason why supersaturated solutions are termed metastable is because the critical nucleus first needs to form before a macroscopic crystal can grow. The metastability of the solution is inversely proportional to the level of supersaturation¹⁸. Every solution has a maximum amount that it can be saturated before it becomes unstable. The zone between the solubility curve and this unstable zone is termed the 'metastable zone'.

This discussion refers to homogeneous nucleation, which is nucleation within a homogenous substance²⁶. However, in practice, a much more frequently encountered form of nucleation (as explained via CNT) is that of heterogeneous nucleation.

Heterogeneous nucleation may be described as nucleation which has taken place on phase boundaries, surfaces (such as container walls) and impurities such as dust particles. The energy required for nucleation via a heterogeneous nucleation route is much lower than that required for homogenous nucleation²⁶.

The existence of such heterogeneous surfaces promote nucleation at lower energies due to an increased wetting effect. Particles can interact more favourably due to non-zero wetting angles.

1.E Protein crystal nucleation requires an alternative to CNT

Despite the usefulness of CNT, the theory is based on a number of assumptions which limit the theory's usefulness to particular situations²⁴⁻²⁵. For example:

- 1) The building blocks of the stable cluster are ordered, thus the molecular arrangement in a crystal embryo is the same as that of a large crystal.
- 2) The curvature dependence of the surface tension is neglected and the surface energies are assumed to be temperature independent.
- 3) The growth of clusters takes place one monomer at a time. Collisions between more than two particles are ignored. The cluster is also assumed to be at rest and not subject to any motion (translational, vibrational or rotational). In other words, the various entropic components of the Gibbs free energy change are not properly accounted for.

Given that most of the assumptions detailed above do not apply to the process of protein crystal nucleation it is with little wonder that a number of shortcomings²⁴ are found when CNT is used to describe the protein crystal nucleation process.

An alternative approach was therefore considered which views proteins in solution as colloidal systems which have highly anisotropic short range interactions²⁵. These particular types of systems are known to display a region of liquid-liquid phase separation on their phase diagrams²⁷. This phase separation behaviour has been observed on many occasions²⁸⁻²⁹. Moreover, these experimental findings have been supported via computer simulation³⁰ which has found that high density fluctuations near a critical point of liquid-liquid phase separation greatly lowers the energy barrier to nucleation and is therefore a favourable nucleation route.

Both experimental and theoretical results suggest the presence of liquid phase protein micro-droplets within the crystallizing solution which fluctuate or oscillate³¹ between a high-entropy/low-enthalpy states (low protein concentration) and a low-entropy/high-enthalpy states (high protein concentration). The density fluctuations are said to be powered by the short range attraction between protein monomers³¹, which are in turn are mediated via the chemical nature of the solution (for example pH , salt type and concentration).

Within these high concentration protein droplets, the protein molecules are extremely close to one another and the transition to a lower energy crystalline state can be easily achieved.

For lysozyme, the formation of liquid droplets (of high protein concentration) was found to be the rate-determining step in the nucleation process²⁴. Furthermore, it has been suggested that the formation of ordered solid phases within the high density liquid intermediates were also a rate-determining²⁴ process.

The implication here is of a two-stage nucleation process, proceeding firstly by liquid-liquid phase separation which causes the formation of high density/high concentration droplets that undergo internal structural rearrangements to form crystalline nuclei^{24, 32}. The process is depicted in cartoon form in Figure 1.7. In any case, there is an overwhelming body of experimental evidence based on a variety of different experimental techniques which lends support to the applicability of the two-step nucleation mechanism to the nucleation of lysozyme protein crystals^{26, 33-34} and to possibly other protein crystal systems as well. . Experimentally, the formation of metastable liquid-like cluster which may precede the actual nucleation event has mostly been found via light scattering ^{24, 36} studies.

The new alternative to CNT, the two-step mechanism has been shown to be valid for a number of non-protein based systems such as several organic³³, inorganic and colloidal systems³⁴. Additionally, some cases of biomineralization³⁵ have been found to display this type of nucleation mechanism

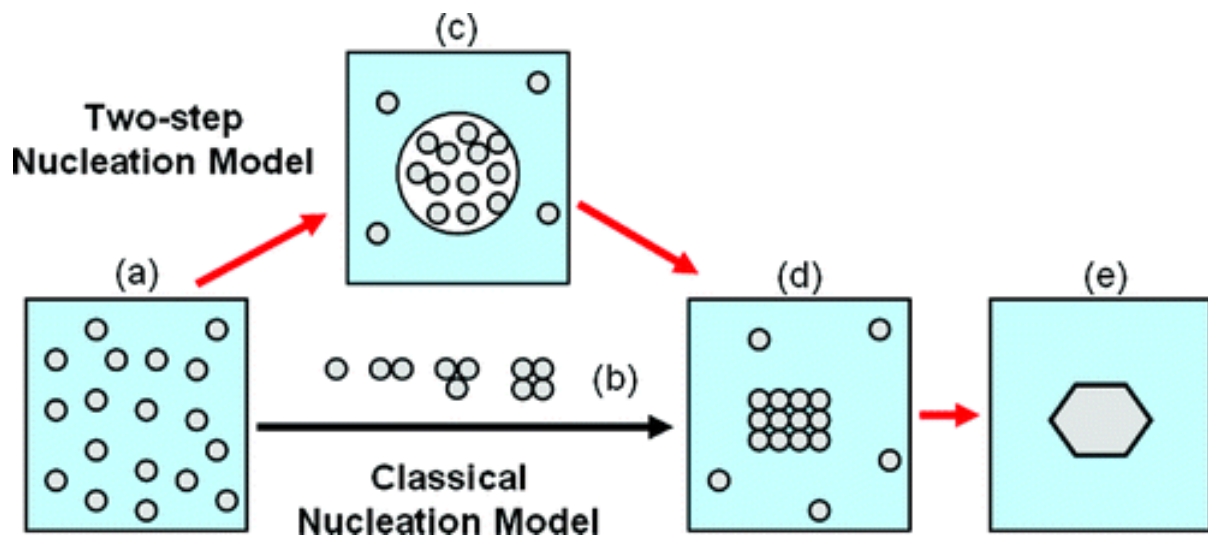


Figure 1.7 Alternative pathways leading from solution to solid crystal: (a) supersaturated solution; (b) ordered subcritical cluster of solute molecules, proposed by classical nucleation theory; (c) liquid-like cluster of solute molecules, dense precursor proposed by two-step nucleation theory; (d) ordered crystalline nuclei; (e) solid crystal. Figure taken from ref.24

Another important aspect of the nucleation process is the “induction time”. The induction time is defined as the time between achieving sufficient supersaturation for nucleation to occur and the actual appearance of nuclei³⁷. The proper measurement of the ‘real’ induction time is difficult, due to the extremely small size of the critical nuclei.

However, a ‘pseudo-induction time’ can be measured, which involves waiting additional time for newly formed crystalline nuclei to reach experimentally measurable size³⁷. At the risk of some re-iteration (as has already been stated within the subsection detailing metastability), typical induction times for protein solutions used within this thesis are in the range of about one to two hours³⁷⁻³⁸.

1.F Protein crystal growth

Crystallization occurs in two stages, the first stage is nucleation as just discussed. The second stage is that of the growth of the nuclei into a macroscopically-sized protein crystal. The process of protein crystal growth has been studied extensively with the aid of *in-situ* AFM and there are a number of excellent and authoritative articles/reviews (the reader is referred to references 41-44 in particular for further reading) on this vast and interesting subject.

As with nucleation, the degree to which a solution is saturated plays a central role in the growth of protein crystals³⁹. For crystal growth to proceed, the surface of a growing crystal must be able to accept incoming molecules and incorporate them into the growing crystal surface. The way in which this process usually proceeds is described with the aid of the Terrace-Ledge-Kink (TLK) model of crystal growth⁴⁰. The model describes how a growth unit must first diffuse from the bulk solution to a developing crystal face in order to be incorporated. Once at the crystal surface, the growth unit can exist in one of three different states:

- 1) The growth unit may have landed directly onto an available kink site and has therefore become incorporated directly into the crystal.
- 2) The growth unit may land away from an available kink site, and needs to 'migrate' (via diffusion) toward a step edge and finally adhere to a kink site for incorporation.
- 3) The growth unit will desorb and return to the bulk.

Kink sites are of supreme importance in the crystal growth process, as they present energetically favourable binding conditions/sites for incoming growth units. Mostly because the incorporation of growth units at these sites involves the 'formation' of a larger number of 'bonds' than that for a growth unit landing on another area of the crystal surface. A kink site is depicted in Figure 1.8.

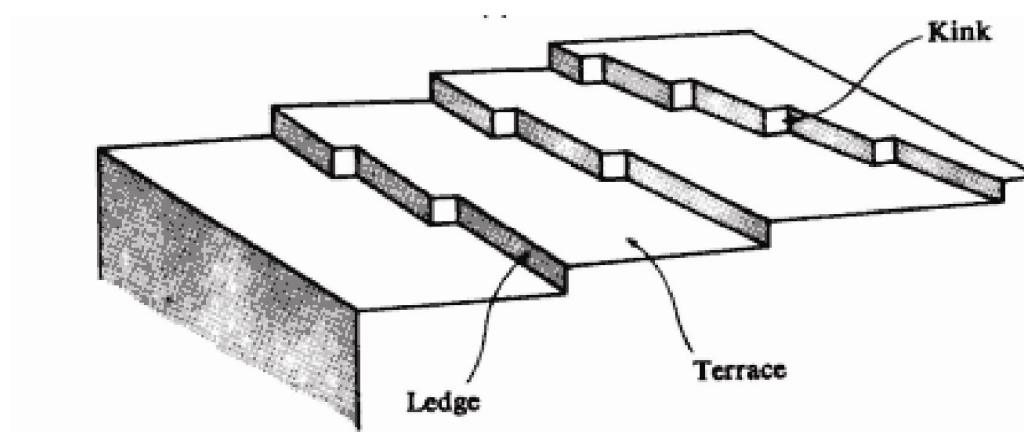


Figure 1.8 A cartoon representation of a developing crystal face which shows the positions of the kink, the ledge and the terraces as described by the TLK model of crystal growth. Growth units will find more energetically favourable attachment at kink sites than any other position on the crystal surface. Figure taken from ref. 40

There are four main mechanisms which can be used to describe the growth and development of crystal faces of protein crystals. The mechanisms are analogous to those found in non-protein crystals⁴¹. Because of the lack of similarity between crystal growth faces, these four growth mechanisms may occur simultaneously on each different crystal face³⁹. The four mechanisms are spiral dislocation growth, two dimensional island growth, three dimensional growth and normal growth. All four proceed by the process described by TLK theory but operate in different ways to generate step edges and kink sites.

Over a broad range of medium supersaturation levels most protein crystals are able to generate step edges and new growth layers via the process of two dimensional nucleation (Figure 1.9). This growth mechanism is usually observed at higher supersaturation^{39, 41-42} and is not found at lower supersaturation, where growth by spiral dislocation dominates.

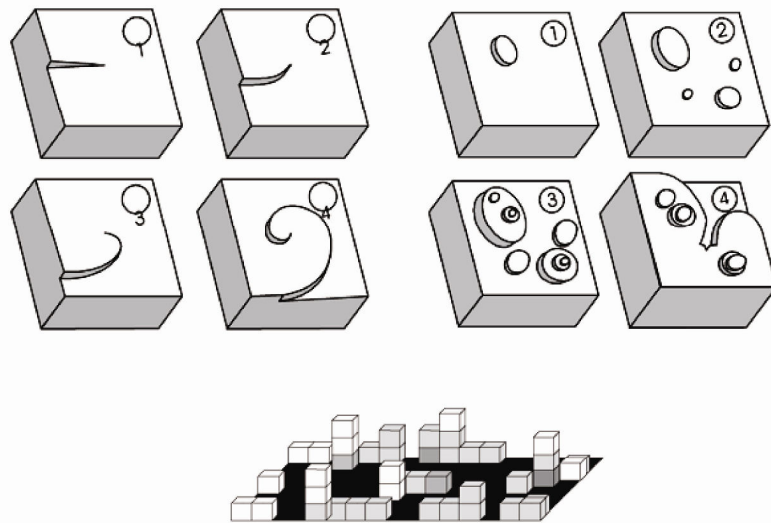


Figure 1.9 A cartoon representation of top left: spiral dislocation growth, top right: two dimensional nucleation growth and bottom middle: a surface making a transition from the two dimensional mode of growth to three dimensional mode of growth. Figure adapted from ref.43

As has just been mentioned, at lower supersaturation, step edges are generated via spiral dislocations (Figure 1.9) and growth units are incorporated into kink sites only⁴³. An example of supersaturation induced changes in crystal growth mechanism from spiral dislocation growth to two dimensional nucleation growth can be seen on the lysozyme crystal as the level of supersaturation is increased⁴¹⁻⁴².

At very high levels of supersaturation it has been observed that crystal growth proceeds by the addition of three dimensional nuclei (even as whole microcrystals sometimes) to the growing crystal face⁴¹ (Figure 1.9). A fourth, but rare growth mechanism has been observed for protein crystals, which is termed normal growth. This involves the surface developing normal to itself without the need for step-wise growth mechanisms, and is usually only observed on crystals grown from the melt or from the vapour phase⁴¹.

1.G Protein phase diagrams and protein crystallization

The Miers diagram¹⁸ (Figure 1.10), was traditionally used by crystal growers to illustrate the effects of temperature on crystallization. The diagram is divided into 3 regions

- 1) The stable zone, an area where protein solubility is may be termed undersaturated.
- 2) The metastable zone, where protein concentration is greater than the solubility limit. Existing crystals may grow within this zone but generally no crystal nucleation occurs here.
- 3) The labile zone, where supersaturation is high and spontaneous nucleation and a small amount of crystal growth can occur.

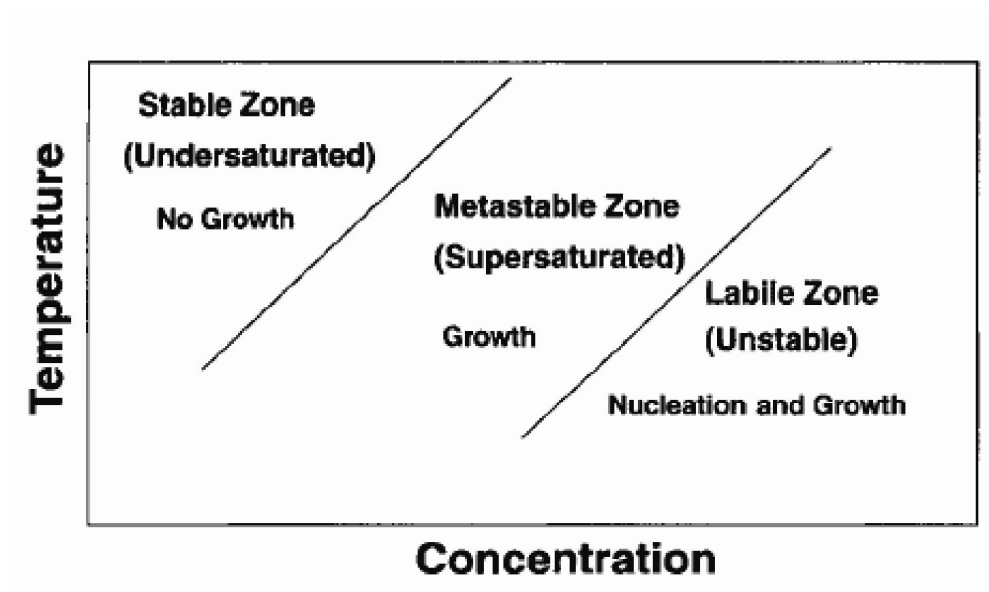


Figure 1.10 The Miers diagram indicating three main zones on the temperature/protein phase diagram.
Figure from ref. 18

A more generic phase diagram for protein crystallization studies exists²². The generic diagram is shown in Figure 1.11. By adding various precipitants¹⁹ (for example ammonium sulphate, ethanol or polyethylene glycol), as one usually does when crystallizing a protein, the extent of the anisotropic short range protein-protein interactions are be altered^{19, 28}. As a result, zone widths and zone boundaries, as indicated in Figure 1.11 may also be altered. The alteration is due to the nature of the precipitant and cannot be predicted easily²².

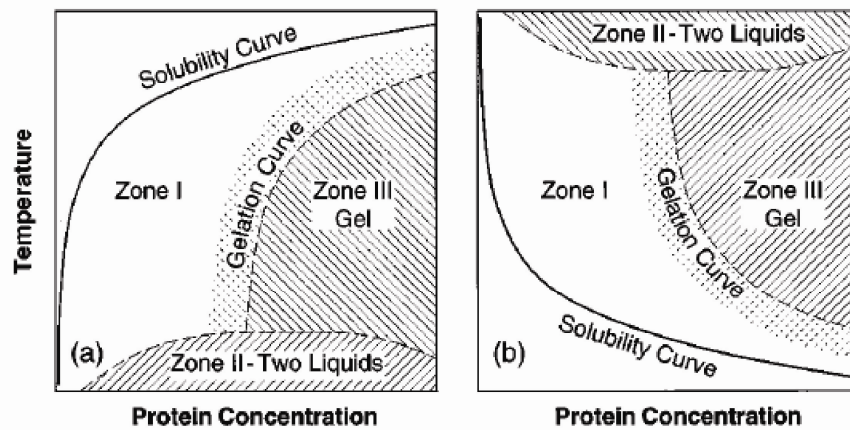


Figure 1.11 Generic phase diagram proposed by Muschol²² and co-workers. Panel (a) indicates a phase diagram for proteins with conventional solubility behaviour. Panel (b) indicates phase diagram for proteins with retrograde solubility. Solution conditions above the solubility curve in (a) and below the solubility curve in (b) are metastable with respect to crystallization. Zone II indicates an area of liquid-liquid phase separation. Gelation is common in Zone III and indicative of very high protein concentrations. Cross hatched area on the border between Zone I and Zone III is an area of amorphous precipitate formation. The best position for protein crystallization is in Zone I, just outside the cross hatched area and near Zone II^{19, 28}.

Figure taken from ref.22

A phase diagram which is of more practical utility is a protein/precipitant phase diagram, elucidated at constant temperature (Figure 1.12). Again the three main zones are indicated on this phase diagram.

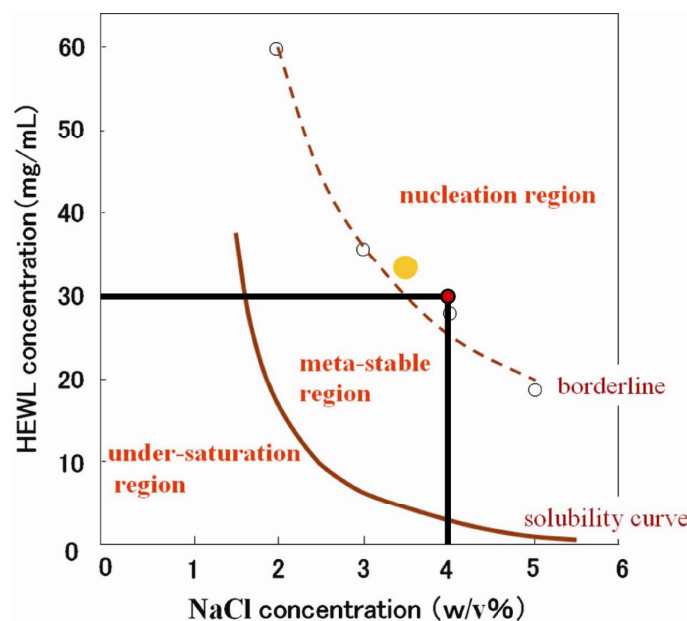


Figure 1.12 The lysozyme/NaCl phase diagram at pH 4.5 taken from Iwai and co-workers⁴⁴. An arbitrary solution starting condition is indicated by a red-dot on the diagram. Figure taken and adapted from ref.44

Within this thesis and Chapter 2 in particular, we have made extensive use of lysozyme-NaCl phase diagrams compiled by Iwai et al.⁴⁴. This diagram was compiled by crystallizing lysozyme over a wide range of different pH conditions. Specifically, the phase diagrams were compiled using crystals grown via the dialysis method, using a 50 μ l micro-dialysis button with a membrane which had a cut-off weight of 1000 Daltons.

The borderline between the metastable and the nucleation zone was determined in the following way. The concentration of precipitant (in this case NaCl) was increased incrementally in steps of 0.1 (w/v) % for a specific protein concentration at a specific pH. With each incremental step, the solution was left for a period of 8 days at 293 K. Solutions were checked to see if any crystallization had occurred. If a crystallization event was indeed observed, a point was thus marked on the diagram which gave the corresponding precipitant and protein concentrations (at a specific pH) which led to the crystallization event. The borderline between the metastable zone and the nucleation zone was thus compiled by joining these points on the diagram as shown in Figure 1.12.

The solubility curve was determined by dissolving previously grown crystals within a dialysis button. Specifically, precipitant concentrations were decreased in increments of 0.1 (w/v) % per day. At the end of each day, an observation was made to see if crystals had completely dissolved. If complete dissolution had occurred, a point was marked on the lysozyme-NaCl diagram. If complete dissolution had not occurred, the precipitant concentration was further lowered by 0.1 (w/v) % and the process continued until complete dissolution was achieved. The solubility curve (at different pH) was compiled by joining the points on the phase diagram.

Based on 3 years of experimental experience with lysozyme crystallization in the presence of NaCl under 'batch' type conditions, and by using bulk solution conditions (of the type featured within Chapter 2), we have found these phase diagrams (Figure 1.12) to have reasonable accuracy with regards the prediction of a crystallization and a non-crystallization event. Specifically, we have found that under 'crystallizing' conditions (such as those found within the nucleation zone at a particular pH) a crystallization event would occur within a 1-4 hour time period (depending on level of supersaturation). At higher levels of supersaturation one can achieve lysozyme crystallization within as little as 45 minutes. Under non-crystallizing conditions (such as those depicted within the metastable zone in Figure 1.12) no crystallization event would be achieved during a 1-4 hour period.

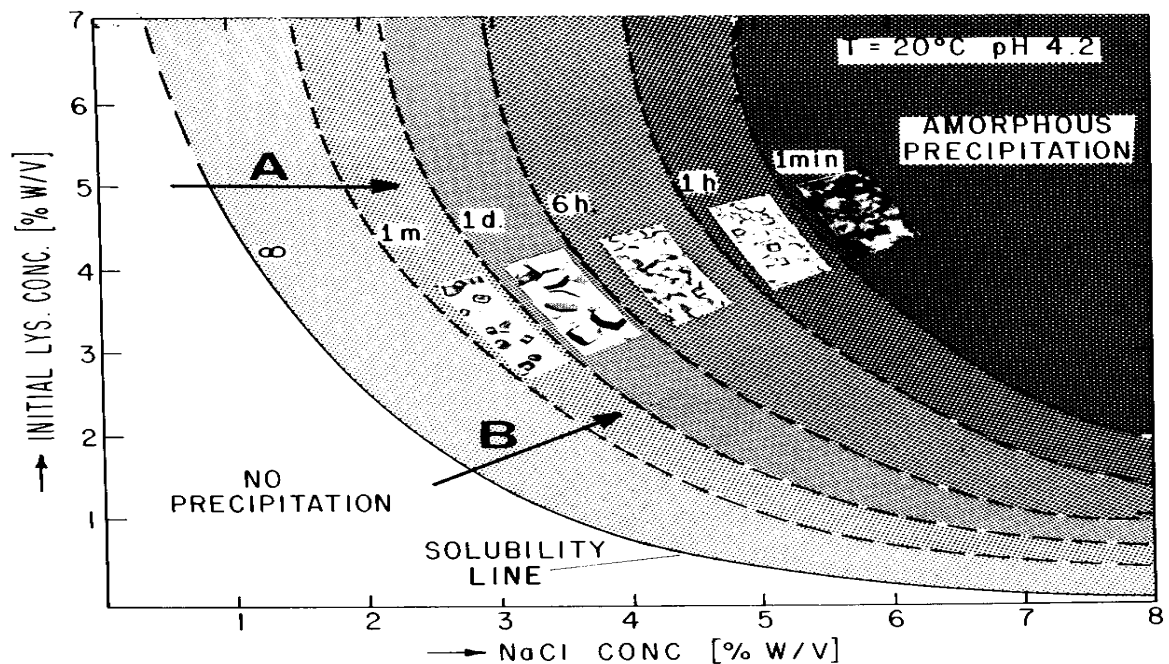


Figure 1.13 A lysozyme-NaCl diagram compiled at pH 4.2 and 20 degrees Celsius, with a temporal element. The figure has been taken from ref. 45. Lines A and B refer to 'paths' taken across the diagram via dialysis and vapour diffusion crystallization experiments respectively. Times to lysozyme crystallization at various lysozyme-NaCl compositions are indicated on the phase diagram.

These experience-based observations can be corroborated via reference to a 'temporal' lysozyme-NaCl diagram⁴⁵ (Figure 1.13). One notes that on this diagram at pH 4.2 and using crystallization conditions of the type found within Chapter 2, lysozyme crystallization may be achieved after an approximately a 1 to 6 hour period.

For a complete picture of the entire lysozyme crystallization process, which would incorporate all reasonable protein and precipitant concentrations at different pH values, one would need an impossible-to-visualize multi-dimensional plot (4 dimensions minimum). This type of plot has never been compiled and is not currently in existence. In fact a suggestion in this regard was made at a recent international conference on macromolecular crystallization. The suggestion was unfortunately met by derisory laughter.

In terms of the relevance of these types of diagrams to experimental work presented within this thesis, they are currently of high relevance. This is mostly due to the fact that these types of diagrams are not easily available or have never been compiled at all. Therefore this is all there is to go on at present. More sophisticated and efficient compilation of such diagrams would require a dedicated experimental set-up with robotic assistance.

1.H Commonly used practical methods for protein crystallization

One is faced with one of two possible starting conditions

- 1) no crystallization protocol exists, in which case one would be screening for possible crystallization conditions.
- 2) a crystallization protocol is in existence and therefore one would be trying to optimise conditions in order to improve either crystal size or quality.

In either case there are series of commonly used “industry standard” techniques which enable one to either screen or optimise protein crystallization conditions.

The most widely used methodology is that of vapour diffusion^{19, 46-47}. In vapour diffusion, small droplets of precipitant solution and protein solution are mixed 1:1 on the surface of a glass coverslip (total volume of droplet is normally and approximately 10 µl) to provide a droplet that is in an initially undersaturated condition.

The coverslip is then inverted over a reservoir of solution which is at higher osmotic pressure than that of the droplet and the arrangement is sealed. Water is then drawn from the droplet by vapour diffusion until an osmotic equilibrium is struck between the droplet and the reservoir. In effect, this increases both protein and precipitant concentrations slowly over a period of time until nucleation hopefully occurs (Figure 1.16). The droplet can be either in the ‘sitting’ or ‘hanging’ type configuration (Figure 1.14).

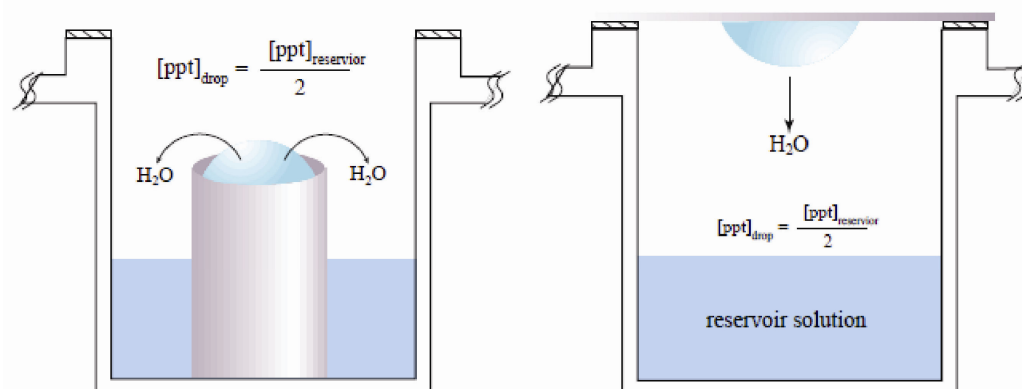


Figure 1.14 The sitting drop (left) and the hanging drop (right) vapour diffusion techniques for screening and optimization of protein crystallization trials. “[ppt]” in diagram refers to the concentration of precipitant and is sometimes half that of the reservoir. Figures taken from ref.48

Another method based on vapour diffusion is the ‘sandwich’ technique⁴⁹ (Figure 1.15). A protein and precipitant mix are placed between two siliconised glass coverslips and the droplet is dehydrated via vapour diffusion. This method allows ease of droplet visualization with microscopy, although the method is almost exactly like that of the standard sitting and hanging drop techniques.

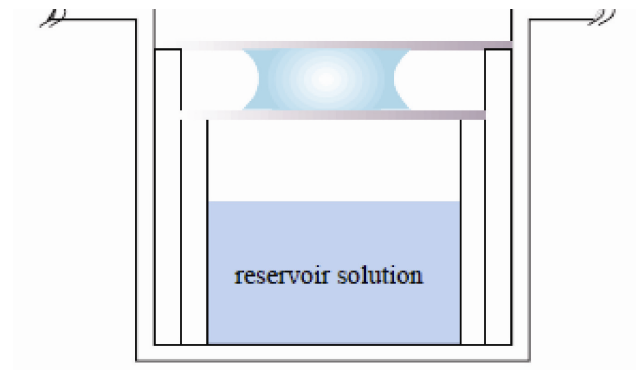


Figure 1.15 The sandwich drop vapour diffusion crystallization technique. The protein solution is sandwiched between a coverslip and water is drawn via vapour diffusion from the droplet by the reservoir.
Figure taken from ref.48.

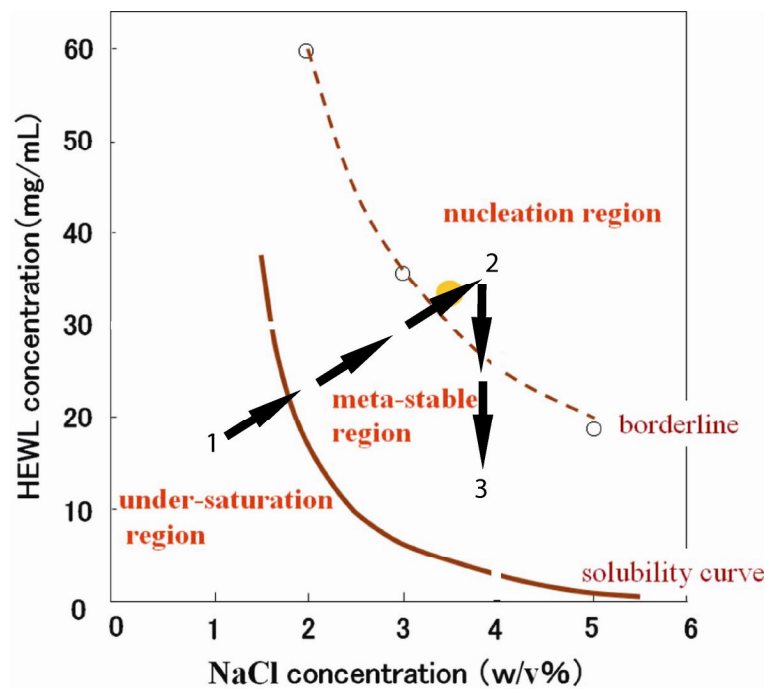


Figure 1.16 Lysozyme/NaCl phase diagram taken from Iwai⁴⁴ and co-workers. A typical path taken across the phase diagram by a successful vapour diffusion experiment is shown by the series of black arrows. At position 1, the solution is undersaturated and is taken to position 2 where nucleation occurs. Due to crystal nucleation, the local protein concentration decreases and the solution is taken to position 3 which is conducive to good crystal growth. Figure adapted from ref. 44

An infrequently used technique is that of free interface diffusion⁵⁰ (Figure 1.17). In this method, protein solutions are placed in liquid contact with precipitant solutions within the confines of a narrow bore capillary tube. Both solutions are allowed to diffuse into one another thereby screening a wide variety of protein/precipitant combinations simultaneously across the length of the capillary. A related technique, called counter diffusion via the 'gel acupuncture' method⁵¹⁻⁵², allows diffusion of precipitant into 'gelled' (via the addition of agarose) high concentration protein solutions within narrow bore capillaries. The gelled protein solution can alternatively be layered with concentrated precipitant solution in a gel-slab type arrangement.

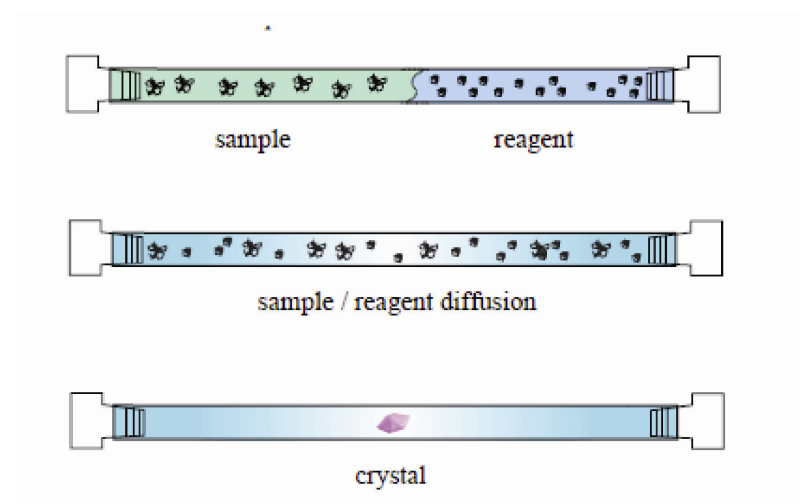


Figure 1.17 An example of a free-interface diffusion set-up. A narrow pore capillary is filled with both protein and precipitant solution and diffusion is allowed to occur. Figure taken from ref.48.

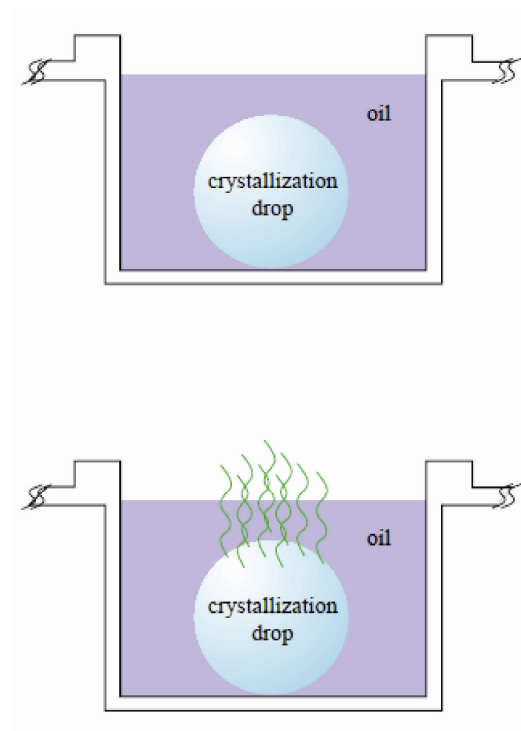


Figure 1.18 The microbatch method showing an oil droplet underneath a layer of oil. The green lines (bottom) indicate water diffusing out of the droplet. Figures taken from ref. 48.

In the microbatch method^{6, 53-56} (Figure 1.18 and explained in more detail further on), small volume droplets of protein and precipitant mix are placed beneath a layer of paraffin oil, silicon oil or a mixture of the two oils. Water can be drawn from the submerged droplet by varying the ratio of silicon oil to paraffin oil, and this is called the modified microbatch method⁵⁷⁻⁵⁸. The degree of supersaturation and hence dehydration may therefore be altered by varying the ratio of silicon and paraffin oils under which the droplet is submerged⁶⁰⁻⁶¹. Under non-dehydrating conditions, protein crystallizing solutions need to nucleate *as is*. This can sometimes be a major set back when using the microbatch method.

An advantage of this technique is the ability to use small protein volumes. Additional advantage is gained by the lack of contact between the droplet and the container walls which can lead to unwanted heterogeneous nucleation^{57, 62-64}.

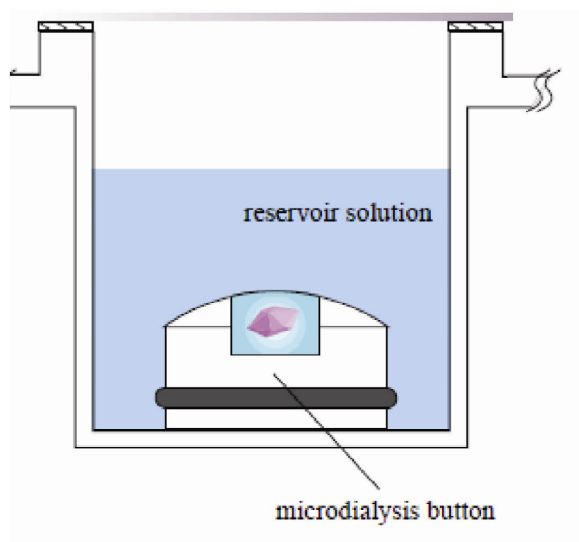


Figure 1.19 A microdialysis arrangement showing a sample within a dialysis button sealed with dialysis membrane. Water and some precipitant are allowed to exchange between the button and the reservoir across the membrane. Figures taken from ref. 48

Protein crystallization by dialysis⁵⁹ (Figure 1.19) involves placing a protein sample in a dialysis button, which is then sealed with the aid of a dialysis membrane. Water and precipitant can exchange freely between the button and the surrounding reservoir through the membrane until an equilibrium is reached. With the dialysis technique one may alter the precipitant concentration whilst keeping the protein concentration constant. Major disadvantages are that protein tends to get stuck to the membrane and is hard to remove.

1.I The microbatch method – an ‘accidental’ example of protein crystallization at the oil/water interface.

The application of water insoluble oils to protein crystallization trials, was originally described by Chayen⁵³⁻⁵⁴ *et al.* who used low density paraffin oil ($\rho = 0.84$ g/cm³) as an inert sealant and to prevent water evaporation from small volume (1-2 μ l) protein crystallization trial droplets containing protein and precipitant. Paraffin oil was deemed suitable for use as it was found that other oils (not explicitly stated which ones within the literature) interacted unfavourably with the crystallization trials (for example precipitation occurred).

The microbatch technique is featured in Figure 1.18 and as mentioned previously, involves dispensing a small volume droplet of protein and precipitant mix underneath a layer of either inert silicon or paraffin oils. A mixture of the two oils is sometimes used. Paraffin oil was found to act largely as a barrier to water loss from the droplet, however water loss from droplets submerged under silicone oil alone was found to be significant^{55, 60}. It was subsequently found⁶⁰ that by using different ratios of the two oils the rate of dehydration from the covered droplet could be controlled.

Using the microbatch method for protein crystallization involves obtaining approximately the correct solution conditions (i.e. conducive to nucleation) at the beginning of the ‘experiment’ as water losses are greatly reduced in this crystal growth method in comparison to other growth methods (for example vapour diffusion relies solely on water dehydration to invoke nucleation and growth).

In addition to providing a clean and inert environment which aids trial reproducibility⁵⁵, the microbatch method is said to reduce the occurrence of heterogeneous nucleation from container walls which is detrimental to production of high diffraction quality protein crystals^{55, 61}.

For all the benefits of the microbatch method^{54, 56, 58, 60, 62}, the technique suffers from a major limitation⁵⁵ in that the use of volatile organics as precipitants and/or additives within the crystallizing droplet is forbidden⁵⁵. Volatile organics interact strongly with oils used in the microbatch method.

Microbatch is widely used for high throughput, low throughput and low volume protein crystallization trials and illustrates a current example, albeit co-incidental, of protein crystallization at an oil/water interfaces a subject which is encountered in more detail within Chapter 3.

1.J An introduction to the oil-water interface

Oil and water, under normal conditions⁶³, do not mix. This well known phenomenon is due to water-water bonds and oil-oil bonds being more favourable than the oil-water bond. If two immiscible liquids of different densities are placed within the same volume, the less dense fluid will rest upon a layer of the fluid which is the denser of the two, forming an interface between the liquids. Our interest here is not focussed on bulk solution, which will comprise either pure oil or pure aqueous phase, but on the *interface* between the two immiscible liquid phases and how such an interface may affect the extent of the lysozyme crystallization process.

The interface between two immiscible liquids, or the oil/water interface, has been shown to exhibit properties that differ greatly from properties found in bulk. For example, the ability to create large electric fields due to asymmetric charge distribution (if electrolyte is present at varied concentration within each liquid phase), effects on solute distribution - due to energies required to partition solute between the two liquid phases and the development of interfacial catalytic sites which allow reactions to occur at the interface which would not normally occur in bulk⁶⁴.

Biological processes occurring at liquid/liquid interfaces are fundamental to life itself⁶⁴, as most biological energy conversions occur at the interface between two liquids (the liquids are of course, separated from each other by a lipid bilayer). Liquid/liquid interfaces have importance within an industrial setting too, as the oil/water interface has a variety of uses within the pharmaceutical, cosmetic, paint, detergent and mining industries⁶⁴.

The oil/water interface has recently been identified as an up and coming⁶⁵ research area with regards crystallization and the directed self-assembly of molecules (both organic and inorganic). The literature has a great many examples of this and a few are given here to illustrate the wide variety of self-assembly processes that have been studied on oil/water interfaces; these include, but are not limited to, the self assembly of mesostructured porous silica⁶⁶, gold nanocrystals⁶⁷, nanoparticles⁶⁵, viruses⁶⁸⁻⁶⁹, carbon nanotubes⁷⁰ and nanowires⁷¹. One may ask as to why the oil/water interface provides such an attractive locale for the assembly and self assembly process? The main answer to this question is that at an oil/water interface, drastic reductions in interfacial energy are possible.

The placement of a single spherical particle of radius r at a planar interface between an oil phase and a water phase leads to a reduction in interfacial energy $\Delta E = E_0 - E_1$ ⁷² (where E_0 is the initial interfacial energy and E_1 is the interfacial energy after particle adsorption), which has the following form

$$E_0 - E_1 = \Delta E = -\frac{\pi r^2}{\gamma_{O/W}} \left[\gamma_{O/W} - (\gamma_{P/W} - \gamma_{P/O}) \right]^2 \quad (1.5)$$

Examining (1.5) one identifies three specific contributions to the total interfacial energy. One notices that a portion comes from the oil/water interface ($\gamma_{O/W}$), a portion from the particle/water interface ($\gamma_{P/W}$) and a portion from the particle/oil interface⁷³ ($\gamma_{P/O}$). In addition, one also notes that the particle radius has a large effect on the total change in interfacial energy.

For macroscopic particles, the total decrease in energy is larger than thermal energy ($\Delta E > k_b T$), therefore macroscopic particles become confined and 'locked to' the interfacial region⁷³.

In contrast for particles of nanoscopic size, thermal energy is comparable to the total energy reduction ($\Delta E \approx k_b T$) and therefore nanoscopic particles are able to become thermally detached from the oil/water interface⁷³. This process could be described as "the reversible thermal adsorption" of nanoscopic particles.

The size-dependence on the interfacial adsorption process becomes important in self assembly processes, as larger nanoscopic assemblies are able to find their equilibrium positions at the interface over an extended period of time, whereas macroscopic particles could be trapped in non-equilibrium states and may retard the self-assembly process. In addition to particle size (1.5) reveals that the effects of surface tension or wettability make important contributions to the overall total reduction in interfacial energy for a particle at the oil/water interface.

Wettability, is defined by the contact angle θ (Figure 1.20) between a particle and the oil/water interface⁷³. The stability, and indeed the propensity for an oil/water or water-oil emulsion, is dependent on the contact angle between the particle and the interface. Generally, the less wetting liquid becomes the dispersed phase⁷³. In other words, if the contact angle is lower than 90 degrees, oil in water emulsions are favoured. At contact angles greater than 90 degrees water in oil emulsions are favoured⁷³(Figure 1.20).

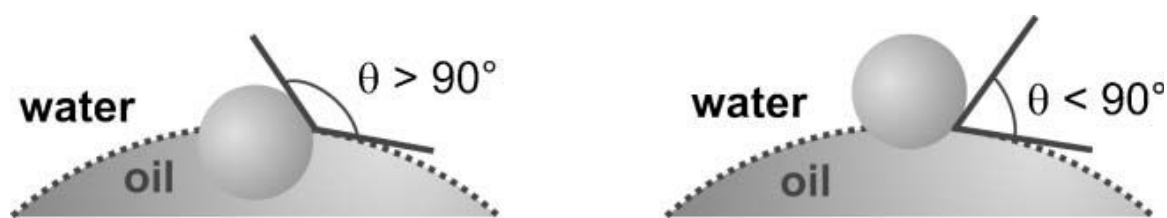


Figure 1.20 Varied contact angles for a particle at an oil/water interface. Figure from ref. 11.

The framework just described works well for spherical nanoparticles and can be adjusted for other standard Euclidean geometries⁷³. We however, deal almost exclusively with lysozyme within this thesis, which is dynamic, geometrically irregular (as are most other proteins) and has a hydrodynamic radius of approximately 1.8 nm⁷⁴.

This size classification would classify lysozyme as nanoscopically-sized. Moreover, lysozyme is able to unfold at the liquid interface⁷⁵ and possesses inhomogeneous surface properties⁷⁶. As such, one might question the applicability of the previously described conceptual framework⁷², in describing a biomolecule such as lysozyme. The framework would however appear to be largely applicable to lysozyme at low protein concentration where reversible adsorption processes are common place^{75,77}. However, at higher concentrations, where the irreversible adsorption processes of nanoscopic particles dominate⁷⁷, the applicability of (1.5) becomes questionable.

Though there have been a great many studies detailing the adsorption of proteins to oil/water interfaces, there are only a handful of studies which describe self-assembly or crystallization processes of proteins at such interfaces⁷³. Proteins possess (after purification procedures) a truly monodisperse size distribution and a variety of interesting and easily modifiable surface functionalities⁷³, which highlight them as good ‘building blocks’ for interfacial self-assembly processes. The self assembly of cowpea chlorotic mottle virus⁷³, cowpea mosaic virus⁷³, turnip yellow virus⁶⁹, tobacco mosaic virus⁷⁸, M13 bacteriophage and ferritin⁷³ have all been studied at a variety of oil/water interfaces. A small body of previous work has focussed on the generation of ordered 2D arrays of proteins for nanotechnology applications and for structural determination via electron crystallography. In particular Nagayama *et al.* have assembled different 2D protein crystals at the air/water⁸³⁻⁸⁴, mercury-water⁸⁵⁻⁸⁶ and hexane-water⁷³ interfaces.

1.K Lysozyme adsorption to oil-water and air-water interfaces

The adsorption of proteins to fluid interfaces (both air/water and oil/water) plays a key role in many areas of biology and food technology⁷⁹. From a technological point of view, protein adsorption to the fluid interface and protein behaviour in the adsorbed state is a major factor in the formulation and stabilization of various foam-based and emulsion based products in the food industry⁸⁰⁻⁸². Experimental arrangements used within Chapter 3 are able to, in some cases, generate both air/water and oil/water interfaces upon which protein crystallization can be monitored and compared. Within this subsection, we briefly outline previous work concerning protein adsorption processes which occur at fluid interfaces. Although a vast number of different proteins have been used within previous studies, in the interests of both clarity and brevity, we have decided to keep the emphasis solely on lysozyme.

Protein adsorption to a fluid interface generally follows a three stage regime⁸³⁻⁸⁴ (as defined by temporal changes in interfacial surface tension), this is true regardless of whether adsorption occurs at an air/water or an oil/water interface.

The first stage is termed the *induction period*, the second stage is that of *monolayer saturation* and the third is defined by a process of *interfacial gelation*. At higher protein concentrations (above 10 $\mu\text{g/ml}$) the induction period becomes non-existent⁸⁵, and the adsorption process becomes dominated by monolayer saturation and interfacial gelation. The general three stage adsorption process is illustrated in Figure 1.21

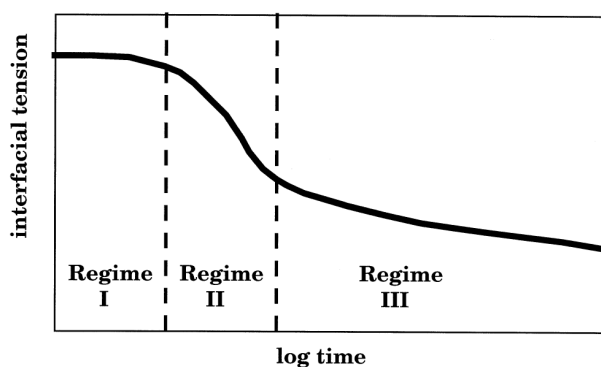


Figure 1.21 The three stage protein adsorption regime prevalent at low protein concentration. Regime I is absent at high protein concentration. Cartoon has been taken from ref. 23.

In the first stage (*induction period*, Regime I, Figure 1.21) no decrease in interfacial tension is seen, and the interfacial tension remains stable for an extended period. This lag is often seen with low concentration protein solutions adsorbing to an air/water interface⁸³, and is thought to be the result of reversible protein adsorption⁷⁵. This type of behaviour is consistent with that described by (1.5).

The reader is reminded, that within this thesis, we deal with protein concentrations well in excess of that required for the measurement of the lag phase and hence none will be evident.

The second stage is that of *monolayer saturation* (Regime II, Figure 1.21). Beyond a certain unspecified amount of interfacially adsorbed protein, interfacial tension begins to rapidly decline. The rapid decline continues for a short period and is said to herald the onset of the irreversibility of protein adsorption⁸³. The attractive interaction forces between protein already adsorbed to the interface and protein present in bulk, hastens the diffusion of further protein to the interfacial area⁸⁵.

The interface, in either case, becomes saturated with protein and the development of a multilayer film-like arrangement becomes a highly probable event⁸³. In addition, the rate of the decline in interfacial tension slows as the interface becomes increasingly saturated.

The third stage (Regime III, Figure 1.21) is that of *interfacial gelation*. As protein continues to adsorb to the interfacial region, conformational rearrangements in protein tertiary structure occur^{83, 86}, although it should be mentioned that a protein can retain its native state within this backing layer without unfolding^{83, 86}. These conformational rearrangements facilitate favourable hydrophobic and hydrophilic interactions with the surrounding solvent and protein monomers leading to the formation of multilayered, viscoelastic, amorphous, gel-like network structures on the interface⁸⁴⁻⁸⁵. The entanglement and lateral overlap of adsorbing monomers dictate the resulting structure of these 'networks'^{83, 87}.

The multilayer arrangement becomes stabilised by intermolecular interactions and the film can continue to form and evolve for a number of hours after the initial adsorption event, thus resulting in interfacial protein films with significant thickness and mechanical strength⁸⁵.

We can obtain a 'picture' of the interfacial protein structure at the air/water interface from neutron reflectivity studies⁹⁶⁻⁹⁷. These studies have shown that lysozyme retains its globular structure with no significant denaturation after adsorption to the air/water interface. At the highest protein concentrations used within these reflectivity studies by Lu⁹⁶⁻⁹⁷ *et al.* (1 mg/ml), lysozyme was found to switch conformation from a sideways configuration to an end-on configuration at the air/water interface. Structurally, the adsorption process was found to be described by a two layer model⁸⁴, consisting of a close packed inner layer (≈ 40 Å thickness) and a loosely packed sub-layer of approximately 30 Å thickness.

At protein concentrations comparable to that used within our studies film thickness at the air/water interface are found to be in the range of approximately 100 Å⁸⁴, which correspond to previously described⁸³⁻⁸⁴ multilayered film/gel arrangements at the air/water interface^{84, 88}.

Whilst no real denaturation/unfolding of lysozyme occurs at the air/water interface⁸⁹, the same cannot be said of lysozyme adsorption to a hydrophobic oil/water interface, where partial unfolding and conformational rearrangement in the interfacial region is known to occur^{79, 86}. Beverung⁸³ *et al.* did not directly observe any denaturation of lysozyme at low concentration at the water/heptane interface, although lysozyme was found to unfold at low surface pressure at the decane/water interface⁹⁰.

Due to this partial unfolding, one may expect that a protein multilayer film/gel structure at the oil/water interface might be dissimilar to that found at the air/water interface, both in terms of structure and thickness. It has been shown that lysozyme film formation at oil/water interfaces can occur rapidly⁸⁵⁻⁸⁶ and becomes stable after approximately 3.5 hours with the film continuing to evolve for up to 24 hours after the initial adsorption event⁸⁵. This evidence alone⁸⁵ suggests that lysozyme film thicknesses at oil/water interfaces should be at least thicker than that found at air/water interfaces. Because partial unfolding can also occur, one might expect that due to increases in the protein-protein interaction (between unfolded proteins); protein films would display a higher degree of mechanical strength at the oil/water interface.

It is therefore suggested that the thick interfacial protein film, formed at an oil/water interface, has a structure which consists of a network of partially unfolded, irreversibly adsorbed, aggregated lysozyme (on the actual interface itself) followed by a thick percolating network of interconnected monomeric protein with native tertiary structure (as a backing layer). The thick percolating network is almost liquid-like at early times, but with aging, transforms to either a gel or glassy film-like structure^{86, 91}. The actual thickness of the layer is unknown but one may argue that it may reach sizes in excess of 100 Å after a few hours of adsorption.

Simulations conducted by Radke⁸⁷ *et al.* using artificial protein-like heteropolymers, indicated that the attempt to maximise favourable solute-solvent interactions at the oil/water interface will localise the ‘protein’ at the interface with some penetration across the interface into the oil phase. This is not surprising when one considers that lysozyme has limited but significant solubility in some organic solvents⁹² (*viz.* 1.4 μM in benzene, 17.48 μM in chloroform and 1.4 μM in heptane). One may assume that some penetration into the oil phase by an adsorbed protein is likely and the formation of some type of microemulsion could form as a result.

It should therefore be clear that varied interfacial films can form at both air/water and oil/water interfaces with protein adsorption to both interfaces following more or less the same adsorption regime. Interestingly, a concept has emerged from the literature which views the oil/water and air/water interfaces not only as benign sinks for protein adsorption, but rather as an ‘energy field’⁸² of sorts.

This particular viewpoint has emerged from experimental evidence which shows that protein diffusivity to the air/water interface, with respect to negatively charged proteins, was slightly higher than that of bulk diffusivity, whilst the diffusion of positively charged proteins (*viz.* lysozyme) to the air/water interface was approximately one order of magnitude smaller than bulk diffusivity⁸².

Furthermore, experimental studies by Sengupta⁸¹ and co-workers found that all proteins, regardless of charge state, adsorbed to planar triolein-water interfaces with diffusivities approximately two orders of magnitude greater than bulk diffusivity. These discrepancies were put down to the role of either an attractive or repulsive dispersive interaction⁸¹ between the protein and the interface. In the particular case of lysozyme, the studies concluded that lysozyme adsorption to the air/water interface will be hindered by an energy barrier, whilst adsorption to the oil/water interface is rapid and unhindered. The importance of this will be seen later on within the thesis (Chapter 3)

1.L An introduction to the electrified oil/water interface.

The interface between two immiscible electrolyte solutions (ITIES) is useful as it allows for external control of the interfacial properties and confining potentials (various forces which seek to confine charged particles to the aqueous phase) of most particles located at the oil-water interface⁹³. When a potential difference is applied across the ITIES (which is about 1 nm in width⁹⁴ and consists of two ‘back-to-back’ double layers), a potential drop occurs and hence large interfacial electric fields and electric field gradients are created in this small area⁶⁴ (in the order of 2×10^8 V/m). The structure of the ‘back-to-back’ double layers at the ITIES is a contentious issue with two opposing views of the interfacial structure⁹⁵. One view predicts the existence of a molecularly sharp interface, whilst the other suggests an interfacial region which is essentially mixed⁹⁵. There is however experimental evidence to support both views⁹⁵, and the debate continues.

By adjusting the magnitude of the potential applied to the ITIES (with a potentiostat), one is able to control the adsorption/desorption and

stabilization/destabilization of particles adsorbed or located very near this region⁹³. Work in this regard has focussed mostly on the use of metallic nanoparticles^{103, 106}. Furthermore, interfacial nanoparticle adsorption was found to be fully reversible with respect to the applied potential¹⁰⁶⁻¹⁰⁷. Functionalization of the ITIES by the voltage induced localization of charged⁹⁶⁻⁹⁷ and uncharged⁹³ nanoparticles has therefore been suggested with the aim of producing oil-water interfaces that incorporate localised nano-objects for use as tuneable liquid mirrors and lenses⁹⁴.

A logical extension of work presented in Chapter 3 would involve the application of a potential to the oil/water interface in order to influence the lysozyme crystallization process. Previous work of this kind which is vaguely related to the work presented herein has focussed on the use of the ITIES in order to provide label free detection systems for a variety of proteins⁹⁸⁻¹⁰¹.

Pioneering work by Vanysek found that when 4 µg/ml of ovalbumin was adsorbed to the water-nitrobenzene interface, the ion transfer characteristics of Cs⁺ across the ITIES was altered¹⁰². With regard to lysozyme⁹⁸, it was found that lysozyme adsorbs to the polarised aqueous/1,2-dichloroethane interface (Chapter 2) and may facilitate the transfer of some organic anions across the ITIES¹⁰³. Care should be taken when trying to draw comparison between work presented herein and previous protein based electroanalytical work as lysozyme concentrations used within this chapter are necessarily 100 times in excess of that used within previous studies. This high protein concentration facilitates the formation of thick viscoelastic protein films at the 1,2-dichloroethane-water interface over a period of a few hours (Chapter 3).

To our current knowledge no previous work has been conducted on the use of an electrified oil-water interface in order to influence protein crystallization, the study in Chapter 4 is therefore the first study of its kind.

1.M The ideally polarisable liquid interface

It can be established¹⁰² that useful measures and relationships can be obtained by studying and quantifying the partitioning of ions between two immiscible liquid phases¹⁰². In some cases, external energy inputs may be required in order to drive the transfer of some very hydrophobic or very hydrophilic ions across some oil/water interfaces¹⁰². For example, lithium chloride and tetrabutylammonium tetraphenylborate (TBATPB) are commonly electrolytes in the aqueous phase and in the organic phase respectively⁹⁵. Ions such as Li^+ and TPB^- for example need definite energy inputs in order to drive them from one liquid phase to another.

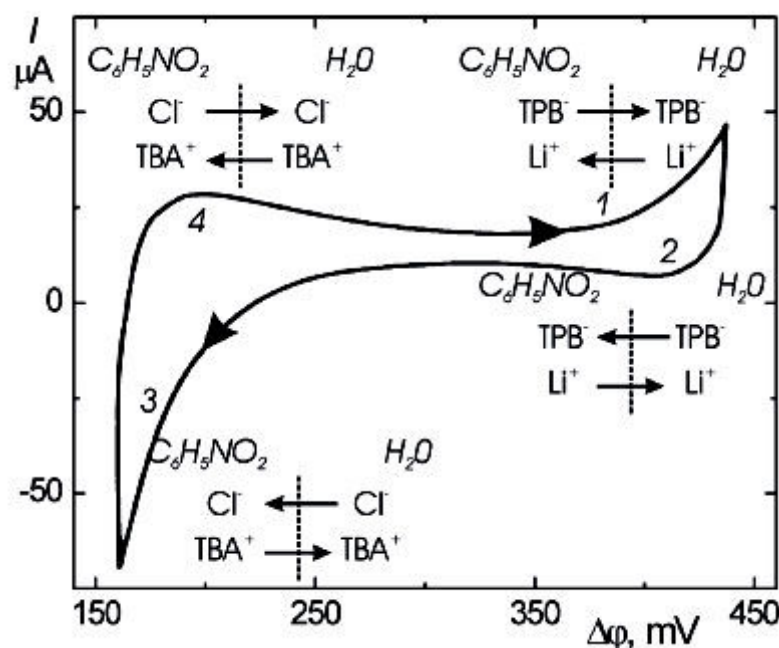


Figure 1.22 A cyclic voltammogram indicating the transfer of ions (Li^+ , Cl^- , TBA^+ , TPB^-) between two liquid phases (water and nitrobenzene) as a function of applied potential. Figure from ref. 4.

The standard ion transfer potentials at the water/nitrobenzene for Li^+ , Cl^- , TBA^+ and TPB^- are 398, -316, -250 and 372 mV respectively⁶⁴. Figure 1.22 indicates that when the potential of the aqueous phase is made positive via an external power supply, Li^+ will transfer from the aqueous phase to the oil phase and TPB^- will transfer from oil phase to aqueous phase at potentials approximately given by their standard ion transfer potentials. Similarly, when the aqueous phase becomes more negative Cl^- ions will transfer from the aqueous phase to the oil phase and TBA^+ ions will transfer from the oil phase to the aqueous phase.

Between the potential limits required for ion transfer of the various ions just given, there exists a '*potential window*'. The potential window is defined as the potential range at which no ions will transfer across the ITIES. The oil/water interface at potentials within the potential window can be said to mimic the properties of an ideally polarisable metal electrode (Hg electrode in deaerated KF solution for example).

1.N Experimental arrangements for electrochemical work at the oil/water interface

Since one may seek to apply potential across the oil/water interface (Chapters 4,5 and 6) we need electrodes. Further, we need electrodes (in each phase) that are non-polarisable to ensure that changes in the electrode potential reflect changes in liquid phase potentials and not electrode potentials relative to solution. We shall concern ourselves with a two electrode arrangement, of the kind used within this chapter.

The four electrode arrangement¹⁰² consisting of two reference electrodes and two counter electrodes (one of each in each phase), incorporating a reference interface is considered the 'gold standard' for any serious electrochemistry on the oil-water interface. The four electrode arrangement virtually eliminates any IR drop on the system and is widely used.

The two electrode arrangement, permissible for measurement if small currents are passed (due to small IR drops), consists of two non-polarisable electrodes of the second kind, one located in the oil phase and one located in the aqueous phase. Since we use chloride based electrolytes in the aqueous phase and draw rather small currents, Ag/AgCl electrodes are used. Similarly, we use AgTPB electrodes in the oil phase such as the type described by Schiffren and co-workers¹⁰⁴, in the presence of TBATPB dissolved within 1,2-dichloroethane.

1.O General electrochemical basics

There are two ways in which one may apply a DC electrical field to a protein crystallizing solution. The field can be applied either externally or internally. By an external application of an electrical field, we refer to DC fields applied via metal electrodes which are located outside the confines of the solution, therefore making no electrical contact with the solution itself. Conversely, internal fields are fields which are applied via metal electrodes having electrical contact with the solution. Throughout this thesis we refer to the use of internally applied DC electrical fields only. This subsection (1.O) has been written with the aid of three key texts¹⁰⁵⁻¹⁰⁷.

Electrochemistry could be considered the science of electron transfer across a solution/electrode interface. Consider a system as shown in Figure 1.23, which consists of two dissimilar metallic electrodes immersed in a solution containing an ionic electrolyte acting as an ionic conductor.

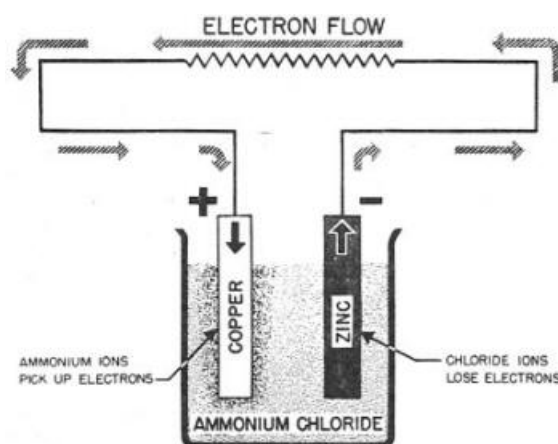


Figure 1.23 A simple voltaic cell consisting of zinc and copper metallic strips (acting as electrodes) immersed in a solution of ammonium chloride and connected by some wire. Figure taken from ref. 108

The zinc strip has lower electronegativity than the copper strip, and thus the zinc strip has a thermodynamic tendency to lose electrons which are gained by the copper strip. This difference in electronegativity causes a flow of electrons through the wire from zinc to copper. The reaction in which loss of electrons at the zinc strip results in the formation of zinc ions in solution is illustrated in (1.6)



Current will flow until most of the zinc strip is converted to zinc ion of charge state +2.

If one considers the same experimental arrangement as that given in Figure 1.23, but with two metals placed into the electrolyte solution which are of exactly the same composition. Here, there is no difference in electronegativity between the metal electrodes and thus no current will spontaneously flow. However, one can force current to flow between the two electrodes by application of a potential difference with the aid of an external power source.

By application of a potential difference to the two similar metal electrodes, charge can be made to flow across the metal/solution interfaces. The direction of flow can occur either

- a) from metal to solution across the metal/solution interface
- b) from solution to metal across the metal/solution interface.

A more detailed view of the induced electron transfer process across the metal/solution interface can be garnered by considering the idea of the “Fermi level” and how it relates to electron energy within the metallic conductor (i.e. the electrode).

The Fermi level concept is used to describe the highest collection of electron energy levels at absolute zero (0 K) within a metallic conductor. The electrons within a metal at 0 K cannot exist in identical states (Pauli’s exclusion principle). The electrons therefore tend to pack into all the available lowest energy states and form what is known as a “Fermi Sea”.

The Fermi level can therefore be further defined as the surface of the “Fermi Sea” at which no electron will have enough energy to rise above the “sea-level”. Due to the close atomic packing inherent in most metals, metallic conductors do not possess a series of well defined energy levels. Instead, metals possess a continuum of states which can be viewed as series of energy levels which are smeared.

Thus at ambient temperature and as more energy is added to the metallic electrode via the external power source, the energy states begin to become occupied by “electron seas” of ever increasing energy. In this way, one can control the energy of the Fermi level within a metallic conductor via the application of voltage from an external power source.

If one now considers placing an ionic species in solution (say NaCl giving Na^+ and Cl^- ions). The ions, will be in the immediate vicinity of the electrode surface (at a distance of typically less than 2 nm). One then applies a potential difference to the electrode. If the ionic species present have vacant molecular orbitals which are at lower energy states than the energy of the Fermi level in the metal electrode, electrons will begin to flow (or rather tunnel) from the metal electrode to the ion in solution across the metal/solution interface. Conversely, if the ionic species has an occupied energy level of a higher energy state than the Fermi level within the electrode, electrons will tunnel from the ion in solution to the metal across the metal/solution interface.

When electron transfer occurs from metal to solution, the ionic species is said to be reduced (as an electron has been gained by the ion), and in cases where electron transfer occurs from ionic species to metal, the species is said to be oxidised (as an electron has been lost by the ion to the electrode).

A single electron transfer process under an applied potential is described by (1.7) in which we see an oxidised species (O) gaining an electron to become reduced (R).



Faraday established that 96485 Coulombs of charge needs to pass in order for 1 mole of species to be consumed or produced at an electrode surface. Since 1 Ampere is equal to 1 Coulomb per second, by simple inspection we see that the electrical current (i) produced by either the oxidation or reduction of species reactions at an electrode of area (A), at a certain fixed potential is given by (1.8)

$$\begin{aligned}
 i &= -k_{red}FA[O]_s \\
 i &= -k_{ox}FA[R]_s
 \end{aligned}
 \tag{1.8}$$

k_{red} and k_{ox} refer to the rate of reduction and oxidation respectively, F is the Faraday constant (C/mol). $[O]_s$ and $[R]_s$ are the concentrations of solution based species which have been either oxidised or reduced at the metal/solution interface.

(1.8) describes current flow at an undefined fixed voltage. The question naturally arises as to how the rates of both the oxidation and reduction reactions change with applied potential.

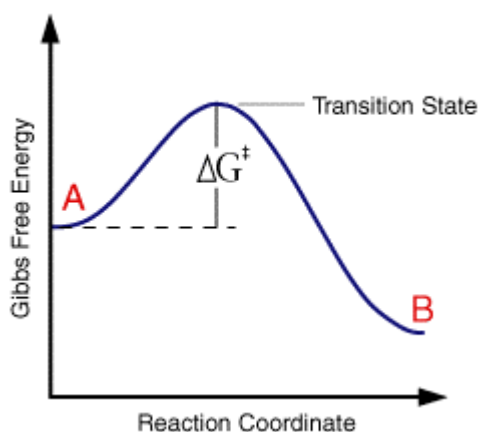


Figure 1.24 Diagram illustrates the existence of an activation energy barrier (ΔG^\ddagger) which must be overcome in order to get from substrate A to product B. Figure taken from ref.105

The conversion of substrate A into product B at a certain rate k at an electrode surface is represented by



Transition state theory explains how such a reaction may proceed only after an activation energy barrier has been overcome (Figure 1.24). The theory also goes on to predict that the rate of the reaction (k) will be given by (1.10)

$$k = Ze^{\left(\frac{-\Delta G}{RT}\right)} \quad (1.10)$$

where U is a pre-exponential factor, R is the gas constant, T is the temperature and ΔG is the activation energy.

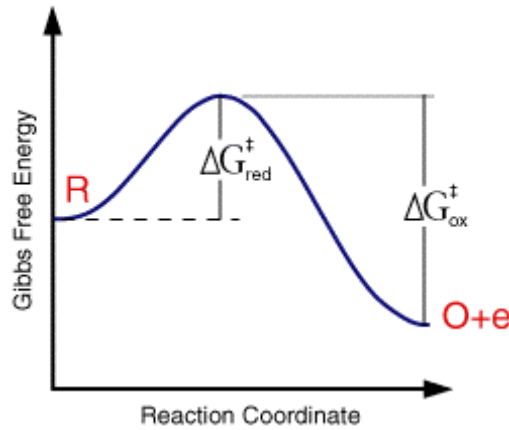


Figure 1.25 The difference in activation energy in order to achieve the oxidised state (O) from an initially reduced state (R) and vice versa. Figure adapted from ref.105

Figure 1.25 indicates that the oxidised state will be of a lower energy than the reduced state. So that the activation free energy change for the reduction (ΔG_{red}) and oxidation (ΔG_{ox}) reactions is given by (1.11). G_O and G_R represent the ground states for the oxidised and reduced forms and G'' is the energy of the transition state.

$$\begin{aligned} \Delta G_{red} &= G'' - G_O \\ \Delta G_{ox} &= G'' - G_R \end{aligned} \quad (1.11)$$

Thus by substitution into (1.10) we obtain an expression for the rates of both oxidation (k_{ox}) and reduction (k_{red})

$$k_{red} = Ze^{\left(\frac{-\Delta G_{red}}{RT}\right)}$$

$$k_{ox} = Ze^{\left(\frac{-\Delta G_{ox}}{RT}\right)}$$
(1.12)

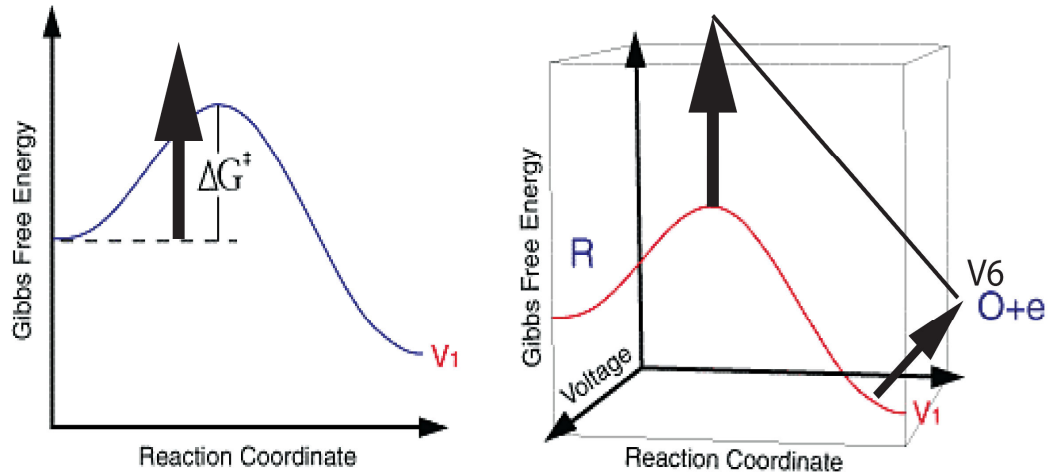


Figure 1.26 The activation energy shows a dependence on the applied potential. Figure taken and adapted from ref. 105

The activation free energy barrier is found to be dependent on the magnitude of the applied voltage (Figure 1.26)^{105, 107}. The rates of oxidation and reduction must therefore be reformulated to take this effect into account.

Using an assumption that the change in activation free energy varies linearly with voltage for both the oxidation and reduction reactions, we find that the activation energy for the oxidation and reduction reactions can be given by

$$\Delta G_{red} = \Delta G_{red}^0 + \alpha F \phi$$

$$\Delta G_{ox} = \Delta G_{ox}^0 - (1 - \alpha) F \phi$$
(1.13)

where α is the transfer coefficient and shows how the transition state is influenced by the applied potential. Its value is usually set to 0.5 and is physically interpretable as the fraction of the applied potential that goes into lowering the activation energy barrier for the electrochemical reaction. F is the Faraday constant and ϕ is applied potential.

By substituting the new potential dependent activation free energy terms given in (1.13) into the rate constant expressions for the oxidation and reduction given in (1.12) we obtain the following expression which shows how the rate of an electrochemical reaction is affected by the applied potential (ϕ).

$$\begin{aligned} k_{red} &= Ze^{\left[\left(\frac{-\Delta G_{red}}{RT} \right) \left(\frac{-\alpha F \phi}{RT} \right) \right]} \\ k_{ox} &= Ze^{\left[\left(\frac{-\Delta G_{ox}}{RT} \right) \left(\frac{(1-\alpha) F \phi}{RT} \right) \right]} \end{aligned} \quad (1.14)$$

It is seen that the rate of electrolysis at the electrode surface has an exponential dependence on the applied potential. This is assuming that the species undergoing electrolysis are at a distance away from the electrode surface at which they are always available for electron transfer to occur. In reality this is not the case, as a simple one electron reduction at an electrode will result in a decrease in the concentration of species O at the electrode with a corresponding increase in the concentration of species R.

It is precisely for this reason that account needs to be taken of the manner in which various ionic species are transported to and from the surface of the electrode.

1.P Mass transport

(written with the aid of references ^{105-106, 109-110})

The transport of an ionic species from bulk solution to the surface of an electrode, regardless of whether an oxidation or reduction is taking place, is governed by three types of mass transport which are diffusion, convection and migration^{105-106, 109-110}.

Mass transport by diffusion, is defined mathematically by Fick's First Law (1.15). The Law relates the flux (J) of a particular substance to its concentration gradient ($\frac{\partial C}{\partial x}$) in one spatial dimension. The diffusion of a substance occurs due to entropic effects, in that diffusion will occur from regions of high concentration (C denotes concentration of species) to regions of low concentration.

Relating this concept back to the electrode surface and again considering a one electron reduction, "R" is produced at the surface of the electrode and so "R" will diffuse from regions of higher concentration (electrode surface) to a region of low concentration (bulk solution) at a certain rate given by D which is the diffusion coefficient for the species (D has units of area per unit time).

$$J = -D \frac{\partial C}{\partial x} \quad (1.15)$$

The relationship is very useful and can be further extended to define how a concentration field changes over time in one spatial dimensions and this information is provided Fick's second Law (1.16)

$$\frac{\partial C}{\partial t} = -D \frac{\partial^2 C}{\partial x^2} \quad (1.16)$$

Another form of mass transport which affects the concentration of species in the vicinity of the electrode during electrolysis is that of convection. Convection is a type of mass transport that results from the action of force upon a solution, be it gravitational or otherwise^{105-106, 109-110}. Natural convection is a manifestation of this, and occurs because of small thermal or density differences in solution. Natural convection in the vicinity of an electrode will result in concentration behaviour that is extremely unpredictable and therefore concentration predictions become unreliable.

Since measurements of current at an electrode surface are all about predictability and concentration, steps are usually taken to remove the stochastic nature of this process. Forced convection can be used to eliminate natural convection which allows predictable laminar flow patterns to be established near the electrode surface. Also, if the time scale of the electrochemical current measurement is shorter than 20 seconds, the effects of convection can largely be ignored.

The final form of mass transport which can influence the transport of species to and from an electrode surface is that of migration. Migration can be considered a largely electrostatic effect which involves the movement of charged species under the influence of an electric field gradient. The electric field can either repel from or attract charged species to the surface of a polarised electrode.

Under normal conditions (in which small current measurements need to take place), large excesses of supporting electrolyte (which do not undergo electrolysis) are added to solution which counteract the effects of migration via charge screening. The flux of a charged ionic species (C) via migration in one dimension under the influence of an spatially varied electric field ($\frac{\partial \phi}{\partial x}$) is given by

$$J = \frac{zFC}{RT} \frac{\partial \phi}{\partial x} \quad (1.17)$$

where R is the gas constant, T is the absolute temperature, F is the Faraday constant and z is the valence of the charged species.

The total flux ($J_T = J_{\text{Diffusion}} + J_{\text{Migration}}$) in one dimension due to both a concentration gradient and migration effects is given by the Nernst-Planck equation which has the form

$$J_T = -D \frac{\partial C}{\partial x} + \frac{zFC}{RT} \frac{\partial \phi}{\partial x} \quad (1.18)$$

1.Q Confocal Laser Scanning Microscopy (CLSM)

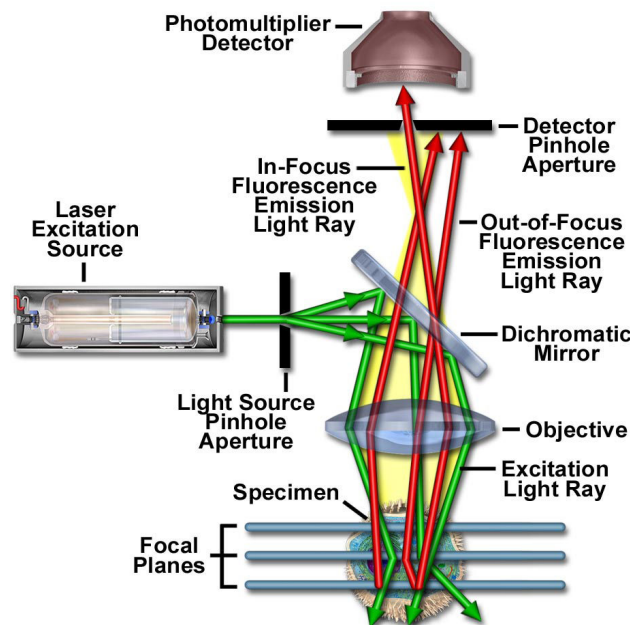


Figure 1.27 A cartoon schematic showing the major components of a modern CLSM. Picture taken from ref. 111

Figure 1.27 illustrates the ‘insides’ of a conventional CLSM, as the name suggests the microscope makes use of a scanning laser beam which via the use of electronically controlled mirrors raster scans the surface of a specimen under examination. The scanning motion enables high resolution images of the specimen to be built up one pixel at a time.

A simple pinhole aperture is placed in front of the photomultiplier detector which serves to block any stray or reflected light that is not confocal with the focal point of the laser beam impinging the specimen. In this way only laser light which originates from a very thin section of the specimen is used to construct the final electronic image¹¹¹.

The depth at which the laser scans into the specimen can be adjusted; therefore the entire volume of an optically transparent specimen may be mapped in the x, y and z-directions. Clear three dimensional images of the specimen are thus constructed quickly and easily. Modern day conventional CLSM's (of the type used within this thesis) can achieve horizontal resolutions in the order of approximately 0.2 μm . Vertical resolutions in the order of about 0.5 μm are also obtainable¹¹¹. The speed at which the specimen is scanned is under tight electronic control, and at the fastest scan rate a 512 x 480 image is produced every 1/30th of a second. The rapid scanning option is extremely useful when good temporal and spatial resolutions are required¹¹¹.

Because monochromatic laser light is used as an illumination source, a variety of fluorescent probes may be used in conjunction with the specimen. The ability to solely produce excitation light and to subsequently collect emitted fluorescent radiation almost simultaneously is made possible via the use of the interference filter or dichroic mirror.

Interference filters allow the passage of certain wavelengths of light whilst effectively blocking out others. This spectral selectivity is achieved by placing transparent spacers between two semi reflective coatings, which cause multiple reflections and interference to select desired wavelengths¹¹¹. Generally filters are termed low-pass (allowing wavelengths lower than a set cut-off wavelength), high-pass (allowing wavelengths higher than set cut-off) or band-pass (allowing wavelengths between two set cut-off wavelengths)¹¹¹.

Special mention is made of fluorescein (Figure 1.28), which displays a pH dependent fluorescence response¹¹² and is used within Chapter 2.

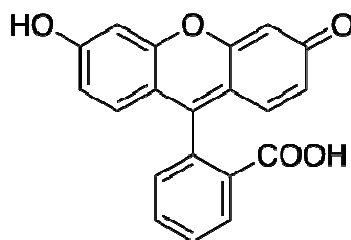


Figure 1.28 The molecular structure of fluorescein (see references 113-114).

The remarkable pH-dependent fluorescence response is achieved in the following manner. When both the hydroxyl and carboxyl group are deprotonated (*circa* pH 5 and above), the molecule is able to absorb light at wavelengths of around 496 nm. The resulting emission is Stoke shifted by approximately 24 nm from the excitation wavelength. However at low pH, when the carboxyl and hydroxyl groups are protonated, the resulting fluorescence is extremely weak. The molecule can thus be used as a non-invasive indicator of local pH, especially useful for monitoring pH gradients at the surface of electrodes¹¹³⁻¹¹⁴.

A pH-independent analogue of fluoroscein is commercially available and provides usefulness when fluorescence is required at low pH using easily accessible excitation and emission wavelengths generated via common argon-ion lasers.

1.R Reference

1. A. McPherson, *Journal of Crystal Growth*, 1991, **110**, 1-10.
2. N. E. Chayen, *Trends in Biotechnology*, 2002, **20**, 98-98.
3. M. L. Pusey and N. E. Chayen, *Trends in Biotechnology*, 2002, **20**, 322-323.
4. T. L. Blundell, *Progress in Biophysics and Molecular Biology*, 2005, **88**, 283-284.
5. J. Fruton, *Historical essays on the interplay between Chemistry and Biology*, Wiley-Interscience, New York, 1972.
6. V. M. Bolanos-Garcia and N. E. Chayen, *Prog. Biophys. Mol. Biol.*, **In Press**, **Uncorrected Proof**.
7. J. A. Shapiro, *Ann N Y Acad Sci*, 2009, **1178**, 6-28.
8. M. J. Gething and J. Sambrook, *Nature*, 1992, **355**, 33-45.
9. B. Alberts, *Molecular Biology of the Cell*, Garland Science, New York, 2008.
10. S. D. Durbin and G. Feher, *Journal of Crystal Growth*, 1986, **76**, 583-592.
11. Y. S. Huang, U. S. Jeng, Y. J. Shiu, Y. H. Lai and Y. S. Sun, *J. Appl. Crystallogr.*, 2007, **40**, S165-S169.
12. D. J. Vocadlo, G. J. Davies, R. Laine and S. G. Withers, *Nature*, 2001, **412**, 835-838.
13. T. Imoto, H. Yamada, K. Okazaki, T. Ueda, R. Kuroki and T. Yasukochi, *J. Protein Chem.*, 1987, **6**, 95-107.
14. M. van der Veen, W. Norde and M. C. Stuart, *Colloids and Surfaces B: Biointerfaces*, 2004, **35**, 33-40.
15. B. Lee and F. M. Richards, *Journal of Molecular Biology*, 1971, **55**, 379-400, IN373-IN374.
16. K. P. Wilson, B. A. Malcolm and B. W. Matthews, *J. Biol. Chem.*, 1992, **267**, 10842-10849.
17. M. Nakasako, *Philosophical Transactions of the Royal Society of London. Series B: Biological Sciences*, 2004, **359**, 1191-1206.
18. A. S. Myerson, *Handbook of Industrial Crystallization*, Elsevier Science & Technology, Oxford, 2002.

19. A. McPherson, *Methods*, 2004, **34**, 254-265.
20. Y. Zhang and P. S. Cremer, *Curr. Opin. Chem. Biol.*, 2006, **10**, 658-663.
21. Y. Zhang and P. S. Cremer, *PNAS*, 2009, **106**, 15249-15253.
22. M. Muschol and F. Rosenberger, *The Journal of Chemical Physics*, 1997, **107**, 1953-1962.
23. F. Rosenberger, S. B. Howard, J. W. Sowers and T. A. Nyce, *J. Cryst. Growth*, 1993, **129**, 1-12.
24. D. Erdemir, A. Y. Lee and A. S. Myerson, *Accounts of Chemical Research*, 2009, **42**, 621-629.
25. J. Manuel García-Ruiz, *J. Struct. Biol.*, 2003, **142**, 22-31.
26. R. P. Sear, *Journal of Physics Condensed Matter*, 2007, **19**.
27. P. R. Ten Wolde and D. Frenkel, *Theor. Chem. Acc.*, 1999, **101**, 205-208.
28. K. Schätzel and B. J. Ackerson, *Physical Review Letters*, 1992, **68**, 337.
29. M. Manno, C. Xiao, D. Bulone, V. Martorana and P. L. San Biagio, *Physical Review E*, 2003, **68**, 011904.
30. P. R. t. Wolde and D. Frenkel, *Science*, 1997, **277**, 1975-1978.
31. J. Drenth, *Crystal Growth & Design*, 2005, **5**, 1125-1127.
32. P. G. Vekilov, *J. Cryst. Growth*, 2005, **275**, 65-76.
33. J. E. Aber, S. Arnold, B. A. Garetz and A. S. Myerson, *Phys. Rev. Lett.*, 2005, **94**, 145503.
34. J. R. Savage and A. D. Dinsmore, *Phys. Rev. Lett.*, 2009, **102**, 198302.
35. E. M. Pouget, P. H. H. Bomans, J. A. C. M. Goos, P. M. Frederik, G. de With and N. A. J. M. Sommerdijk, *Science*, 2009, **323**, 1455-1458.
36. O. Galkin, W. Pan, L. Filobelo, R. E. Hirsch, R. L. Nagel and P. G. Vekilov, 2007, **93**, 902-913.
37. A. Bernardo, C. E. Calmanovici and E. A. Miranda, *Cryst. Growth Des.*, 2004, **4**, 799-805.
38. B. Biscans and C. Laguerie, *J. Phys. D: Appl. Phys.*, 1993, **26**, B118.

39. A. McPherson, Y. G. Kuznetsov, A. Malkin and M. Plomp, *J. Struct. Biol.*, 2003, **142**, 32-46.
40. D. P. Woodruff, *The solid-liquid interface*, Cambridge University Press, Cambridge, U.K., 1973.
41. A. J. Malkin, Y. G. Kuznetsov, T. A. Land, J. J. Deyoreo and A. McPherson, *Nat. Struct. Biol.*, 1995, **2**, 956-959.
42. I. Yoshizaki, T. Sato, N. Igarashi, M. Natsuisaka, N. Tanaka, H. Komatsu and S. Yoda, *Acta Crystallogr., Sect D: Biol. Crystallogr.*, 2001, **57**, 1621-1629.
43. M. Giuliatti, M. M. Seckler, S. Derenzo, M. I. Ré and E. Cekinski, *Brazilian Journal of Chemical Engineering*, 2001, **18**, 423-440.
44. W. Iwai, D. Yagi, T. Ishikawa, Y. Ohnishi, I. Tanaka and N. Niimura, *Journal of Synchrotron Radiation*, 2008, **15**, 312-315.
45. S. D. Durbin and G. Feher, *Annu. Rev. Phys. Chem.*, 1996, **47**, 171-204.
46. N. E. Chayen and E. Saridakis, *Nat. Methods*, 2008, **5**, 147-153.
47. J. M. Wiencek, *Annu. Rev. Biomed. Eng.*, 1999, **1**, 505-534.
48. Crystal growth 101, http://hamptonresearch.com/documents/growth_101/2.pdf.
49. L. Sun, J. Li, C. Xu, F. Yu, H. Zhou, L. Tang and J. He, *Acta Biochim. Biophys. Sin.*, 2010, **42**, 332-336.
50. F. R. Salemme, *Arch. Biochem. Biophys.*, 1972, **151**, 533-539.
51. A. Moreno, E. Saridakis and N. E. Chayen, *J. Appl. Crystallogr.*, 2002, **35**, 140-142.
52. N. Mirkin, B. A. Frontana-Urbe, A. Rodriguez-Romero, A. Hernandez-Santoyo and A. Moreno, *Acta Crystallographica - Section D Biological Crystallography*, 2003, **59**, 1533-1538.
53. N. E. Chayen, P. D. Shaw Stewart, D. L. Maeder and D. M. Blow, *J. Appl. Crystallogr.*, 1990, **23**, 297-302.
54. N. E. Chayen, P. D. Shaw Stewart and D. M. Blow, *Journal of Crystal Growth*, 1992, **122**, 176-180.
55. N. E. Chayen, *Structure*, 1997, **5**, 1269-1274.
56. N. E. Chayen, *J. Cryst. Growth*, 1999, **196**, 434-441.

57. A. D'Arcy, A. Mac Sweeney, M. Stihle and A. Haber, *Acta Crystallographica Section D*, 2003, **59**, 396-399.
58. A. D'Arcy, A. M. Sweeney and A. Haber, *Methods*, 2004, **34**, 323-328.
59. M. Zeppezauer, H. Eklund and E. S. Zeppezauer, *Arch. Biochem. Biophys.*, 1968, **126**, 564-573.
60. A. D'Arcy, C. Elmore, M. Stihle and J. E. Johnston, *Journal of Crystal Growth*, 1996, **168**, 175-180.
61. D. M. Blow, N. E. Chayen, L. F. Lloyd and E. Saridakis, *Protein Sci.*, 1994, **3**, 1638-1643.
62. N. E. Chayen, *Acta Crystallogr. Sect. D-Biol. Crystallogr.*, 1998, **54**, 8-15.
63. R. M. Pashley, *The Journal of Physical Chemistry B*, 2003, **107**, 1714-1720.
64. A. G. Volkov, D. W. Deamer, D. L. Tanelian and V. S. Markin, *Liquid interfaces in chemistry and biology*, John Wiley & Sons, Inc., United States of America, 1998.
65. D. Y. Wang, H. W. Duan and H. Mohwald, *Soft Matter*, 2005, **1**, 412-416.
66. S. Schacht, Q. Huo, I. G. VoigtMartin, G. D. Stucky and F. Schuth, *Science*, 1996, **273**, 768-771.
67. F. Reincke, S. G. Hickey, W. K. Kegel and D. Vanmaekelbergh, *Angew. Chem.-Int. Edit.*, 2004, **43**, 458-462.
68. J. B. He, Z. W. Niu, R. Tangirala, J. Y. Wan, X. Y. Wei, G. Kaur, Q. Wang, G. Jutz, A. Boker, B. Lee, S. V. Pingali, P. Thiyagarajan, T. Emrick and T. P. Russell, *Langmuir*, 2009, **25**, 4979-4987.
69. G. Kaur, J. He, J. Xu, S. Pingali, G. Jutz, A. Boker, Z. Niu, T. Li, D. Rawlinson, T. Emrick, B. Lee, P. Thiyagarajan, T. P. Russell and Q. Wang, *Langmuir*, 2009, **25**, 5168-5176.
70. J. Matsui, K. Yamamoto and T. Miyashita, *Carbon*, 2009, **47**, 1444-1450.
71. H. Y. Shi, B. Hu, X. C. Yu, R. L. Zhao, X. F. Ren, S. L. Liu, J. W. Liu, M. Feng, A. W. Xu and S. H. Yu, *Adv. Funct. Mater.*, 2010, **20**, 958-964.
72. P. Pieranski, *Phys. Rev. Lett.*, 1980, **45**, 569.
73. A. Boker, J. He, T. Emrick and T. P. Russell, *Soft Matter*, 2007, **3**, 1231-1248.

74. A. Valstar, W. Brown and M. Almgren, *Langmuir*, 1999, **15**, 2366-2374.
75. R. Miller, D. O. Grigoriev, J. Krägel, A. V. Makievski, J. Maldonado-Valderrama, M. Leser, M. Michel and V. B. Fainerman, *Food Hydrocoll.*, 2005, **19**, 479-483.
76. G. Pellicane, G. Smith and L. Sarkisov, *Phys. Rev. Lett.*, 2008, **101**, 248102.
77. V. B. Fainerman, R. Miller, J. K. Ferri, H. Watzke, M. E. Leser and M. Michel, *Adv. Colloid Interface Sci.*, 2006, **123-126**, 163-171.
78. J. He, Z. Niu, R. Tangirala, J.-Y. Wang, X. Wei, G. Kaur, Q. Wang, G. Jutz, A. Boker, B. Lee, S. V. Pingali, P. Thiyagarajan, T. Emrick and T. P. Russell, *Langmuir*, 2009, **25**, 4979-4987.
79. C. S. Rao and S. Damodaran, *Langmuir*, 2000, **16**, 9468-9477.
80. T. Sengupta and S. Damodaran, *J. Colloid Interface Sci.*, 1998, **206**, 407-415.
81. T. Sengupta and S. Damodaran, *Langmuir*, 1998, **14**, 6457-6469.
82. T. Sengupta, L. Razumovsky and S. Damodaran, *Langmuir*, 1999, **15**, 6991-7001.
83. C. J. Beverung, C. J. Radke and H. W. Blanch, *Biophys. Chem.*, 1999, **81**, 59-80.
84. V. S. Alahverdijeva, D. O. Grigoriev, J. K. Ferri, V. B. Fainerman, E. V. Aksenenko, M. E. Leser, M. Michel and R. Miller, *Colloids and Surfaces A: Physicochemical and Engineering Aspects*, 2008, **323**, 167-174.
85. S. G. Baldursdottir, M. S. Fullerton, S. H. Nielsen and L. Jorgensen, *Colloids and Surfaces B: Biointerfaces*, 2010, **79**, 41-46.
86. E. M. Freer, K. S. Yim, G. G. Fuller and C. J. Radke, *The Journal of Physical Chemistry B*, 2004, **108**, 3835-3844.
87. R. E. Anderson, V. S. Pande and C. J. Radke, *The Journal of Chemical Physics*, 2000, **112**, 9167-9185.
88. V. B. Fainerman, E. H. Lucassen-Reynders and R. Miller, *Adv. Colloid Interface Sci.*, 2003, **106**, 237-259.
89. C. Postel, O. Abillon and B. Desbat, *J. Colloid Interface Sci.*, 2003, **266**, 74-81.
90. D. E. Graham and M. C. Phillips, *J. Colloid Interface Sci.*, 1979, **70**, 415-426.
91. P. Cicuta, E. J. Stancik and G. G. Fuller, *Phys. Rev. Lett.*, 2003, **90**, 236101.

92. J. T. Chin, S. L. Wheeler and A. M. Klibanov, *Biotechnol. Bioeng.*, 1994, **44**, 140-145.
93. M. E. Flatté and et al., *J. Phys.: Condens. Matter*, 2008, **20**, 073102.
94. M. E. Flatté, A. A. Kornyshev and M. Urbakh, *PNAS*, 2008, **105**, 18212-18214.
95. P. Vanysek and L. B. Ramirez, *J. Chil. Chem. Soc.*,, 2008, **53**.
96. H. Girault, A. A. Kornyshev, C. W. Monroe and M. Urbakh, *J. Phys.: Condens. Matter*, 2007, **19**, 370301.
97. H. H. Girault, *Nat. Mater.*, 2006, **5**, 851-852.
98. M. D. Scanlon, E. Jennings and D. W. M. Arrigan, *Phys. Chem. Chem. Phys.*, 2009, **11**, 2272-2280.
99. M. D. Scanlon, J. Strutwolf and D. W. M. Arrigan, *Phys. Chem. Chem. Phys.*, 2010, **12**, 10040-10047
100. P. Jing, Y. Kim and S. Amemiya, *Langmuir*, 2009, **25**, 13653-13660.
101. T. Osakai, Y. Yuguchi, E. Gohara and H. Katano, *Langmuir*, 2010, **26**, 11530-11537.
102. P. Vanysek, ed., *Electrochemistry on Liquid/Liquid Interfaces*, Springer-Verlag, Berlin , Germany, 1985.
103. R. A. Hartvig, M. A. Méndez, M. v. d. Weert, L. Jorgensen, J. Østergaard, H. H. Girault and H. Jensen, *Anal. Chem.*, 2010, **82**, 7699-7705.
104. D. J. Clarke, D. J. Schiffrin and M. C. Wiles, *Electrochim. Acta*, 1989, **34**, 767-769.
105. A. C. Fischer, *Electrode Dynamics* OUP Oxford, Oxford.
106. A. J. Bard and L. R. Faulkner, *Electrochemical Methods : Fundamentals and Applications*, John Wiley & Sons, Limited, Australia, 2001.
107. J. Albery, *Electrode kinetics*, Oxford University Press, Oxford, UK, 1975.
108. *Electricity - Basic Navy Training Courses (NAVPERS 10622)*, U.S. GOVERNMENT PRINTING OFFICE, 1945.
109. D. T. Sawyer, A. Sobkowiak and J. L. Roberts, *Electrochemistry for Electrochemists*, John Wiley and Sons, Inc, New York , USA, 1995.
110. R. G. Compton and G. H. W. Sanders, *Electrode Potentials*, OUP Oxford, Oxford.

111. Olympus, Theory of Confocal Microscopy,
<http://www.olympusfluoview.com/theory/index.html>.
112. N. C. Rudd, S. Cannan, E. Bitziou, I. Ciani, A. L. Whitworth and P. R. Unwin,
Anal. Chem., 2005, **77**, 6205-6217.
113. E. Bitziou, N. C. Rudd, M. A. Edwards and P. R. Unwin, *Anal. Chem.*, 2006, **78**,
1435-1443.
114. N. C. Rudd, S. Cannan, E. Bitziou, I. Ciani, A. L. Whitworth and P. R. Unwin,
Anal. Chem., 2005, **77**, 6205-6217.

2. Electrochemically-assisted growth of lysozyme crystals

Results reported herein have formed the basis of a published paper namely, Barry R. Silver and Patrick R. Unwin, "Protein crystals make it big at electrode surfaces", Chemical Communications, 2008, 5179-5181. I conducted all experiments and wrote the paper in conjunction with P.R.Unwin.

2.A Previous work

The literature contains a small body of experimental work which details the use of internally applied DC potentials and currents to influence a protein crystallization process. In addition to our own work¹, the literature contains research conducted by Mirkin² *et al.* (2003), Sazaki³ *et al.* (2004), Moreno and Sazaki⁴ (2004), Moreno⁵ *et al.* , Nieto-Mendoza⁶ *et al.* (2005), Perez *et al.* (2008), Hammadi⁷ *et al.* (2007) and Hammadi⁸ *et al.* (2009). Experimental arrangements used within each study are briefly described and a brief outline of the results obtained provided.

2.A.1 Experimental arrangements used in previous studies

Mirkin² *et al.* made use of an experimental arrangement based on the modified ‘gel-acupuncture’ method. The experimental set-up was housed within a modified “Granada Crystallization Box” (Figure 2.1). Platinum wires and graphite rods were used as electrodes. Currents ranging from 0.9 μA to 1 μA were used and a maximum current density of 0.0286 A/m^2 was reached during trials.

Protein solution, housed within the capillaries (capillaries were between 1 mm and 1.5 mm in diameter), consisted of 100 mg/ml lysozyme in 0.1 M sodium acetate buffer (pH 4.5). Precipitant (20% NaCl (w/v)) was laid on top of the gel which is typical for the ‘gel-acupuncture’ method⁹. Thaumatin (a protein used as a low calorie sugar alternative¹⁰, pI *circa.* 12) was also investigated within this study. With respect to the part of the investigation pertaining to thaumatin, capillary solutions contained 100 mg/ml thaumatin in 100 mM phosphate buffer (pH 7) and 25% (w/v) sodium potassium tartrate was the precipitant.

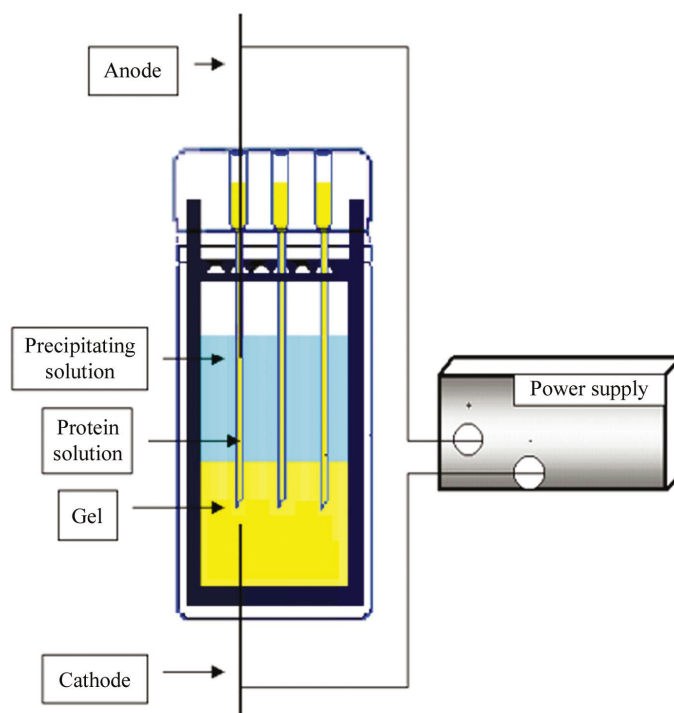


Figure 2.1 A schematic of the galvanostatic experimental arrangement used in the Mirkin study. Protein solutions are within capillaries and precipitant was in the gel. Figure taken from ref. 2

After 24 hours of applied current, lysozyme crystals were found located on the anode. In a separate experiment, after also 24 hours of applied current, thaumatin crystals had also appeared around the anode. Anode located thaumatin crystals were found to be larger and had appeared at a shorter time in comparison to crystals obtained via control experiments.

The authors describe the effect of the electrode separation distance on the induction time. In particular, with increasing electrode separation, the more the induction time of crystals formed (using an applied current) became to resemble that of the control experiments. Acid-base indicators were used to check for possible pH changes around the anode and no pH change could be detected in this study. Unfortunately, the authors do not state which acid-base indicator was used to test for the pH change.

The crystals that formed on the surface of electrodes were found to maintain their space group when analysed using X-ray diffraction methods.

Sazaki³ *et al.* made use of an *ad-hoc* crystallization cell (Figure 2.2) which housed two parallel platinum (Pt) wire electrodes. The study dealt with the effect of an internally applied current in addition to that of a static magnetic field on lysozyme crystallization. The two electrodes were separated by a set distance and allowed to penetrate the crystallizing solution to a constant depth. In essence, providing a uniform electrode surface in contact with the crystallizing solution. Crystallizing solutions used within this study comprised lysozyme and NaCl solutions (of varied concentration) in 200 mM sodium acetate buffer (pH 4.5). Experiments were conducted under both conditions of normal solution and under ‘gelled’ conditions. ‘Gelled’ conditions were those obtained by the addition of small quantities of agarose to the crystallization solution. Currents of 2 μA were applied to the Pt wire electrodes for a period of approximately 8 hours.

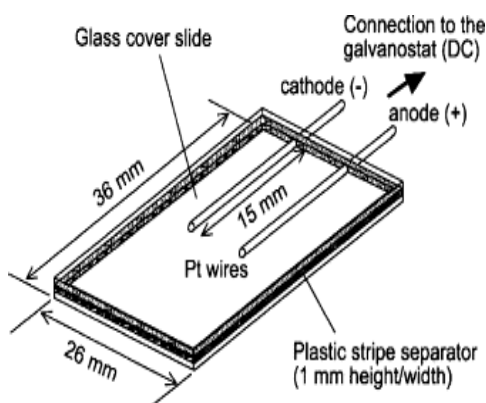


Figure 2.2 Experimental arrangement used within both the Moreno and Sazaki⁴ and Sazaki³ *et al.* studies. Figure taken from ref. 3

A study by Moreno⁴ *et al.* used the same approach and experimental configuration as Sazaki³ *et al.* (Figure 2.2). Results obtained from the Moreno⁴ paper are represented in Figure 2.3 and are the same as that achieved by Sazaki³.

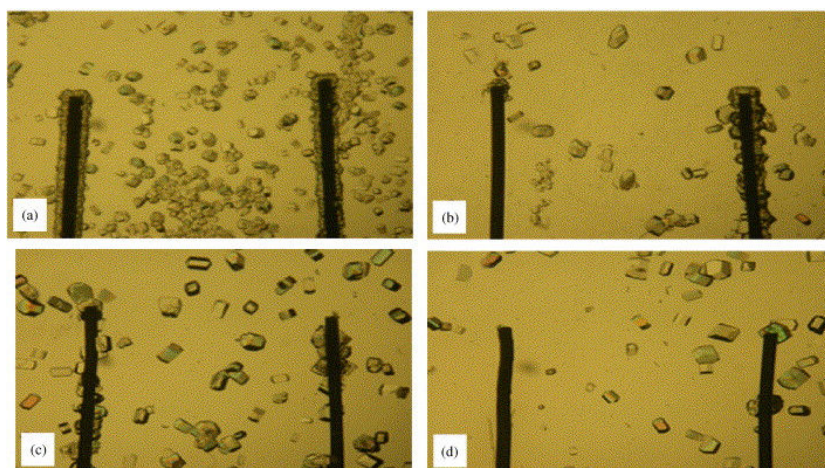


Figure 2.3 Micrographs of lysozyme crystals obtained using apparatus indicated in Figure 2.2 at a supersaturation ratio of $\beta=3.0$. Distance between electrodes was 0.5 cm. (a) Experiment in solution without current, (b) with current, (c) growth in gels without current, and (d) growth in gels in the presence of a constant current. The cathode is on the right and the anode is on the left. Current applied was $2\mu\text{A}$. Figure from ref. 4.

Figure 2.3 is representative of the results obtained using the apparatus shown in Figure 2.2. In contrast to the Mirkin² study, crystals were found by the Moreno⁴ and the Sazaki³ studies to be primarily located around the cathode (Figure 2.3) under ‘gelled’ conditions. A faint precipitate was reported as being formed around the anode after 8 hours of applied current. In agreement with Mirkin², the authors report a general decrease in the nucleation induction time.

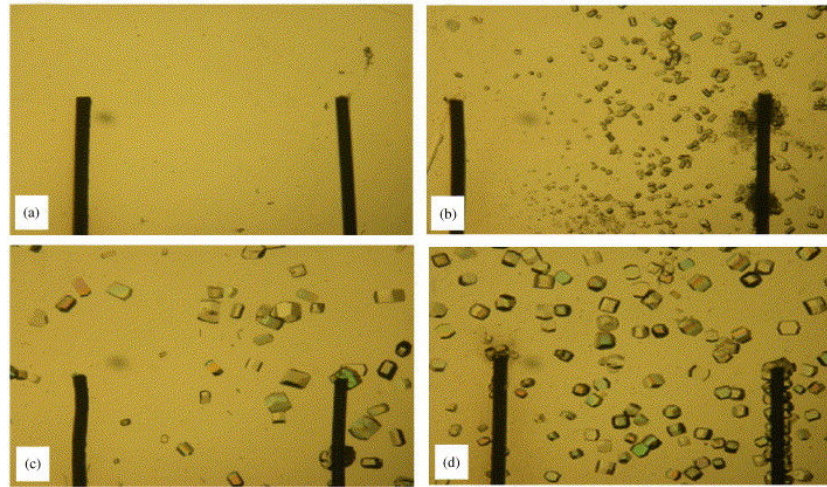


Figure 2.4 Crystals formed on the surface of electrodes at different values of supersaturation with an applied DC current (2 μ A). Panel (a) $\beta=1.0$, (b) $\beta=2.0$, (c) $\beta=3.0$ and (d) $\beta=5.0$. Distance between electrodes was maintained constant at 0.5 cm. Crystal growth was performed using a gelled media. Cathode is on the right and anode is on the left. Figure from ref. 4.

Supersaturation ratios (β in Figure 2.4) were given by $\frac{C - C_e}{C_e}$ where C is the protein concentration in solution and C_e the solubility of the protein (10 mg/ml). It is clear that under ‘gelled’ crystallizing conditions (Figure 2.4), crystals had predominantly formed on the cathode. This particular localization of the crystals occurred over a wide range of supersaturation values. As with Mirkin¹¹, no change in pH around the electrodes was detected.

Nieto-Mendoza⁶ *et al.* studied the effects of using different electrode configurations, in conjunction with internally applied DC currents and potentials on protein crystallization. The study considered both lysozyme and catalase ($pI \approx 5.5$ ⁶). 0.2 mm diameter Pt wire electrodes were used, and were introduced into the crystallization cell at penetration depths of 5 mm through designed orifices (Figure 2.5). The crystallization cell had a two dimensional area of 20 x 20 mm with a width of 1 mm (making a volume equal to 400 μ l).

Lysozyme solutions were reported as comprising approximately 30 mg/ml lysozyme and 40 mg/ml NaCl (4 % (w/v)) with the addition of 0.066 % (w/v) agarose at pH 4.5 (200 mM sodium acetate buffer). Catalase solutions consisted of 10 mg/ml catalase with 4% (w/v) sodium citrate buffer at pH 8.5 (0.1 M Tris-HCl buffer). Galvanostatic experiments (using currents of approximately 2 μ A) were conducted on all cell geometries indicated in Figure 2.5. In contrast, potentiostatic studies were conducted using the electrode geometry indicated by cell configuration 'A' only (Figure 2.5). Potentiostatic experiments were conducted using potentials between -0.6 V and 0.6 V.

Potentials were applied using a 3-electrode arrangement. However the reference and counter electrodes were shorted out and a 'two-electrode' configuration was used. Galvanostatic experiments were conducted with a galvanostat.

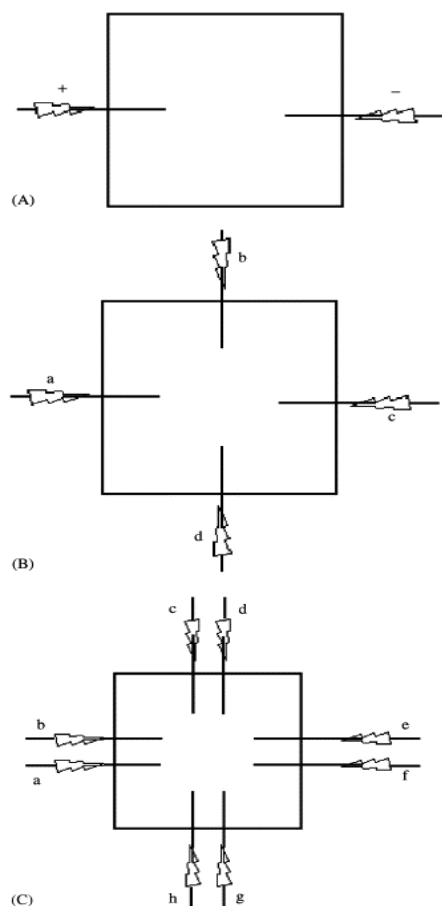


Figure 2.5 Different cell geometries used by Nieto-Mendoza⁶. Cell (A) was used exclusively for experiments under potentiostatic control. Cell B and Cell C refer to other cell geometry arrangements. The sharp linear objects are electrodes which are placed within different cell geometries. Figure from ref. 6.

Nieto-Mendoza⁶ *et al.* report that after 24 hours, under galvanostatic control, with all electrode geometries, decreases in the induction time for nucleation were evident. Lysozyme crystals had formed exclusively around the cathode. Using geometry 'A' (Figure 2.5), the authors note a doubling in the normal lysozyme crystal size on the cathode. With respect to catalase, experiments were conducted potentiostatically at potentials of -0.7 V. The authors report that catalase crystals had the same physical shape as that of the control and congregated around the anode with the c-axis aligned perpendicular to the electrode. In contrast, on the cathode, catalase crystal numbers were reported as smaller and no alignment was evident.

The authors observed gas formation during some experiments, but were unable to detect any pH change around the cathode after 30 hours electrolysis (at an unspecified potential/current) using additions of phenolphthalein (and geometry 'B') to a buffered crystallizing solution without any protein. The cathode was monitored with a stereomicroscope during and after electrolysis.

Under potentiostatic control (-0.5 V), large crystals were observed ($400\text{ }\mu\text{m}$) in solution after 5 hours of applied potential. Figure 2.6 represents the typical crystal size and crystal number obtained after 24 hours of applied potential using “cell geometry A”. The effects of applied potential and current on the crystallization of both lysozyme and catalase were concluded as being due to electromigration effects.

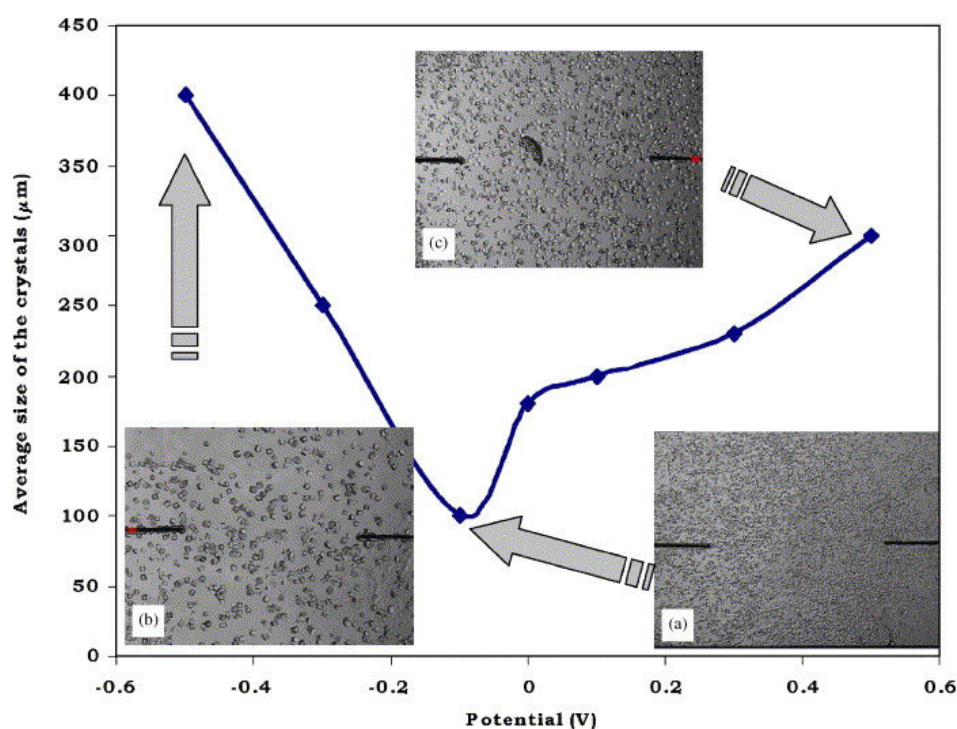


Figure 2.6 Plot of the average size of lysozyme crystals obtained under controlled potential conditions⁶. Cell geometry used is type A, which contains 30 mg/ml lysozyme in 200mM acetate buffer (pH 4.5) and NaCl 40 mg/ml, after 24 h at 15 °C. Figure taken from ref. 6.

Another study by Moreno⁵ *et al.* detailed the use of a 3-electrode arrangement in order to facilitate what they term the “electrocrystallization of ferritin”. Using highly ordered pyrolytic graphite (HOPG) as the working electrode, a platinum wire as a counter electrode and a silver wire as the reference electrode, the authors swept potentials between -950 mV to 500 mV at a rate 40 mV/s for a number of cycles. The ferritin used within this study was separated into fractions which consisted monomers, tetramers and oligomers. Crystallization experiments were then carried out on the three fractions to determine which fraction would give the ‘best response’ in terms of standard crystallization with the conventional precipitant used for ferritin (CdSO_4). It was found that the tetrameric fraction performed the best and was therefore utilised in subsequent ‘electrocrystallization’ experiments.

A 50 μl liquid AFM cell was used to contain a crystallizing solution which consisted of a 1:1 mixture of 22 mg/ml horse spleen ferritin and 0.25 M CdSO_4 (the pH of this solution is estimated to be pH 5, although the authors do not state this explicitly). The results obtained in these ‘electrocrystallization studies’ after approximately 1 hour of cycling the potential are represented in Figure 2.7 and Figure 2.8

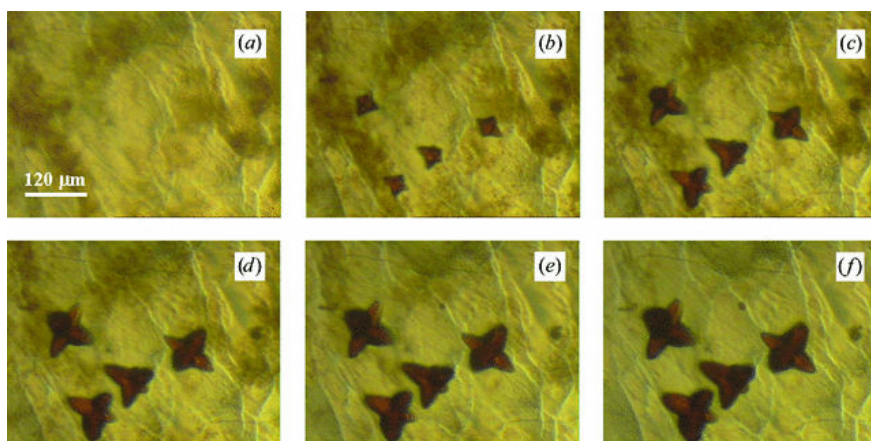


Figure 2.7 Micrographs of the HOPG working electrode at (a) 0, (b) 20, (c) 40, (d) 60, (e) 80 and (f) 100 min from the beginning of the experiment. Control experiment without any applied potential. Figure taken from ref. 5

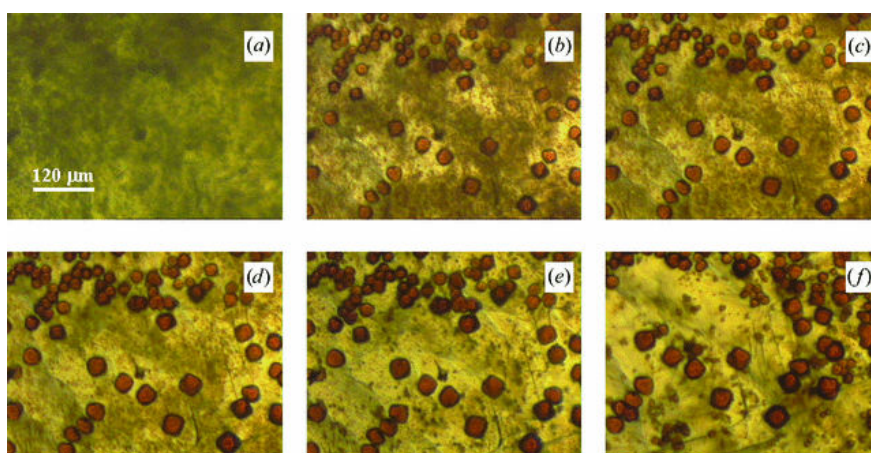


Figure 2.8 Micrographs of the HOPG working electrode at (a) 0, (b) 20, (c) 40, (d) 60, (e) 80 and (f) 100 min from the beginning of the experiment. Potential were cycled between -0.95 V to 0.5 V at a rate 40 mV/s for 1 ½ hours. Figure from ref. 5.

Additionally, the Moreno⁵ *et al.* study had found that small nuclei of cadmium had formed on the HOPG surface, as verified via SEM-EDX analysis. The method was heralded, by the authors, as a means to transform dendritic crystal forms (Figure 2.7) into well defined cubic forms of ferritin (Figure 2.8) via the application of potential.

More recently, Hammadi⁷ *et al* (2007) investigated the crystallization of lysozyme and bovine pancreatic trypsin inhibitor (BPTI). BPTI is similar to lysozyme, in that it is positively charged at pH below 10.5 and requires NaCl as a precipitant⁷. The pH of experimental solutions used in this study was 4.5. The experimental arrangement used, was as indicated in Figure 2.9 and consisted of two tungsten (W) wires (125 μm diameter) which had been electrolytically sharpened to an extremely sharp point.

Crystallizing solutions were covered with a layer of inert paraffin oil to prevent evaporation and the electrodes were separated by a distance of 600 μm . Importantly, crystallizing solutions used within this study were supersaturated but metastable, meaning that supersaturation was insufficient to produce any nucleation (as noted after a 24 hour period). Potentiostatic control of the crystallizing system was used.

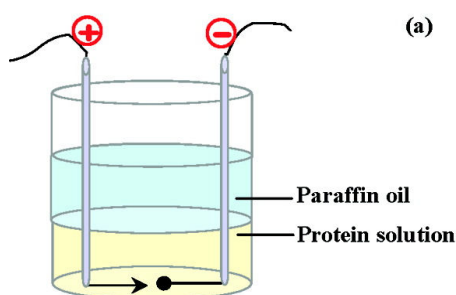


Figure 2.9 Experimental arrangement used for the Hammadi⁷ *et al* (2007) study .
Figure taken from ref. 7.

A decrease in induction times were yet again reported. BPTI crystals were found located around the anode (Figure 2.10) and lysozyme crystals were found located around the cathode (Figure 2.11). No change in pH, via the use of a methyl orange indicator, was evident.

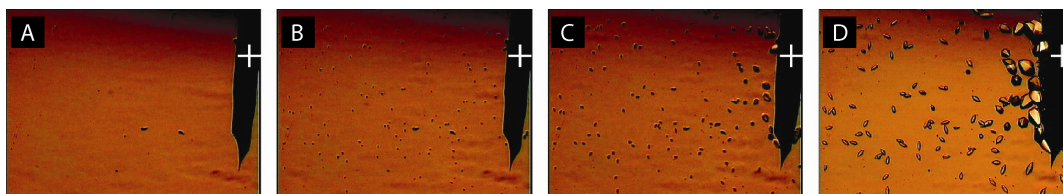


Figure 2.10 BPTI crystallization under an applied potential of 0.785 V. Note localization of BPTI crystals at the anode. Panel (a) indicates the start of the experiment. Panels from left to right, (b) to (d), indicate 7, 11, and 20 hours at the applied potential. Polarity of the electrode is indicated. Figure adapted from ref. 7



Figure 2.11 Lysozyme crystals were found to be located on the cathode in the Hammadi⁷ *et al.* study. Lysozyme crystallizing solution contained 25 mg/ml lysozyme in 0.7 M NaCl and 80 mM sodium acetate buffer at pH 4.5. A potential of 0.9 V was applied for (a) 0 and (b) 12 hours. Polarities of electrodes are as indicated. Panel (c) shows higher magnification view of panel (b), the presence of gel and mass nucleation are notable. Figure from ref. 7.

A slightly different approach was taken by Perez¹² *et al.* who manufactured an ‘electrochemical cell’ within the confines of a quartz dynamic light scattering (DLS) cell. The authors used cytochrome c (pI approximately 10.5). The experimental arrangement was as indicated in Figure 2.12. Platinum wires were used as electrodes and experiments were conducted under galvanostatic control with DC currents of approximately 0.9 μA .

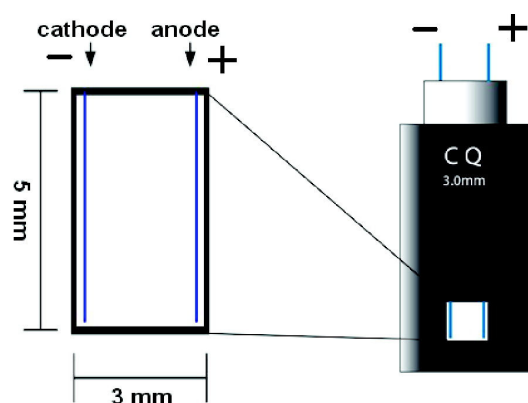


Figure 2.12 Quartz DLS cell with platinum electrodes used by Perez¹² et al. Figure from ref. 11.

Crystallizing solutions used by Perez¹² *et al.* contained 1:1 mixtures of cytochrome c solution (62 mg/ml) and PEG 1000 (50–60% w/v), both dissolved in 100 mM phosphate buffer (pH 7). Temperatures were maintained constant at 10 °C and the cell was DLS monitored every 2 hours for 5 days. On the fifth day small needle-like crystals were observed on the cathode (Figure 2.13) at which time the cell was disconnected from the DC power supply and stored at 18 °C. Crystals were reported as reaching maximal size after one week after the cell was electrically disconnected.

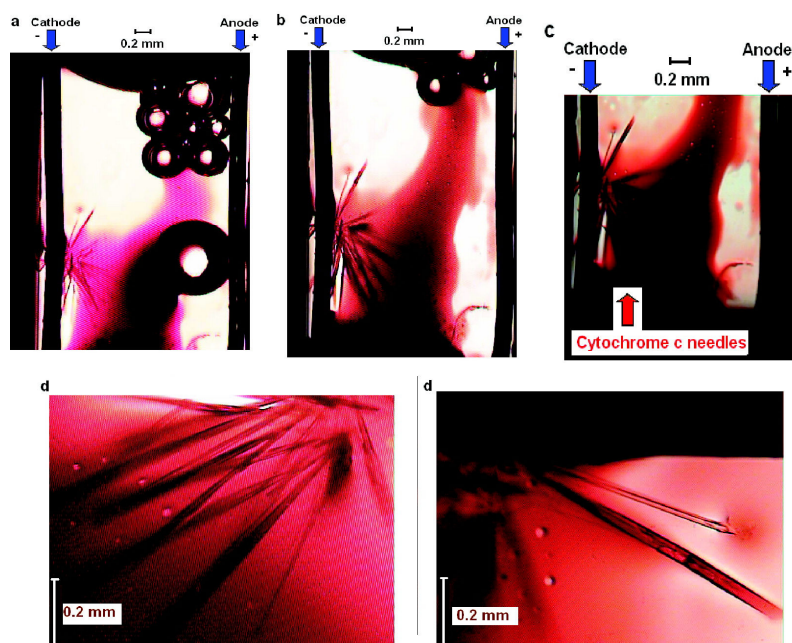


Figure 2.13 The crystallization of cytochrome c in a DLS modified cell at 10 °C reported by Perez et al. (a) After 3 days of experiment. (b) After 5 days of crystal growth. (c) Cytochrome c needle-like crystals after 8 days of experiment. (d and e) Close-up of the needles shown in (c). There is a typo in the original graphic from the literature and the 'second (d)' should read 'e'. Figure from ref. 11.

Another study by Hammadi⁸ (2009) details the use of insulated nanometre sized tungsten electrodes (125 μm) to spatially localise the nucleation of BPTI crystals. The authors report that high electric fields and electric field gradients created at such nanometre sized electrode tips are of potential benefit to the nucleation process (Figure 2.14). Specifically, Hammadi⁸ reports to have created so-called 'nucleation waves' (Figure 2.15) by application of increasing, successive anodic potentials (ranging 0 V – 1 V) which draw currents in the 0.5 μA range. The study made use of 20 mg/ml BPTI at pH 4.9 in 1.6 M NaCl under 'gelled' conditions (an incorporation of agarose).

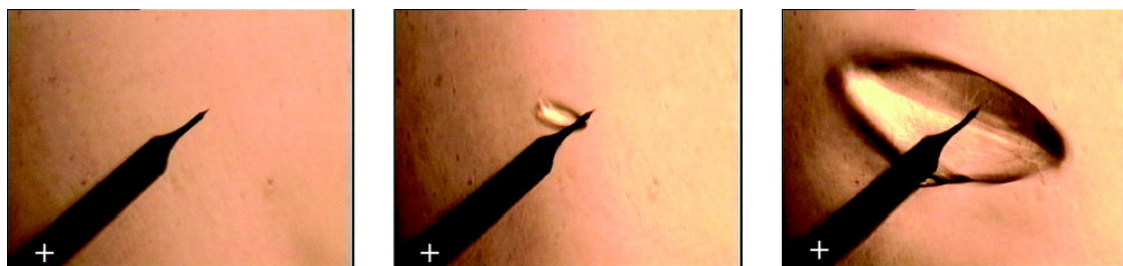


Figure 2.14 The extent of BPTI (20 mg/ml - NaCl 1.6M) nucleation in the vicinity of the tip in 0.5% agarose gel (0.8 V - 0.74 μ A) as reported by Hammadi⁸ et al. The experiment was conducted over 12 hours. W-electrode wires shown are 125 μ m in diameter. Figure from ref. 8.

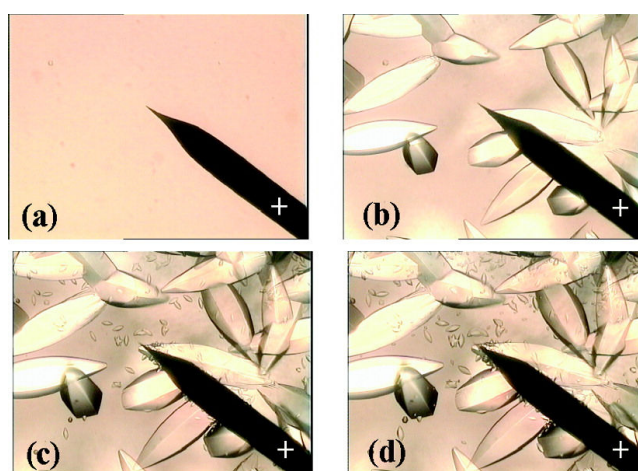


Figure 2.15 "Nucleation waves" created by Hammadi⁸ et al. in a BPTI (20 mg/ml, NaCl 1.6 M, pH 4.6) solution at 20 °C with DC voltage. The anode had been coated with wax, leaving the electrode tip exposed. The W wire electrode was 125 μ m in diameter. Initially, nucleation occurred at the wax-coated anode (panels (a) and (b)) after 2 hours at 0.8 V (0.74 μ A). The voltage was subsequently increased to 0.9 V (0.73 μ A), a second nucleation wave was reported by the authors after 1 hour (panel c). The voltage was again increased to 1 V (1.40 μ A), and a third nucleation wave was recorded within 1 hour of the voltage increase (panel d). Figure from ref. 8.

2.B Experimental

An initial experimental set-up involved a simple two-electrode galvanostatic system housed within a Teflon well (volume 3 cm³) which enabled an electrical current to be passed through a lysozyme crystallizing solution. In contrast to conventional lysozyme crystallization, crystallizing solutions used herein were not buffered. The omission, of what is conventionally an acetate buffer¹³⁻¹⁸, was to allow the creation a zone of relatively low pH in the vicinity of one electrode within our electrochemical cell. This contrasts with previous work (2.A Previous work) using electrical currents for protein crystallization, where pH changes at the electrode surface are reported as being rendered more or less negligible via buffer additions^{4, 14, 19}.

Crystallizing solutions were made from equal aliquots of 75 mg/ml lysozyme (Sigma-Aldrich, UK) and 8.73 (w/v) % NaCl. Both constituents were dissolved in Milli-Q water and the solution was centrifuged for 30 min. Typically, anodic currents of 5 μ A was applied to a 2 mm diameter platinum disc electrode using a homemade galvanostat with a platinum gauze serving as a counter electrode (measured potentials were in the range 1.5 to 1.8 V). For comparison with the electrochemical crystallization method, two types of control experiment were carried out (*vide infra*). The first consisted of crystallizing solution without applied current (control A) and a second consisted of crystallizing solution with a pH of 3.5 (control B). This second control was important and necessary, as it allowed us to approximate conditions generated electrochemically at the anode surface, with the low pH uniform throughout the solution. In all cases, solutions were left for a period of up to 2 h.

In some cases, lysozyme was conjugated to a fluorescent succinimidyl ester, (Alexa Flour 488, Invitrogen, UK) and the conjugation reaction was carried out as per manufacturer's instruction. The crystals were made fluorescent by the addition of a total of 0.5% (v/v) Alexa Flour 488 labelled protein to the crystallizing solution. The fluorescent crystals so obtained were visualized *in situ* using confocal laser scanning microscopy (CLSM, model Zeiss LM 510) at various time periods using an excitation wavelength of 488 nm, with detection of emission above 505 nm. All crystals (whether fluorescent or non-fluorescent) were also viewed *in-situ* using optical microscopy.

10 μ M fluorescein was added to some crystallization solutions which allowed any pH changes near the electrode surface to be monitored using CLSM. Fluorescein is a commonly used fluorophore in CLSM studies which exhibits a pH-sensitive fluorescence signal²⁰⁻²¹. The fluorescence signal increases in aqueous solution from pH \sim 5 to a maximum as the pH rises above pH \sim 7²¹.

In order to utilise smaller volumes of protein solution, and to investigate a wider range of experimental conditions simultaneously, an alternative experimental arrangement was designed. This second arrangement involved a 'multi-well' Teflon block, containing six wells. Each well had a volume of 1 cm³ and was designed to incorporate a hand cast 7.5 mm diameter acrylic resin rod (cold cast with Clarocit cold mounting resin, Struers, UK) which encased a 750 μ m diameter Pt wire as an electrode. Both exposed Pt wire and resin surface were polished to mirror finish on metallographic polishing wheels using micron sized diamond pastes at the final polishing stage. Pt gauze was used as a counter electrode in all cases.

Protein crystallizing solutions, consisting of various concentrations of protein and precipitant were prepared as described previously¹ (and as above), using unlabelled protein. Each well filled with 1 cm³ of crystallizing solution comprising equal volumes of protein and precipitant solution (the protein aliquot was administered first). The pH of the 18 M Ω .cm (Millipore) water was approximately 6.0 to 6.5.

Each of the six wells was connected to a separate handmade galvanostat and anodic current densities of 0, 0.9, 1.8, 2.7, 3.6 and 4.5 A/m² were applied to polished Pt working electrodes. After a period of two hours the surface of each electrode was examined via optical microscopy.

2.C Results

2.C.1 The “one well” arrangement

The significant effect of the applied anodic current is illustrated in Figure 2.16. Large crystals were obtained, with sizes in excess of 180 μm , a crystal size commonly seen after 2 hours under non-electrochemical conditions. The experiment with no applied current (control A) exhibits a higher number of crystals, but with sizes of approximately 80 μm common. The second control (control B) shows even more nucleation, with crystal sizes of approximately 20–30 μm obtained after 2 h.

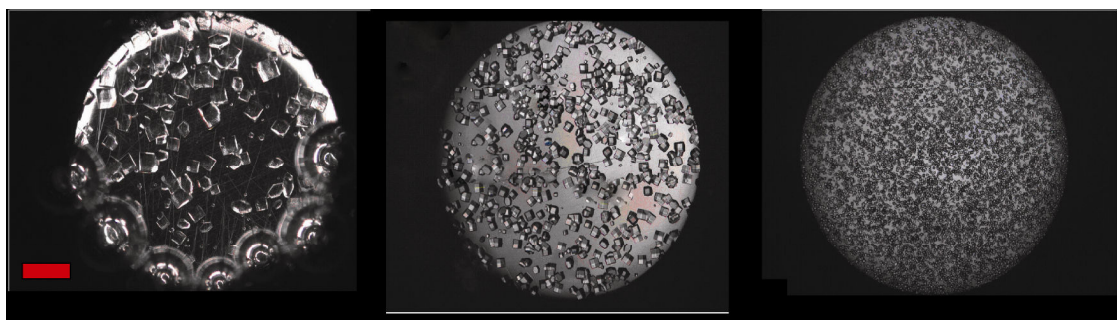


Figure 2.16 Lysozyme crystals formed at an electrode surface after 2 h. From left to right: 5 μA applied current; no current (Control A); and no current with solution pH of 3.5 (Control B). Scale bar shown is 350 μm . The crystals were viewed in-situ via optical microscopy.

Crystal sizes obtained using the part-fluorescently labelled crystallizing solutions were similar both in magnitude and habit to those obtained using the unlabelled solution.

The fluorescently labelled lysozyme allowed ready visualization of the crystals which had nucleated on the electrode surface, as well as those which had nucleated and grown on the surrounding insulating Bakelite material. Figure 2.17 clearly shows that much larger crystals are formed on the electrode surface compared to the insulating material after 45 min of applied anodic current.

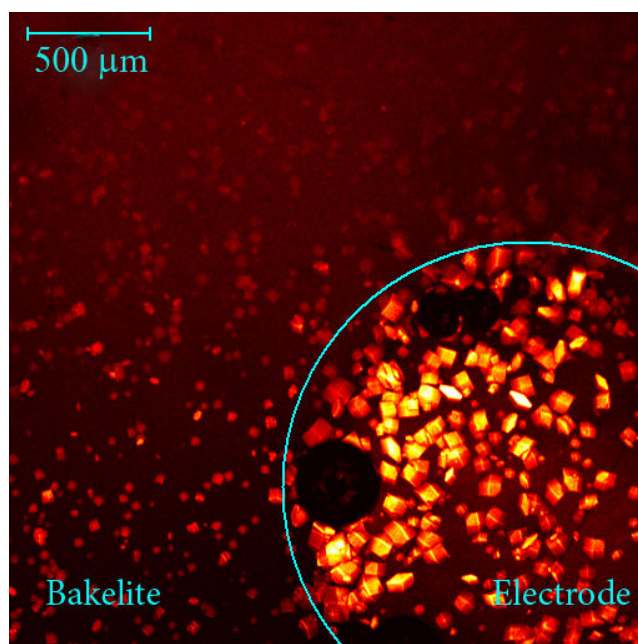


Figure 2.17 In situ laser scanning confocal micrograph of the electrode interface and the surrounding layer of insulating Bakelite after 45 min of applied current. The blue line indicates the interface between the electrode and the surrounding insulating material. Dark circles within the blue line are oxygen bubbles formed via electrolysis.

Since an anodic current was applied to the electrode, the pH was expected to change in the solution immediately above the electrode surface²¹ due to the oxidation of water.



The evolution of oxygen is evident in Figure 2.17 (as bubbles) while the extent of the pH gradient in the vicinity of the active surface of the electrode was visualised using the unlabelled crystallizing solution, described herein, but with the addition of 10 μM fluorescein. With the same anodic electrochemical conditions, the solution above the electrode surface was monitored *via* z-stack imaging with CLSM. Figure 2.18 demonstrates the extent of the pH gradient above the electrode surface, as reflected in the fluorescence signal. The white area in Figure 2.18 was indicative of the fluorescent intensity of the bulk solution ($\text{pH} = 6.5$) and was colour saturated, *via* imaging software, in order to highlight the pH gradient that had developed below it.

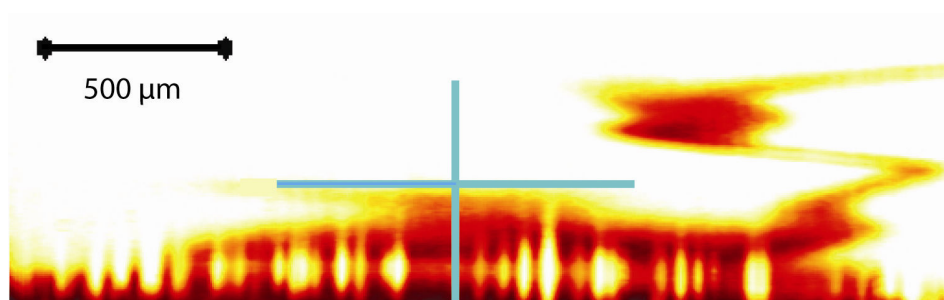


Figure 2.18 Fluorescence intensity map perpendicular to the 2 mm diameter platinum disc electrode (5 μA applied). White areas indicate a $\text{pH} \geq 6.5$ whilst darker areas are $\text{pH} < 5$. Elongated white areas on the electrode surface are lysozyme crystals which have incorporated fluorophore during growth. The scale bar is indicated. The blue cross has horizontal arms of 500 μm in length either side of the centre-point (giving a total of 1 mm in horizontal distance). The base of the blue cross is located over the approximate centre of the electrode.

By tuning the magnitude of the applied current it was found that both lysozyme crystal 'growth' and 'dissolution' could be promoted. The 'dissolution' regime was established when an anodic current of 12 μA (or greater) was applied. Growth and subsequent dissolution of lysozyme crystals is illustrated in Figure 2.19 which shows changes in the fluorescent intensity at the electrode surface for a fluorescently-labelled lysozyme crystallizing solution as the applied current was varied. The fluorescence intensity was monitored for 30 min of 'normal' growth with a 5 μA current.

The resulting fluorescence intensity at this time was used for background subtraction. The fluorescence intensity for subsequent images was taken over the entire image area. The 5 μA current was applied for a further 1777 s and the fluorescence intensity increased approximately linearly with time, indicative of crystal growth. From 1777 s to 1924 s, 12 μA was applied and the intensity decreased slightly, indicating loss of material from the electrode due to dissolution.

The application of 5 μA current between 1924 s and 2649 s caused growth to resume, but at 2649 s, a current of 20 μA caused rapid dissolution and some physical removal of crystals from the surface due to oxygen bubble formation. This resulted in a sharp decrease in fluorescence intensity.

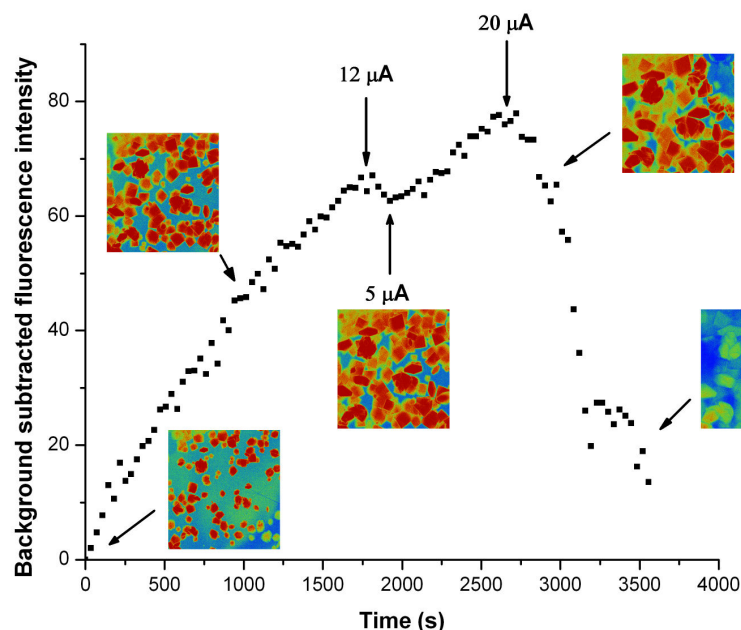


Figure 2.19 Time dependence of fluorescence intensity at the electrode surface as a result of growth and dissolution of fluorescently labelled lysozyme crystals. From 0–1777 s, 5 μA current was applied. The current was then switched to 12 μA from 1777–1924 s and dissolution was seen. From 1924–2649 s 5 μA was again applied and growth resumed. For 2649 s onwards a current of 20 μA was applied and rapid dissolution resulted. In situ CLSM images at several times are shown (not background subtracted, area shown $550\text{ }\mu\text{m} \times 550\text{ }\mu\text{m}$).

Rapid growth of crystals was observed using anodic currents ranging from $\approx 4\text{ }\mu\text{A}$ to $\approx 10\text{ }\mu\text{A}$ in our apparatus which correspond to current densities of approximately $1.3\text{--}3.1\text{ A/m}^2$. At higher applied current, a dissolution process was observed. Application of cathodic currents to the disc electrode of the same magnitude ($4\text{--}10\text{ }\mu\text{A}$) resulted in mass ‘precipitation’ of protein after a few minutes with no crystals observed.

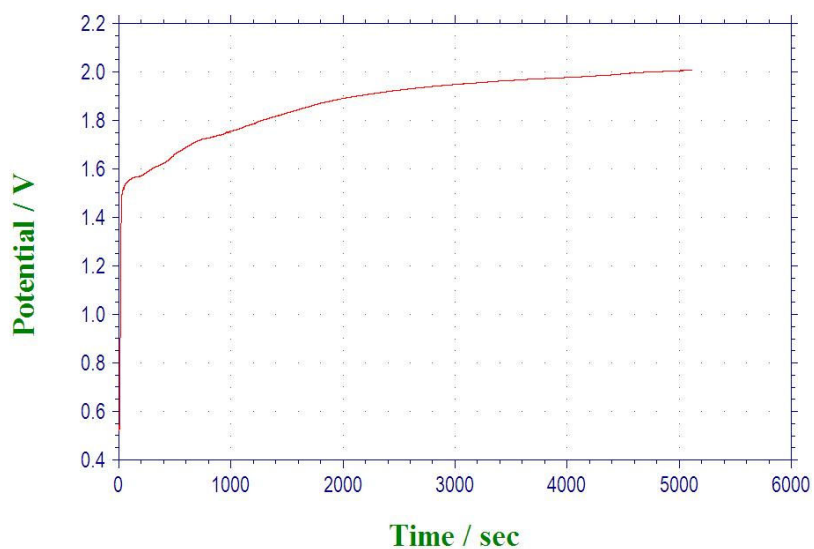


Figure 2.20 The rise in potential for a crystallizing solution ('one-well' arrangement) containing 37.5 mg/ml lysozyme and 4% (w/v) NaCl under galvanostatic control (2 A/m^2). The working electrode was 2 mm diameter Pt disc electrode and counter electrode was platinum gauze. Note that potentials were well over 1.4 V for most of the time and no clear transition time is evident.

2.C.2 The “multi-well” arrangement

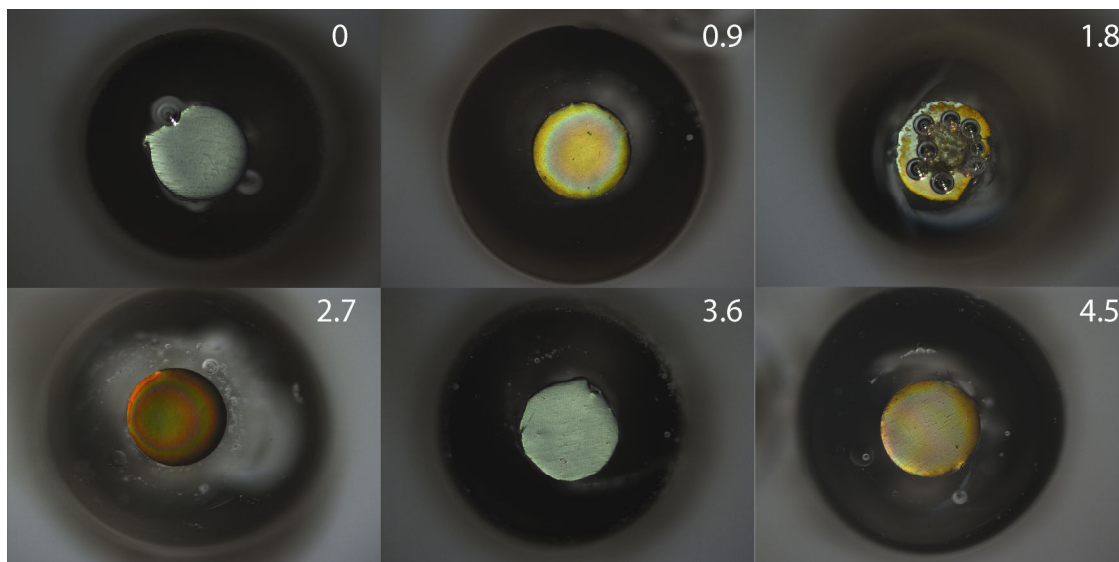


Figure 2.21 Initial solution conditions 37.5 mg/ml lysozyme and 3.5 % (w/v) NaCl (pH circa 6.5). Numbers on panels indicate applied anodic current densities in A/m². Micrographs taken after 2 hours. 750 μm diameter Pt electrodes. Gas bubbles from electrolysis are evident in panel “1.8”.

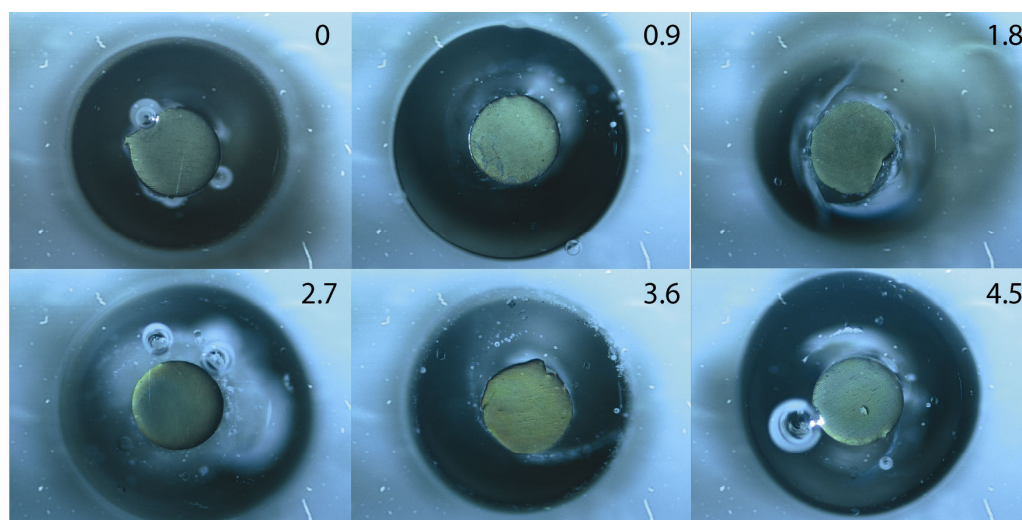


Figure 2.22 Initial solution conditions 45 mg/ml lysozyme and 3.5 % (w/v) NaCl (pH circa 6.5). Numbers on panels indicate applied anodic current densities in A/m². Micrographs taken after 2 hours. 750 μm diameter platinum electrodes.

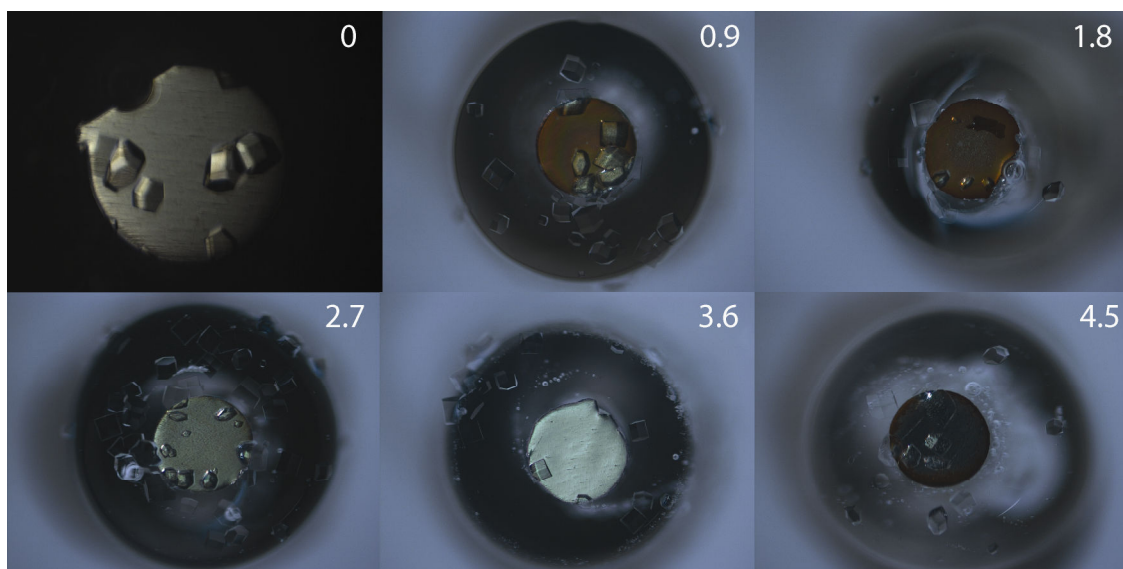


Figure 2.23 Initial solution conditions 37.5 mg/ml lysozyme and 4 % (w/v) NaCl (pH circa 6.5). Numbers on panels indicate applied anodic current densities in A/m². Micrographs taken after 2 hours. 750 μ m diameter platinum electrodes. Micrograph panel 0 was taken at a magnification different from other panels.

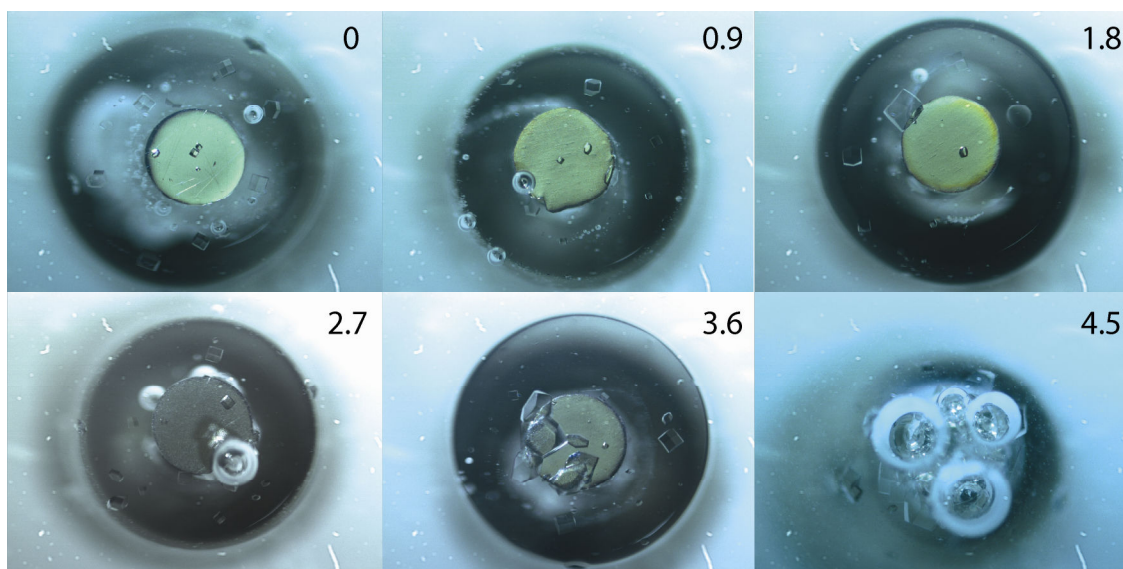


Figure 2.24 Initial solution conditions 45 mg/ml lysozyme and 4 % (w/v) NaCl (pH circa 6.5). Numbers on panels indicate applied anodic current densities in A/m². Micrographs taken after 2 hours. 750 μ m diameter platinum electrodes.

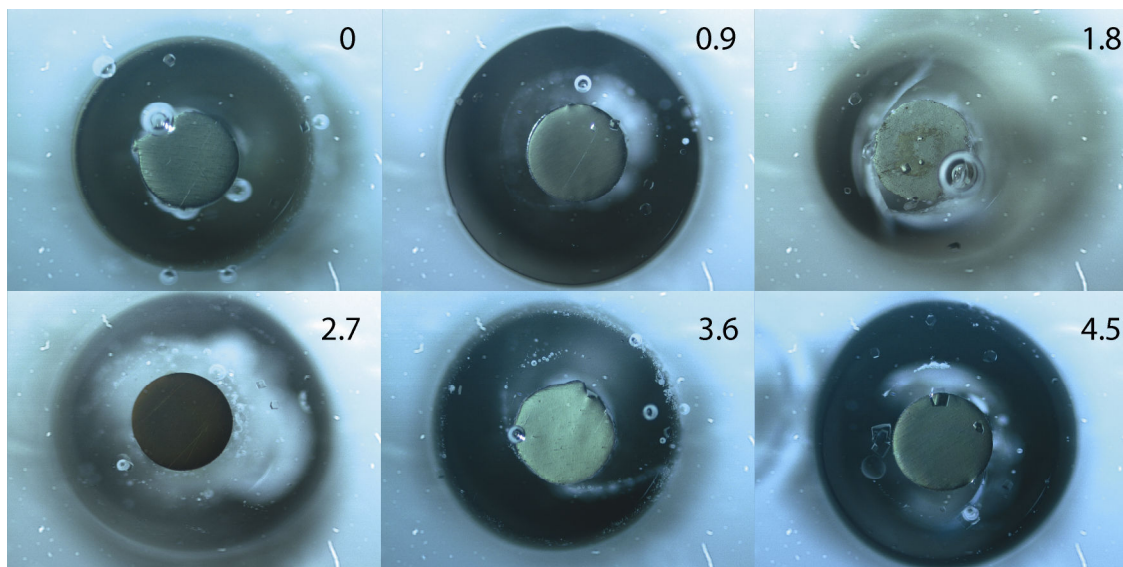


Figure 2.25 Initial solution conditions 30 mg/ml lysozyme and 4.5 % (w/v) NaCl (pH circa 6.5). Numbers on panels indicate applied anodic current densities in A/m². Micrographs taken after 2 hours. 750 μ m diameter platinum electrodes.

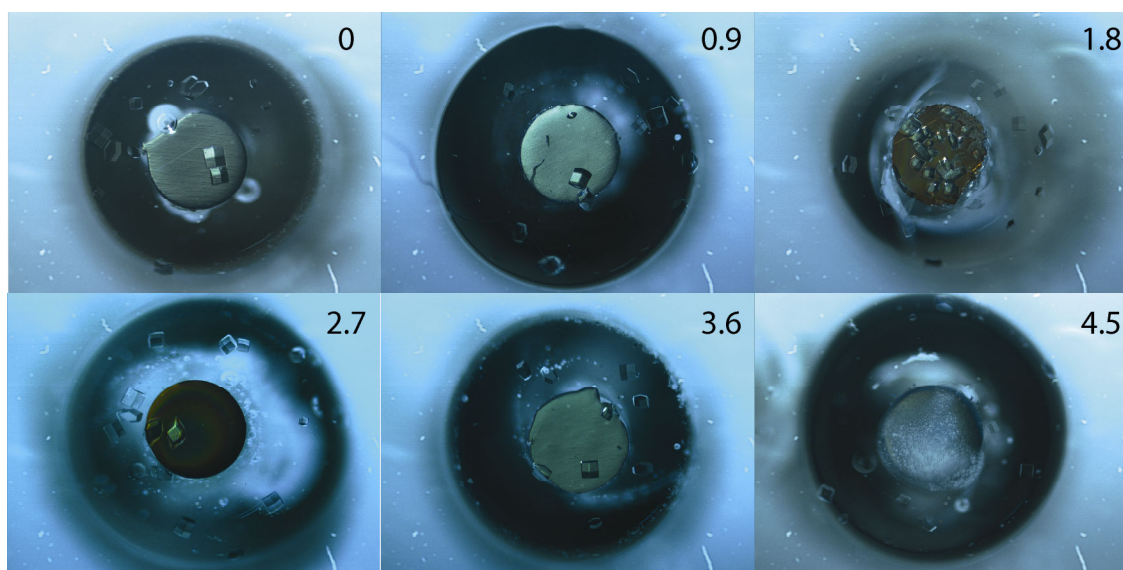


Figure 2.26 Initial solution conditions 37.5 mg/ml lysozyme and 4.5 % (w/v) NaCl (pH circa 6.5). Numbers on panels indicate applied anodic current densities in A/m². Micrographs taken after 2 hours. 750 μ m diameter platinum electrodes.

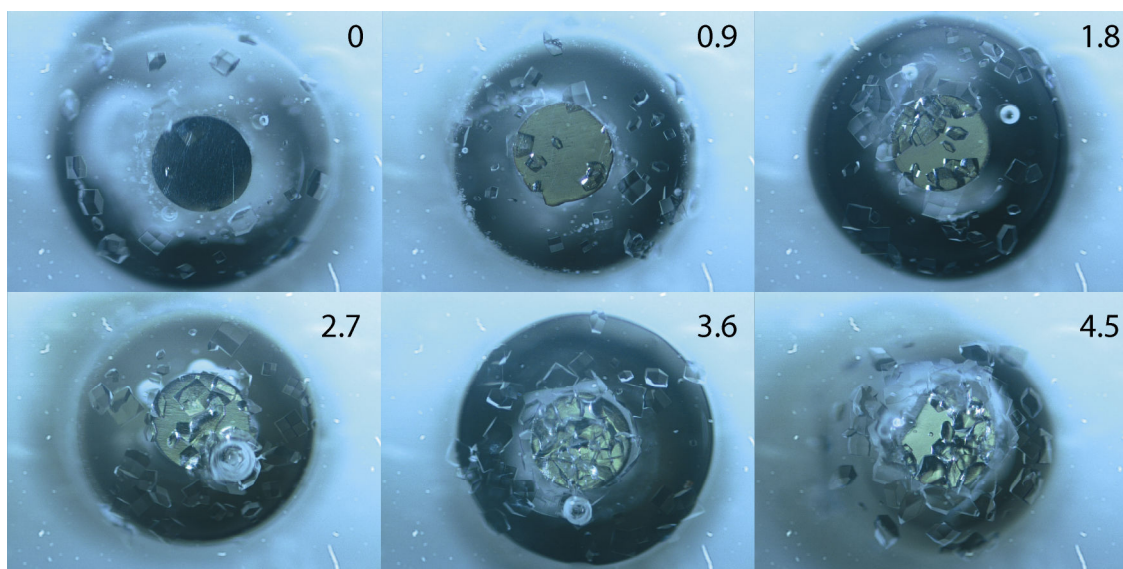


Figure 2.27 Initial solution conditions 45 mg/ml lysozyme and 4.5 % (w/v) NaCl (pH circa 6.5). Numbers on panels indicate applied anodic current densities in A/m². Micrographs taken after 2 hours. 750 μ m diameter platinum electrodes.

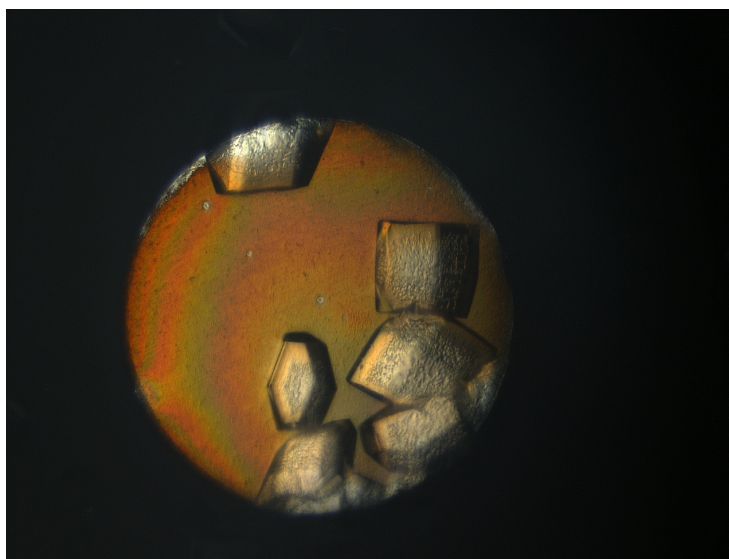


Figure 2.28 Protein film is evident on the surface of one of the electrodes in the 'multi-well' arrangement. Note two dimensional islands on the surface of growing crystals indicative of crystal growth at high levels of supersaturation. The well contained 37.5 mg/ml lysozyme and 4% (w/v) NaCl and a current density of 0.9 A/m² was used. The platinum electrode was 750 μ m in diameter.

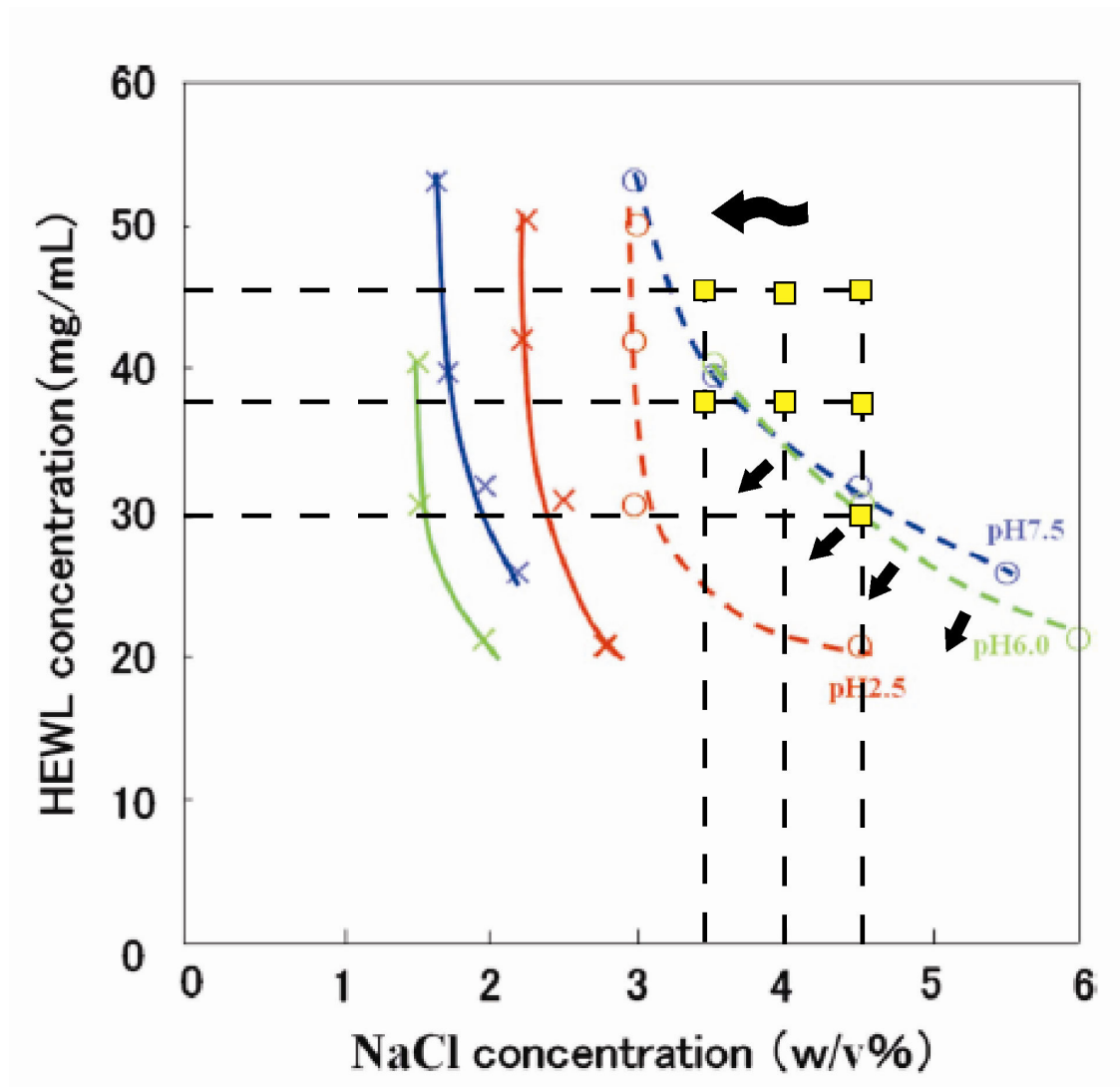


Figure 2.29 A lysozyme/NaCl phase diagram representing initial solution conditions of all experimental conditions used in conjunction with the 'multi-well' arrangement. Yellow squares represent initial crystallization conditions before applied current. Black wavy arrow (top right) indicates shift direction due to chloride oxidation (*vide infra*). Small black arrows indicate 'shift' direction of nucleation zone lines due to water oxidation (*vide infra*). The width of the metastable zone (between a solid and a dashed line of the same colour) and the position of the zone of undersaturation (to the left of solid coloured lines) are also shown to 'shift' with changes in pH. Figure adapted from ref.22.

2.D Discussion

2.D.1 An interpretation of the results via electrochemically-induced shifts in solution conditions at the electrode surface

Crystallizing solutions of the type used herein¹, under galvanostatic control become more resistive over time as higher and higher potentials are needed to maintain the current constant (Figure 2.20). Initial increases in resistance are attributed here to a layer of protein²³ which coats the electrode surface when current was first applied (Figure 2.28). Potentials reached during the course of electrolysis are in excess of that required for both chloride and water oxidation. Protein adsorption to some electrode surfaces is commonplace and often results in the blocking of electron transfer reactions and general fouling²⁴⁻²⁶ of the surface. Previous work²⁶ with regards lysozyme adsorption to Pt electrodes, at concentrations of 3 mg/L, found that films of at least 1 nm were formed at potentials of 1 V. As we use concentrations of approximately 35 mg/ml and potentials in excess of 1 V within this Chapter we expect a relatively thick protein layer to form on the electrode surface. A thick, hard to remove coating was observed on the surface of the electrode (Figure 2.28) after experiments, as vigorous washing and polishing of the electrode surface was needed in order to remove it.

A crystal dissolution process was observed on experiments conducted within the ‘one-well’ arrangement using CLSM (Figure 2.19). The dissolution process was also observed using optical microscopy (not shown). The dissolution process was found to occur at higher current densities ($\approx > 3.82 \text{ A/m}^2$). The dissolution process cannot be reasonably explained solely via water electrolysis alone. Proton production at anodic potentials would result in increased nucleation and at even lower pH values, and protein precipitation could occur. This is because lower pH has the effect of increasing levels of lysozyme supersaturation (Figure 2.29)^{27, 13, 28}. Some precipitate is evident on the electrode surface in Figure 2.26.

Considering that anodic potentials were largely in excess of 1.5 V during the course of galvanostatic experiments (Figure 2.20) suggests that chloride oxidation [(2.2) to (2.4)] was also a significant electrochemical process at the electrode surface²⁹⁻³¹.



Chloride oxidation can make the area around the electrode more acidic, as evolved chlorine undergoes hydrolysis^{30, 32} (2.3). Additionally, as the solution at the electrode becomes more acidic, the potential at which water oxidation (E_{O_2}) occurs becomes more anodic too according to the equation³²

$$E_{\text{O}_2} = 1.23 \text{ V} + \frac{RT}{F} \log(a_{\text{H}^+}) + \frac{RT}{4F} \log P_{\text{O}_2} \quad (2.5)$$

where R, T and F are the gas constant, absolute temperature and the Faraday constant respectively. a_{H^+} is the proton activity at the anode surface and P_{O_2} is the partial pressure of oxygen at the anode. In contrast, the first step in chloride oxidation (2.2) is pH independent³⁰.

Chloride oxidation may even replace water oxidation at potentials above 1.8 V³⁰. In practice however, at current densities $< 10 \text{ A/m}^2$, water oxidation is considered the dominant process. Chloride oxidation will become mass transport limited³⁰ after a period of time at potentials $> 1.8 \text{ V}$ and at high current densities³², although no such behaviour was immediately obvious in Figure 2.20. Considering that water concentration in bulk is extraordinarily high and that the process of water oxidation was dominant, reductions in Cl^- concentration at the anode may have been masked by water oxidation. Exemplified, via the lack of transition time in Figure 2.20. The lack of clear transition time at low current density is also typical for chloride electrolysis at polished platinum electrodes³¹.

The lack of a clear transition time on the chronopotentiogram (in Figure 2.20) does not suggest that Cl^- concentrations were not reduced during electrolysis experiments. Since crystallizing solutions were in excess of 1.8 V for periods of approximately 1 ½ hours reasonably suggests that a zone of depletion, with regards Cl^- may have developed in the vicinity of the electrode surface. The suggested chloride concentration gradient would be additional to proton gradients which had been previously observed via confocal microscopy experiments (Figure 2.18).

The presence of a relatively thick protein layer on the electrode surface (shown in Figure 2.28 and seen previously on electrodes in the literature ³³), coupled with the fact that the electrode was stationary within an unstirred beaker (does not possess well defined mass transport for example ³⁴) makes an accurate estimate of the rate of chloride oxidation very difficult (if not impossible).

One cannot determine accurately as to how the total current was shared between the two proposed electrochemical processes of water and chloride oxidation. Suffice to say that both processes should have occurred as potentials were easily high enough. Direct measurement of the chloride concentration at the electrode surface was unsuccessfully attempted using the chloride-dependent fluorescence from the fluorophore lucigenin³⁵ in conjunction with CLSM. It was found that the intensity of the background fluorescence from the Pt electrode was far greater than the intensity of fluorescence produced from excitation of the fluorophore.

With reference to experiments featured from Figure 2.21 to Figure 2.27, it is clear that the extent of lysozyme crystal nucleation and growth was extremely varied. This large variation was obtained using a wide range of initial solution conditions (Figure 2.29) in conjunction with a wide range of anodic current conditions.

As proton concentrations change in the vicinity of the electrode surface (via water oxidation), the crystallizing solution may be placed into different 'physical

conditions' which could be conducive to nucleation or conducive to growth. The propensity for either behaviour is represented by pH dependent zones on the lysozyme/NaCl phase diagram Figure 2.29. Considering that chloride oxidation may have also been a significant electrochemical process at the electrode surface in addition to that of water oxidation, it is reasonable to suggest that solution conditions could for example:

- 1) Be initially conducive to nucleation, yet over time become further conducive to nucleation, resulting in very little crystal growth, mass nucleation and possible precipitation.
- 2) Be initially conducive to nucleation, yet over time being 'shifted' out of the 'nucleation zone' before nucleation has had a chance to occur. The result may be no crystallization even though initial solution conditions may have had the propensity to form nuclei.
- 3) Be initially conducive to nucleation and after nucleation has occurred been made conducive to growth. The result could be the production of large crystals.
- 4) Be initially not conducive to nucleation, yet being made so over time by electrolysis. Possibly giving the appearance of an 'instant crystallization' effect even though conditions were initially undersaturated.

A simple tabular representation of the proposed hypothetical processes just described above (in list form) can be made by considering that initial crystallizing solutions could be in one of three possible starting conditions namely undersaturated,

metastable or conducive to nucleation³⁶⁻³⁹. Additionally, electrochemical reactions at the surface of the electrode can be either anodic or cathodic. In the anodic case, water and chloride oxidation can occur, and in the cathodic case only water reduction can occur (at the magnitude of potentials reached herein).

Electrochemical processes may therefore be able to ‘shift’ the state of the crystallizing solution at the electrode surface.

Table 2.1 A table representing hypothetical initial solution conditions (Start) and final hypothetical solution conditions (Finish) of hypothetical lysozyme crystallizing solutions. The path taken to the final solution state (Path) via electrolysis is given. The likely outcome (Result) of that path is also given.

U represents an undersaturated solution, M represents a metastable solution and N represents a solution in which nucleation is likely to occur.

Start	Finish	Path	Result
U	U	n/a	nothing
U	Met.	Cathodic. No Cl^- loss. $\text{U} \rightarrow \text{M}$	nothing
U	N	Cathodic. No Cl^- loss. $\text{U} \rightarrow \text{M} \rightarrow \text{N}$	Only likely at high pH
M	U	Anodic, $\text{M} \rightarrow \text{U}$	nothing
M	M	n/a	nothing
M	N	Anodic, $\text{M} \rightarrow \text{N}$	Small crystals
N	U	Anodic, $\text{N} \rightarrow \text{M} \rightarrow \text{U}$	Possible large crystals which may dissolve after a period of time
N	M	Anodic, $\text{N} \rightarrow \text{M}$	Few large crystals
N	N	Anodic, $\text{N} \rightarrow \text{N}$	Mass nucleation, small crystals. Possible precipitation

Hypothetical conditions detailed in Table 2.1 seek to highlight how variations in the extents of lysozyme crystallization which are evident on electrode surfaces after electrolysis could arise (Figure 2.21 to Figure 2.27).

Using this simple framework we propose that it also may be possible to explain the seemingly anomalous observation of the ‘no crystal’ condition (even though solution conditions were initially amenable to crystallization (Figure 2.22 for example)).

2.D.2 Toward a simple semi-quantitative description of the “electrochemically-induced solution shifts” interpretation.

There are many technical difficulties regarding the provision of a strictly quantitative description of the electrochemically-assisted lysozyme crystal growth process, mostly in terms of determining the rates of various electrochemical processes at the electrode surface. The rates of these processes could in turn dictate the rates at which the zones on the phase diagram could evolve starting from an initial set of arbitrary conditions.

A simplistic, yet more detailed semi-quantitative description of the electrochemically-assisted protein crystallization process may be garnered by making a few basic but reasonable assumptions. Some of which may have been already been mentioned or alluded to previously in the text.

1) Protein crystallizing solutions are initially (without any applied current) at an arbitrary set of concentrations with regard to protein, NaCl and also proton concentration (Figure 2.29). Initial ‘physical condition’ of the solution (*viz.* conducive either to nucleation (within the nucleation zone) or crystal growth (a formed crystal which may be present in metastable conditions) could be represented by a point on the lysozyme/NaCl phase diagram. In particular, we use phase diagrams produced by Iwai²² and co-workers. We thus assume that the ‘physical condition’ of the solution at the electrode surface is assumed to be dynamically ‘shifted’ across the phase diagram via electrolysis reactions. Electrochemical ‘shifts’ in terms of both proton (pH) and Cl⁻ concentrations over a two hour period are therefore reasonably assumed.

The rate of the proposed dynamic 'shifts' will in turn be dependent on the magnitude of potentials and pH attained during the course of a galvanostatic experiments. Further, there are three zones present on the phase diagram (delineated by pairs of coloured lines which denote line pairs at different pH). The first zone is found to the left of the solid line, this is an area of *undersaturation*. The second zone is between the dotted and solid line, is termed here as the *metastable zone*. The third zone is to the right of the dotted line and is termed here the '*nucleation zone*'.

2) The phase diagram (Figure 2.29) is read as follows. Initial solution conditions are given by the yellow-black bordered dot at 'A' which is at pH 6 (for example). The 'physical condition' of the solution at the electrode surface will be on the border of the 'pH 6 nucleation zone' and just outside the 'pH 6 metastable zone'. With an applied constant anodic current, water oxidation could occur first, the pH decreases, and the solution at the electrode surface will be 'shifted' into the low pH nucleation zone marked by the coloured dotted lines. The 'final position' of the solution on the diagram depends on the pH attained and the extent of chloride oxidation that has taken place at the electrode surface after 2 hours electrolysis.

By way of an example, if a crystallizing solution attains a pH of 2.5 at the surface of the electrode after 2 hours, and has lost close to 1 % (w/v) chloride at the anode, the 'physical condition' will be at point C which is slightly within the 'pH 2.5' (red line pair) nucleation zone and just outside the pH 2.5 metastable zone. If solution conditions have remained within the nucleation zone for long enough (see assumption 3 *vide infra*) nucleation can occur⁴⁰⁻⁴¹. The extent of nucleation will depend on the 'depth' within the nucleation zone and the initial starting conditions of the solution.

Any pre-formed crystal nuclei 'shifted' into the metastable zone via electrolysis will grow. Any pre-formed crystals 'taken' into the undersaturated zone will dissolve.

3) There is an unspecified induction time for nucleation⁴⁰⁻⁴¹. In other words, a solution must remain in a 'physical condition' conducive to nucleation longer than an unspecified period of time for a series of successful nucleation events to occur. The depth within the nucleation zone dictates the degree of supersaturation and hence the extent of nucleation⁴¹. The induction time increases exponentially with decreasing supersaturation⁴⁰, and typically with lysozyme and NaCl concentrations used herein, nucleation events should occur after approximately 1-2 hours⁴² at room temperature (20 °C) without any applied current. The 1-2 hour induction time is typically what we have observed in practice under conditions of no applied potential.

4) Since lysozyme is added at concentrations of approximately 2.4 mM and precipitant concentrations are approximately 0.6 M, we ignore mass transport via migration for lysozyme⁴³. Additionally, the pH of unbuffered lysozyme crystallizing solutions were experimentally measured and were found to always be between 5.5 and 6.5 before the application of current.

5) A protein film/layer was formed on the electrode surface upon the application of potential (Figure 2.28). We assume therefore that the diffusion coefficient for Cl^- may be somewhat slower than that found in bulk (Cl^- diffusion coefficient in water at 25 °C is $20 \times 10^{-6} \text{ cm}^2/\text{s}$ ⁴⁴). We further assume, for the sake of calculation, (*vide infra*) that the chloride ion has a diffusion coefficient of $3 \times 10^{-7} \text{ cm}^2/\text{s}$ through the protein film. This figure has been derived empirically through ‘rough’ calculation and by observing the extent of crystallization at the electrode surface (in conjunction with the phase diagrams²²). We assume this to be a conservative estimate and could in practice be much lower.

6) As a crystal dissolution process was observed at higher anodic current densities (Figure 2.19), and that lysozyme electromigration has been considered negligible. We suggest that chloride oxidation was a significant process at the electrode surface. We therefore assume that the total applied current was shared in the range 0-30 % toward chloride oxidation and in the range of 50-90 % for water oxidation. We choose a single value of 30% (for the sake of calculation) of the total applied current to go to chloride oxidation for the following reasons:

a) It is a conservative estimate and

b) we operate at low current density⁴⁵ (below 1 mA/cm²) where water oxidation **is** the dominant process (will have a > 50 % current share). In general, current efficiencies for chloride oxidation on platinum anodes are much higher ($\approx 75\%$) for higher applied current densities⁴⁶ (> 250 A/m²). The maximum current density used within this chapter was 4.5 A/m².

7) An approximate value for the pH at the electrode surface may be deduced by assuming a linear proton concentration gradient and noting that bulk solution is recovered at a distance, $\delta \sim 300 \mu\text{m}$, as seen Figure 2.18. This distance is of the order of the Nernst diffusion layer as measured at macroscopic electrodes⁴⁷. The approximate pH at the electrode surface may be deduced from

$$i = \frac{nFAD(C^* - C_b)}{\delta} \quad (2.6)$$

where $n = 1$ is the number of electrons passed per proton generated, F is the Faraday constant (96 500 C mol⁻¹), A is the electrode area (0.0314 cm²), D is the proton diffusion coefficient ($7.5 \times 10^{-5} \text{ cm}^2/\text{s}$)¹, C^* is the concentration of protons at the electrode surface, C_b is the proton concentration at boundary layer (pH ~ 6.5), δ is the boundary layer thickness and i is the applied current.

We have chosen a singular value for the current efficiency for chloride oxidation and thus we have allotted the remaining current (70 % of total) to water oxidation in subsequent calculations (*vide infra*). Because of the small size of the proton⁴⁸, we assume that the proton diffusion coefficient is not significantly affected by the presence of the protein film.

Using the above assumptions, the extent of chloride oxidation at the electrode surface may be estimated via a modelling approach. The 750 μm diameter disc electrode is represented by one dimensional line within a two dimensional domain (representing a 1 cm^3 well). The insulating material surrounding the electrode is assumed to be 7.5 mm in diameter. Oxidation at the electrode surface is represented by a constant flux term (J_{flux} in $\text{mol/m}^2\text{s}$), which is found by dividing the applied current density (I) by the Faraday constant (F). Chloride diffusion from bulk to the depleted area around the electrode surface is modelled using Fick's second law .

This simple modelling scheme was solved using the finite element method within COMSOL Multphysics (COMSOL Inc., Burlington, MA, USA) to give an approximation of the rate of change of chloride concentration at the electrode surface and hence the final chloride concentration at the electrode surface after 2 hours of electrolysis. Initial values for the bulk chloride concentrations at $t = 0$ are given as 3.5, 4 and 4.5% (w/v) respectively (as per conditions used in conjunction with the 'multi-well' arrangement). It is widely known that Na^+ cations are unimportant for lysozyme crystallization, we thus take values obtained for Cl^- (after electrolysis) to mean NaCl concentrations when using calculated Cl^- values in conjunction with the phase diagrams. The Cl^- diffusion coefficient was assumed to be $3 \times 10^{-7} \text{ cm}^2/\text{s}$.

$$J_{flux} = \frac{I}{F} \quad (2.7)$$

$$\frac{\partial[\text{Cl}]}{\partial t} = D\left(\frac{\partial^2[\text{Cl}]}{\partial x^2}\right) \quad (2.8)$$

We are aware that the ‘real’ physical system is much better described by chloride diffusion from bulk, followed by chloride diffusion through a protein film of undetermined thickness and finally by chloride oxidation at the electrode surface. We are also very aware that the interplay between the processes of water and chloride oxidation on the electrode surface³⁰⁻³¹, is itself a very complex and dynamic process and depends on the potentials reached during experiment and the pH of solution at the electrode. With low pH hindering the oxidation of water and chloride oxidation becoming dominant at potentials between 1.8 and 2.2 V³⁰.

However, for the sake of an initial approximation, we model chloride diffusion as just diffusing from bulk with a reduced diffusion coefficient to the electrode surface. We also use static current efficiencies. This will enable approximate chloride concentrations at the very electrode surface to be estimated. This scheme cannot be used to approximate the extent of the possible chloride concentration gradient above the electrode surface. In order for one to do this, a more sophisticated model is needed.

Using simulation conditions just described, we obtain a table which tabulates Cl⁻ (and therefore NaCl) concentrations at the electrode surface after 2 hrs electrolysis using 30% of the total applied currents (given in Table 2.2). pH values obtained using 70% of the total applied current and are also given (Table 2.2)

Table 2.2 Chloride concentrations obtained at the electrode surface after 2 hours of electrolysis at prescribed current densities. The current densities correspond to that used within the ‘multi-well’ arrangement. The pH attained at the electrode surface is also indicated. 30% of the total current was allotted to chloride oxidation and 70% of the total current was allotted to water electrolysis.

INITIAL [NaCl] (w/v) %	APPLIED CURRENTS	0 A/m ²	0.9 A/m ²	1.8 A/m ²	2.7 A/m ²	3.6 A/m ²	4.5 A/m ²
3.5%		3.5	3.3	3.1	2.9	2.7	2.5
4%		4	3.8	3.6	3.4	3.2	3
4.5%		4.5	4.3	4.0	3.9	3.7	3.5
RESULTING pH		6.5	3.58	3.28	3.11	2.98	2.88

The reader is reminded that the conceptual framework presented herein demonstrates proof of concept and represents, for the first time, a mechanistic understanding of the electrochemically assisted crystallization process. It is semi-quantitative at best, but provides a very good starting point for future study with more advanced equipment and more advanced modelling approaches.

The importance of the phase diagram to the interpretation of results generated by studies similar to those presented herein should be immediately apparent. It appears that one may need to have in one's possession, protein/precipitant phase diagrams that have been compiled over a wide range of protein, precipitant and pH combinations before one embarks on such studies. In order to compile such diagrams a crystallization protocol would necessarily need to be in existence beforehand.

2.D.3 An alternative interpretation of the results based on protein crystallization at electrode surfaces via electrophoretic effects and the effect of the protein film

Very recent work has highlighted how lysozyme crystals grown at the surface of indium tin oxide electrodes can be imaged via AFM³³. This ease of imaging is due to the firm attachment of the crystals to the electrode surface. This observation is in accordance with our own observations with regards the formation of a 'hard-to-remove' protein film when the current is first applied. This study has also noted a distinct roughening of the crystal surface with higher applied currents, again corroborating observations presented within this Chapter.

Previously, within this Chapter, we have interpreted current-induced roughening of crystal faces as being caused by electrochemically-induced changes in solution conditions surrounding the growing crystal. An alternative explanation of this and other phenomena (such as the localization of protein crystals on either the anode and cathode for example) has been presented by other researchers³³, which is

based on an electro-focussing/electro-dialysis argument. In order to present a more nuanced interpretation of our results, this alternative interpretation is presented. However, we also show below that this interpretation is less likely than an interpretation based upon electrochemically-induced shifts of solution conditions at the surface of electrodes.

Electro-focussing is a type of zone electrophoresis, enabling molecules to be separated by differences in their surface charge. At a basic level, molecules (such as lysozyme for example) under an ‘electro-focussing’ operation are allowed to migrate between two electrodes through an immobilised pH gradient which is usually contained within a carrying medium (such as a gel for example)⁴⁹.

As an electric current is passed through the medium, positively charged molecules are attracted to the cathode (the negatively-charged electrode) and negatively charged molecules are attracted toward the anode (the positively-charged electrode). Potential differences utilised within these operations are rather large and are in the order of a 100 V⁴⁹. The molecule being electro-focussed will reach a point (at a particular pH) at which it has no net electric charge and therefore cannot migrate any further (the molecules isoelectric point)⁴⁹ under the applied potential.

The alternative interpretation³³, has as its foundation, mass transport effects via migration and the possibility of the influence of the adsorbed protein film on the

crystallization process. We show (*vida infra*) that there are a number of problems associated with this kind of interpretation.

Lysozyme under conditions experienced within our experimental arrangement would have been exposed to pH values (at the anode) from approximately 3 to 7 (Figure 2.18). pH conditions experienced around the cathode would reasonably range from pH 7 upwards due water reduction and subsequent OH^- evolution³².

Experiments conducted under cathodic conditions (by us) were abruptly ended, as a dark precipitate appeared within a few minutes of applying the cathodic current. We did however notice the presence of very small crystals on the surface of the cathode *at the end* of experiments conducted under anodic conditions (at the platinum disc electrode). At no time was remarkable crystal growth evidenced on the cathode surface. If anything, conditions at the cathode were conducive to solely nucleation and not growth.

Crystal nucleation may have been influenced by the presence of a protein film. However, evidence presented within Chapter 2 suggests that it was not (the reader is referred to all experiments conducted within the multi-well arrangement) . It has been shown previously that lysozyme adsorbs to platinum under conditions of 'no

applied potential' ²³, giving films of about 11 Å in thickness²³. Under anodic potential lysozyme has been reported as adsorbing to gold electrodes (at approximately 1 mg/m² from solutions containing 3 mg/L lysozyme⁵⁰).

It is therefore reasonable to assume that under conditions of applied current, some type of film/protein-based layer would have resulted⁵⁰. However, under a number of conditions of applied current there was no crystal nucleation nor was there any growth evident. This observation alone suggests that the presence of a protein film on the electrode surface may have had a small but insignificant effect on nucleation process.

Protein may have migrated toward various electrodes at the instant the current was applied⁵⁰, as large electric field gradients are known to exist at nm length scales at the very electrode surface ⁵¹ and lysozyme is somewhat charged. However, it is doubtful that electric field effects would have had any influence over (frequently) about a hundred microns above the surface of the electrode (typically the vertical height above the electrode surface at which the surface roughness of crystal faces are affected). The pH gradient has been shown (Figure 2.18) to extend over this distance, and is therefore the most likely cause of surface roughening effect on the crystal faces.

In the absence of NaCl, and at pH 4.5 lysozyme has an overall surface charge of approximately +10 to +11⁵². However, with the addition of 350 mM NaCl (approximately ½ the concentration used within this Chapter), the charge falls to approximately +2 and the Debye length (at pH 4.5) and at this salt concentration is 5 Å⁵². These charge characteristics alone suggest short-range interaction between electrode and protein. In particular, an electrode could for example, electrostatically attract either an overall positively charged lysozyme molecule to the cathode as well as a positively charged lysozyme molecule to the electrode surface (by virtue of surface negative charges and a large electric field gradient).

The range of this interaction would be however in the order of a few angstroms⁵²⁻⁵³. Once the initial molecular layer has been attracted to the electrode, most of the charge on the electrode should have been screened. We reiterate that this seems to have had no significant effect on nucleation under anodic conditions. Although we acknowledge that under cathodic conditions it may have had some effect even though the application of cathodic currents to the working electrode resulted in mass precipitation-type behaviour. As such this line of investigation was discontinued.

It is therefore unlikely that any electric field emanating from the electrode surface, in the face of that much precipitant⁴³, could have extended distances ranging from 10 to 100's of microns to affect the roughness of protein crystal faces under conditions of higher applied current (at potentials of below 2 V)

It is therefore much more likely that crystal face roughening (or rather growth mechanism changes via changes in supersaturation from spiral to two-dimensional

growth) occurred via electrochemical shifts in solution conditions caused by electrolysis.

2.E Suggestions and Recommendations

Due to time and equipment constraints it was not possible to carry out experiments and suggestions in the preceding sub-sections. They are however included as a basis for future work.

2.E.1 The extent of the pH gradient at various heights above the anode

Protein solutions, under crystallizing conditions such as that described herein, may be said to represent atypical experimental systems (in terms of electrochemistry). In that the electrode is partially blocked^{50, 54}, large density gradients are undoubtedly present at the electrode surface in the concentration boundary layer (density of crystal vs. supersaturated solution), a phase change is occurring on the surface of the blocking film and the protein has significant buffering capacity.

Due to the atypical nature of these systems we cannot naively use, with great certainty anyway, standard electrochemical techniques which have been established for 'well behaved' systems which usually involve relatively low concentrations of electroactive species undergoing mostly reversible electron transfer on unblocked, highly polished electrode surfaces.

In effect, our electrode surfaces have been immediately fouled and thus accurate measurement on such a fouled is very difficult and not all desirable. That is not to say that we cannot make attempts to glean useful approximations from such techniques, as it is clear that such 'traditional' approaches can provide very useful information about both the crystallizing system and the surrounding solution.

Experimental measurements of the pH gradient at the electrode surface using a combination of fluorescein²¹ and confocal microscopy are possibly unreliable (in our particular case), mostly due to the low pH achieved at the electrode surface and the complex buffering capacity behaviour of lysozyme⁵⁵. Fluorescein exhibits pH dependent adsorption and emission over the pH range 5-9²¹, and for a solutions with pH below 5, extrapolation is used.

The pH at the surface of the anode under conditions used herein was at most times below pH 5 and due to the complex buffering effects from lysozyme renders an accurate determination of the pH at height 'z' above the anode using extrapolation uncertain.

Moreover, we (data not shown) and others⁵⁶ have found that lysozyme crystals are able to easily incorporate fluorescein into the crystal matrix as the crystal grows and thus the additional possibility of error may be reasonably high due to the extremely low concentrations of fluorescein used in comparison to the concentration of lysozyme (mM lysozyme vs. μ M fluorescein). Despite these shortcomings, estimates of the extent of the pH gradient above the electrode surface can still be made (as is demonstrated herein).

Whilst it is clear that accurate prediction will need to be made in the future, which will undoubtedly be based on established electrochemical techniques, the only way to provide very accurate information on the system at the present time would be via direct measurement from *above* the electrode surface.

We therefore suggest the use of iridium oxide based pH microelectrodes of the type previously described⁵⁷, which could provide accurate real-time pH measurement at the surface of the electrode or film. Using such measurements, one could appraise and validate the accuracy of pH gradient approximations used within this study.

2.E.2 The measurement of the proposed temporal evolution of chloride concentration at various heights above the anode.

Due to the presence of the presumably porous protein film/layer^{50, 58} on the electrode surface (Figure 2.28), an accurate estimate of the current efficiency (in terms of chloride oxidation) at the platinum disc electrode was not possible. Moreover, we have assumed that the porous film provides a barrier to diffusion for chloride, which decreases the chloride diffusion coefficient by an order of magnitude. This assumes that diffusion of chloride to the electrode surface could be affected by film thickness and structure, as is suggested in previous studies using layered polyelectrolyte films⁵⁹.

A possible determination of the chloride diffusion coefficient may be obtained by repeating the potentiostatic experiment (Figure 2.20), but at much lower chloride concentration. Perhaps then a transition time may be obtained and used to find the chloride diffusion coefficient.

The structure and thickness of the protein film needs to be determined in order to provide key values for more realistic modelling conditions.

The fact that protein crystals begin to dissolve at higher current densities does suggest strongly that chloride oxidation is also a main process at the electrode surface.

Direct measurement of the chloride concentration at various heights above the electrode surface at various times during a galvanostatic experiment is highly recommended for future work using microelectrodes.

2.E.3 Protein film structure and thickness and different electrode materials

We also recommend the use of QCM (quartz crystal microbalance) techniques in order to measure the extent of the protein adsorption processes under applied anodic potentials. Previous work^{50, 58}, which focussed on lysozyme adsorption on the surface of gold electrodes at pH 5, suggest possible values of about 2 mg/m² protein adsorption and accumulation rates (of protein) of approximately 0.06 mg/m² per second under anodic potentials of approximately 1 V.

The film thickness could be also measured via AFM, by ‘scratching’ off the film and measuring the height difference between the two layers which coupled to QCM studies could give an indication of film density.

The use of different electrode materials for the electrochemically assisted crystallization of lysozyme is highly recommended, as it has been shown that different electrode materials either positively or negatively influence protein adsorption^{50, 58}. In addition, various electrode materials possess different current efficiencies with regards chloride and water oxidation³² and thus could be used to either enhance pH or chloride ‘shifts’ in the case chloride containing crystallization systems.

2.E.4 The dynamic phase diagram

The extents of the three zones evident on the diagram constantly change during the electrolysis process. Thus it is important to ascertain how these zones change in relation to the initial solution conditions (which in turn rely on the rates of each electrochemical reaction). The extents of the three zones are pH and chloride concentration dependent. One therefore needs to determine with greater resolution, the lysozyme/NaCl diagram under both basic and acidic conditions. The proposed newly improved diagram may be compiled in the same way as given previously²²

2.E.5 New experimental arrangements

Microelectrodes, as suggested for pH and chloride measurement, may be mounted side by side under the control of a micropositioner, thus allowing the simultaneous and direct temporal measurement at various heights above the electrode surface of both important quantities. Although it is hard to predict the extent of various component gradients above the electrode surface, we assume that there is

indeed some sort of gradient present¹ and therefore pH and chloride concentrations may be varied in the z-direction above the electrode.

Depending on the extent of such gradients, the possibility of placing previously nucleated crystals at various heights above the electrode surface comes to mind. In effect exposing the crystals to a wide range of easily accessible crystal growth conditions. Used in conjunction with computer control, one may envisage the usefulness of such an approach.

A schematic of the proposed experimental arrangement is shown in Figure 2.30 . The cryoloop featured in Figure 2.30, may also function as a nucleating surface⁶⁰ upon which to initiate heterogeneous nucleation. This suggested arrangement may be used to control both the nucleation and growth processes of lysozyme crystals at various heights above the electrode surface.

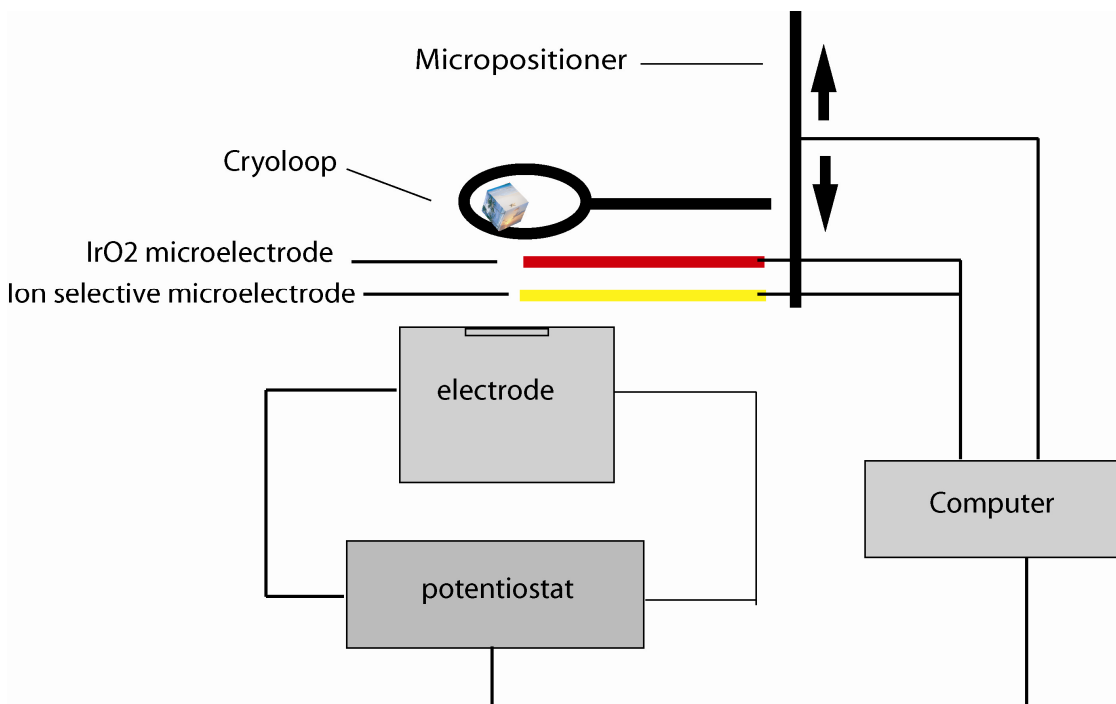


Figure 2.30 A proposed experimental arrangement for the direct measurement of pH and chloride ion concentration measurement above the surface of an electrode with feedback control. The computer is able to control both the micropositioner and the potentiostat via feedback from the electrodes.

2.E.6 X-ray diffraction quality of crystals produced on electrode surfaces

We are ultimately concerned with the X-ray diffraction quality of protein crystals obtained by these and other crystal growth methods. Within this study we did not have the opportunity to measure the crystal perfection via X-ray diffraction methods. Visually, the crystals looked good, but that is not to say they had good diffraction quality. Harvesting crystals from the electrode surface for diffraction studies could prove problematic, although this potential problem could be alleviated by allowing crystals to nucleate on the cryoloop as suggested above.

Increases in supersaturation, presumably induced by electrolysis, were clearly visible on the surface of crystals as the growth mechanism (Figure 2.28) is one of two dimensional island growth, as opposed to the conventional dislocation growth at lower ranges of supersaturation¹⁵.

Previous studies have shown that crystals grown at higher levels of supersaturation can lead to decreases in crystal diffraction quality¹⁵. The previous studies altered supersaturation ratios via changes in protein concentration, not via altering pH and precipitant concentration (as we have). Whether or not there is any difference between the two methods of altering supersaturation, in terms of crystal quality, is yet to be tested.

2.E.7 Alternative protein/precipitant systems for future work

Phase diagrams of the type compiled by Iwai *et al.*²² (for lysozyme), appear to be nonexistent or at least not easily available for other protein/precipitant systems. There does however appear to be fragmented pieces of data within the literature which we have collated (*vide infra*) to give one an idea of how another protein/precipitant system may fare under the methodology utilised and presented herein⁶¹. Basic requirements that need to be met by such an alternative system would be the following

- 1) pH dependence on protein solubility.
- 2) A precipitant that is able to undergo either oxidation or reduction on the electrode surface at reasonable potential.
- 3) A reasonably sized metastable zone width.
- 4) Comprise protein which is easily available and in high quantity.
- 5) Protein that does not degrade under electrolysis

These basic requirements appear to be mostly met by the well known and well studied glucose isomerase/ ammonium sulphate system.

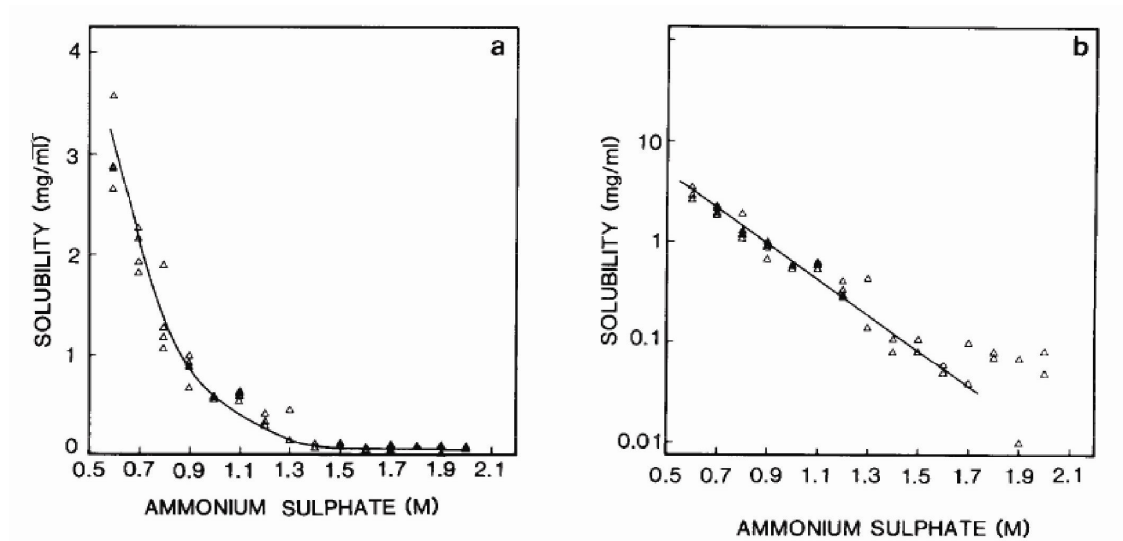


Figure 2.31 The solubility of crystalline glucose isomerase in the presence of ammonium sulphate taken at approximately pH 5.5 from work by Chayen⁶¹. Panel (b) same as (a) except that the solubility has been plotted on a log scale. Figures taken from ref. 61

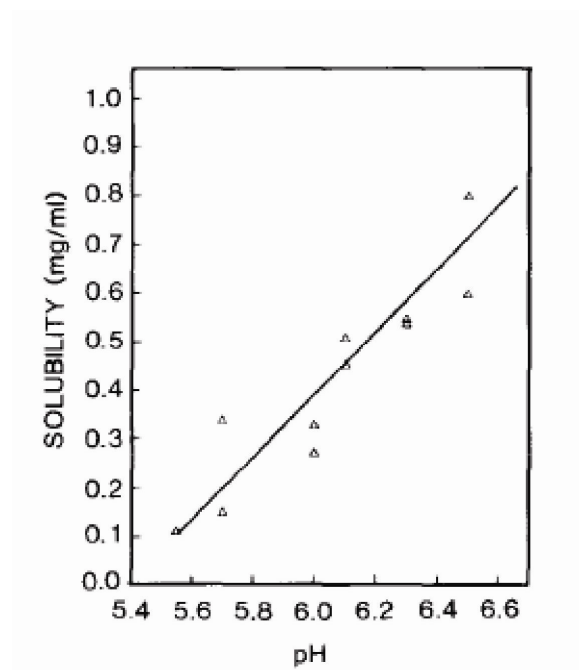
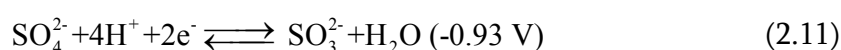
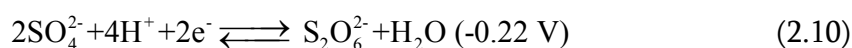
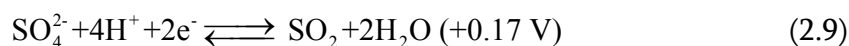


Figure 2.32 The solubility of glucose isomerase as a function pH from 61.

Ammonium sulphate dissociates into NH_4^+ and SO_4^{2-} ions in solution and some sample reduction reactions and associated potentials (vs. NHE)⁶² for both the cation and anion are given below



By application of relatively small positive and negative potentials, one may be able to decrease the concentration of either cation or anion in the vicinity of the electrode. Although some sample reactions⁶², particularly for the sulphate ion indicate the situation appears more advanced than the relatively more simple electrochemical processes evident with a NaCl precipitant. In any case, the major advantage with the glucose isomerase/ $(\text{NH}_4)_2\text{SO}_4$ system is fact the lower potentials may be possibly used reduce the precipitant at the electrode surface, thus enabling the separation of water oxidation/reduction from precipitant oxidation/reduction.

The glucose isomerase/ammonium sulphate system appears to be a good system for future work. Although electrochemically, the reactions taking place at the electrode will be far from simple. One should also note that the isoelectric point of glucose isomerase⁶³ is around pH 5 and glucose isomerase readily forms crystals between pH 6 – pH 8, but is known to rapidly degraded below pH 5 and thus only cathodic potentials may possibly be used. The protein is also known to show solubility decreases with increasing temperature⁶⁴, enabling further degrees of control over protein solubility via control of temperature.

Having identified another possible model system with which one could further investigate our proposed conceptual framework, it may be useful to consider protein/precipitant systems which would be considered *unsuitable* for this method.

We have conducted some preliminary work on ferritin (Figure 2.34), which we have found to be *unsuitable* at this present time. This ‘unsuitably’ was thought to be mostly due to the lack of control caused by a very short metastable zone⁶⁵. The short width of the metastable zone is particular to the ferritin/CdSO₄ system (Figure 2.33). It is thought that due to the short metastable zone width one is able to move from being supersaturated to undersaturated (via pH changes and cadmium reduction) in a very short space of electrolysis time.

Additionally, we considered our level of control over Cd^{2+} reduction insufficient as large cadmium formations (islands and whiskers) were found to form on the platinum electrode surface (Figure 2.34). A neater, more controllable system could be formed by using stripping voltammetry (with a mercury droplet), which would enable fine control over the Cd^{2+} concentration at the droplet surface. This lack of control over Cd^{2+} concentration was further evidenced by what appeared to be ‘drifting’ between mass nucleation, dendritic skeletal crystal morphology and no crystals at all using the same experimental conditions.

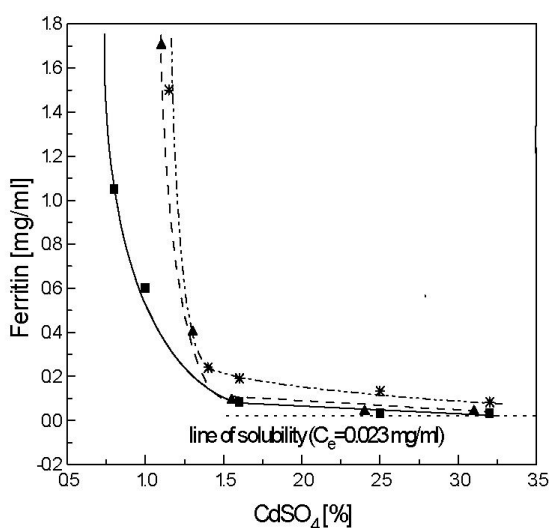


Figure 2.33 A phase diagram for the ferritin/ CdSO_4 system in 0.2 M sodium acetate buffer (pH 5). Note the very short width of the metastable zone. The solubility curve is the solid line and the dashed lines indicate the beginning of the nucleation zone. Figure taken from ref. 65.

Ferritin ‘electrocrystallization’ was previously attempted by Moreno⁵ *et al.* who found that triangular wave pulses (incorporating both cathodic and anodic potentials) resulted in changes to crystal morphology (a change from dendritic to cubic). We found that although ferritin crystals appeared to grow preferentially under cathodic regimes, the crystal morphology became skeletal and dendritic via what appears to be a mechanism based on polyhedral instability⁶⁶.

With regards our own findings, Cd^{2+} became reduced on the electrode surface at cathodic potentials which produced large islands and sometimes 'whiskers' of cadmium on the electrode surface. Although deemed unsuitable at this point in time, the ferritin/ CdSO_4 system does represent a good challenge and a yardstick against which one may measure the degree of ones control over the concentration gradients at the electrode surface via electrolysis.

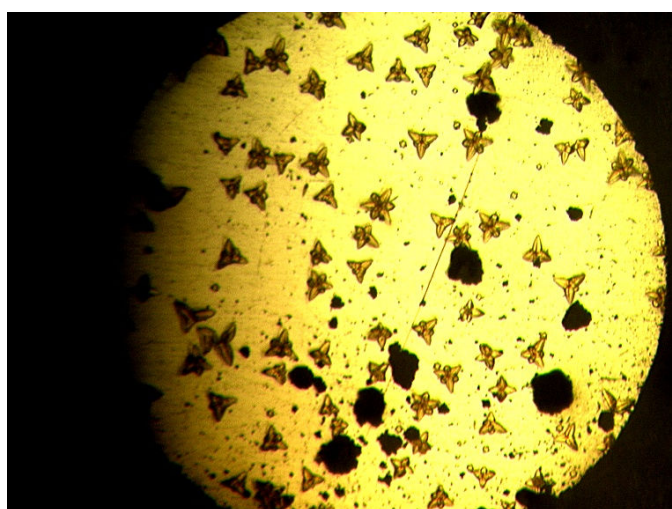


Figure 2.34 The crystallization of ferritin on a 2mm diameter Pt disc electrode under a 2 A/m^2 cathodic regime after 2 hours. Black areas are cadmium islands. Crystal morphology is showing signs of becoming dendritic.

2.E.8 In-situ systems for fundamental study

The results from our proof of concept studies are of importance because they show clearly, for the first time, the real effects of applied current on a model protein crystallizing system. The results may also point toward the successful and facile control of such systems via electrochemical means. This in essence is not only another protein crystal growth method which has been developed, but a platform upon which to investigate, *in situ*, fundamental aspects of the protein crystal nucleation and growth process itself. This provides one with the opportunity to localise the usually stochastic nucleation event both spatially and temporally for atomic level study via high resolution scanned probe techniques for example. Very recent work³³ (prior to the submission of this thesis) within the literature has conducted experiments of the type suggested within this sub-section.

2.E.9 Large protein crystals for neutron crystallography applications ?

Since hydrogen atoms constitute nearly 50 % of the atoms within a protein molecule⁶⁷ and crystal quality limits the diffraction to between 1.5 – 2.5 Å, most of the hydrogen present in the protein cannot be visualised via X-ray diffraction.

In order to ‘view’ these hydrogens one needs ultra-high resolution crystal structures which constitute, at present, less than 1% of the structures in the protein databank⁶⁷. Most of the hydrogen positions are predicted with fair accuracy, however hydrogens with rotational freedom and those which are associated with titratable functional groups are predicted with less confidence⁶⁷. Thus a mechanistic understanding of ligand recognition, enzyme catalysis and particularly protein hydration mechanisms remain unclear in some cases⁶⁷. Neutron crystallography, in contrast, can locate hydrogen atoms at resolutions of 1-5 -2.5 Å and therefore is invaluable for the elucidation of protein hydration structures.

Because neutron crystallography is a low intensity (low flux of available neutrons) technique, which requires long data collection times and really large protein crystals. We suggest that our electrochemically assisted crystal growth method may prove useful for those wanting to grow large crystals (crystal volumes > 1 mm³) for neutron crystallography studies.

2.F References

1. B. R. Silver and P. R. Unwin, *Chemical Communications*, 2008, 5179-5181.
2. N. Mirkin, B. A. Frontana-Urbe, A. Rodriguez-Romero, A. Hernandez-Santoyo and A. Moreno, *Acta Crystallogr. Sect. D-Biol. Crystallogr.*, 2003, **59**, 1533-1538.
3. G. Sazaki, A. Moreno and K. Nakajima, *J. Cryst. Growth*, 2004, **262**, 499-502.
4. A. Moreno and G. Sazaki, *J. Cryst. Growth*, 2004, **264**, 438-444.
5. A. Moreno and M. Rivera, *Acta Crystallographica Section D*, 2005, **61**, 1678-1681.
6. E. Nieto-Mendoza, B. A. Frontana-Urbe, G. Sazaki and A. Moreno, *J. Cryst. Growth*, 2005, **275**, e1437-e1446.
7. Z. Hammadi, J.-P. Astier, R. Morin and S. Veessler, *Crystal Growth & Design*, 2007, **7**, 1472-1475.
8. Z. Hammadi, J.-P. Astier, R. Morin and S. p. Veessler, *Crystal Growth & Design*, 2009, **9**, 3346-3347.
9. J. M. García-Ruiz, A. Moreno, F. Otálora, D. Rondón, C. Viedma and F. Zauscher, *J. Chem. Educ.*, 1998, **75**, 442-null.
10. R. Kaneko and N. Kitabatake, *Chem. Senses*, 2001, **26**, 167-177.
11. N. Mirkin, B. A. Frontana-Urbe, A. Rodriguez-Romero, A. Hernandez-Santoyo and A. Moreno, *Acta Crystallographica - Section D Biological Crystallography*, 2003, **59**, 1533-1538.
12. Y. Pérez, D. s. Eid, F. Acosta, L. Marín-García, J. Jakoncic, V. Stojanoff, B. A. Frontana-Urbe and A. Moreno, *Crystal Growth & Design*, 2008, **8**, 2493-2496.
13. R. A. Judge, R. S. Jacobs, T. Frazier, E. H. Snell and M. L. Pusey, *Biophys. J.*, 1999, **77**, 1585-1593.
14. M. I. Al-Haq, E. Lebrasseur, H. Tsuchiya and T. Torii, *Crystallography Reviews*, 2007, **13**, 29-64.
15. I. Yoshizaki, T. Sato, N. Igarashi, M. Natsuisaka, N. Tanaka, H. Komatsu and S. Yoda, *Acta Crystallogr., Sect D: Biol. Crystallogr.*, 2001, **57**, 1621-1629.
16. G. Alderton and H. L. Fevold, *J. Biol. Chem.*, 1946, **164**, 1-5.
17. M. Ataka and S. Tanaka, *Biopolymers*, 1986, **25**, 337-350.
18. J. M. P. H. W. B. Ying-Chou Shih, *Biotechnol. Bioeng.*, 1992, **40**, 1155-1164.
19. G. Sazaki, A. Moreno and K. Nakajima, *J. Cryst. Growth*, 2004, **262**, 499-502.
20. E. Bitziou, N. C. Rudd, M. A. Edwards and P. R. Unwin, *Anal. Chem.*, 2006, **78**, 1435-1443.
21. N. C. Rudd, S. Cannan, E. Bitziou, I. Ciani, A. L. Whitworth and P. R. Unwin, *Anal. Chem.*, 2005, **77**, 6205-6217.

22. W. Iwai, D. Yagi, T. Ishikawa, Y. Ohnishi, I. Tanaka and N. Niimura, *Journal of Synchrotron Radiation*, 2008, **15**, 312-315.
23. B. A. Ivarsson, P.-O. Hegg, K. I. Lundström and U. Jönsson, *Colloids Surf.*, 1985, **13**, 169-192.
24. R. R. Ueta and F. B. Diniz, *Colloids and Surfaces B: Biointerfaces*, 2008, **61**, 244-249.
25. S. E. Moulton, J. N. Barisci, A. Bath, R. Stella and G. G. Wallace, *J. Colloid Interface Sci.*, 2003, **261**, 312-319.
26. S. G. Roscoe and K. L. Fuller, *J. Colloid Interface Sci.*, 1992, **152**, 429-441.
27. S. D. Durbin and G. Feher, *J. Cryst. Growth*, 1986, **76**, 583-592.
28. S. B. Howard, P. J. Twigg, J. K. Baird and E. J. Meehan, *J. Cryst. Growth*, 1988, **90**, 94-104.
29. A. Kraft, M. Stadelmann, M. Blaschke, D. Kreysig, B. Sandt, F. Schröder and J. Rennau, *J. Appl. Electrochem.*, 1999, **29**, 859-866.
30. H. K. Abdel-Aal, K. M. Zohdy and M. A. Kareem, *The Open Fuel Cells Journal*, 2010, **3**, 1-7.
31. J. S. Mayell and S. H. Langer, *Electrochim. Acta*, 1964, **9**, 1411-1416.
32. J. E. Bennett, *Int. J. Hydrogen Energy*, 1980, **5**, 401-408.
33. G. Gil-Alvaradejo, R. R. Ruiz-Arellano, C. Owen, A. Rodríguez-Romero, E. Rudíño-Piñera, M. K. Antwi, V. Stojanoff and A. Moreno, *Cryst. Growth Des.*, 2011, null-null.
34. J. Albery, *Electrode kinetics*, Oxford University Press, Oxford, UK, 1975.
35. K. D. Legg and D. M. Hercules, *The Journal of Physical Chemistry*, 1970, **74**, 2114-2118.
36. D. M. Blow, N. E. Chayen, L. F. Lloyd and E. Saridakis, *Protein Sci.*, 1994, **3**, 1638-1643.
37. A. Penkova, N. Chayen, E. Saridakis and C. N. Nanev, *Acta Crystallographica Section D-Biological Crystallography*, 2002, **58**, 1606-1610.
38. R. P. Sear, *Journal of Physics Condensed Matter*, 2007, **19**.
39. N. E. Chayen and E. Saridakis, *Nat. Meth.*, 2008, **5**, 147-153.
40. B. Biscans and C. Laguerie, *J. Phys. D: Appl. Phys.*, 1993, **26**, B118.
41. A. Bernardo, C. E. Calmanovici and E. A. Miranda, *Cryst. Growth Des.*, 2004, **4**, 799-805.
42. S. Talreja, S. L. Perry, S. Guha, V. Bhamidi, C. F. Zukoski and P. J. A. Kenis, *The Journal of Physical Chemistry B*, 2010, **114**, 4432-4441.
43. E. J. F. Dickinson, J. G. Limon-Petersen, N. V. Rees and R. G. Compton, *The Journal of Physical Chemistry C*, 2009, **113**, 11157-11171.
44. L. Yuan-Hui and S. Gregory, *Geochim. Cosmochim. Acta*, 1974, **38**, 703-714.
45. R. Balaji, B. S. Kannan, J. Lakshmi, N. Senthil, S. Vasudevan, G. Sozhan, A. K. Shukla and S. Ravichandran, *Electrochem. Commun.*, 2009, **11**, 1700-1702.

46. H. K. Abdel-Aal and I. A. Hussein, *International Journal of Hydrogen Energy*, 1993, **18**, 485-489.
47. C. Amatore, S. Szunerits, L. Thouin and J.-S. Warkocz, *J. Electroanal. Chem.*, 2001, **500**, 62-70.
48. O. Markovitch, H. Chen, S. Izvekov, F. Paesani, G. A. Voth and N. Agmon, *The Journal of Physical Chemistry B*, 2008, **112**, 9456-9466.
49. S. Ghosal, *Annual Review of Fluid Mechanics*, 2006, **38**, 309-338.
50. J. M. Kleijn, D. Barten and M. A. Cohen Stuart, *Langmuir*, 2004, **20**, 9703-9713.
51. A. J. Bard and L. R. Faulkner, *Electrochemical Methods : Fundamentals and Applications*, John Wiley & Sons, Limited, Australia, 2001.
52. A. Tardieu, A. Le Verge, M. Malfois, F. Bonneté, S. Finet, M. Riès-Kautt and L. Belloni, *J. Cryst. Growth*, 1999, **196**, 193-203.
53. A. Ducruix, J. P. Guilloteau, M. Ries-Kautt and A. Tardieu, *J. Cryst. Growth*, 1996, **168**, 28-39.
54. D. Barten, PhD Thesis, Wageningen University dissertation no. 3475 2003.
55. J. Luo, W. Olthuis, P. Bergveld, M. Bos and W. E. van der Linden, *Sensors and Actuators B: Chemical*, 1994, **20**, 7-15.
56. A. Cvetkovic, M. Zomerdijs, A. J. J. Straathof, R. Krishna and L. A. M. v. d. Wielen, *Biotechnol. Bioeng.*, 2004, **87**, 658-668.
57. E. E.-D. M. El-Giar and D. O. Wipf, *J. Electroanal. Chem.*, 2007, **609**, 147-154.
58. D. Barten, Met lit. opg. - Met samenvatting in het Engels en Nederlands, s.n.], 2003.
59. J. J. Harris, J. L. Stair and M. L. Bruening, *Chem. Mater.*, 2000, **12**, 1941-1946.
60. N. E. Chayen, E. Saridakis and R. P. Sear, *PNAS*, 2006, **103**, 597-601.
61. N. Chayen, J. Akins, S. Campbell-Smith and D. M. Blow, *J. Cryst. Growth*, 1988, **90**, 112-116.
62. D. R. Lide *CRC Handbook of Chemistry and Physics* CRC Press, 2003.
63. W. Kong, X. Zhang, M. L. Gao, H. Zhou, W. Li and J. C. Shen, *Macromol. Rapid Commun.*, 1994, **15**, 405-409.
64. Hampton Research " Glucose isomerase user guide, HR7-100 & HR7-102 " http://hamptonresearch.com/documents/product/hr001174_7-102_web_user_guide.pdf.
65. D. Tsekova, S. Popova and C. Nanev, *Acta Crystallographica Section D*, 2002, **58**, 1588-1592.
66. C. N. Nanev, *Prog. Cryst. Growth Charact. Mater.*, 1997, **35**, 1-26.
67. D. A. A. Myles, *Curr. Opin. Struct. Biol.*, 2006, **16**, 630-637.

3. Protein crystallization at the oil/water interface

This chapter has formed the basis of a published paper. Barry R. Silver, Vilmös Fülöp and Patrick R. Unwin, "Protein crystallization at oil-water interfaces", New J. Chem., 2011, 35, 602-606. I conducted the majority of the experiments for this paper and wrote the paper in conjunction with P.R.Unwin.

3.A Experimental

Protein solutions (typically 75 mg/ml) were mixed 1:1 (v/v) with a NaCl solution. NaCl solution concentrations used, typically in the range between 5-9% (w/v), allowed ample lysozyme crystallization to occur over the 24 hour experimental time period, and resulted in the production of good sized lysozyme crystals which were easily viewed with an optical microscope. The pH of the solution was approximately 6.5. Droplets of mixed solution were placed within an ad-hoc Teflon crystallizing cell (Figure 3.1), designed to allow easy viewing of the oil/water and air/water interfaces (when applicable).

The depression within the insert, was loaded with typically 150 μ l of aqueous crystallizing solution or organic solvent (when more dense than the aqueous phase) to form a hemispherical droplet. The droplet was then carefully covered with either 600 μ l of aqueous solution or organic solvent. A lightly greased cover slip was placed on the end of the barrel to prevent evaporation. The sealed cell was left for a period of 24 hours at room temperature (20 °C) to allow sufficient time for crystals to nucleate and grow. The oil/water and air/water interfaces were monitored via optical microscopy after this 24 hour period.

Drop shape analysis (Appendix I) was conducted using a DSA 100 drop shape analysis system from Krüss (Germany). The drop shape analysis method for the determination of dynamic interfacial tension is given in the appendix in section 3.D

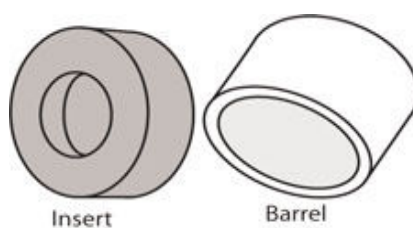
In addition, the instrument provided low power optical microscopy capabilities for viewing extruded pendant droplets in various organic solvents from a sideways aspect. Protein solutions used for dynamic surface tension data were prepared as detailed above.

Solvents used within this study are tabulated in Table 3.1. ‘Active’ solvents are indicated in bold (*vide infra*).

Table 3.1 Summary of main properties of the oil phases used within this study. ‘Active’ solvents are indicated in bold

Liquid	ϵ	μ	S	γ	W
1,2-dichloroethane	10.42	1.83	0.852	23.1 ¹	1.865e-3 g/100 g
Chloroform	4.807	1.04±0.02	0.825	27.9 ²	5.744e-1 mole percent
Halothane	4.66	≈2	0.355	NA	0.035e-2 g/100 g
Dichloromethane	8.93	1.60±0.03	0.172	28 ³	8.226e-1 mole percent
Nitrobenzene	35.6	4.22±0.08	0.2	26 ⁴	0.2 g/100 g
Bromoform	4.404	0.99±0.02	0.314	40.85 ⁵	2.21e-2 mole percent
1-octanol	10.3	1.76	-	10.8 ²	2.949 mol/L
Silicon oil	2.7	-	-	≈40 ⁶	0.04 mol/L
Paraffin oil	≈2.3	-	-	52 ⁵	Insoluble
Heptane	1.92	-	-	51.9 ⁷	2.6 g/100 g
Toluene	2.379	0.375±0.01	0.047	32.5 ⁷	2.28 g/100 g
Cyclohexane	2.02	-	-	50 ⁸	9 g/100 g
Xylene	≈2.2	0.64±0.05	-	≈35 ²	0.032 mol/L
Benzene	2.282	-	0.08	32.3 ²	0.032 mol/L
Ethyl acetate	6.081	1.79±0.09	8.3	6.68 ⁹	3 g/100 g
Diethyl ether	4.266	1.15±0.02	6.9	10.9 ²	1.468 g/100 g

ϵ = static relative permittivity, μ = dipole moments in debye units, **S** = solubility of the solvent in water g per 100 g of water values from IUPAC-NIST Solubility Database, Version 1.0¹⁰, γ = oil-pure water interfacial surface tensions (mN/m), **W** = solubility of water in the solvent . g/100 g grams of substance per 100 g of solvent. Mole percent is the mole fraction x 100. All other values taken from CRC handbook of Chemistry and Physics¹¹ unless otherwise referenced. †- this is the solubility of water in PDMS (mol/dm³)¹². NA = not available

**Figure 3.1** Apparatus used to monitor the oil/water and air/water interfaces optically during crystallization. The insert was slid within the barrel and a lightly greased, glass cover-slip placed on the end of the barrel. The depression within the insert contained either a droplet of oil or aqueous solution depending on which phase was more dense.

3.B Results

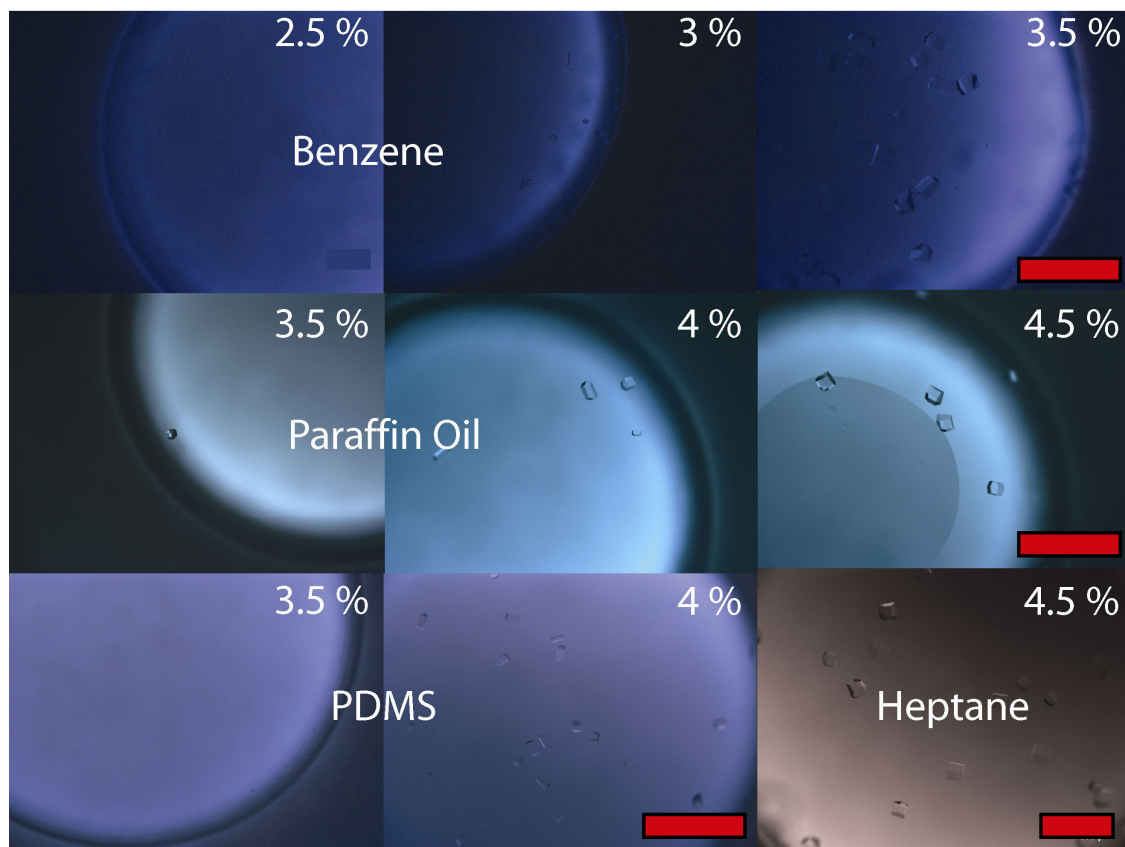


Figure 3.2 The extent of protein crystallization at a variety of 'inactive' oil/water interfaces. Percentages indicated refer to the (w/v) % of NaCl present in the aqueous phase. The aqueous phase contained 37.5 mg/ml lysozyme in all cases. Scale bars indicated are 1 mm in length. PDMS is polydimethylsiloxane (or silicone oil)

Figure 3.2 shows the extent of lysozyme crystallization at a variety of 'inactive' oil/water interfaces at varied NaCl concentration. In each case, the oil phase was less dense than the aqueous phase and hence no air/water interface was present. Some nucleation and crystal growth was evident. The crystallization process appears largely retarded in comparison to 'active' oil/water interfaces (*vide infra*) and indeed some air/water interfaces.

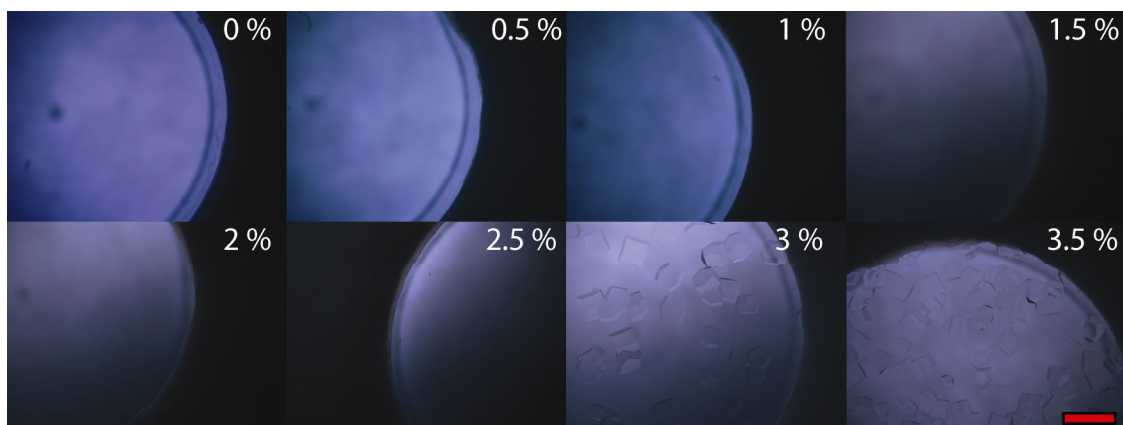


Figure 3.3 The extent of lysozyme crystallization on the bromoform/aqueous interface at varied aqueous phase salt concentrations. Percentages indicate (w/v) % NaCl in the aqueous phase. 37.5 mg/ml lysozyme was used within the aqueous phase in all cases. Scale bar is 1 mm and applies across all panels.



Figure 3.4 Optical micrographs illustrating, for comparative purposes, the extent of lysozyme crystallization air/aqueous (left) and bromoform/aqueous (right) interfaces after 24 hours at room temperature. 37.5 mg/ml lysozyme with 3% (w/v) NaCl was used. Large crystals of approximately 500 μm were seen on the oil/water interface. Scale is 1.5 mm.

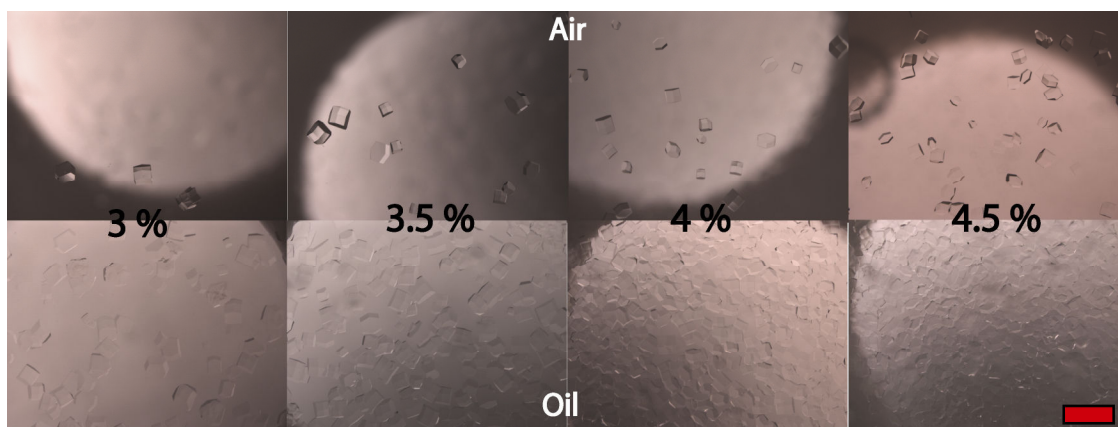


Figure 3.5 A comparison of the extent of lysozyme crystallization on the chloroform/aqueous interface and the corresponding air/aqueous interface at varied salt concentrations. Percentages indicate (w/v) % NaCl in the aqueous phase. Scale bar applies to all panels and is 1 mm in length. 37.5 mg/ml lysozyme was used within the aqueous phase in all cases.

Figure 3.5 compares the extent of lysozyme crystallization on the air/water interface with that found on the chloroform/water interface. The extent of crystallization is greatly enhanced at the oil/water interface in comparison to that found at the air/water interface. The oil/water interface becomes completely crowded with crystals at higher salt concentration.

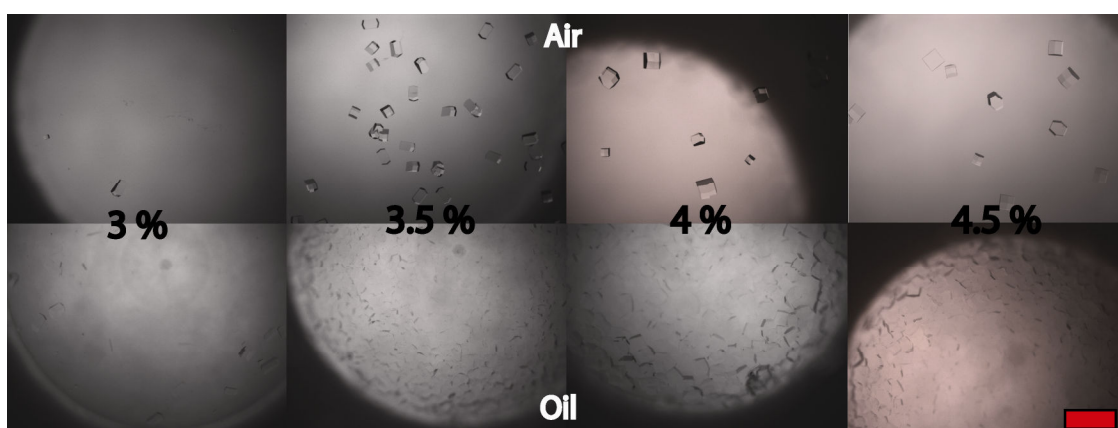


Figure 3.6 A comparison between the extent of lysozyme crystallization on the 1, 2-dichloroethane/aqueous interface and the corresponding aqueous/air interface. Percentages indicate (w/v) % NaCl in the aqueous phase. 37.5 mg/ml lysozyme was used in the aqueous phase in all cases. The crystals are seen to 'sink' into the oil phase somewhat. Scale bar is 1 mm and applies across all panels.

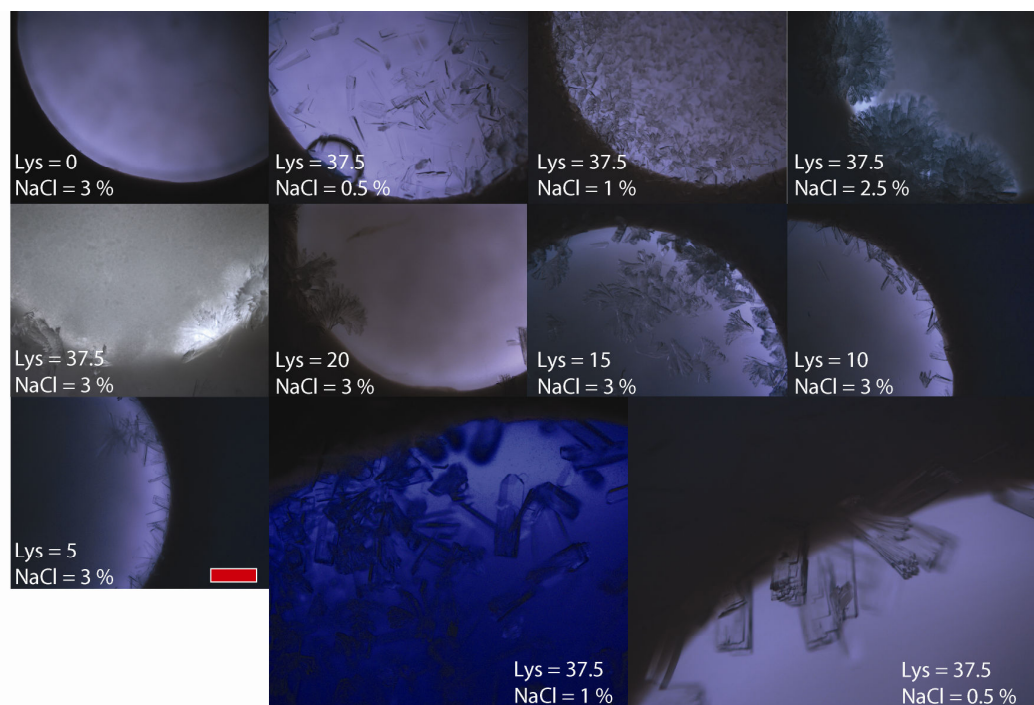


Figure 3.7 The extent of lysozyme crystallization on the aqueous/BMIM-PF₆ interface. 'Lys' indicates the concentration of lysozyme in mg/ml and NaCl concentration is given in (w/v) %. Scale bar indicated is 1 mm and applies to all small panels. A close up (large panels) of two panels is given bottom right which highlights the morphology of lysozyme crystals formed at this specific ionic liquid/aqueous interface.

Figure 3.7 illustrates the extent of lysozyme crystallization on the BMIM-PF₆/aqueous interface. Crystal morphology is vastly different from that found on other oil/water interfaces which might suggest interaction between anions of the ionic liquid and protein. The crystal morphology here appears monoclinic; this is in contrast to the apparent conventional tetragonal morphology found at other oil/water interfaces. Note that very low NaCl concentrations (in comparison to other oil/water interfaces) are required for crystallization which suggests that crystallization may proceed via the presence of another anion, probably PF₆⁻.

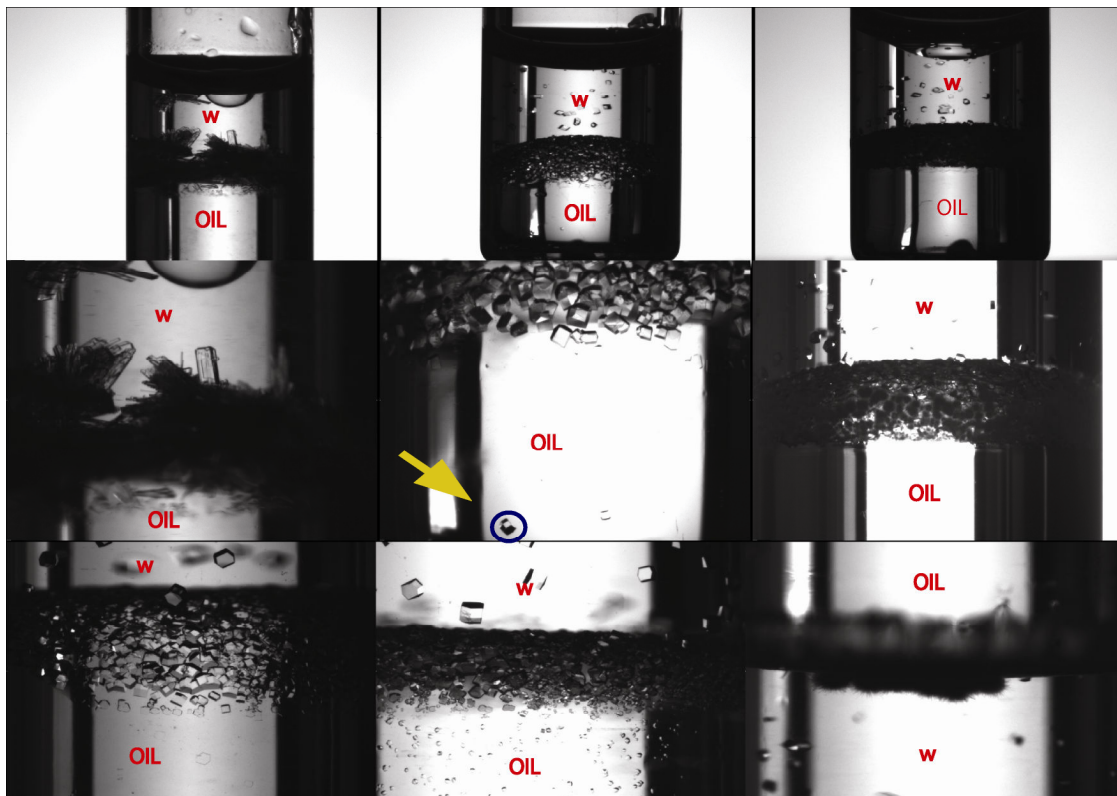


Figure 3.8 Sideways aspect of the extent of lysozyme crystallization on the oil/water interface after 24 hours. Oil/water interfaces were made by filling a small glass vial of approximately 13 mm diameter with equal volumes of aqueous and oil phase. The same volume glass vial is used in all cases. The aqueous phase in all cases contained 37.5 mg/ml and 3.5 % (w/v) NaCl. From **top left to right**: aqueous /BMIM-PF6 interface, aqueous/ 1:1 chloroform and benzene interface and aqueous/nitrobenzene interface. **Middle left to right** same as top left to right except the interface is viewed at a higher magnification. **Bottom left to right**: aqueous/1, 2-dichloroethane, aqueous/haloethane and aqueous/octan-1-ol interfaces. 'W' denotes aqueous phase and 'OIL' denotes the oil phase. Arrow in middle centre panel points toward crystal growth within the oil phase. Spherulites are seen on the 1-octanol interface.

Figure 3.8 illustrates that extensive (perhaps monoclinic) crystal growth occurs at the BMIM-PF6/interface and extensive tetragonal crystal growth occurs on other oil/water interfaces. Spherulitic growth was seen on the 1-octanol interface, which suggests the occurrence of a liquid-liquid phase separation. Crystals are seen to be growing at large distances away from the actual interface in the case of the BMIM-PF6 oil phase.

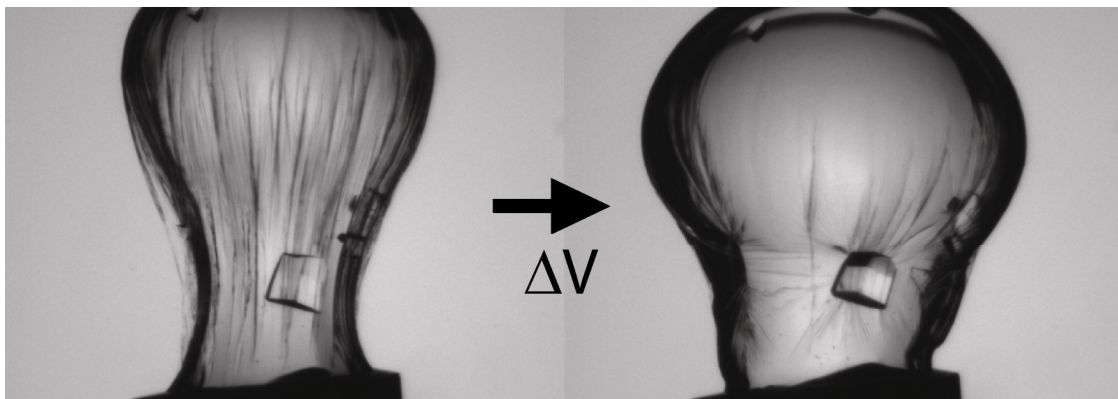


Figure 3.9 A flaccid pendant droplet (left) containing 30 mg/ml lysozyme and 3% (w/v) NaCl in 1, 2-dichloroethane after 3 hours of immersion. The same droplet (right) after increasing the hydrostatic pressure via the additions of small volumes of aqueous solution (ΔV). The extent of the protein skin is clearly evident and it appears to be thick. Additionally, the protein film displays quite marked mechanical strength under the induced hydrostatic pressure. Note that crystal growth occurred on the aqueous side on the interface.

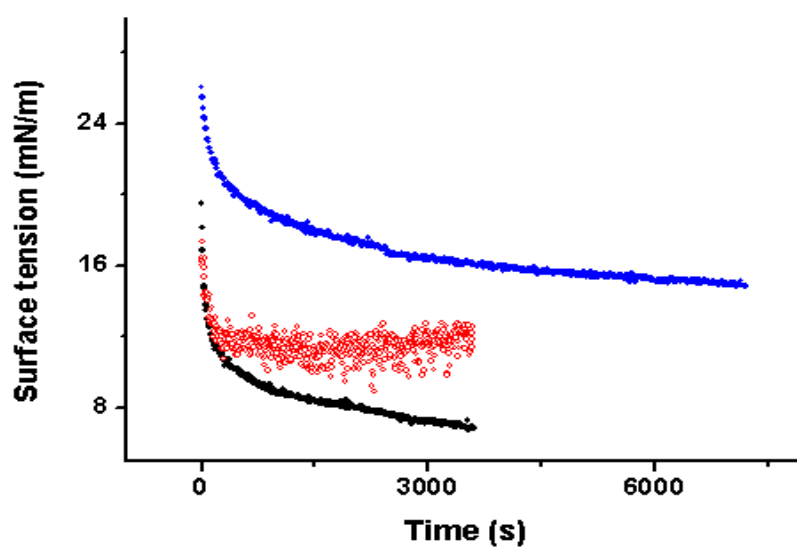


Figure 3.10 Dynamic interfacial tension data from pendant drop analysis. 30 mg/ml lysozyme as the aqueous phase with benzene (blue); 1, 2-dichloroethane (red) and chloroform (black) as the oil phase. Protein free chloroform-water, 1, 2-dichloroethane-water and benzene-water interfacial tensions were approximately 27.1, 28.9 and 24 mN/m respectively (**Table 3.1**). Aqueous protein solutions contained no precipitant making them 'non-crystallizing' for this analysis.

3.C Discussion

It should be mentioned and emphasized at this juncture that protein crystallization processes at oil/water interfaces were monitored using optical microscopy through an optically transparent path length of significant distance. This optical path consisted of millimeter-sized sections consisting of air and a significant amount of aqueous solution containing protein. Any entity smaller than an approximately 1 μm size-limit (crystalline or otherwise), would be 'invisible' using optical microscopy. Hence, in cases of apparent 'no crystallization', some micro-crystalline entities may have been present that may have been smaller than this micron size-limit. One should therefore view interfaces labeled within this Chapter as 'inactive', being 'inactive' when monitored via an optical microscope.

This measurement limitation may have implications for the results presented herein; however the extent of this limitation is unknown at present. It is rather likely that if a nucleation event had indeed occurred, at typical protein and precipitant concentrations used within this Chapter, a lysozyme crystal would have grown to a size range that may have been detectable via optical microscopy.

There are obviously better *in-situ* (at the oil/water interface) monitoring methods, such as those based on evanescent waves and neutron reflectivity¹³⁻¹⁴ which could be used in future studies.

By comparing the extent of lysozyme crystallization at a range of different oil/water interfaces, it is clear that some oil/water interfaces enhance the extent of nucleation whilst others do not. Oil phases considered herein are categorised in Table 3.1 as providing either 'active' (in bold) or 'inactive' oil/water interfaces. An 'active' oil/water interface was defined as one which enhanced the extent of lysozyme crystallization in comparison to the air/aqueous interface under identical crystallizing conditions when viewed and monitored using optical microscopy. Alternatively, 'inactive' interfaces were defined as those which provided no enhancement or reduced the extent of lysozyme crystallization compared to the air/water interface under identical crystallizing conditions when viewed and monitored using optical microscopy.

Significantly, silicon and paraffin oils seemed to retard the lysozyme crystal nucleation process and were therefore categorized as 'inactive'. Considering that no deterioration in crystal diffraction quality under conditions of high heterogeneous nucleation was found (*vide infra*), the practice of using paraffin and silicon oil mixtures within a microbatch set-up, currently considered standard procedure within large scale, high-throughput crystallization trials¹⁵, may require consideration. With this in mind, other oil/water interfaces may usefully promote crystallization on a shorter timescale and at lower precipitant concentration than prescribed silicon and paraffin oils and their mixtures.

Bromoform was found not only to enhance lysozyme crystal nucleation, but also lysozyme crystal growth. Furthermore, mixing an ‘active’ with an ‘inactive’ solvent (Figure 3.3) produced a positive effect on crystallization by providing an ‘active’ oil/water interface. Side-on views of the crystallization process on the chloroform+benzene/water interface and the 1,2-dichloroethane-water interface (Figure 3.8), highlight the considerable extent to which these oil/water interfaces truly promote crystallization.

The water/ionic liquid interface appears to provide different lysozyme morphologies than that found at other oil/water interfaces and some spherulitic growth is seen in the case of 1-octanol. Reasons for this effect are discussed at a later stage within this chapter.

A small amount of crystal growth was also evident within some of the ‘active’ oil phases, which may be rationalised by the fact that lysozyme has some but limited solubility within these solvents¹⁶ (Figure 3.8).

In terms of any specific trend which may be extractable from solvents listed in Table 3.1, there appears to be none that are immediately apparent. If one were to propose some characteristics shared by ‘active’ and ‘inactive’ solvents they would be the following: ‘Active solvents’ tend to have higher dielectric constants than that of ‘inactive solvents’. The solubility of water in these solvents tends also to be higher (not the solubility of the solvent in the water). ‘Active solvents’ tend also to have lower oil-water interfacial tensions than that of ‘inactive solvents’. A number of ‘inactive’ interfaces were of lighter density than those which were ‘active’.

Due to the location of the crystals growing in the oil phase and the way the crystals have anchored on the side of glass container walls, we have ruled out crystals falling from the oil/water interface and landing on the side of the container walls. However, some crystals do sometimes appear to 'fall' from the interface, particularly when the 1, 2-dichloroethane/water interface is used (Figure 3.6). This was evidenced by a large number of crystals found at the bottom of the container after a 24 hour time period. This observation further suggests that crystals have densities greater than that of the oil phase. These proposed large density increases, tentatively suggests some oil adsorption by protein crystals.

This observation may be significant as protein crystals are known to possess very high water contents (sometimes in excess of 50 %)¹⁷, which is known to affect the crystal vitrification process during cryo-cooling¹⁸. A possible adsorption of the oil phase by the protein crystal further suggests a lower overall water content for the protein crystal which could go on to positively aid the vitrification process. However, due to time constraints this important aspect has not been explored within this chapter and should form the basis of future work.

We have demonstrated that some oil/water interfaces enhance the extent of lysozyme crystallization whilst others do not. One may argue that the cause of this effect may be due to the formation of an interfacial film. In essence, forming a surface upon which heterogeneous nucleation could take place thereby causing increases in the extent of nucleation. We would however counter this argument by suggesting that interfacial films should form to varying extents (with varying degrees of macroscopic visibility) at all oil/water interfaces¹⁹⁻²³, and thus the origin of this effect could lie elsewhere.

A possible clue to the origin of this effect may be found in Figure 3.3 and Figure 3.4. These figures, which illustrate the effect of varying salt concentration on the extent and occurrence of lysozyme crystals on the bromoform/aqueous interface, also indicate the transition between the occurrence of no crystals (2.5% (w/v) NaCl) and crystals (3% (w/v) NaCl) remains typical for this protein/precipitant combination. This 'transition' is found on a number of interfaces (Figure 3.3, Figure 3.4 and Figure 3.5), whether they be oil/water interfaces or air/water interfaces.

The reader is also referred to Figure 3.5 and Figure 3.6, where it is found that at the air/water interface crystals have formed, albeit of small number, at 3 % (w/v) NaCl. These observations suggest that the protein crystallization process has sufficient energy to initiate. In other words has sufficient energy to overcome any energy barriers to nucleation and is being prevented from achieving its 'true' number of critical nuclei by an unknown factor.

Interestingly though, the extent of nucleation evident on a number of air/water interfaces (counted as approximately 3 crystals after 24 hours, Figure 3.4 for example), when compared to the nucleation rate seen on the corresponding oil/water interface, appears increased by approximately a similar amount at 3% (w/v) NaCl on the oil/water interface. Again, suggesting the reduction in some 'barrier' to nucleation. However, this is only a qualitative statement and further work is needed to turn this type of observation into a strict quantitative statement. More work is needed to improve the certainty of this observation.

It should be mentioned at this point that accurate kinetic data (related to crystallization) could not be collected on our equipment due to the following reasons

- 1) Protein crystals appeared *en masse* and with some degree of spontaneity, filling the small interface quickly (especially at higher precipitant concentrations) after a period of time. Ostwald ripening on the small-area interface after the interface had been covered in crystals (Figure 3.5 for example) may actually retard 'real' nucleation rates, giving nucleation rates different for those that may be experienced at a larger-area interface. By Ostwald ripening we refer to an Ostwald ripening effect caused by already nucleated and growing crystals which may prevent further nucleation from occurring in the surrounding solution.
- 2) Optical microscopy was used. Crystal nuclei sizes are in the order of nanometres and thus the process would be 'detected' long after it had actually occurred.

Despite these large limitations, it makes sense at this point to discuss the extent of the nucleation and crystal growth in terms of qualitative language. As this chapter details the discovery of an effect, we concentrate here on the explanation of this effect and await more sophisticated equipment in order to detail important crystallization parameters and characterization of oil/water interfaces in terms of more accurate quantitative terms.

Despite the apparent increase in ‘the extent of nucleation, crystals which appear on some of these ‘active’ oil/interfaces appear to be of different size, suggesting that these interfaces have had a similar effect on the nucleation rate but a different effect on the extent of crystal growth. The reason to as why this should be is discussed in detail further on.

**3.C.1.Increases and decreases in the extent of protein
crystallization on ‘active’ and ‘inactive’ oil/water interfaces.
Towards a plausible explanation of the results presented
within this chapter.**

3.C.1.1. The protein hydration shell

The interaction between a protein and the surrounding solvent environment is highly complex²⁴. This complexity is often attributed to the distribution of hydrophobic and hydrophilic patches on the protein surface, and how these patches interact with surrounding water molecules in order to produce fully hydrated protein structures²⁴. Proteins are not geometrically spherical; they do however possess a complicated and irregular surface geometry²⁴⁻²⁵. Due to surface irregularities, solvent accessible protein surfaces will not be structurally or energetically homogeneous.

Under correct solution conditions the inhomogeneous structural and energetic protein surface features may produce areas which initiate weak anisotropic protein-protein interactions²⁶. These weak anisotropic protein-protein interactions are typical for protein bonding within a critical nuclei and within protein crystals²⁷.

The protein surface, when in contact with an aqueous solution, is hydrated, and generally water will form one or more distinct, dynamic hydration shells around a particular protein²⁵. These hydration shells consist of water which is different, both structurally and dynamically, from water found in bulk. In particular, the first of these hydration layers is said to extend approximately 3 Å from the protein surface and has a water density of 10-15 % in excess of that found in bulk²⁸⁻²⁹. Of this first hydration shell water, about 5-30 % of the water molecules display rotational and translational diffusional times that are significantly reduced (in the order of tens of picoseconds) in comparison to other 'water' found within the first hydration shell, and may be termed 'long residence time' water²⁵.

In particular, it is the diffusional component, perpendicular to the protein surface, which is dramatically reduced²⁵. 'Long residence time' water is said to occupy various preferential locations on a protein surface, with water which displays the longest residence times of all, found within deep protein surface cavities²⁵.

At this juncture it would be prudent to make the reader aware of a debate within the literature, regarding the classification of water found on the surface of hydrated proteins³⁰. Crystallographers usually term protein surface water, found via diffraction methods in crystal structures as either 'free' or 'bound', with 'bound' water referring to water that is found at high frequency at one site on the protein surface within the crystal structure³⁰. It has been argued, maybe correctly, that diffraction data does not give any indication of the rates of the molecular movement of water, and hence the term 'free' and 'bound' are incorrect and should not be used³⁰.

Furthermore, it is suggested that the term 'bound' insinuates a largely exothermic water adsorption process at the protein surface³⁰. Additionally, it is presented that water molecules are not 'bound' on the protein surface in either a thermodynamic or kinetic sense, and that 'in the absence of co-solvents every exposed hydration site is populated with water' which is free to reversibly exchange with bulk water.

One may therefore find it more appropriate to think in terms of short and long-residence time water instead of 'free' and 'bound' water which gives no weight to the strength of the protein-water interaction³⁰. Although, it may be said that viewed with a sufficiently low temporal resolution, the dynamics of long residence time water could be considered immobile and hence bound in some sense.

For a protein to achieve and maintain successful folding, the folded protein must maintain favourable interactions between its amino acid side chains and the surrounding solvent environment²⁵. The enforcement of favourable protein-solvent interactions leads to the well known hydrophobic effect³¹, in which non-polar residues which do not contribute significantly to the aqueous solvent interaction are sequestered to the protein interior whilst polar residues which interact favourably with the solvent, are found in abundance on the protein surface^{25, 31}. However, not all hydrophobic residues are found buried within the protein interior. Indeed, some are found on the protein surface, and are said to have hydration shells which display some type of structural order which comes with an associated entropic cost³².

The formation of ‘ordered’ hydration structures (polygonal or clathrate-like) around hydrophobic residues or hydrophobic areas is also a contentious issue with some papers presenting evidence for order³³⁻³⁴, whilst others present evidence against some form of geometrical ordering³⁵. These opposing views of hydrophobic solvation appear to be the result of interpretations based on either dynamic or structural arguments.

Time resolved measurements³⁶ have shown that hydrophobic hydration shells can display liquid-like structural characteristics but dynamically the hydration shells are better described as ‘ice-like’, with ‘ice-like’ dynamics being more prevalent at higher solute concentration³⁵. Although no ‘cage’ or ‘iceberg’ like structures are readily seen, water orientational dynamics are slow enough around hydrophobic moieties to warrant description as ‘long residence time’ water as well as displaying some kind of structure on an appropriate time scale.

Water surrounding polar residues can exchange freely with bulk and display fast bulk-like orientational dynamics and thus water molecules in the vicinity of polar or charged residues have ‘short residence’ time on the protein surface and display bulk-like structural characteristics.

Since proteins have evolved almost exclusively in an aqueous environment, one may find it surprising that proteins can function and even exist in a variety of solvents with physical properties either very similar or remotely different to that of water³⁷. Most of the work conducted in this area has centred on enzyme catalysis in nonaqueous solvents³⁸ and forms the basis of the field described as 'nonaqueous enzymology'. Because of the different physical and chemical properties of these nonaqueous solvents, protein hydration mechanisms and protein stability within such solvents is, in some cases, very different from that found in water³⁷. For example, earlier studies by Parker³⁹ *et al.* using sensitive NMR techniques in conjunction with deuterated water, compared the degree of hydration of subtilisin Carlsberg (an endopeptidase) in air, and within various polar and nonpolar solvents. They found that 'strongly bound water' adsorption was hardly affected by nonpolar solvents whilst 'loosely bound water' was significantly reduced³⁹. Parker's³⁹ work illustrates that when immersed within nonpolar solvents (*viz.* hexane, toluene and benzene) water is preferentially localised in the most polar regions on the enzyme surface whilst in nonpolar regions it becomes reduced or even stripped off⁴⁰.

Additional evidence for this difference in protein hydration within nonaqueous solvents is provided by work by Gorman⁴⁰ *et al.* who found that when three different enzymes (chymotrypsin, subtilisin Carlsberg and horse radish peroxidase) were hydrated with tritiated (T_2O) water, the enzymes lost the most water in solvents of moderate to high polarity, whilst in nonpolar solvents it was found that water desorption was minimal. The study⁴⁰ also found that both solvent dielectric and a measure of the saturated molar solubility of water in the given solvent was a good indicator of the solvents ability to allow T_2O desorption from the enzyme. Gorman⁴⁰ *et al.* conclude by stating that 'water stripping in nonaqueous environments does indeed occur and can be significant in polar solvents'.

These experimental findings, just described, are substantiated via molecular modelling studies of protein hydration within nonpolar solvents by Soares⁴¹ *et al.* who found that nonpolar solvents enhanced the formation of ‘large water clusters’ that are tightly bound to the enzyme surface, whereas water in polar organic solvents is fragmented in ‘small clusters’ loosely bound on areas of the enzyme surface. The Soares⁴¹ *et al.* study also found that water was localised preferentially on the protein surface in similar regions regardless of the solvent used.

In summary, one may say that within an aqueous environment, hydrophilic and charged residues have preferential hydration and ‘protein water’ exchange with bulk water is extremely rapid. Hydrophobic residues, on the other hand (within an aqueous solvent), experience hydration which is characterised by slow dynamics and slow water exchange with bulk. This ‘slowdown’ may cause a modicum of ‘structuring’ of the hydration water around hydrophobic residues to occur by virtue of slow hydrogen bond dynamics²⁵.

By placing the same protein in a nonaqueous environment, one of low polarity for example, we find that the situation reverses, in that water around hydrophilic residues now becomes ‘long residence time’ water whilst water around hydrophobic residues becomes desorbed from the protein surface. The ability of the hydrophilic residues to retain water appears to be a function of solvent polarity and the higher the solvent polarity the more likely it is for solvent molecules to exchange or replace with strongly held water molecules on the hydrophilic patches on the protein surface. Since proteins require a certain critical amount of water to be present on the surface in order to maintain native structure, high polar solvents can act as denaturants by effectively competing with water molecules for hydration sites³⁷.

3.C.1.2. Protein hydration and the location of hydration waters

To return to the main focus of this chapter, namely, the formation of lysozyme protein crystals on the oil/water interface. It is common knowledge that every macroscopic crystal has originated from a nucleus⁴². These nuclei, which provide the basis for the formation of macroscopic crystals, are composed of protein monomers held together via a series of very weak anisotropic protein-protein interactions⁴³. The locations of the weak bonding sites on each protein monomer are termed *crystal contacts*. It would therefore be advantageous to try and ascertain the nature of these crystal contacts and how they may relate to the various protein hydration mechanisms we have just described.

A number of recent large scale statistical studies have been conducted⁴⁴⁻⁴⁵ which have analysed the physical and chemical nature of the crystal contact areas. Cieřlik⁴⁴ *et al.* analysed a large database of 821 unambiguously monomeric proteins and concluded that the propensity of a given residue on the surface of a protein to be included in crystal contact areas was not a linear function of its solvent accessible surface area (*one would expect that hydrophilic residues would have a higher solvent accessible areas than hydrophobic residues for example*).

They also found that for a given solvent exposed surface area, small and hydrophobic residues had a higher propensity to become involved in the formation of crystal contacts than large and charged residues. Using a completely different computational approach and a similarly large dataset, support for the conclusions made by Cieřlik⁴⁴ and co-workers was provided by a study by Price II *et al*⁴⁵, who came to almost identical conclusions. It was noteworthy that both studies considered surface entropy to be a major factor in the formation of a crystal contact.

3.C.1.3. Entropy gains and losses may be a major driving force in the protein crystallization process.

The second law of thermodynamics states that a system in isolation, which is not in equilibrium, must show a gain in entropy over time with maximum entropy being attained at equilibrium conditions⁴⁶. The process of transferring monomeric protein molecules in solution to a crystal, at constant temperature and pressure is governed by the change in the Gibbs free energy (ΔG_{cryst}^0)⁴⁷.

According to the Gibbs-Helmholtz equation (3.1) the change in ΔG_{cryst}^0 (at constant temperature) is expressed by the opposing contributions of the enthalpy (ΔH_{cryst}^0 , the amount of heat released or absorbed by a chemical substance during a change of state) and entropy ΔS_{cryst}^0

$$\Delta G_{cryst}^0 = \Delta H_{cryst}^0 - T \Delta S_{cryst}^0 \quad (3.1)$$

If $\Delta G_{cryst}^0 < 0$ the process becomes thermodynamically favourable.

Recent studies³² concerning protein crystallization thermodynamics have indicated that ΔG_{cryst}^0 is only moderately negative with values in the range -10 to -100 kJ/mol. These values contrast rather heavily with figures obtained for inorganic crystallization thermodynamics which are significantly higher (for example NaCl has a standard Gibbs energy of formation of -384.14 kJ/mol⁴⁸). Because of this tendency for protein crystallization processes to be only *slightly* thermodynamically favourable, the spontaneity of the process could easily become shifted by small changes in the surrounding solution conditions.

Closer examination of protein crystallization thermodynamics has revealed either moderately negative or almost non existent enthalpy values (for example -70 kJ/mol for lysozyme⁴⁹ and ± 0 kJ/mol for apoferritin⁵⁰, ferritin³² and lumazine synthase⁵¹).

The small enthalpy values are unsurprising as it is well known that magnitude of the protein-protein interaction found within protein crystals is not strong at all and are considered to be the weakest of all protein-protein interaction^{26, 43}. Since enthalpy effects are so small, they cannot play a dominant role in the crystallization process, one must therefore consider the various entropic contributions as a major factor which can influence the protein crystallization and growth process³². The reader should be made aware that enthalpy effects can play a dominant role in some rare cases of protein crystallization, such as in the case haemoglobin C which displays large positive enthalpic values which disfavours the crystallization process.

Estimates⁴⁷ of the unfavourable energy barrier due to entropic loss at room temperature are in the range of 30-100 kJ/mol, which taken with the low values of ΔG_{cryst}^0 could be large enough in some cases to halt the entire crystallization process altogether. Recent molecular dynamics studies²⁴ have highlighted how the removal of water from the protein surface at hydrophobic crystal contact areas in lysozyme can be an important entropic driving force for crystal contact formation and therefore nucleation.

3.C.1.4. Towards a possible mechanism to help rationalise the results.

One observes that lysozyme nucleation appears to be thermodynamically feasible at 3% (w/v) NaCl and 37.5 mg/ml lysozyme after a 24 hour period (Figure 3.3, Figure 3.4 and Figure 3.5) and that some interfaces enhance crystallization while other do not. We therefore suggest that the increase in nucleation is due to the removal of an amount of water around the crystal contact areas by certain organic solvents. Water removal could enhance the frequency of successful anisotropic protein-protein interactions at crystal contact area. The associated gain in entropy may be reflected in increases in the extent of crystal nucleation.

The ‘inactive’ solvents, on the other hand, may cause water to be retained around the crystal contact areas and thus nucleation may be inhibited / slowed at ‘inactive’ oil/water interfaces. In fact the nucleation process could be slowed to such an extent that it appears not to occur at all on a reasonable timescale. The extent of the retention of water in different solvents is as suggested by previous work^{39, 41}.

A cartoon of the proposed mechanism is therefore shown in Figure 3.11.

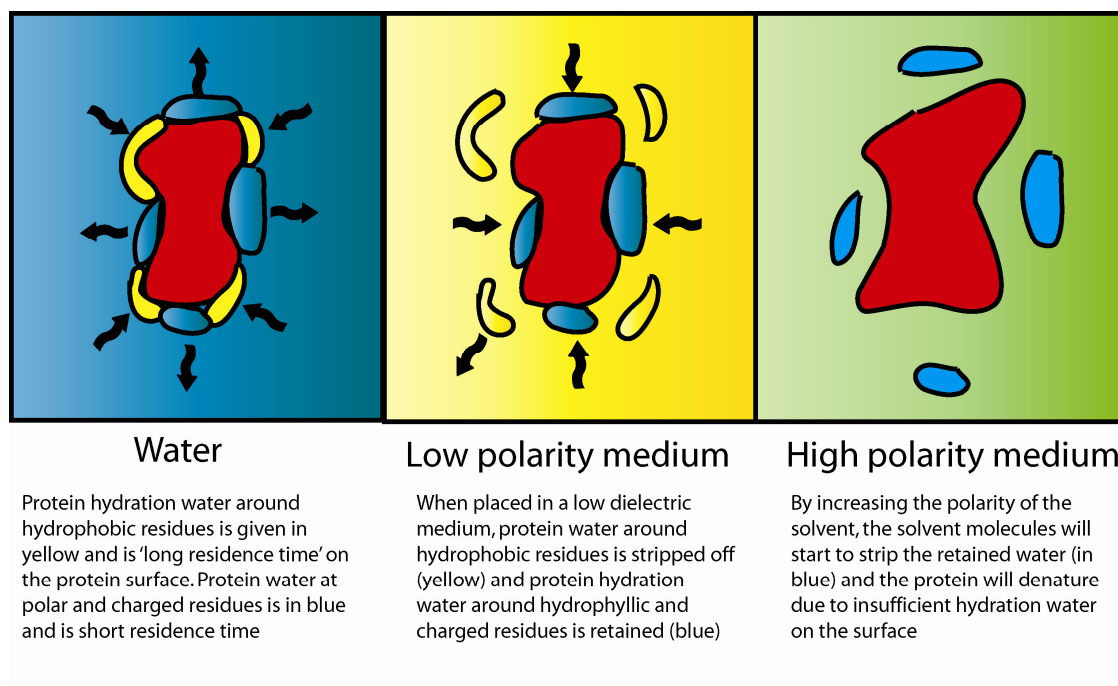


Figure 3.11 A cartoon depicting the proposed water stripping and water retention behaviour propose solvents of different polarity.

3.C.1.5. No organic solvent was found bound to lysozyme and the location of lysozyme hydration water was similar to that found within protein databanks.

Because large amounts of nucleation (as seen on 'active' interfaces) are considered deleterious to crystal quality⁵²⁻⁵⁴, we conducted a brief X-ray diffraction study which involved the collection of a 4.7-fold redundant full data set between 2.1-1.7 Å resolution at 100K using Cu-K α X-ray radiation from crystals grown on the chloroform/water and 1,2-dichloroethane/water interfaces. The crystallographic unit cell was $a=b=79.24$, $c=37.91$ Å, very similar to that of 1HEL ($a=b=79.1$ $c=37.9$ Å) used for refinement in the tetragonal space group of P43212. The refinement gave an identical structure with an overall RMSD of 0.12 Å calculated for all 129 C α atoms. The final R-value was 0.171 and the solvent structure was very similar to that of 1HEL (refined structure and diffraction pattern in 3.D.2).

Anomalous difference Fourier synthesis did not reveal any bound solvent ions.

That no bound solvent was found in the crystal structure and that the hydration shell was similar to that of other lysozyme molecules found within the protein databanks, lends support to the concept (Figure 3.11) that water is being removed from crystal contact areas, leading to an enhancement in nucleation.

One would therefore expect to see the same hydration shell present on the protein in the presence of both ‘active’ and ‘inactive’ interfaces, as crystals contact areas due to the shared tetragonal morphology, would be the same between ‘active’ and ‘inactive’ interfaces despite differences in the extent of nucleation. Since we are proposing that water is eventually removed from the crystal contact areas, the hydration shells over the rest of the protein would be essentially the same, consistent with work by Soares and co-workers⁴¹

Future work in this area should be aimed at correlating the location and amount of water on the protein surface to crystal contact areas in the presence of a wide range of solvents via experimental methods such as that used by Parker³⁹ and co-workers and via modelling methodologies of the type utilised by Soares⁴¹ and Pellicane²⁴. Using these suggested approaches it is hoped that one would be able to predict a series of organic solvents which might usefully enhance the nucleation behaviour of a wide variety of protein crystallization systems.

3.C.1.6. The difference in the extent of crystallization between air/water and oil/water interfaces

The extent of crystallization at air/water interfaces (where an air/water interface was in existence) was much reduced in comparison to that of corresponding oil/water interfaces, in all cases. This is significant, as most large scale protein crystallization trials are conducted at the air/water interface using vapour diffusion type methods. This might be due to suggested entropic effects⁵⁵, where crystal contact waters are not being removed efficiently resulting in lower extents of crystallization.

Although, returning to arguments by Sengupta and co-workers^{21, 56-57}, could this be a manifestation of interactions between the air/water interface and the positively charged lysozyme molecule? Or could the air/water interface constitute just another 'inactive' interface? If the former were true then large scale protein crystallization methodologies concerning protein crystallization at the air/water interface (i.e.: the hanging drop technique) would have to take into account the charge state of the protein in order to maximise success rates.

If the latter were true, then steps could be taken to improve properties of such an interface, for example the hydrophobicity and surface tension. Specifically, interfacial properties might be adjusted by the use of gases for example Xe, Kr and CO₂⁵⁸, which in addition could exhibit additional functionality as heavy atom derivatives within the isomorphous replacement method of structure determination⁵⁸. This is an interesting prospect and should form the basis of future work.

3.C.1.7. Lysozyme exhibits different surface activities at different oil/water interfaces

Dynamic interfacial data (Figure 3.10) indicate that lysozyme under non-crystallizing conditions exhibits different surface activities at different oil/water interfaces. In particular, at the benzene/water interface, lysozyme exhibits the lowest surface activity and at the chloroform/water interface lysozyme exhibits the highest surface activity of the three oil/interfaces trialled herein. This is not surprising, as we have established that different protein-solvent interactions could lead to different modes of protein surface hydration and affect protein stability.

With reference to Figure 3.10, and dynamic interfacial tension data gathered from lysozyme adsorption to the 1, 2-dichloroethane/water interface, a very rapid initial decline in the interfacial tension at early times is evident and a steady-value is observed after just a few minutes. This behaviour is not seen on the benzene/water and chloroform/water interfaces where lysozyme adsorption behaviour appears to be following regime II (**Error! Reference source not found.**) at times in excess of 1 hour. In contrast, lysozyme at the 1,2-dichloroethane/water interface appears to have entered regime III almost immediately.

The initial adsorption of lysozyme to all oil/water interfaces (Figure 3.10) is rapid, and this behaviour is consistent with previous work^{56-57, 59} conducted on lysozyme adsorption to the hexadecane/water and other oil/water interfaces. Adsorption processes occurring within regime II, involve protein interactions with the interface⁵⁹⁻⁶⁰, with the dominant processes being aggregation and rearrangement of protein sub-layers.

In comparison, lysozyme, at the 1,2-dichloroethane-water interface, appears to enter regime III within minutes of initial adsorption. Regime III is defined as one of interfacial gelation and film formation^{59, 61}, and thus one could expect that at such an oil/water interface lysozyme has begun the rapid formation of multilayered film/gel-like networks. The interfacial film is readily visible on a macroscopic level (Figure 12) and displays marked mechanical strength and porosity. These two attributes are hallmarks of multilayered film/gel network formation^{59, 61}. Some unfolding of lysozyme here would not be surprising, as 1,2-dichloroethane has large solubility in water and a dielectric constant almost double that of chloroform (Table 3.1). Additionally, suggested unfolding behaviour is consistent with previous work which indicates that lysozyme maintains structural stability in pure solvents but not in solvent/water mixtures⁶². One notes that in the case of 1,2-DCE/aqueous interface the data appears ‘noisier’ than the other data sets, it is currently unclear to why this should be. This noise was a constant occurrence with the lysozyme/DCE system, but the noise itself was not categorised nor was it measured.

In general, the dynamic interfacial surface tension data suggests that lysozyme films developed at different oil/water interfaces may have different structural characteristics, which in turn, may have different effects on lysozyme crystallization behaviour (nucleation and growth). Our results suggest that a simple surface excess type argument cannot convincingly account for the increase in nucleation evident on ‘active’ oil/water interfaces, as all oil/water interfaces may have the propensity to form a variety of multilayered film-like structures which transition from liquid-like to gel-like at longer times⁵⁹.

Some interfaces afford considerable increases in crystal growth (Figure 3.4). We suggest that this behaviour might be explained in terms of an interfacial protein film/gel which might possess structural characteristics which enable the supply of amorphous precursor material to feed the growth of crystals. This proposed crystal growth mechanism⁶³⁻⁶⁴, which is gaining ground as an important route for the formation of some inorganic crystals⁶⁵⁻⁶⁷ in homogeneous solution, particularly at high supersaturation, and appears to operate for lysozyme at some 'active' oil/water interfaces. Moreover, suggested increases in entropy, afforded by liberation of protein surface waters, may also enhance the crystal growth process in some instances³². This particular aspect requires further work.

3.C.1.8. The aqueous-ionic liquid (BMIM-PF6) interface and its effect on lysozyme crystallization

The crystallization of lysozyme on the ionic liquid/water interface (Figure 3.7) produces lysozyme crystals which give the visual appearance of maybe belonging to a monoclinic space group. We did not conduct any X-ray diffraction studies which would be able to determine the space group unequivocally, but by all accounts these crystals appear to display monoclinic features when viewed with the aid of an optical microscope. The apparent morphology is in contrast to lysozyme crystals grown on other oil/water interfaces which display tetragonal morphology, typical of the lysozyme-NaCl crystallization system.

The appearance of the monoclinic polymorph has previously occurred in lysozyme solutions which use precipitants based on polyatomic anions of the type NO_3^- and SCN^- ⁶⁸, which suggests that polyatomic anions from the ionic liquid (PF_6^-) may have penetrated the aqueous phase. This is unsurprising since the solubility of BMIM-PF6 in water⁶⁹ is approximately 2.4 (w/w) % and the solubility of water in BMIM-PF6⁶⁹ is approximately 2.6 (w/w) %. The suggested penetration could be further evidenced by the retention of the presumed monoclinic morphology in the aqueous phase at very large distances from the ionic liquid-water interface. Although, a small body of recent work has been conducted on the crystallization of lysozyme in water miscible ionic liquids⁷⁰⁻⁷², this is the first time such a study has utilised water immiscible ionic liquids and an ionic liquid/water interface for the crystallization of lysozyme.

Penetration of the water soluble BMIM⁺ cation into the aqueous phase could also be *likely* and possibly responsible for the proposed space group change. Although, previously cited literature supports the assumption that this type of effect would be caused by the anion. One could also possibly envisage the growth of protein crystals on the oil/water interface by using different electrolytes and hence anions in an organic phase. This has been trialled to a certain extent (with Chapter 4). In this case, the presence of the TPB^- anion did not seem to have any effect on the lysozyme crystal morphology, although an attempt was not made with an electrolyte which contained the PF_6^- . The effects of different cations and anions on the interfacial lysozyme crystallization process should be a topic for future research.

Previous work has reported⁷¹ that by using a range of ionic liquids, as additives within the lysozyme crystallization system, no change in morphology was seen and no ionic liquid was found bound to the lysozyme molecule. The diffraction quality of resulting crystals was found to be the same as for crystals grown by more traditional means⁷¹. However, a study⁷³ by Wang and co-workers did find morphological change, which they attributed to a possible enhancement of crystal contacts which can influence the nucleation and crystal growth of lysozyme.

We found that lysozyme crystals appeared at very low NaCl concentration on the BMIM-PF₆-water interface (Figure 3.7), which is also consistent with an anion affect⁶⁸. The presence of anions drastically affects the solubility of lysozyme⁶⁸ which follows a reversed Hofmeister series at pH of 4.5 for example



pTS = *para*-toluenesulfonate.

Using precipitants based on the anions within the reversed⁷⁴ Hofmeister series, it is possible to crystallize lysozyme in a wide range of space groups. For example NapTS and NaCl can produce the tetragonal space group, NaI the monoclinic, NaNO₃ the monoclinic and KSCN the monoclinic space groups⁶⁸. We therefore suggest that occurrence of crystals at low NaCl concentration is due to low solubility of lysozyme in the presence of PF₆⁻. In contrast, we have previously established that lysozyme crystallization on other oil/water interfaces typically occurs between 2.5 – 3 % (w/v) NaCl.

The question arises as to how one would classify the BMIM-PF6/water interface in terms of our 'active', 'inactive' categorization. We would argue that since the 'active'/'inactive' definition is based upon the enhancement of the extent of lysozyme crystallization (in the tetragonal space group) at various oil/water interfaces, the BMIM-PF6/water interface is not really comparable as such. The incompatibility is due to the presence of another space group and hence the terminology is only applicable within a particular space group. We therefore suggest, for future work in this area, a series of experiments using different lysozyme space groups (induced by different anions) at various oil/water interfaces. This will be to see if the enhancement in the extent of crystallization could be realised for different space groups at different oil/water interfaces. One would also hope to obtain 'active'/'inactive' oil/water interface classifications based on different lysozyme space groups (of which there are four⁶⁸) which should lead to further understanding of the mechanisms at work here.

Spherulitic growth is seen on the 1-octanol interface (Figure 3.8). Previous studies⁷⁵ have shown that spherulitic growth in the lysozyme/NaCl system can occur under conditions of liquid-liquid phase separation and due to the presence of heterogeneous nuclei in the crystallization solution. The spherulitic growth appears to have originated in the vicinity of the glass surface; however a large amount is evident at considerable distance away from the glass surface which points to the possibility of liquid-liquid phase separation of the crystallizing solution at the liquid-liquid interface. We did not see any other spherulitic growth or liquid-liquid separation at other oil/water interfaces (both 'active' and 'inactive') and thus we do not know if this is a general feature of some oil/water interfaces or an anomaly presented by the 1-octanol-water interface.

The above observation is important because previous work has suggested that nucleation rates can be controlled by moving the position of the liquid-liquid phase boundary on a temperature vs. protein concentration phase diagram⁷⁶⁻⁷⁸. The position of this phase boundary was moved in previous studies⁷⁷ by adding water miscible solvents to crystallizing solutions which altered the extent of the protein-protein interactions (such as polyethylene glycol and glycerol). By referring to phase diagrams presented within these studies⁷⁶, one might see how a surface excess or a drop in temperature could cause the appearance of the liquid-liquid separation at the oil/water interface. However, since we see the appearance of phase separation on only one of many oil-interfaces, we suggest that this behaviour could be specific to lysozyme at the 1-octanol-water interface. Despite this, and considering the possible importance of this effect, we suggest further study in this regard, as no previous work has been conducted on how cloud point temperatures are affected at various oil/water interfaces.

3.D Appendix I

3.D.1. Pendant drop shape analysis for the measurement of dynamic interfacial surface tension.

A convenient and widely used method for measuring the dynamic interfacial surface tension between two fluids, with millisecond time resolution, is via pendant drop shape analysis, based on a technique by Andreas⁷⁹. In this technique, the shape of a pendant droplet suspended or floating from a needle-like orifice under the influence of a homogeneous gravitational field within another fluid medium is measured and is used to determine the interfacial surface tension between the two fluids.

The whole process is digitised^{4, 80} and accurate calculation of droplet shapes, and hence interfacial tension, can be acquired every few milliseconds by computer.

The method works as follows. A droplet suspended from a needle, such as that illustrated in Figure 3.12, within a homogeneous gravitational field is considered to be in mechanical equilibrium, and at any given horizontal plane

$$F1 + F3 = F2 \quad (3.2)$$

$F1$ represents the apparent weight of the droplet under the given horizontal plane, $F2$ is the vertical projection of the boundary tension which acts parallel to the interface at the horizontal plane under consideration and $F3$ is the vertical component of the excess pressure due to the curvature of the interface. This excess pressure is given by the Laplace equation

$$P = \gamma \left(\frac{1}{\rho} + \frac{1}{R} \right) \quad (3.3)$$

γ is the boundary tension and R represents the internal radius of curvature given by

$\frac{X}{\sin \phi}$, ρ represent the external radius of curvature given by $\frac{dS}{d\theta}$.

By substitution, (3.2) will simplify to

$$(2 + \beta Z) = \frac{d\theta}{dS} + \frac{\sin \theta}{X} \quad (3.4)$$

where Z, X, S, θ are dimensionless coordinates defined as

$$Z = \frac{z}{b}, \quad X = \frac{x}{b}, \quad S = \frac{s}{b}, \quad \cos \theta = \frac{dX}{dS}, \quad \sin \theta = \frac{dZ}{dS} \quad (3.5)$$

$$\text{and } \beta = \frac{g \Delta \rho b^2}{\gamma} \quad (3.6)$$

Where b is the radius of curvature at the drop apex, z is the axial coordinate of the described point to the drop apex, x is the distance of the point from the axis of the drop, s is the arc length to the point from the drop apex, $\Delta \rho$ is the difference in density between the two fluid phases, g is the gravitational acceleration and γ is the interfacial surface tension.

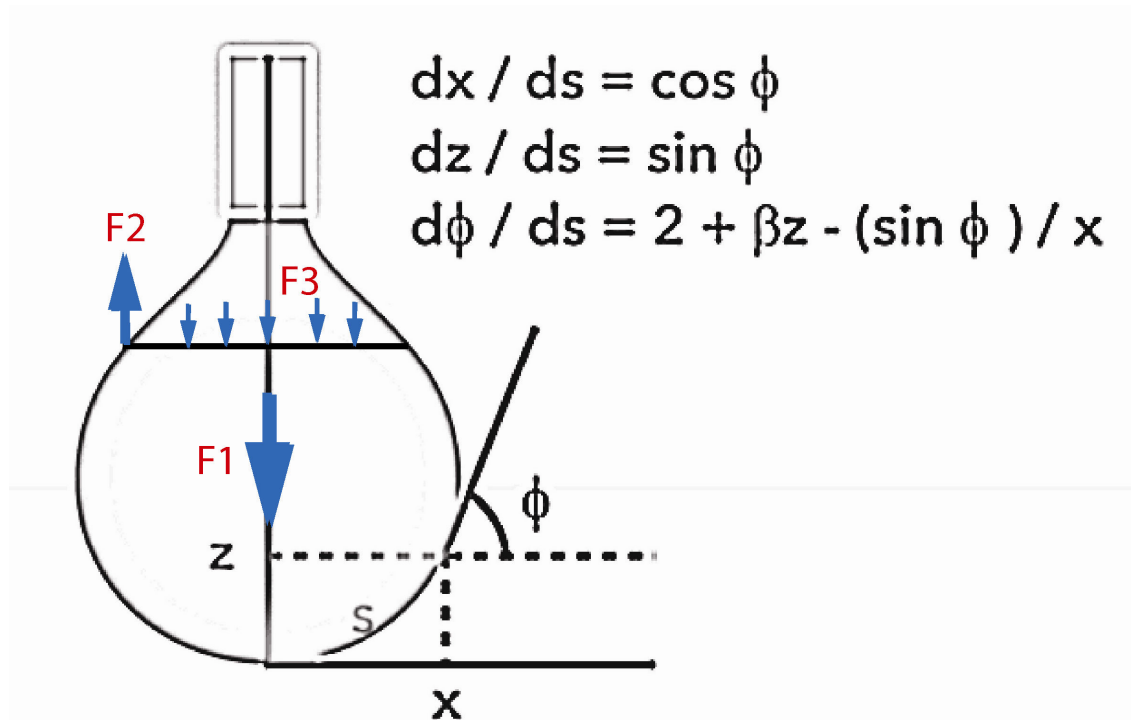


Figure 3.12 A pendant droplet suspended from a needle point. Three dimensionless first order differential equations used to evaluate the shape factor of the pendant droplet are shown. Vertical and horizontal force components are also shown.

The shape factor can be estimated rapidly via computer from 3 dimensionless first order differential equations shown in Figure 3.12. Thus for any pendant droplet where the densities of the two fluids (say air and water) in contact are known, the dynamic interfacial surface tension can be measured. The method obviously has wide use in adsorption studies where adsorption of substance to the interface causes a decrease in the surface tension.

3.D.2. X-Ray Diffraction Patterns and Refined protein structure

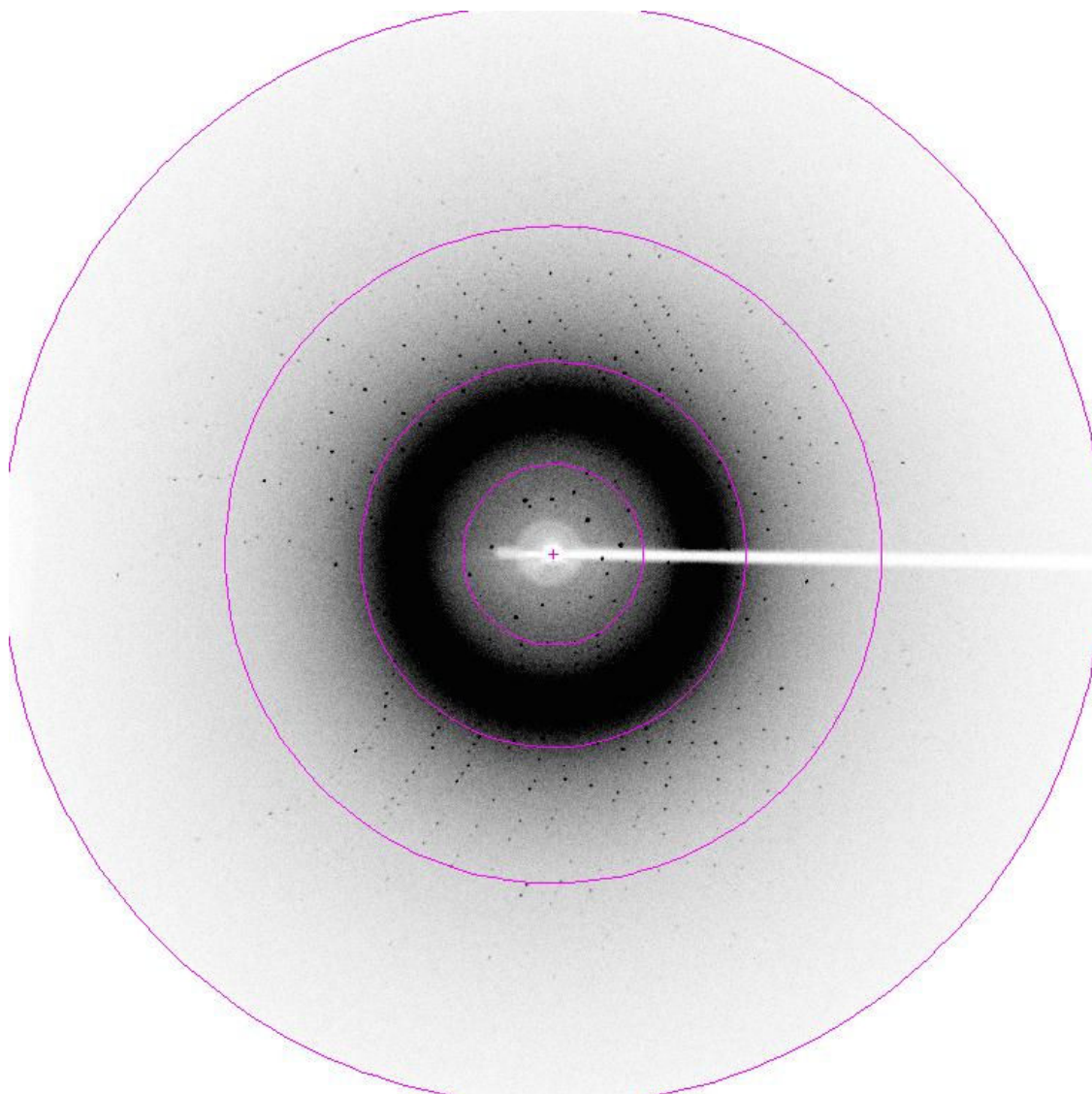


Figure 3.13 Diffraction pattern of lysozyme grown on the chloroform/water interface. The resolution rings are at 1.7, 2.2, 3.3 and 6.6 Å.

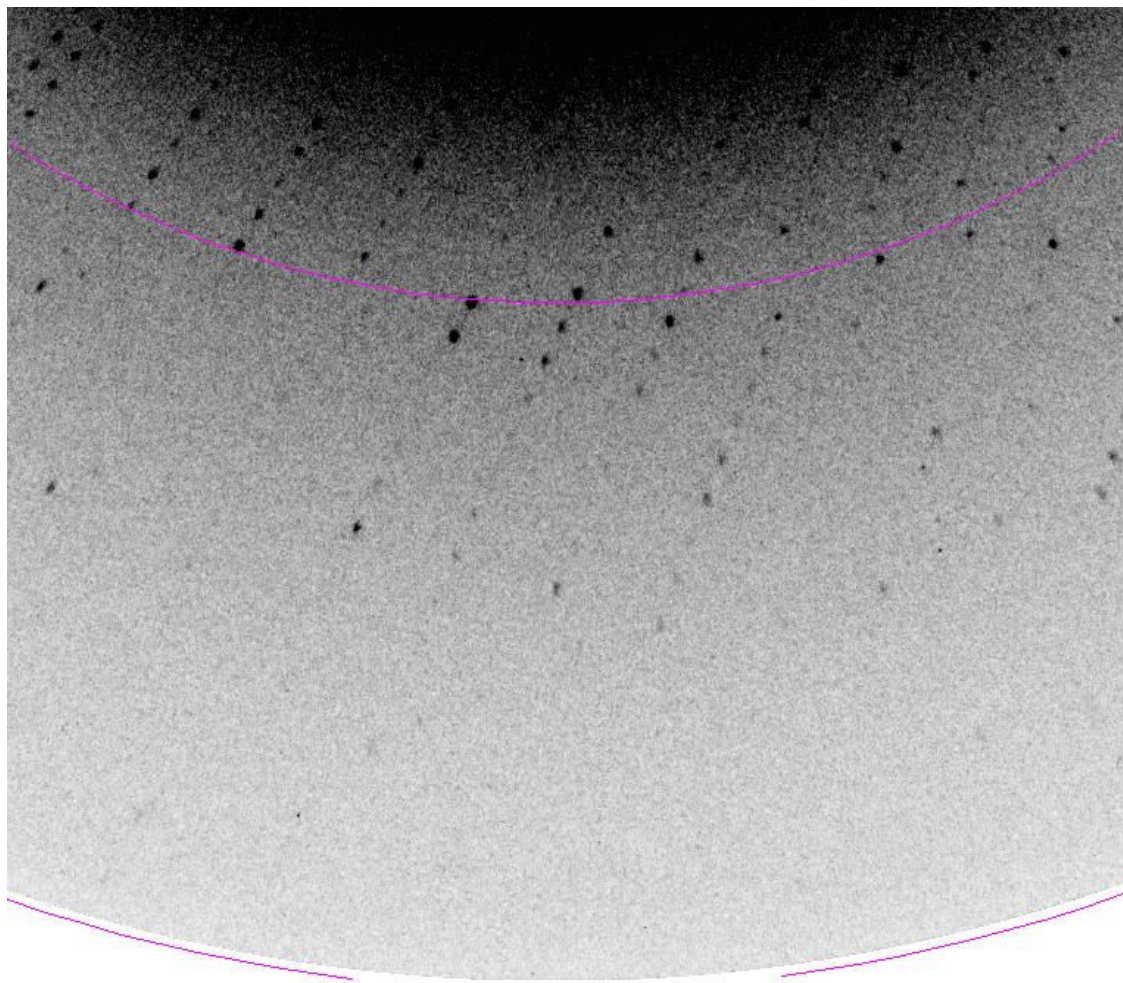


Figure 3.14 A close-up of diffraction pattern featured in Figure 3.13. The zoom shows that diffraction spots go out to the edge of 1.7 Å

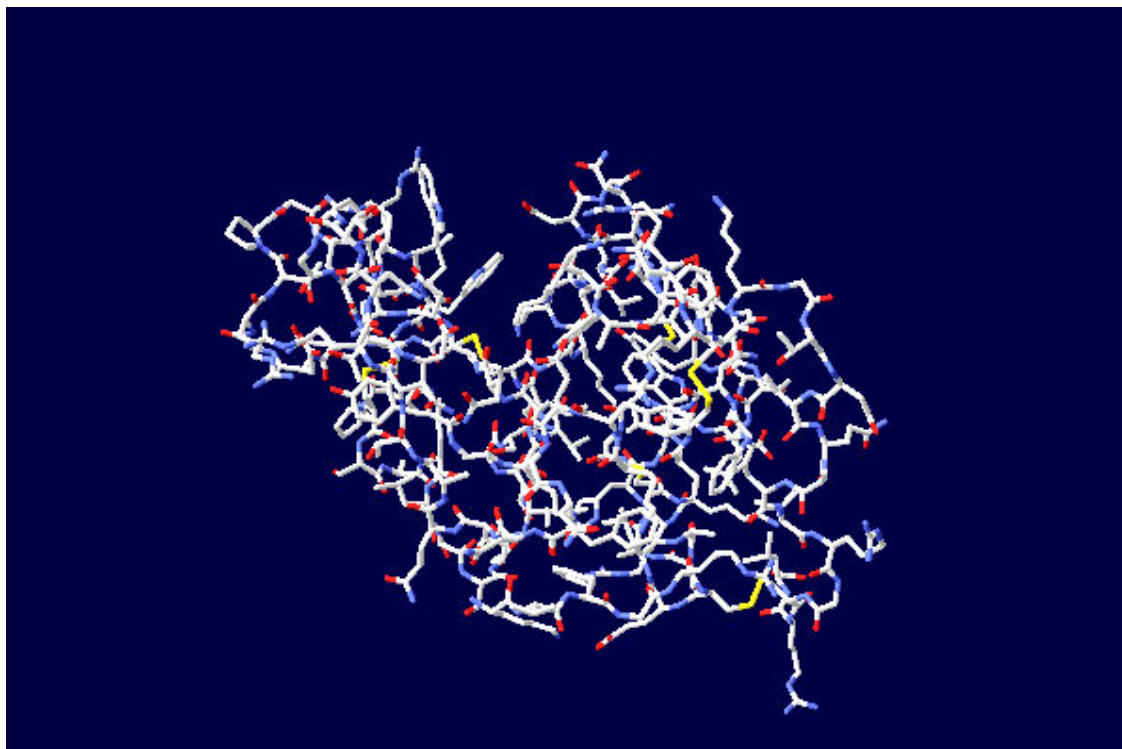


Figure 3.15 The refined lysozyme structure from previous diffraction patterns

3.E References

1. D. S. Walker, M. G. Brown, C. L. McFearn and G. L. Richmond, *The Journal of Physical Chemistry B*, 2004, **108**, 2111-2114.
2. P. L. du Nouy, *J. Gen. Physiol.*, 1925, **7**, 625-631.
3. A. Malzert-Fréon, J.-P. Benoît and F. Boury, *Eur. J. Pharm. Biopharm.*, 2008, **69**, 835-843.
4. H. H. Girault, D. J. Schiffrin and B. D. V. Smith, *J. Electroanal. Chem.*, 1982, **137**, 207-217.
5. E. W. Washburn, ed., *International critical tables of numerical data, physics, chemistry and technology*, National Research Council, 1928.
6. T. H. Williamson, *Vitreoretinal Surgery* Springer, 2007.
7. A. Goebel and K. Lunkenheimer, *Langmuir*, 1997, **13**, 369-372.
8. D. J. Donahue and F. E. Bartell, *J. Phys. Chem*, 1952, **56**, 480-484.
9. J. F. Boyce, S. Schürch, Y. Rotenberg and A. W. Neumann, *Colloids Surf.*, 1984, **9**, 307-317.
10. IUPAC, IUPAC-NIST SOLUBILITY DATA SERIES, <http://srdata.nist.gov/solubility/>.
11. D. R. Lide *CRC Handbook of Chemistry and Physics* CRC Press, 2003.
12. G. C. Randall and P. S. Doyle, *Proc. Natl. Acad. Sci. U. S. A.*, 2005, **102**, 10813-10818.
13. A. Stocco, T. Mokhtari, G. Haseloff, uuml, nter, A. Erbe and R. Sigel, *Physical Review E*, 2011, **83**, 011601.
14. X. Zhao, F. Pan and J. R. Lu, *J. Royal Soc. Interface*, 2009, **6**, S659-S670.
15. R. C. Stevens, *Curr. Opin. Struct. Biol.*, 2000, **10**, 558-563.
16. J. T. Chin, S. L. Wheeler and A. M. Klibanov, *Biotechnol. Bioeng.*, 1994, **44**, 140-145.
17. E. T. White, W. H. Tan, J. M. Ang, S. Tait and J. D. Litster, *Powder Technol.*, 2007, **179**, 55-58.
18. C. U. Kim, Q. Hao and S. M. Gruner, *Acta Crystallographica Section D*, 2006, **62**, 687-694.
19. D. E. Graham and M. C. Phillips, *J. Colloid Interface Sci.*, 1979, **70**, 415-426.
20. D. E. Graham and M. C. Phillips, *J. Colloid Interface Sci.*, 1979, **70**, 427-439.
21. T. Sengupta and S. Damodaran, *J. Colloid Interface Sci.*, 1998, **206**, 407-415.
22. T. Lefèvre and M. Subirade, *J. Colloid Interface Sci.*, 2003, **263**, 59-67.
23. A. Malzert-Fréon, J.-P. Benoît and F. Boury, *Eur. J. Pharm. Biopharm.*, 2008, **69**, 835-843.
24. G. Pellicane, G. Smith and L. Sarkisov, *Physical Review Letters*, 2008, **101**, 248102.

25. M. Feig, ed., *Modeling Solvent Environments, Applications to Simulations of Biomolecules*, WILEY-VCH Verlag GmbH & Co., Weinheim, 2010.
26. A. Paliwal, D. Asthagiri, D. Abras, A. M. Lenhoff and M. E. Paulaitis, *Biophys. J.*, 2005, **89**, 1564-1573.
27. G. M. Thurston, *Proceedings of the National Academy of Sciences*, 2007, **104**, 18877-18878.
28. D. I. Svergun, S. Richard, M. H. J. Koch, Z. Sayers, S. Kuprin and G. Zaccai, *Proc. Natl. Acad. Sci. U. S. A.*, 1998, **95**, 2267-2272.
29. F. Merzel and J. C. Smith, *Proc. Natl. Acad. Sci. U. S. A.*, 2002, **99**, 5378-5383.
30. B. Halle, *Philosophical Transactions of the Royal Society of London. Series B: Biological Sciences*, 2004, **359**, 1207-1224.
31. O. Keskin, A. Gursoy, B. Ma and R. Nussinov, *Chemical Reviews*, 2008, **108**, 1225-1244.
32. P. G. Vekilov, A. R. Feeling-Taylor, S.-T. Yau and D. Petsev, *Acta Crystallogr., Sect. D: Biol. Crystallogr.*, 2002, **58**, 1611-1616.
33. C. Petersen, K.-J. Tielrooij and H. J. Bakker, *The Journal of Chemical Physics*, 2009, **130**, 214511.
34. M. Nakasako, *Philosophical Transactions of the Royal Society of London. Series B: Biological Sciences*, 2004, **359**, 1191-1206.
35. D. Laage, G. Stirnemann and J. T. Hynes, *The Journal of Physical Chemistry B*, 2009, **113**, 2428-2435.
36. Y. L. A. Rezus and H. J. Bakker, *Physical Review Letters*, 2007, **99**, 148301.
37. C. Mattos and D. Ringe, *Curr. Opin. Struct. Biol.*, 2001, **11**, 761-764.
38. A. M. Klibanov, *Nature*, 2001, **409**, 241-246.
39. M. C. Parker, B. D. Moore and A. J. Blacker, *Biotechnol. Bioeng.*, 1995, **46**, 452-458.
40. L. A. S. Gorman and J. S. Dordick, *Biotechnology and Bioengineering*, 1992, **39**, 392-397.
41. N. M. Micaêlo and C. M. Soares, *FEBS Journal*, 2007, **274**, 2424-2436.
42. J. Manuel García-Ruiz, *Journal of Structural Biology*, 2003, **142**, 22-31.
43. Y. Matsuura and A. A. Chernov, *Acta Crystallographica Section D*, 2003, **59**, 1347-1356.
44. M. Cieslik and Z. S. Derewenda, *Acta Crystallographica Section D*, 2009, **65**, 500-509.
45. W. N. Price II, Y. Chen, S. K. Handelman, H. Neely, P. Manor, R. Karlin, R. Nair, J. Liu, M. Baran, J. Everett, S. N. Tong, F. Forouhar, S. S. Swaminathan, T. Acton, R. Xiao, J. R. Luft, A. Lauricella, G. T. DeTitta, B. Rost, G. T. Montelione and J. F. Hunt, *Nat Biotech*, 2009, **27**, 51-57.
46. P. W. Atkins, *Physical Chemistry*, Oxford University Press, Oxford, 1990.
47. Z. S. Derewenda and P. G. Vekilov, *Acta Crystallogr., Sect. D: Biol. Crystallogr.*, 2006, **62**, 116-124.

48. E. Djamali and J. W. Cobble, *The Journal of Physical Chemistry B*, 2009, **113**, 5200-5207.
49. C. A. Schall, E. Arnold and J. M. Wiencek, *Journal of Crystal Growth*, 1996, **165**, 293-298.
50. S. T. Yau, B. R. Thomas and P. G. Vekilov, *Phys. Rev. Lett.*, 2000, **85**, 353.
51. O. Gliko, N. Neumaier, W. Pan, I. Haase, M. Fischer, A. Bacher, S. Weinkauf and P. G. Vekilov, *Journal of the American Chemical Society*, 2005, **127**, 3433-3438.
52. N. E. Chayen, P. D. Shaw Stewart and D. M. Blow, *Journal of Crystal Growth*, 1992, **122**, 176-180.
53. N. E. Chayen, *Structure*, 1997, **5**, 1269-1274.
54. N. E. Chayen, *J. Cryst. Growth*, 1999, **196**, 434-441.
55. Z. S. Derewenda and P. G. Vekilov, *Acta Crystallogr., Sect. D: Biol. Crystallogr.*, 2006, **62**, 116-124.
56. T. Sengupta and S. Damodaran, *Langmuir*, 1998, **14**, 6457-6469.
57. T. Sengupta, L. Razumovsky and S. Damodaran, *Langmuir*, 1999, **15**, 6991-7001.
58. T. Prangé, M. Schiltz, L. Pernot, N. Colloc'h, S. Longhi, W. Bourguet and R. Fourme, *Proteins: Struct., Funct., Bioinf.*, 1998, **30**, 61-73.
59. E. M. Freer, K. S. Yim, G. G. Fuller and C. J. Radke, *The Journal of Physical Chemistry B*, 2004, **108**, 3835-3844.
60. R. E. Anderson, V. S. Pande and C. J. Radke, *The Journal of Chemical Physics*, 2000, **112**, 9167-9185.
61. C. J. Beverung, C. J. Radke and H. W. Blanch, *Biophys. Chem.*, 1999, **81**, 59-80.
62. K. Griebenow and A. M. Klibanov, *Journal of the American Chemical Society*, 1996, **118**, 11695-11700.
63. P. R. Unwin, *Faraday Discuss.*, 2007, **136**, 409-416.
64. P. G. Vekilov, *Cryst. Growth Des.*, 2004, **4**, 671-685.
65. S. E. Wolf, J. Leiterer, M. Kappl, F. Emmerling and W. Tremel, *JACS*, 2008, **130**, 12342-12347.
66. T. H. Zhang and X. Y. Liu, *Journal of the American Chemical Society*, 2007, **129**, 13520-13526.
67. S. Weiner, J. Mahamid, Y. Politi, Y. Ma and L. Addadi, *Frontiers of Materials Science in China*, 2009, **3**, 104-108.
68. M. C. Vaney, I. Broutin, P. Retailleau, A. Douangamath, S. Lafont, C. Hamiaux, T. Prange, A. Ducruix and M. Ries-Kautt, *Acta Crystallogr. Sect. D-Biol. Crystallogr.*, 2001, **57**, 929-940.
69. D. S. H. Wong, J. P. Chen, J. M. Chang and C. H. Chou, *Fluid Phase Equilib.*, 2002, **194-197**, 1089-1095.

70. X. Li, X. Xu, Y. Dan and M. Zhang, *Crystallography Reports*, 2009, **54**, 1285-1288.
71. R. A. Judge, S. Takahashi, K. L. Longenecker, E. H. Fry, C. Abad-Zapatero and M. L. Chiu, *Crystal Growth & Design*, 2009, **9**, 3463-3469.
72. M. L. Pusey, M. S. Paley, M. B. Turner and R. D. Rogers, *Crystal Growth and Design*, 2007, **7**, 787-793.
73. Z. Wang, L. Dang, Y. Han, P. Jiang and H. Wei, *J. Agric. Food Chem.*, 2010, **58**, 5444-5448.
74. Y. Zhang and P. S. Cremer, *PNAS*, 2009, **106**, 15249-15253.
75. P. S. Chow, X. Y. Liu, J. Zhang and R. B. H. Tan, *Appl. Phys. Lett.*, 2002, **81**, 1975-1977.
76. M. Muschol and F. Rosenberger, *The Journal of Chemical Physics*, 1997, **107**, 1953-1962.
77. O. Galkin and P. G. Vekilov, *Proceedings of the National Academy of Sciences of the United States of America*, 2000, **97**, 6277-6281.
78. P. R. Ten Wolde and D. Frenkel, *Theor. Chem. Acc.*, 1999, **101**, 205-208.
79. J. Jůza, *Czech J. Phys.*, 1997, **47**, 351-357.
80. H. H. J. Girault, D. J. Schiffrin and B. D. V. Smith, *J. Colloid Interface Sci.*, 1984, **101**, 257-266.

4. The electrified oil/water interface – a new approach to lysozyme crystallization

This chapter has formed part of a published paper. Barry R. Silver, Vilmös Fülöp and Patrick R. Unwin, "Protein crystallization at oil-water interfaces", New J. Chem., 2011, 35, 602-606. I conducted all experiments and wrote the paper in conjunction with P.R.Unwin

4.A Experimental

Using a two electrode cell given by (4.1)



with 'crystallizing solution' containing typically 30 mg/ml lysozyme and 4 % (w/v) NaCl (as prepared in previous chapters). A potential was applied using a CHI 800b potentiostat (CHI instruments) for a period of 2 hours. The working electrode was placed in the aqueous phase and the counter/reference electrodes were placed in the oil phase. Potentials and polarities quoted are that of aqueous phase electrode against the organic phase electrode and were + 0.2V, - 0.2V and 0 V (*vide infra*). '0V' refers to Cell 1 at open circuit which is not the same as 0V.

The sign convention used is that the aqueous phase will be the most positive at the right extreme of the CV¹.

Ag/AgCl electrodes were produced by the overnight electrolysis of clean, degreased silver wire in saturated KCl solution. AgTPB electrodes were made by overnight electrolysis of clean, degreased silver wire in nitrobenzene saturated with TBATPB. AgTPB electrodes were rinsed with 1, 2-dichloroethane after electrolysis to remove any trace of nitrobenzene.

Ag/AgCl wire was 'plumbed' into a syringe. The syringe was filled with crystallizing solution. The syringe was then fitted with a stainless 'hooked' needle which was electrically isolated from the Ag/AgCl wire. The AgTPB wire was placed into the organic phase containing electrolyte (Cell 1).

The experimental arrangement was as illustrated in Figure 4.1. A Krüss DSA 100 drop shape analysis system allowed *in-situ* low-magnification optical microscopy of the oil/water interface, formed by extruding a small pendant droplet of aqueous phase into the organic phase (Cell 1). Additionally, dynamic interfacial surface tension measurements under applied potential were obtained via drop shape analysis of extruded pendant droplets.

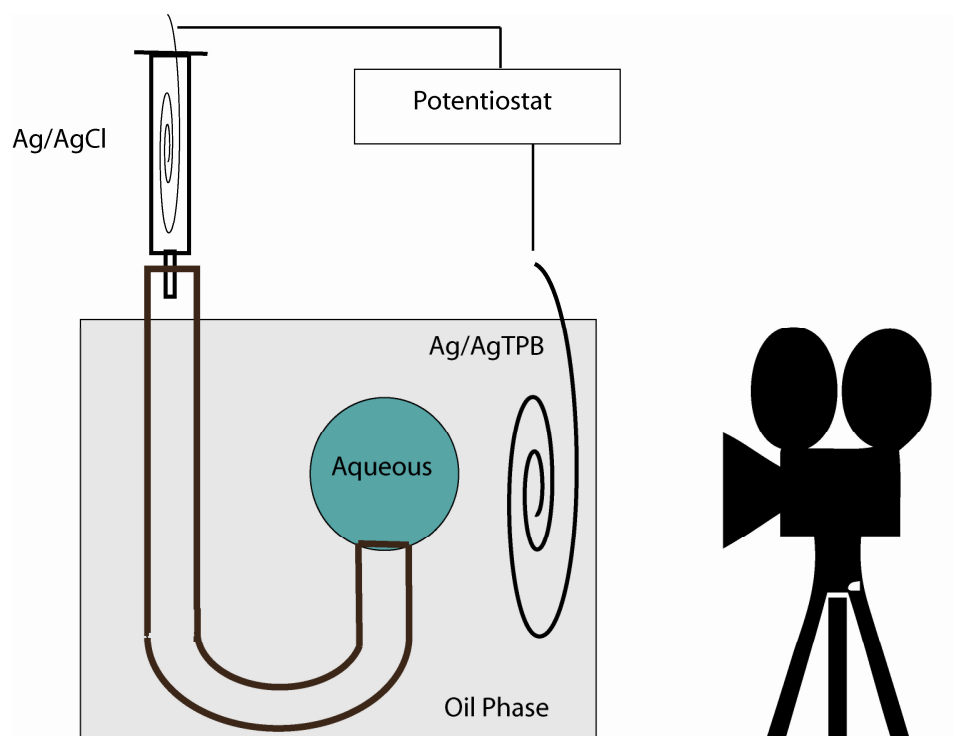


Figure 4.1 A cartoon representation of the experimental arrangement

4.B Results

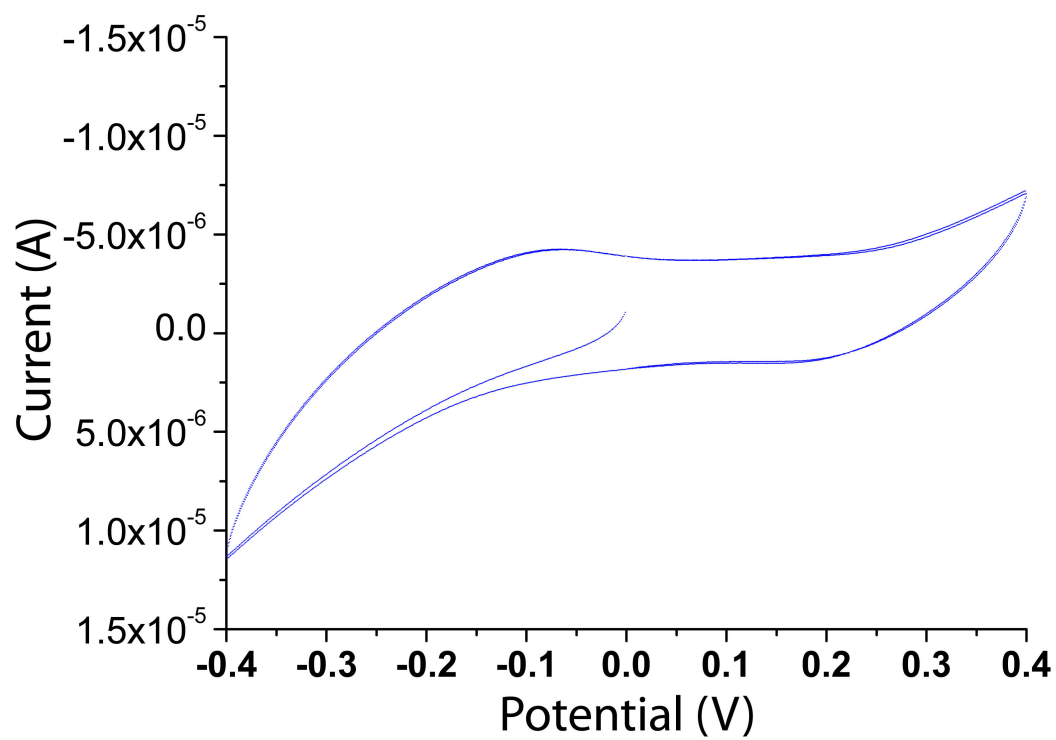


Figure 4.2 Cyclic voltammogram of Cell 1 (4.1) without lysozyme. Initial scan direction was negative. Scan rate 50 mV/s. Polarity was that of the aqueous phase.

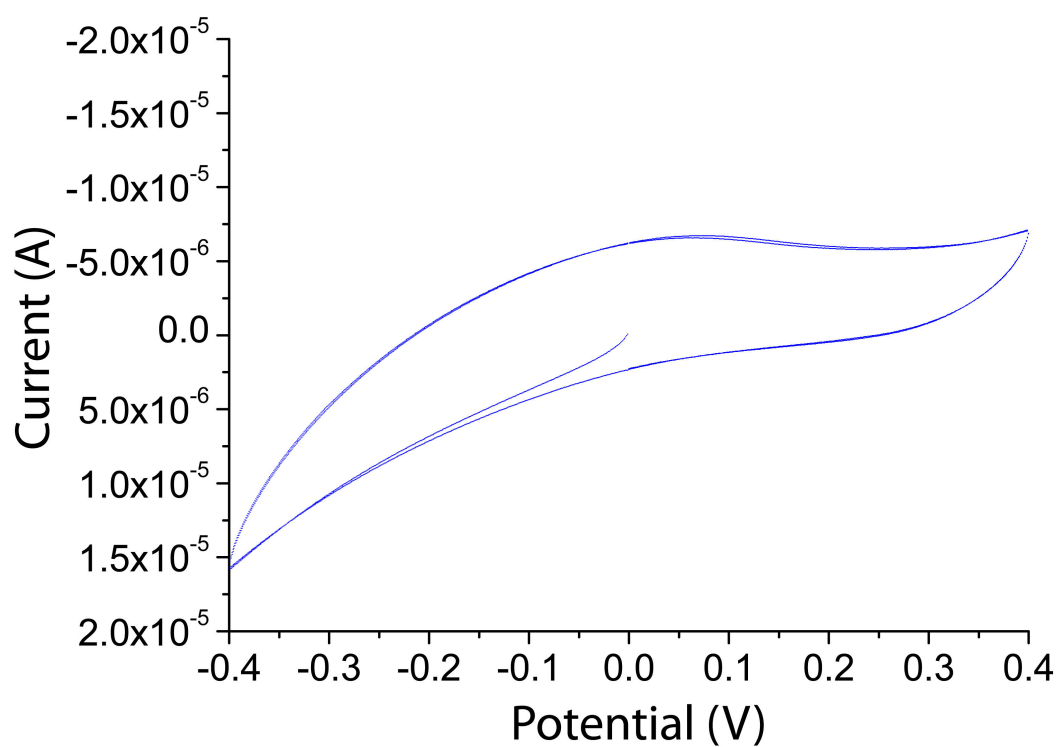


Figure 4.3 Cyclic voltammogram of cell given in (4.1) with the addition of 30 mg/ml lysozyme. Initial scan direction negative. Scan rate 50 mV/s. Polarity is that of the aqueous phase.

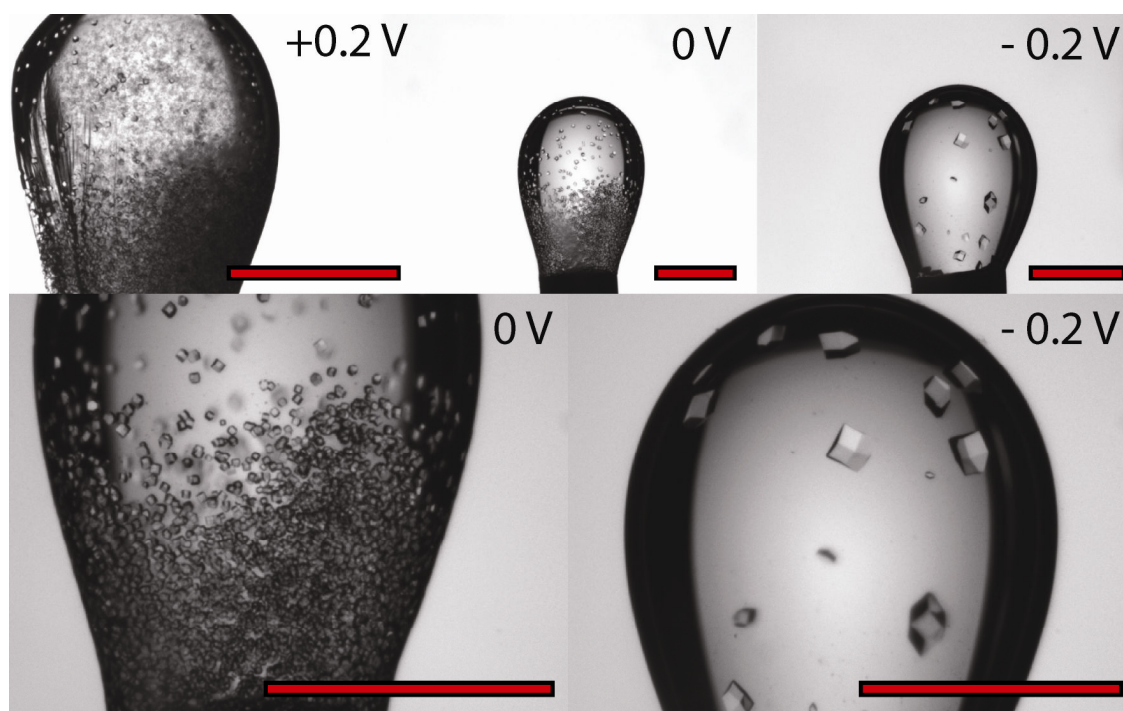


Figure 4.4 The effect of an applied potential on the crystallization of lysozyme at the ITIES. **Top left** : pendant droplet after 2 hours at +0.2 V, **middle top**: control experiment no applied potential (open circuit, referred to as 0 V), **top right**: pendant droplet after 2 hours at -0.2 V. Aqueous phases contained 30 mg/ml and 4% (w/v) NaCl in all cases. Organic phases contained 10 mM TBATPB in all cases. Bottom panels are close-ups of (left) the control and (right) -0.2 V treatment. Scale bars shown are 1.472 mm in length in all cases. Crystals which are seen in the -0.2 V treatment are approximately 430 μm across. Note increased film formation and nucleation on the + 0.2 V treatment (top left). Polarity was of the aqueous phase in all cases.

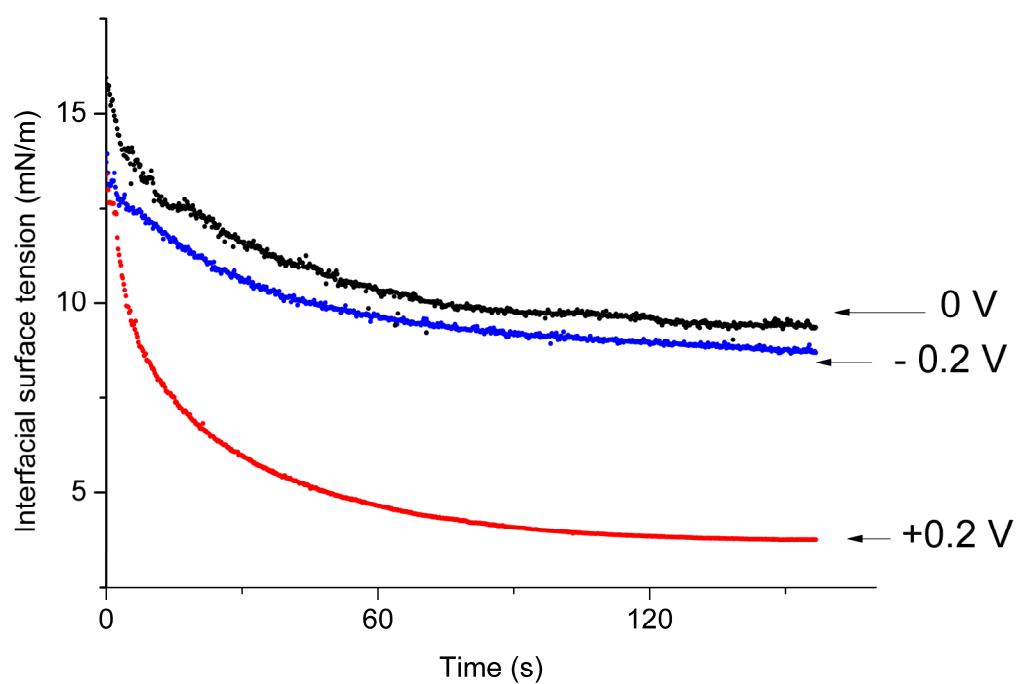


Figure 4.5 Potential-dependent dynamic interfacial surface tension as a function of applied potential (Cell 1). The aqueous phase contained 30 mg/ml lysozyme and 3% (w/v) NaCl. “0 V” refers to an open circuit condition of no applied potential and all polarities are that of the aqueous phase.

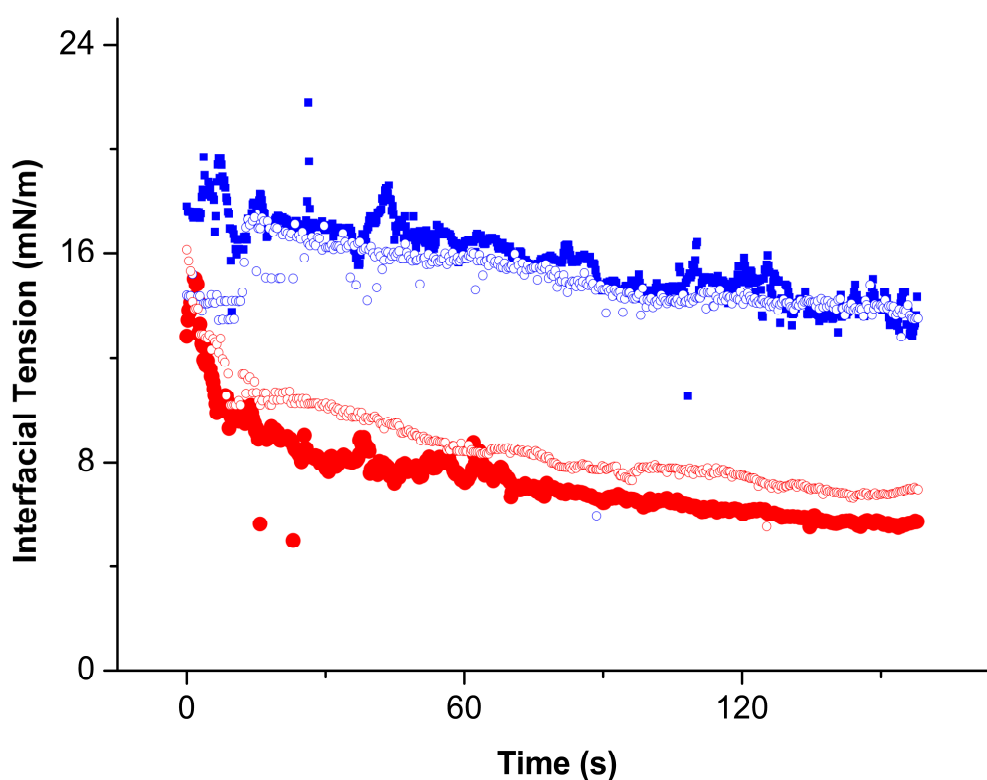


Figure 4.6 Dynamic potential-dependent interfacial tension data for an aqueous phase containing 1 mg/ml lysozyme and 3% (w/v) NaCl. Blue dots and circles indicate an applied potential of -0.2 V at pH 3 and pH 9 respectively. Red dots and circles indicate an applied potential of +0.2 V at pH 3 and pH 9 respectively.

4.C Discussion

Figure 4.4 shows the effect of 2 hours applied positive and negative potential on the extent of lysozyme crystallization at the aqueous/1, 2-dichloroethane interface. By 'extent' of crystallization we refer here to a qualitative assessment of the crystallization process. By reference to Figure 4.4 we see that some experimental conditions resulted in fewer, bigger crystals whilst other conditions resulted in many, small sized crystals. A semi-quantitative assessment of the crystallization process in terms of approximate crystal size has been given.

Truly accurate quantitative assessment of the crystallization process was difficult (within this experimental arrangement) due to the shape of liquid droplet and the position of the 'camera'. We were only able to capture the droplet in a side-ways aspect and hence the extent of crystallization on the rest of the droplet surface cannot be assessed. This Chapter therefore presents data which is rather proof-of-concept rather than strictly quantitative.

The results, indicated in Figure 4.4, appear largely consistent with potential-dependent lysozyme adsorption/desorption into, and away from, the vicinity of the oil/water interface²⁻³. If this was so, the results appear to suggest that a potential-induced 'shift' in local protein concentration occurred. Which in essence traced a path across the phase diagram (Figure 4.7) and caused either increased film formation (by a possible increase in protein concentration at the ITIES) or increased crystal growth (by possible decreases in protein concentration at the ITIES).

This suggestion is further supported by potential-dependent dynamic interfacial tension (γ) data (Figure 4.5) which demonstrates relatively large decreases in interfacial surface tension under the influence of a positive potential. Recent work, has indicated that lysozyme adsorption to the ITIES (such as those used herein) occurs over a wide range of positive potentials²⁻³.

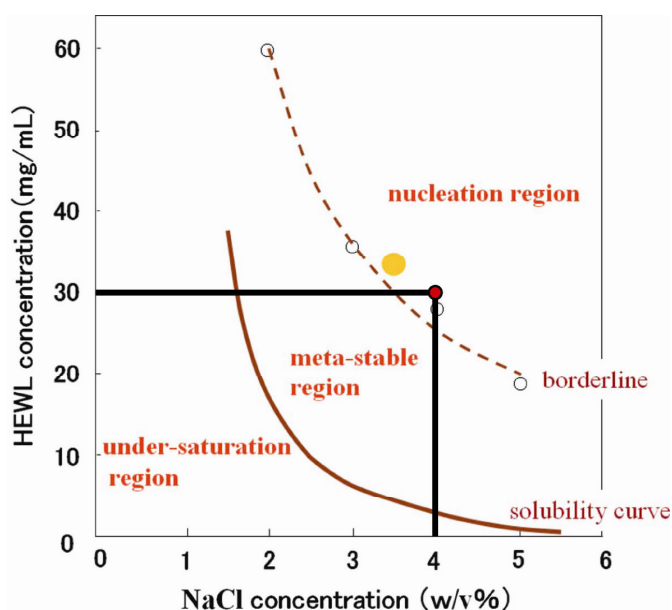


Figure 4.7 Phase diagram by Iwai and co-workers for the lysozyme/NaCl crystallization system at pH 4.5. Initial conditions of 30 mg/ml lysozyme and 4% (w/v) NaCl are indicated. Figure taken and adapted from ref. 15. A decrease in protein concentration around growing crystals will result in a ‘shift’ of solution conditions into the metastable zone.

At open-circuit, lysozyme will naturally adsorb (irreversibly) to the oil/water interface (established in Chapter 3)²⁻³. Interestingly though, the application of negative potentials and the open-circuit condition display similar IFT behaviour, with negative potentials resulting in the adsorption of what seems to be slightly more protein (Figure 4.5). This suggests that there may be complex protein adsorption behaviour at the ITIES (at negative potentials)³. This type of behaviour has been noted previously with TPB^- in the organic phase.

At precipitant concentrations used herein, most of the surface charge on lysozyme should be screened and therefore any electrostatic interaction near the ITIES should be negligible⁴. However it does appear largely that a negatively charged interface is in effect repelling a positively charged protein². This desorption behaviour is in accordance with previous work with lysozyme at the ITIES².

Figure 4.6 shows the similarity in potential-dependent γ behaviour between lysozyme at pH 3 and pH 9 using reduced lysozyme concentrations (1 mg/ml as opposed to crystallizing conditions of 30 mg/ml). Lysozyme is a cationic protein⁵ with an isoelectric point of approximately 10, and is therefore positively charged at pH below the isoelectric point. The protein will possess less charge⁵ (if any) at pH 9 compared to that at pH 3, and thus one may expect more 'interaction' from lysozyme at pH 3 than at pH 9. This is clearly not the case, as potential-dependent IFT behaviour remains the same regardless of the magnitude of the protein surface charge.

We have neglected changes in pH and chloride ion concentration as contributors to the increase in the size of lysozyme crystals (Figure 4.4) as potentials were too low to cause changes in solution conditions around growing crystals. Currents passed through the interface were in the μA range (Figure 4.3) and therefore any changes in Cl^- (via association with transferred TBA^+ for example) were considered too small to cause any real effect.

The effect of TBA^+ ion transfer was also neglected because of the very small amount of charge that would ultimately be transferred across the large interface (1×10^{-8} M range) using μA currents over the two hour period.

Furthermore, applied negative potentials were well below the standard ion transfer potentials for chloride transfer⁶ (-0.481 V from the aqueous phase to the oil phase).

The adsorption of protein to the oil/water interface², which is apparent from the macroscopically visible 'skin' which has formed there, may have altered the electric double layer at the ITIES. Which in turn may have had an effect on the crystallization process. This in turn may have had some effect on the protein crystallization process. It has been shown previously that adsorption of protein to the oil-water interface results in changes to the interfacial capacitance³. Previous work, considered briefly the effect of the double-layer on the nucleation rate of lysozyme using an externally applied electric field⁷⁻⁸. The applied potential was dropped across an electrode/oil/crystallizing solution interface and was applied at high frequency. It was thought that as the double-layer becomes more unstable (at higher frequency), the nucleation rate would decrease⁷⁻⁸. In light of this work, we could tentatively suggest that at positive potentials that the double-layer became more unstable (possibly by ion-transfer) than at negative potentials. Thereby leading to the observed decreases in nucleation rate. More work on this important aspect is needed and strongly suggested.

In terms of crystal nucleation, it appears that under negative potentials, less nucleation occurred than at positive potentials. The reason for this is at the present time is unclear and more work is needed.

In terms of crystal growth, if one takes into account increases in ion concentration upon external polarization of the ITIES⁹, then one could have a situation in which, upon biasing the aqueous phase positive, an accumulation of lysozyme (as proposed) and sodium ions may result on the aqueous side of the interface^{2,9}. On the 'organic solvent' side one would have the accumulation of TPB⁻ ions. It is hard to envisage how this particular arrangement (with regards to ions alone) would have resulted in mass nucleation and small crystals size as seen in Figure 4.4. (without the accumulation of lysozyme too at the interface).

Conversely, by biasing the aqueous phase negative we should have an accumulation of chloride ions on the aqueous side and an accumulation of TBA⁺ ions of the 'organic solvent' side⁹. Again, it is hard to see how this arrangement would have resulted in a small number of large lysozyme crystals (without lysozyme repulsion/ desorption²) as increases in chloride concentration (at constant lysozyme concentration) would have resulted in small crystals and mass nucleation.

Additionally, we have shown in Chapter 3 that thick interfacial protein films can form at the aqueous-1, 2-dichloroethane, which may hinder ion transfer completely between the two liquid phases¹⁻².

The cyclic voltammograms in Figure 4.2 and Figure 4.3, conducted *in-situ* as per experimental arrangement (Figure 4.1) were, due to the large surface areas used for surface tension measurements (typically 16 -20 mm²), distorted by ohmic¹⁰ and charging effects. The potential drop could not be compensated for within this electrochemical cell arrangement¹¹. Standard ion potentials for TBA⁺ transfer across the water-1,2-dichloroethane interface are given in the literature as -0.225 V¹². Hence, Figure 4.2 and Figure 4.3 indicate that the onset of TBA⁺ transfer appears shifted towards more positive potentials by the addition of lysozyme. This type of distortion is often seen in the case of ion transfer at the ITIES in the presence of protein¹⁻²

This new crystal growth (or indeed protein film thickening) methodology presented herein is similar to that described in Chapter 2, with the essential difference being that no electrolysis occurs and therefore no meaningful change in either the precipitant concentration or pH would occur in the vicinity of growing crystals.

This method may have wider applicability to a number of different protein/precipitant systems as it appears that one may have the ability to tune protein concentration in the vicinity of a growing ITIES-localised protein crystal by the application of potential across the ITIES.

4.D Appendix I

4.D.1 An introduction to liquid – liquid electrochemistry.

(Compiled from ref. ^{1, 6, 13})

Consider a liquid/liquid interface at equilibrium, which is formed by a liquid phase α and by a liquid phase β . Also assume that the two phases are in physical contact, and any ions present are able to freely diffuse between the two phases. Consider now a single ion or a particle (which may be charged or uncharged in the case of a particle) that can partition between the two phases without any external influence, such as that of an externally applied potential. At equilibrium, the transfer of molecules between the two liquid phases will cease and the electrochemical potentials of the two phases will therefore be equal. The electrochemical potential ($\tilde{\mu}_\alpha$ and $\tilde{\mu}_\beta$) of phase α and phase β are given by (4.2)

$$\mu_\alpha^0 + RT \ln a_\alpha + zF\phi_\alpha = \mu_\beta^0 + RT \ln a_\beta + zF\phi_\beta \quad (4.2)$$

where $\mu_{\alpha/\beta}^0$ is the standard chemical potential, R is the gas constant, T is the absolute temperature, $a_{\alpha/\beta}$ is the activity of the ion in phases α and β , z is the valence on the ion, F is the Faraday constant and ϕ is the local electrostatic potential.

Consider the situation described by (4.2) but under conditions where a particle, which bears no charge, is able to partition between the two phases (the ion is uncharged so $z = 0$ and hence the term $zF\phi = 0$) without any external influences. At equilibrium, the electrochemical potentials are equal and thus become

$$\mu_{\alpha}^0 + RT \ln a_{\alpha} = \mu_{\beta}^0 + RT \ln a_{\beta} \quad (4.3)$$

By simple rearrangement of (4.3) we obtain an expression (4.4) for the distribution coefficient ($\frac{a_{\beta}}{a_{\alpha}}$), which allows us to determine the extent of uncharged particle partitioning between the two phases with no externally applied potential.

$$e^{\frac{(\mu_{\alpha}^0 - \mu_{\beta}^0)}{RT}} = \frac{a_{\beta}}{a_{\alpha}} \quad (4.4)$$

Furthermore, the difference between the standard chemical potentials ($\mu_{\alpha}^0 - \mu_{\beta}^0$) in (4.4) is defined as the *standard Gibbs energy of transfer* (ΔG_{tr}^0).

We can therefore use measures of ΔG_{tr}^0 to compare the tendency of different particles to partition between the two liquid phases. Transfers of very hydrophobic particles from the oil phase across the oil/interface into the water phase will be energetically unfavourable and hence ΔG_{tr}^0 will be more positive than say for a transfer involving the movement of a hydrophobic particle into a hydrophobic environment.

Now consider the situation for a charged ion ($z \neq 0$ hence $zF\phi \neq 0$). We obtain the following expression (4.5) for the distribution coefficient

$$\frac{a_{\beta}}{a_{\alpha}} = \exp \frac{1}{RT} ((\mu_{\alpha}^0 - \mu_{\beta}^0) + zF(\phi_{\alpha} - \phi_{\beta})) \quad (4.5)$$

Thus far we have determined expressions for the partitioning of single ions both charged and uncharged between two immiscible liquid phases. This is unrealistic as one may find that an ion seldom exists by itself in solution and the presences of a few counter-ions are needed to ensure electroneutrality.

The partitioning of one ion (either charged or uncharged) into both liquid phases will therefore, not correspond directly to the simple partition coefficient as we have just described, because the presence of counter-ions should influence the partitioning behaviour. Therefore using the simplest situation for a single salt consisting of two ions ($z = +1$ and $z = -1$) which are able to distribute between the two liquid phases at equilibrium, the electrochemical potential of the *all* the cations in each phase must be equal and similarly the electrochemical potential of *all* the anions in each phase must be equal to ensure electroneutrality. The situation is now better described by (4.6)

$$\tilde{\mu}_{\alpha}(+) = \tilde{\mu}_{\beta}(+) \text{ and } \tilde{\mu}_{\alpha}(-) = \tilde{\mu}_{\beta}(-) \quad (4.6)$$

For the cations we obtain the following expression

$$\phi_{\beta} - \phi_{\alpha} = \frac{RT}{F} \ln \frac{a_{\alpha}(+)}{a_{\beta}(+)} + \frac{\mu_{\alpha}^0(+) - \mu_{\beta}^0(+)}{F} \quad (4.7)$$

and similarly for all the anions we obtain

$$\phi_{\beta} - \phi_{\alpha} = -\frac{RT}{F} \ln \frac{a_{\alpha}(-)}{a_{\beta}(-)} - \frac{\mu_{\alpha}^0(-) - \mu_{\beta}^0(-)}{F} \quad (4.8)$$

Since the interfacial potential difference between each phase under conditions of electroneutrality would be equal to zero ($\phi_\beta - \phi_\alpha = 0$), by rearrangement of (4.7) and (4.8) we are able to obtain an expression for the distribution coefficient for the two ion system at equilibrium (4.9)

$$\frac{a_\alpha(+)\alpha_\alpha(-)}{a_\beta(+)\alpha_\alpha(-)} = \exp \frac{1}{RT} (\mu_\beta^0(+) - \mu_\alpha^0(+) + \mu_\beta^0(-) - \mu_\alpha^0(-)) \quad (4.9)$$

4.D.2 The standard Gibbs energy of transfer

Generalizing equations (4.7) and (4.8) for ions of any charge ($z \leq 0$ and $z \geq 0$) we are able to obtain the difference between the inner potentials of the two phases from the ion distributions (between the two phases)

$$\phi_\beta - \phi_\alpha = \frac{1}{zF} (\mu_\alpha^0 - \mu_\beta^0 + RT \ln \frac{a_\alpha}{a_\beta}) \quad (4.10)$$

Since $-\frac{\mu_{\alpha/\beta}^0}{zF} = \phi_{\alpha/\beta}^0 + RT \ln \frac{a_\alpha}{a_\beta}$ (by rearrangement)

$$\phi_\beta - \phi_\alpha = \phi_\beta^0 - \phi_\alpha^0 + \frac{RT}{zF} \ln \frac{a_\alpha}{a_\beta} \quad (4.11)$$

Equation (4.11) is analogous to the Nernst equation.

Thus when a very small amount of charged ion contained in one phase has moved into the opposite phase $RT \ln \frac{a_\alpha}{a_\beta} \rightarrow 0$ and the difference in standard electrical potentials (ϕ^0) can be written

$$\phi_\beta^0 - \phi_\alpha^0 = -\frac{\mu_\alpha^0 - \mu_\beta^0}{zF} \quad (4.12)$$

$$\therefore \Delta_\beta^\alpha \phi = \phi_\beta^0 - \phi_\alpha^0 = \frac{\mu_\alpha^0 - \mu_\beta^0}{zF} = \frac{-\Delta G_{tr}^{0,\alpha \rightarrow \beta}}{zF} \quad (4.13)$$

where $\Delta G_{tr}^{0,\alpha \rightarrow \beta}$ is the *standard Gibbs energy of transfer* for a single charged ion from phase α to phase β and $\Delta_\beta^\alpha \phi$ is the difference in standard electrical potential between the two phases.

The *standard Gibbs energy of transfer* is equal to the difference between the Gibbs solvation energy of the ion in the ‘water’ phase and the Gibbs solvation energy of the ion in the ‘oil’ phase.

4.D.3 Gibbs energy of transfer for single ions

An input of energy is therefore required to drive a very hydrophobic ion into a very hydrophilic environment as the situation is energetically unfavourable.

Additional energy may be provided to enable this transfer via the application of an external voltage to a liquid-liquid interface. Since the interfacial potential can also be dependent on the activity of the ion between the two liquid phases, a potential may also be applied across the liquid/liquid interface (within a certain range) by choosing a salt which has a common ion that can partition between the two liquid phases.

Since one can only measure the potential difference between two points in a homogenous conductor, a situation that is not found across the interface between two immiscible liquids, we cannot actually measure the inner potential difference (or Galvani potential) between the two liquid phases. Because the inner potentials remain undefined, we cannot also measure $\Delta G_{tr}^{0,\alpha \rightarrow \beta}$.

This problem is broached via the use of *extrathermodynamic* assumptions. The assumption, which was made by Parker and co-workers¹⁴⁻¹⁵ is as follows, it is assumed that the cation and the anion of the hydrophobic electrolyte tetraphenylarsonium tetraphenylborate (TPAsTPB) have equal standard Gibbs energies of transfer between any given solvent therefore

$$\Delta G_{tr,TPAs+}^{0,oil \rightarrow water} = \Delta G_{tr,TPB-}^{0,oil \rightarrow water} = \Delta G_{tr,TPAsTPB}^{0,oil \rightarrow water} \quad (4.14)$$

Based on Parkers assumption the standard electric potential difference for a single ion is defined as

$$\Delta_{oil}^{water} \phi^0 = \frac{-\Delta G_{tr,i}^{0,oil \rightarrow water}}{z_i F} \quad (4.15)$$

Returning to the equilibrium situation between the liquid two phases and considering again a single ion (4.11) the equilibrium Nernst-Donnan potential is given by

$$\Delta_{oil}^{water} = \Delta_{oil}^{water} \phi_i^0 + \frac{RT}{z_i F} \ln \frac{a_i(oil)}{a_i(water)} \quad (4.16)$$

Therefore, for the transfer of a cation from the aqueous phase to the oil phase a more positive potential than the equilibrium potential is required and for the transfer of an anion from aqueous to oil phase a more negative potential is required. The opposite is true for transfers of cations and anions from the oil phase to the water phase.

4.E References

1. P. Vanysek, ed., *Electrochemistry on Liquid/Liquid Interfaces*, Springer-Verlag, Berlin, Germany, 1985.
2. E. Alvarez de Eulate and D. W. M. Arrigan, *Anal. Chem.*, 2012.
3. R. A. Hartvig, M. A. Méndez, M. v. d. Weert, L. Jorgensen, J. Østergaard, H. H. Girault and H. Jensen, *Anal. Chem.*, 2010, **82**, 7699-7705.
4. E. J. F. Dickinson, J. G. Limon-Petersen, N. V. Rees and R. G. Compton, *The Journal of Physical Chemistry C*, 2009, **113**, 11157-11171.
5. D. E. Kuehner, J. Engmann, F. Fergg, M. Wernick, H. W. Blanch and J. M. Prausnitz, *The Journal of Physical Chemistry B*, 1999, **103**, 1368-1374.
6. A. G. Volkov, D. W. Deamer, D. L. Tanelian and V. S. Markin, *Liquid interfaces in chemistry and biology*, John Wiley & Sons, Inc., United States of America, 1998.
7. H. Koizumi, K. Fujiwara and S. Uda, *Cryst. Growth Des.*, 2010, **10**, 2591-2595.
8. H. Koizumi, K. Fujiwara and S. Uda, *Cryst. Growth Des.*, 2009, **9**, 2420-2424.
9. G. Luo, S. Malkova, J. Yoon, D. G. Schultz, B. Lin, M. Meron, I. Benjamin, P. Vanysek and M. L. Schlossman, *Science*, 2006, **311**, 216-218.
10. Y.-b. Liao, M. Okuwaki, F. Kitamura, T. Ohsaka and K. Tokuda, *Electrochim. Acta*, 1998, **44**, 117-124.
11. H. Girault, A. A. Kornyshev, C. W. Monroe and M. Urbakh, *J. Phys.: Condens. Matter*, 2007, **19**, 370301.
12. T. Wandlowski, V. Marecek and Z. Samec, *Electrochim. Acta*, 1990, **35**, 1173-1175.
13. P. Vanysek and L. B. Ramirez, *J. Chil. Chem. Soc.*, 2008, **53**.
14. A. J. Parker, *Chem. Rev.*, 1969, **69**, 1-32.
15. A. J. Parker, *Electrochim. Acta*, 1976, **21**, 671-679.

5. Large potential-induced changes in interfacial tension between two immiscible electrolyte solutions (ITIES) by the probable electroadsorption/ desorption of proteins.

In chapter 4 we demonstrated how an electrified oil/water interface could be used to enhance a protein crystallization system. In this chapter we investigate potential dependent adsorption/desorption behaviour of a range of different molecules including proteins, surfactants and nanoparticles. We find that large potential-dependent changes in surface tension can be achieved by what appears reversible adsorption/desorption of some proteins to and from a oil-water interface. The extent of these reversible changes in droplet geometry are, in some cases, large and controllable. As such, this methodology warrants serious consideration as a means to further enhance the performance of alternative liquid/liquid ultra low-voltage and conventional electrowetting systems. Although protein-based systems exhibited the “best performance”, we noticed deterioration/precipitation after a small number of adsorption/desorption cycles. We have therefore suggested the manufacture of more robust synthetic ‘designer electrowetting’ molecules. Other surfactants and molecules trialled herein, for their ‘electrowetting enhancement’ ability, were found to be unsuitable, mostly due to what appeared to be irreversible adsorption to the ITIES.

5.A Introduction

Conventional electrowetting systems consist of a sessile droplet of conducting liquid which partially wets the surface of a hydrophobic insulating layer (or dielectric)¹. The insulating layer covers a flat electrode which can be polarised via an external power supply (Figure 5.1). Liquid droplet sizes range from millimetres to tens of millimetres and the dielectric layer ranges in thickness from the nanometre to the micrometre size range. It is often advantageous to choose dielectric layers which afford high droplet contact angles at zero voltage, as electrowetting can only decrease the contact angle between the droplet and the dielectric upon application of potential to the electrode².

When potential is applied between the droplet and the electrode, the contact angle of the droplet (θ) on the dielectric surface decreases according to²

$$\cos \theta = \cos \theta_Y^0 + C \frac{\phi^2}{2d} \quad (5.1)$$

where θ and θ_Y^0 are the voltage dependent contact angles and the Young's angle of the system (at zero voltage) respectively. $C = \frac{\epsilon_m \epsilon_0}{d}$ which is the capacitance per unit area between the droplet and the electrode and ϵ_m is the dielectric of the insulator with ϵ_0 representing the permittivity of vacuum, d is the interfacial tension between drop and ambient medium and ϕ is the applied potential.

Equation (5.1) is often referred to as the Young-Lippmann equation and is an ‘amalgamation’ of Young’s equation ($\gamma_{sv} = \gamma_{lv} \cos \theta_Y + \gamma_{sl}$; sv and sl represent the surface tensions of the solid-liquid and solid-vapour interfaces respectively) which relates the droplet contact angle to the various forces of surface tension acting on the system, and the Lippmann equation ($\frac{d\gamma}{d\phi} = -Q$) which shows how the change in surface energy (γ) at a liquid interface is reduced by the change in capacitance (Q is the surface charge density due to an applied potential (ϕ) with capacitance $= \frac{Q}{\phi}$).

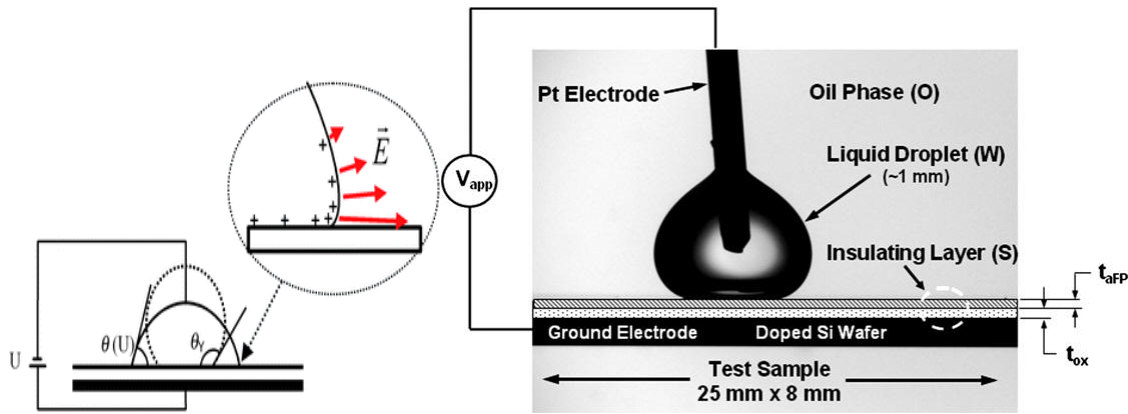


Figure 5.1 Electrowetting on a dielectric with the Young angle and contact angle indicated (left panel). A potential is applied to the droplet. Dielectric is shown in right panel as the insulating layer (S) which covers a doped Si wafer electrode. Schematics from taken from ref. 2-3.

Since the reintroduction of electrowetting technology in the 1990's it has enjoyed use as a means to manipulate liquid droplets of nanolitre volume, to provide lab on chip devices, to enable the control of adjustable focus liquid lenses, as well as to enable the control of electronic displays and micropumps³. Electrowetting systems may also consist of droplets containing electrolyte being surrounded by a layer of nonconductive nonpolar fluid which is usually insulating oil⁴.

When a nonconductive oil comprises the surrounding environment, tens of volts are needed to achieve significant change in the shape of the oil-water interface⁵. In the opposite case, when the droplet itself consists of the nonconductive oil phase, the droplet geometry can be altered by applying as little as 1 or 2 V⁵ potential. The reduction in operating voltages comes with obvious benefit to cost, energy efficiency and portability. Very recent work has suggested the use of the ITIES⁵⁻⁶, for ultra-low voltage electrowetting systems resulting in driving voltages as low as a few hundred millivolts to usefully alter contact angles⁷.

There is almost a constant need to reduce operating costs and to reduce operating voltages. Very recent work has focussed on the use of nonionic surfactants (Tween 20) to lower surface tension at the oil-water interface in order to enhance the performance of conventional electrowetting systems. This reduction in surface energy allows contact angles⁸ to be achieved at lower applied voltages. In a similar vane, another study has also focussed on the use of nonionic surfactants (Tween 8 and Span 3) to lower the switching voltages in electrowetting based optical systems⁹. The latter study concludes by suggesting that the electrical dipole moment of the surfactant is a key feature of the electrowetting process and that surfactants which display low surface activity at the oil-water interface coupled with low dipole moment should be used as 'electrowetting enhancers'.

Observations within this latter study, suggest that molecules which possess large dipole moment interact with the applied electrical field, which diminishes the electric field strength and therefore decreasing the electrowetting ability of the system. We, however, suggest that, in some circumstances, this is an incorrect assumption, and that this effect was mostly due to the irreversibility of surfactant adsorption (*vide infra*).

In connection to electrowetting/ electrocapillary phenomena at the polarised oil-water interface, recent work by Dale¹⁰ shows that the polarised interface can undergo significant reversible expansion during charge transfer processes. This phenomenon assumes more importance when operating electrowetting systems at voltages which are near or over the extremes of the polarisable potential window.

Herein, we demonstrate, for the first time, that by using appropriate surface active molecules at the ITIES, large, reversible potential-dependent changes in pendant drop geometry (or interfacial surface tension γ) can be achieved at very low applied voltages. Contrary to suggestions from previous studies⁹, the performance of alternative ultra low-voltage and conventional electrowetting systems may actually be enhanced by the incorporation of the proposed 'electrowetting particles'. We suggest that enhancements in the electrowetting effect are based on reversible potential-dependent adsorption/desorption¹¹ of surface active molecules (in this case proteins), of large dipole moment at the polarised oil-water interface. In the quest for a more robust system, the manufacture of synthetic 'particles' for this purpose are suggested and possible properties required by these hypothetical 'designer' particles discussed.

5.B Experimental

All chemicals used herein were obtained from Sigma-Aldrich (UK). Sigma product codes for proteins used within this chapter were hen egg white lysozyme (L6876), myoglobin from equine skeletal muscle (M5696), catalase from bovine liver (C40) and cytochrome c from horse heart (105201) (Cyt-c). Also used herein were gold colloid (0.01 % HAuCl_4 , G1527, produced via the Turkevich method which caps and reduces the gold with sodium citrate), Sodium dodecylbenzenesulfonic acid salt (289957), tetrabutylammonium tetraphenylborate (TBATPB) (86897 and 1,2-dichloroethane (1,2-DCE) (319929). All aqueous solutions were made up with 18 M Ω .cm water (Millipore).

Aqueous protein solutions containing varying concentrations of protein (typically between 1 mg/ml and 30 mg/ml, although going as low as 0.05 mg/ml in some cases) was made up in 20 mM sodium citrate buffer solution (pH 3) (Sigma-Aldrich, UK, 82582). In the case of catalase and Cyt-C the lower concentrations were additionally used (*vide infra*). In cases where the required solution pH was pH 4.5 and pH 9, protein solutions were made up using 20 mM sodium citrate (at pH 4.5) (Sigma-Aldrich, UK, 82585) and 20 mM sodium phosphate buffer solution (at pH 9) (Sigma-Aldrich, UK, 82603) respectively. When additions of NaCl were required, protein solutions (as just described) were mixed 1:1 with NaCl solutions to give final protein and salt concentrations.

For example 30 mg/ml lysozyme and 3% (w/v) NaCl at pH 3 was made by adding 60 mg/ml lysozyme (in pH 3 buffer) to 6 % (w/v) NaCl solution (in pH 3 buffer). All protein solutions were centrifuged at 13 000 rpm on a bench top centrifuge for 10 minutes, with the supernatant being used as the aqueous phase in subsequent experiments.

Sodium dodecylbenzenesulfonic acid solutions were made by adding the required amount to an aqueous solution containing 20 mM LiCl.

Gold colloid solutions were made by serial dilution of colloid solution with aliquots of aqueous solution containing LiCl. For instance a '0.5 gold solution' contains half an aliquot of pure gold colloid solution (from the bottle) mixed with an equal aliquot of water. LiCl was then added to give a final concentration of 0.5 gold and 20 mM LiCl. The same methodology was used when making gold colloid solutions with additions of NaCl. Gold colloid solutions contained 20 mM LiCl in all cases to make solutions conductive.

Aqueous solutions (as just described) were extruded as pendant droplets through a 'hook' into an oil phase containing 10 mM TBATPB in 1,2-DCE (in all cases) (Figure 5.2) forming an oil/water interface. Droplet sizes so acquired were typically 1.5 mm in diameter and about 2 μ l.

Potentials were applied between two electrodes with the aid of a CHI 800b potentiostat (CHI instruments). The aqueous phase electrode was the working electrode and the oil phase electrode was used as both the counter and reference electrodes. Quoted potentials¹² were therefore that of the aqueous phase and versus the organic phase electrode. Ag/AgCl (aqueous phase) and Ag/AgTPB (organic phase) electrodes were manufactured as described elsewhere¹³.

The two electrode cell used throughout was as follows, with aqueous solution pertaining to all solutions just described.

Cell 1 : Ag|AgCl| aqueous solution || 10mM TBATPB (in 1,2-DCE)|AgTPB|Ag

Potentials were applied between the two electrodes in three different *ways*.

- i) A potential sweep (referred to as 'CV' *vide infra*) was applied (of the type used within a conventional cyclic voltammetry experiment). Potentials were swept between -0.4 V and 0.4 V and sometimes between -0.8 and 0.8 V. In all cases, the initial sweep direction was negative and the sweep cycle started at 0 V. The scan rate was 50 mV/s in all cases, or as otherwise indicated.
- ii) Constant potentials of either +0.2 V or -0.2 V were applied for the duration of the experiment (typically lasting 200 s)
- iii) A 'no potential' (which was Cell 1 at open circuit, referred to herein as OCP) condition was applied for the duration of the experiment.

Five interfacial surface tension (γ) measurements were taken every second for the duration of the experiment (in all cases). Dynamic interfacial tension measurements were made using the pendant drop shape analysis method within a Krüss DSA 100 (Krüss, Germany) drop shape analysis system.

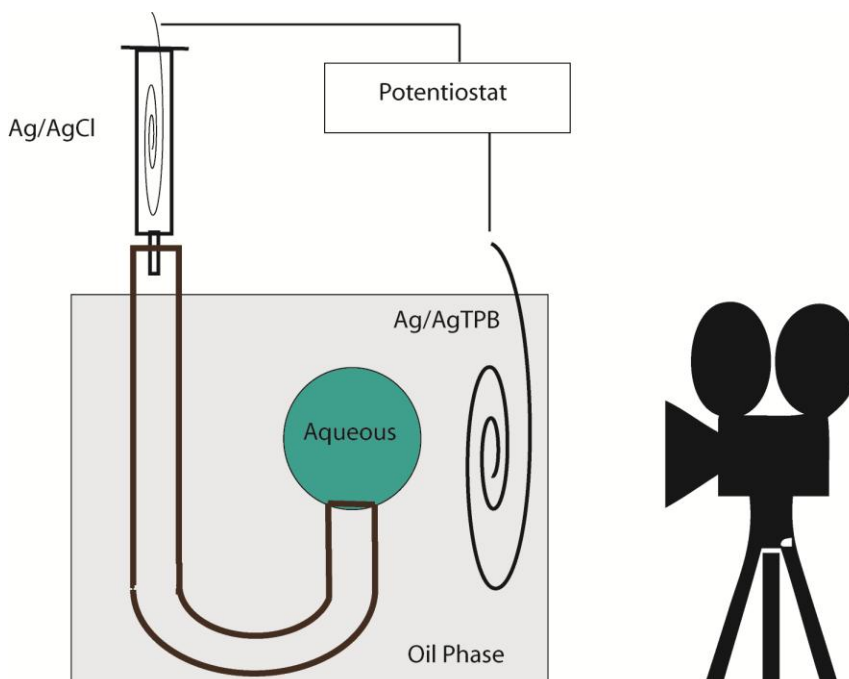


Figure 5.2 Schematic of the experimental set-up. A droplet of aqueous solution is extruded through a stainless steel 'hook' to form a droplet at the hook tip. An Ag/AgCl wire is 'plumbed' into a syringe which contains the aqueous phase. Ag/AgTPB wire is placed within the oil phase. A drop shape analysis system (camera icon) measures dynamic interfacial tension via the pendant drop method when potential is applied between the two electrodes with the aid of a potentiostat. The hook was electrically insulated from both electrodes.

5.C Results and Discussion

5.C.1. The blank. Cell 1 containing no protein or buffer. Aqueous phase contained 3% (w/v) NaCl only.

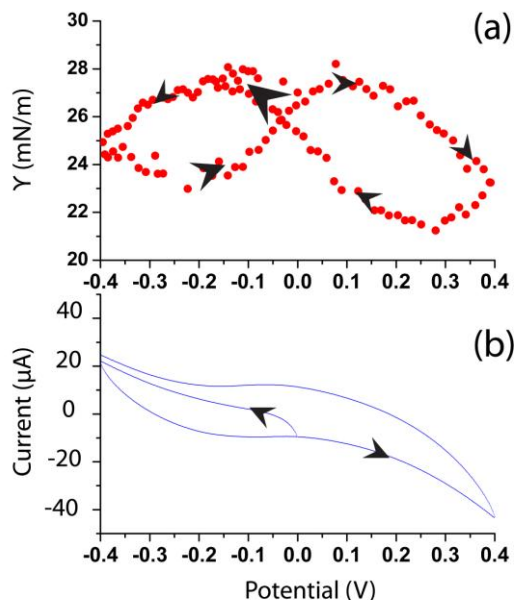


Figure 5.3 (a) Potential-dependent γ behaviour (scan rate 50 mV s^{-1}) for an aqueous phase (Cell 1) containing no protein or buffer. The first cycle is indicated on both (a) and (b). Figure (b) represents corresponding CV's for (a). Black arrows on (b) indicate the potential scan cycle, which was in a negative direction from 0 V to -0.4 V, then to +0.4V and back to negative again

Small, but detectable changes in γ were observed during the CV measurement (Figure 5.3); a distinctive 'figure of eight' pattern in the potential-dependent γ response is evident. The initial scan starts at 0 V and increases slightly until a potential of $\approx -0.2 \text{ V}$. γ then begins to decline at more negative aqueous potentials due to TBA^+ transfer from DCE to the aqueous phase¹⁰. Note the extent of γ change here is in the order of 2-3 mN/m.

The reader will note that this does not give the classical electrocapillary curve, nor is it intended to do so. The CV's in Figure 5.3 are meant **solely** as a 'blank' for protein-based systems used within this Chapter. The CV and γ data presented are not in equilibrium, as is normally the case when one compiles the classical electrocapillary curve, as scan rates were not conducted at steady-state. This diagram will however serve to indicate to some extent, γ -induced changes due to ion transfer reactions.

TBA^+ transfer continues on the reverse scan until ca. -0.15 V; the potential is then insufficient for TBA^+ transfer and γ values increase again. γ rises towards a second maximum at $\approx +0.1$ V, whereupon TPB^- transfer from oil to water commences and continues on the reverse scan until $\approx +0.3$ V. At this potential γ values begin to increase back to a second maximum (at negative potentials).

5.C.2. Lysozyme

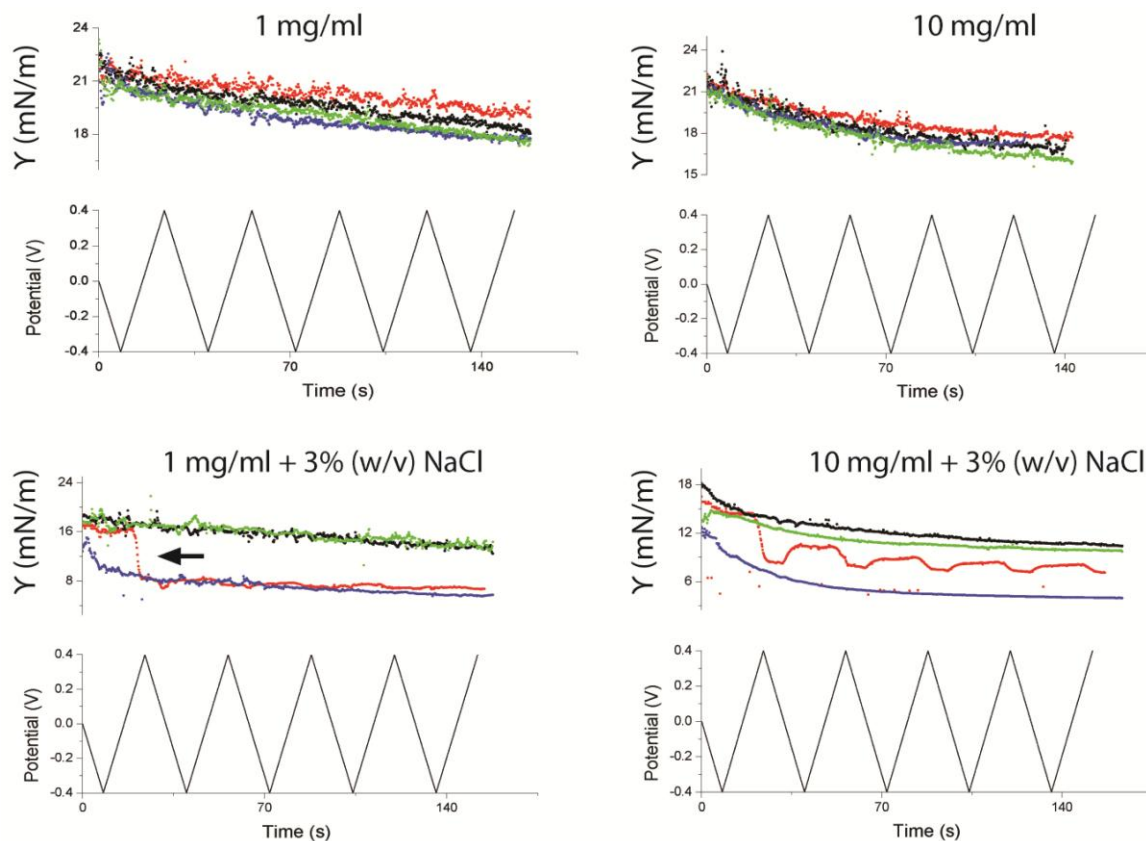


Figure 5.4 γ data from aqueous pendant droplets containing 1 and 10 mg/ml lysozyme with (bottom panels) and without (top panels) 3% (w/v) NaCl (pH 3). Oil phase was 10 mM TBATPB in 1, 2-DCE. The triangular waveform (-0.4 V to +0.4 V at 50 mV/s) used is illustrated. Key for figure in **Table 5-1**

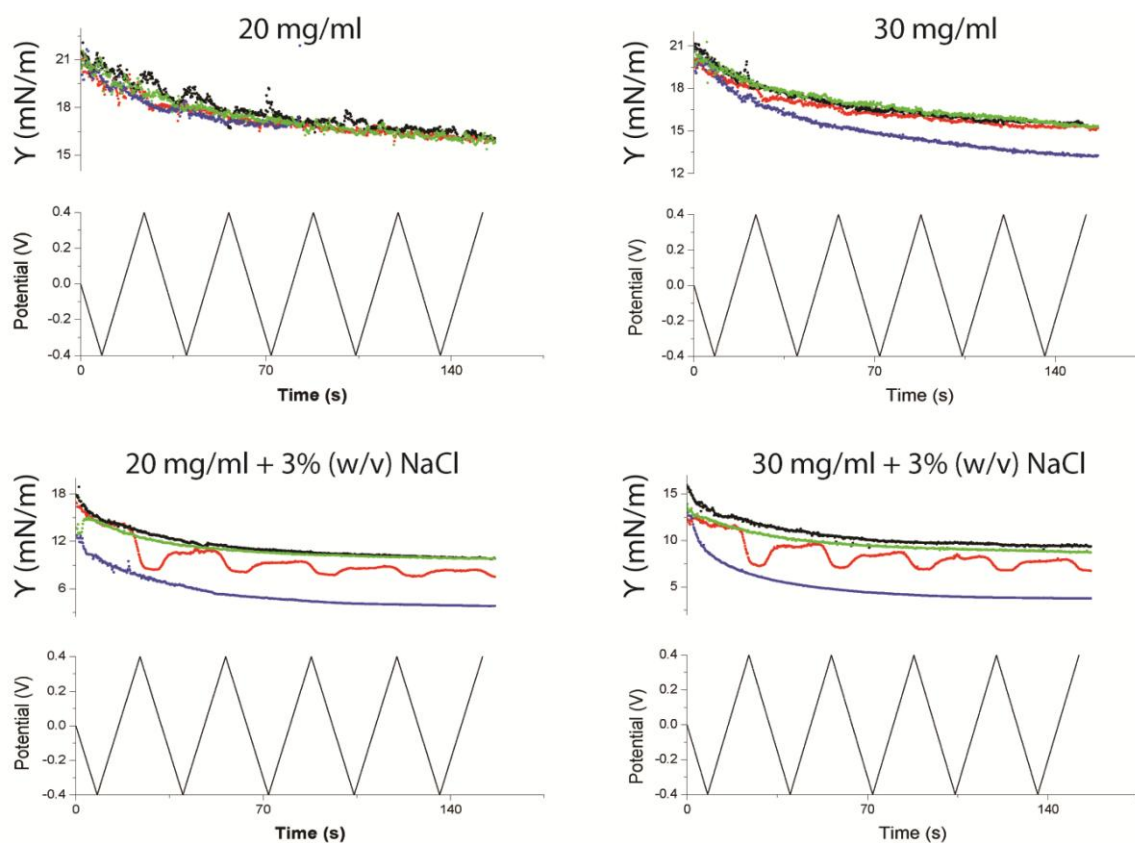


Figure 5.5 γ data for aqueous pendant droplets containing 20 and 30 mg/ml lysozyme with (bottom panels) and without (top panels) 3% (w/v) NaCl (pH 3). Oil phase contained 10 mM TBATPB in 1, 2-DCE. The triangular waveform used (-0.4 V to +0.4 V at 50 mV/s) is illustrated. Key for panels in **Table 5-1**

Table 5-1 Key for Figure 5.4 and Figure 5.5

Protein	Figure	CV	OCP	"+0.2V"	"-0.2V"
Lysozyme	5.4	red	black	blue	green
Lysozyme	5.5	red	black	blue	green

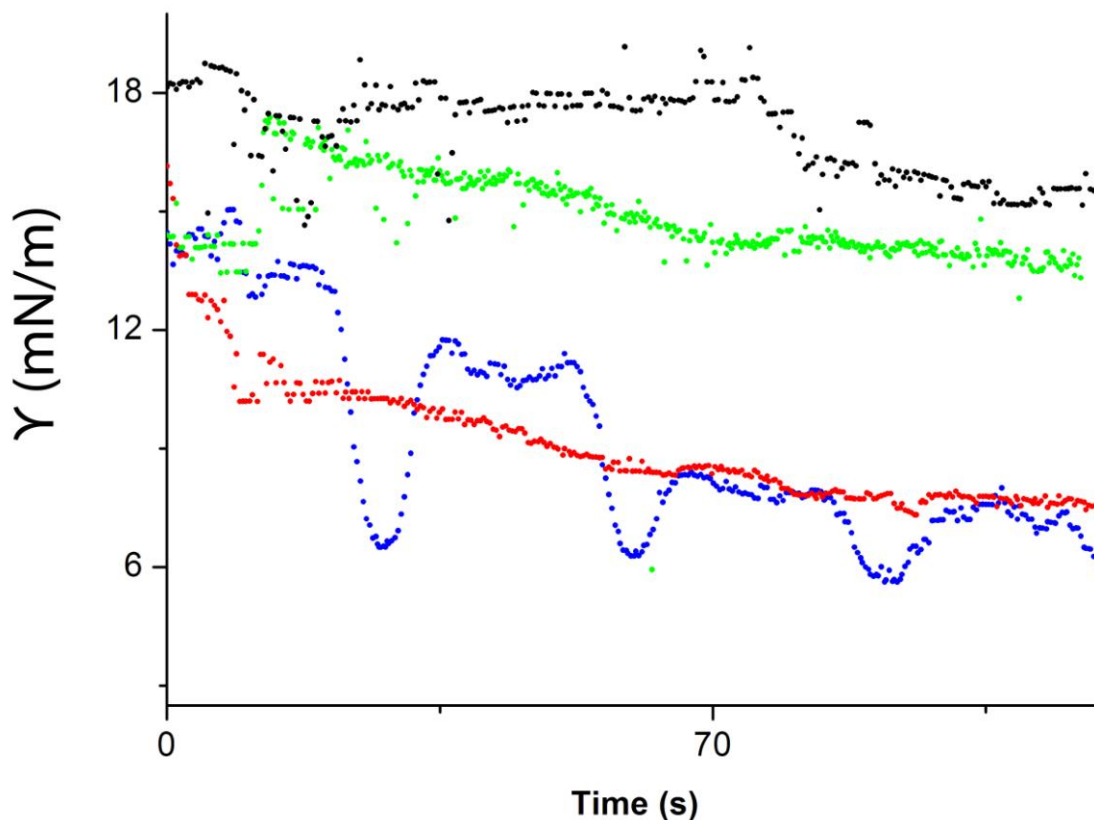


Figure 5.6 Potential-dependent γ data for aqueous pendant droplets containing 1 mg/ml lysozyme and 3% (w/v) NaCl at pH 9. Oil phase contained 10 mM TBATPB in 1, 2-DCE. Key for all panels is blue = CV, black = OCP, red = +0.2 V, green = -0.2 V.

At pH 3 (Figure 5.4 and Figure 5.5), under applied positive potential it appears that lysozyme was adsorbed to the oil-water interface in the presence of NaCl. This observation is consistent with recent work^{11, 14} which reports that the adsorption of lysozyme to the aqueous/DCE interface, takes place over a wide range of potentials more positive than the point of zero charge (pzc)¹⁴.

Presumed lysozyme adsorption to the ITIES occurs at $\approx +0.2$ V. We further suggest that lysozyme may adsorb somewhat irreversibly to this particular oil/water interface, as γ does not return to original values. Additionally, the potential at which postulated protein adsorption and desorption¹¹ processes occur appears shifted toward more negative potentials (Figure 5.7). This observation is concomitant with the adsorption of positively charged protein to the aqueous side of the ITIES¹⁴⁻¹⁶.

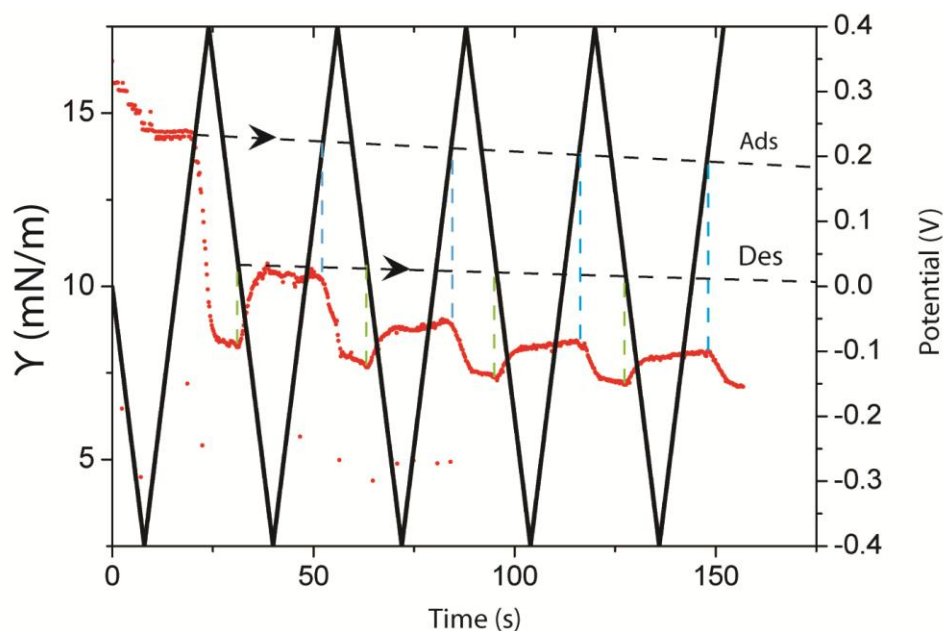


Figure 5.7 Shifts in proposed adsorption (Ads) and desorption (Des) potentials with increasing cycle number. Cell 1 containing 10 mg/ml and 3% (w/v) NaCl (pH 3) in the aqueous phase. The dotted lines indicate the directions of the trend in 'Ads' and 'Des'. Scan rate was 50 mV/s.

Further evidence in favour of the irreversibility of lysozyme adsorption can be found at lower concentration (1 mg/ml lysozyme at pH 3, Figure 5.4) where no 'return' to higher γ values occurs after what appears to be the initial adsorption. The lack of 'return' in γ , in this case, suggests that lysozyme is completely adsorbed (possibly as a monolayer or even a film¹⁷) to the clean oil-water interface¹¹.

At higher concentration, some 'recovery' of γ (to near initial values) is realised, this may further indicate the presence of a multilayer arrangement at higher protein concentration in the presence of NaCl. Additionally, lysozyme is known to be slightly soluble in some organic solvents¹⁸.

In the case of 1 mg/ml lysozyme at pH 9 (Figure 5.6 and Figure 5.8), the charge on lysozyme would be zero or very close to zero ($pI \approx 10^{19}$), and thus an electrostatically based attractive and repulsive force can be considered negligible²⁰. The zero charge on lysozyme at pH 9 is further demonstrated in Figure 5.8, where no shift in the suggested adsorption¹¹ and desorption¹¹ potentials occur with increasing cycle number. The ionic strength of solution should be high enough to screen any surface charge on the protein²⁰.

Suggested potential-dependent lysozyme 'desorption'¹¹ classified in this study by a return of γ values to initial or near initial values was seen at pH 9, but not at pH 3 (Figure 5.4). This observation suggests that lysozyme-lysozyme interactions are attractive at pH 3²¹ at the oil/water interface (in the presence of NaCl). The protein may have been rendered irreversibly adsorbed by the formation of a strong interfacial film^{17, 22}. Film formation may be less at pH 9 than at pH 3 due to a decrease in protein charge and hence protein-protein interaction (within the film) at the oil/water interface²³⁻²⁶. It is therefore suggested that at pH 9, protein-protein interactions may have been greatly reduced and thus lysozyme was able to undergo some 'desorption'¹¹ from the interface at this pH.

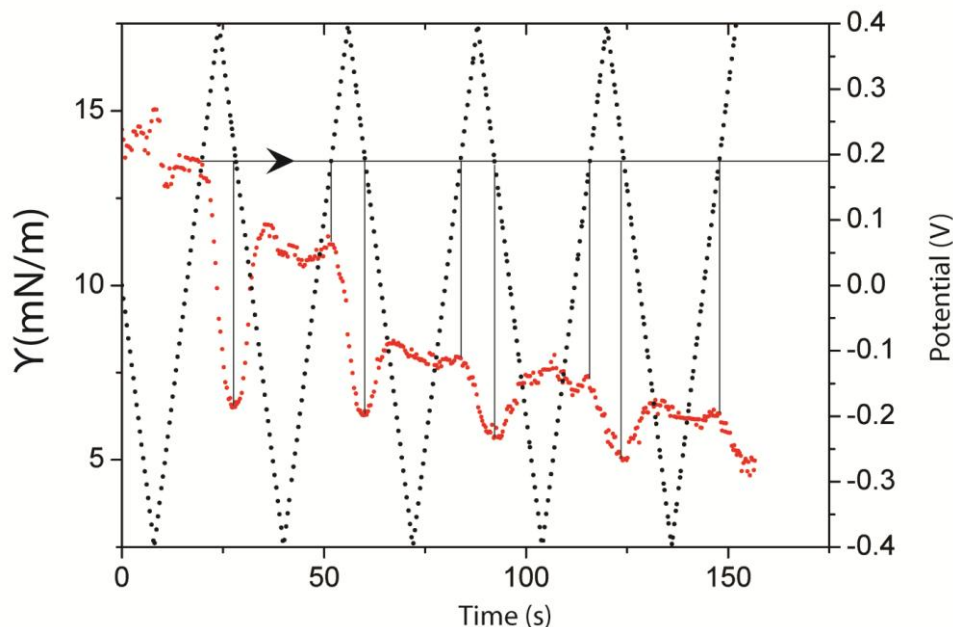


Figure 5.8 No shift in suggested adsorption and desorption potentials with increasing cycle number for lysozyme at pH 9. Cell 1 with an aqueous phase containing 1 mg/ml lysozyme and 3% (w/v) NaCl (pH 9). The charge on lysozyme at pH 9 would be zero or very close to zero. Lysozyme is shown to display 'desorption', not evident for lysozyme under similar experimental conditions at pH 3.

Since the adsorption of neutral molecules should be maximal at the point of zero charge (pzc)¹⁵, these observations suggest that the effect of protein surface charge could be significant after adsorption at the oil/water interface but not so much in bulk. This is reasonable as most of the protein charge would be screened in bulk by the electrolyte²⁰.

The adsorption cycle was seen to last over a range of positive potentials from +0.2 V to +0.4 V (Figure 5.8), which is in accordance with recent work^{11, 14}. Necessarily, a molecule possessing charge, upon adsorption to the oil/water interface should shift the pzc to either more positive or negative potentials²⁷⁻²⁸. PZC 'shifts' should be negative for the adsorption of positively charged molecules and positive for negatively charged molecules¹⁴⁻¹⁶.

5.C.3. Catalase

5.C.3.1. Catalase 0.05 mg/ml at pH 4.5 and pH 9

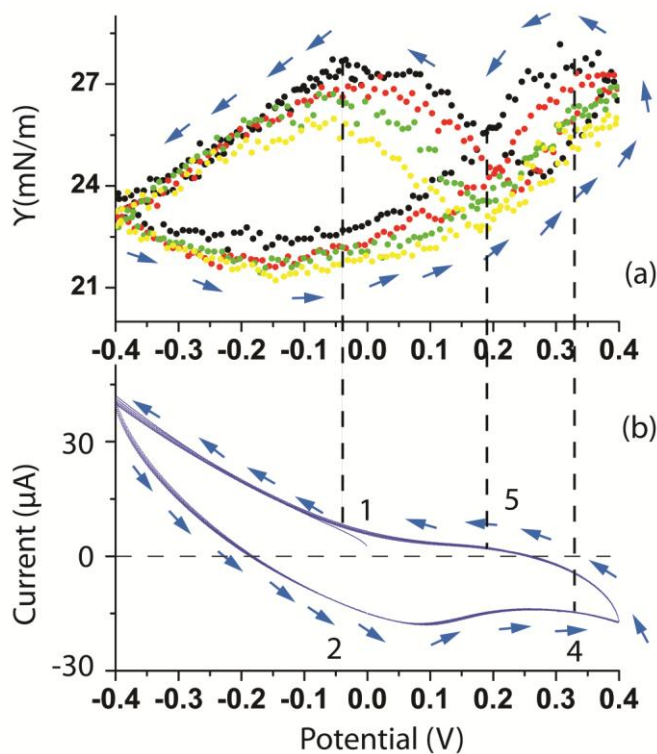


Figure 5.9 (a) Potential-dependent IFT behaviour (scan rate 50 mV s^{-1}) for an aqueous phase (Cell 1) containing 0.05 mg/ml catalase (buffered at pH 4.5). (b) correspond to CV's for (a). Various stages on the CV are numbered in sequence and are explained in further detail within the text. Blue arrows on (b) indicate the potential scan cycle, which was in a negative direction from 0 V to -0.4 V, then to +0.4V and back to negative again. Colours used in (a) indicate the cycle order which is black, red, green and then yellow (4th cycle).

At pH 4.5, catalase is positively charged (pI ca 5.4²⁹). γ values decline almost immediately (point 1) as the aqueous potential is scanned towards negative values (starting at approximately 0 V, Figure 5.9). Initial decreases in γ could be attributed to ion transfer (TBA^+ transfer from the organic to the aqueous phase) between 0 V and -0.4 V, as the magnitude of initial γ decreases are similar to that of the blank. γ values remain relatively constant, until ≈ -0.05 V, where protein desorption is postulated, such that γ values increase to a maximum at $\approx +0.3$ V (point 2 to 4). A slight decrease in γ due to TPB^- transfer between $\approx +0.3$ V and +0.4 V is evident. γ declines further between +0.4 V and $\approx +0.25$ V, until TPB^- transfer is arrested (point 5). The arrest in TPB^- transfer (point 5) results in an γ increase to approximately initial values (point 1).

Comparing the γ -potential/time cycle for this case and that for the blank (Figure 5.3) reveals a decrease and broadening in the γ value in the potential region from -0.4V to 0.2V, but slightly larger values of γ at the extreme positive potentials. Figure 5.9 reveals that TBA^+ transfer occurs over a much larger potential range than TBA^+ transfer of the blank.

The initial γ decline (point 1, Figure 5.9) was seen to tend toward more negative potentials with increasing cycle number. This behaviour is consistent with the adsorption of positively charged protein at the aqueous side of the interface. An effect which has been previously observed with charged TiO_2 particles^{14, 16}.

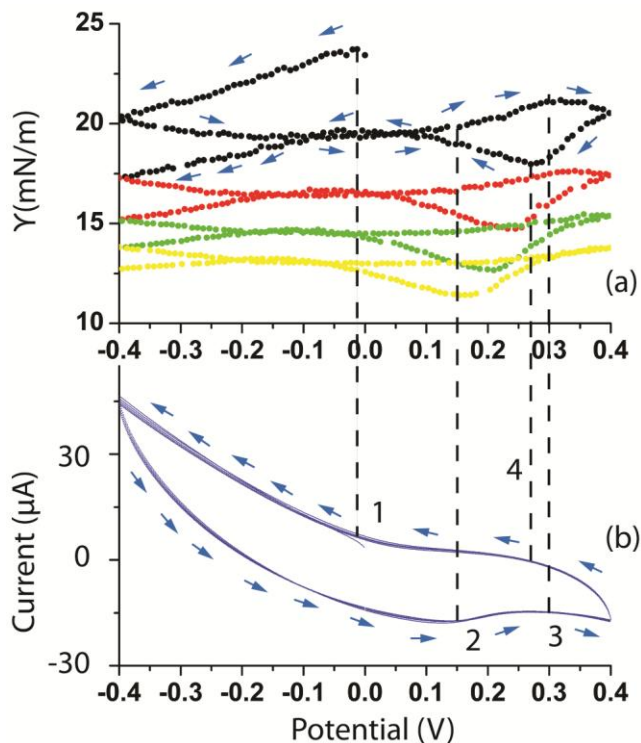


Figure 5.10 (a) Potential-dependent γ behaviour (scan rate 50 mV s^{-1}) for an aqueous phase (Cell 1) containing 0.05 mg/ml catalase (buffered at pH 9). 3(b) corresponds to CV's for 3 (a). Various stages on the CV are numbered in sequence and are explained in further detail within the text. Blue arrows indicate the potential scan cycle, which was in a negative direction from 0 V to -0.4 V, then to +0.4V and back to negative again. Colours used in (a) indicate the cycle order which is black, red, green and then yellow (4th cycle).

As observed at pH 4.5, an initial decrease in γ is evident at pH 9 (Figure 5.10) in the potential region where TBA^+ ion transfer occurs (point 1). On the reverse sweep from -0.4 V to positive aqueous phase potentials, γ values continue to decline until TBA^+ transfer halts at $\approx +0.15 \text{ V}$ (point 2), whereupon γ values increase slightly, only to decline again at $\approx +0.35 \text{ V}$ (point 3). The decline reverses on the return sweep at $\approx +0.25 \text{ V}$ (point 4, cessation of TPB^- transfer), and γ rises until a potential is reached where TBA^+ transfer recommences.

γ -potential curves on subsequent cycles exhibit similar behaviour, but increasingly lower γ values are evident. This may be due to irreversible interfacial adsorption¹¹ of this protein (as is seen in the case of lysozyme^{11, 14}). The suggested irreversibility of adsorption occurs most significantly at aqueous potentials between 0 and -0.4 V. This suggests that negatively charged catalase (at this pH) becomes (at least partially) irreversibly electroadsorbed at negative aqueous potentials.

Additionally, the potential at which TPB^- transfer from water to oil becomes arrested occurs at more negative potentials with increasing cycle number. This may possibly indicate an interaction between TPB^- and catalase (at pH 9) which has been seen previously for lysozyme and TPB^- ¹⁴.

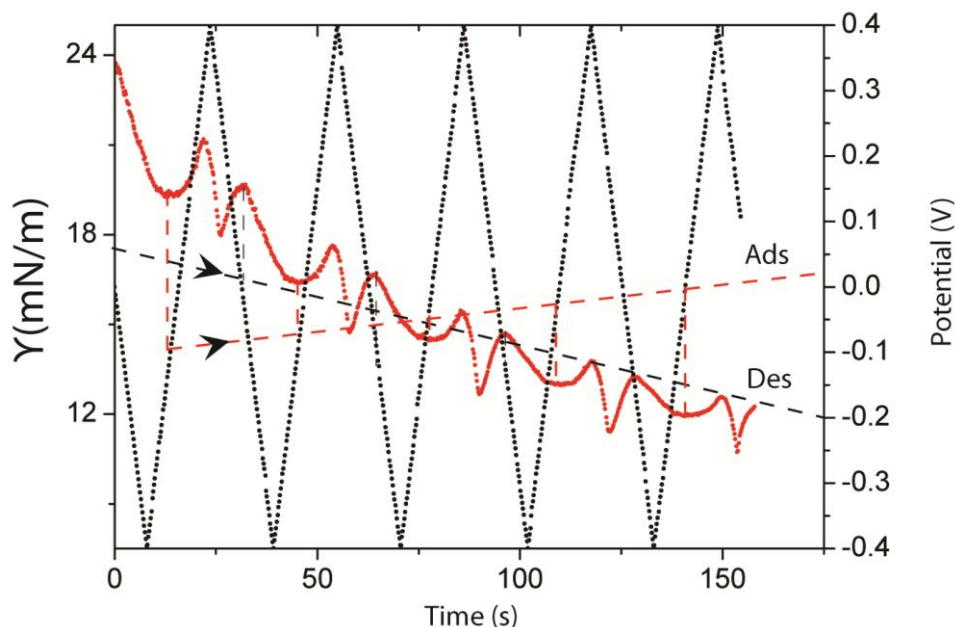


Figure 5.11 Shifts in postulated adsorption (Ads) and desorption (Des) potentials for 0.05 mg/ml catalase at pH 9. Cell 1 with an aqueous phase containing 0,05 mg/ml catalase and 3% (w/v) NaCl .

Figure 5.11 suggests that the proposed potential-dependent adsorption of catalase at pH 9 may have occurred over a range of negative potentials. A shift in the proposed adsorption potential toward more negative potentials is evident. This is in accordance with the adsorption of negatively charged protein to the oil/water interface³⁰⁻³¹. However, a decrease in 'desorption potential' with increasing cycle number was seen further suggests a possible interaction between catalase and the organic phase electrolyte (of the type seen previously for lysozyme and TPB⁻¹⁴)

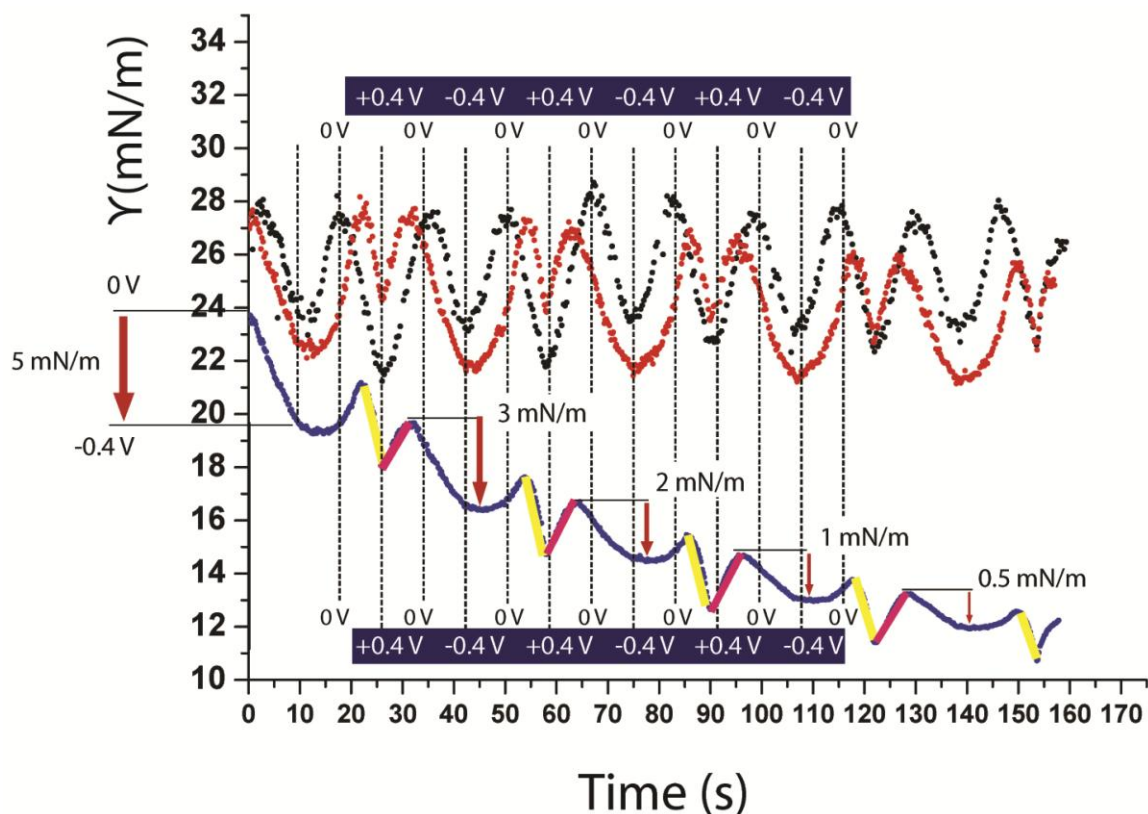


Figure 5.12 Potential/time-dependent γ characteristics for aqueous phases (Cell 1) containing: no protein (black); 0.05 mg/ml catalase at pH 4.5 (red); and 0.05 mg/ml catalase at pH 9 (blue). The data are from Figure 5.3, Figure 5.9 and Figure 5.10. Potential swept between +0.4 V and -0.4 V, initially from 0V to -0.4 V (indicated for catalase pH 9 with the red downward pointing arrows). The dotted, vertical black lines indicate particular potentials. Yellow lines and pink lines superimposed on experimental data (blue line) highlight the magnitude of the γ change for particular 'legs' of each cycle. The red arrows indicate the extent of γ decrease by virtue of protein electroadsorption at negative aqueous potentials.

Data presented in Figure 5.12 allows one an attempt at dissecting the different sections of the γ /time graph. This is an attempt to apportion various stages of the γ -behaviour to different electrochemical and adsorption processes, namely that of protein adsorption and ion transfer.

The blank (Figure 5.12) shows cyclic behaviour, with a typically parabolic shape between -0.4 V and +0.4 V, and an apex centred at approximately 0 V. Even though this curve is not an electrocapillary curve, it is in accordance with typical electrocapillary behaviour with the apex of the parabola centred on the pzc^{28, 32}.

Catalase at pH 4.5 displays general cyclic behaviour, although it is evident that some protein adsorption may have been taking place as the γ /time behaviour indicates some decline after a number of cycles (also evident in Figure 5.9).

Interestingly though, catalase at pH 4.5 appears either not adsorbed to a large extent at the interface or displays some reversibility in adsorption as very small decreases in γ are evident with increasing cycle number. This is similar to the low concentration behaviour exhibited by slightly charged (or zero-charged) lysozyme at pH 9 (Figure 5.4 and Figure 5.6),. Catalase at pH 4.5 is near to its pI and is therefore uncharged. This apparent lack of 'surface activity' (i.e. no real decrease in γ) suggests a possible increase in stability of catalase at pH 4.5 at the ITIES in comparison that exhibited at pH 9³³⁻³⁴. The lack of decrease in γ also suggests lack of protein-protein interaction of catalase at pH close to its pI³⁵⁻³⁶.

The CV in Figure 5.10 indicates that the ion transfer processes of TBA^+ and TPB^- are mostly reversible, therefore one might expect γ changes in Figure 5.12, caused by ion transfer reactions to be constant too. By referring to the blank condition (in 5.C.1), ion transfer of both TBA^+ and TPB^- result in reversible γ reductions of approximately 3-4 mN/m and 5-7 mN/m respectively. However, as more protein appears to become adsorbed (via a background process or via the applied potential), the more ion transfer reactions could become hindered¹². Thus one notes the decreasing effect of TBA^+ transfer until γ changes between 0 and -0.4 V are possibly a sole product of the suggested potential-dependent catalase adsorption/desorption (pH 9) (approximately 0.5 – 1 mN/m).

On the other hand, the potential range over which TPB^- ion transfer from oil to water takes place (yellow + pink legs) alters over time. It appears largely that as increasing amounts of protein may be adsorbed to the ITIES, the extent of γ decrease, as the aqueous potential is scanned towards +0.4 V (yellow leg) becomes smaller with cycle number. But the extent of the γ increase (pink leg) becomes larger. This indicates that for TPB^- transfer in the positive potential region there is a possible interplay between the processes of potential-dependent catalase adsorption/desorption and that of TPB^- interfacial transfer (as has been seen before for lysozyme¹⁴)

5.C.3.2. Catalase 1 mg/ml to 30 mg/ml at pH 3 and 1 mg/ml at pH 9

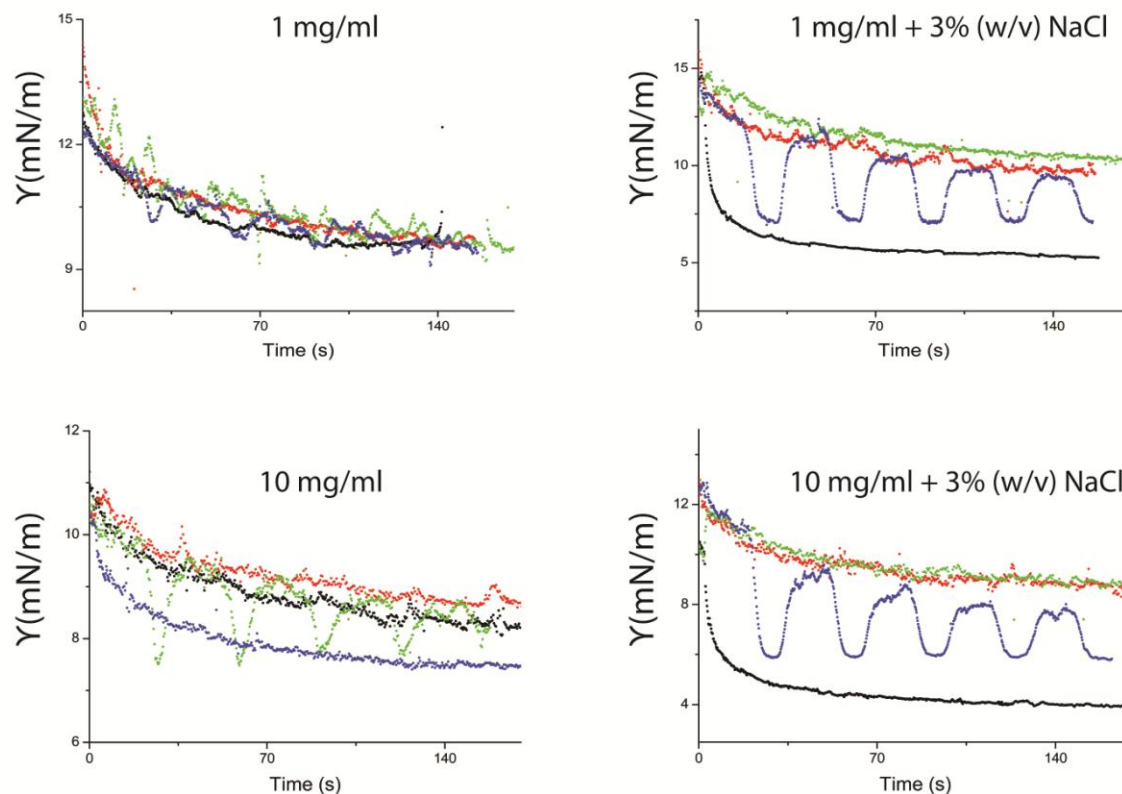


Figure 5.13 Dynamic interfacial tension data from aqueous pendant drops containing 1 and 10 mg/ml catalase with (top and bottom right panels) and without (top and bottom left panels) 3% (w/v) NaCl (pH 3). Oil phase contained 10 mM TBATPB in 1,2-DCE in all cases. Key for panels given in **Table 5-2**

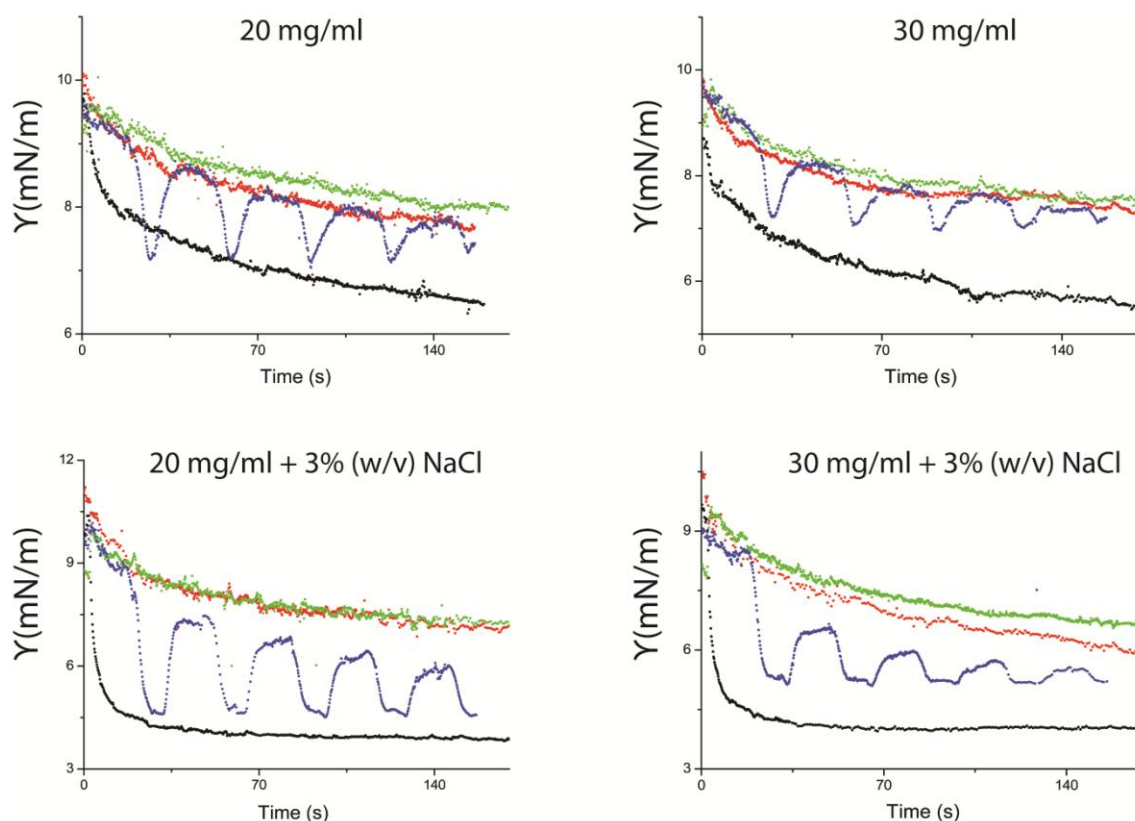


Figure 5.14 Dynamic surface tension data from aqueous pendant droplets containing 20 and 30 mg/ml catalase with (bottom panels) and without (top panels) 3% (w/v) NaCl (pH 3). Oil phase contained 10 mM TBATPB in 1,2-DCE. Key for all panels given in **Table 5-2**

Table 5-2 Key for figures Figure 5.13 and Figure 5.14

Protein	Figure	CV	OCP	" +0.2V"	" -0.2V"
Catalase	5.13 (top left)	blue	red	black	green
Catalase	5.13 (bottom left)	green	black	blue	red
Catalase	5.13 (top right)	blue	red	black	green
Catalase	5.13 (bottom right)	blue	red	black	green
Catalase	5.14	blue	red	black	green

At an increased concentration of 1 mg/ml (pH 3) (Figure 5.13, Figure 5.14 and Figure 5.15), catalase appeared responsive to the applied potential in the presence, and

in the absence of NaCl. A larger response was however seen in the presence of NaCl. It is notable that there is a difference in the adsorption characteristics for catalase under 'salt' and 'no salt' conditions. In the presence of NaCl, a 'U'-shape was seen but in the absence of NaCl a 'V'-shape was evident (Figure 5.13 and Figure 5.14).

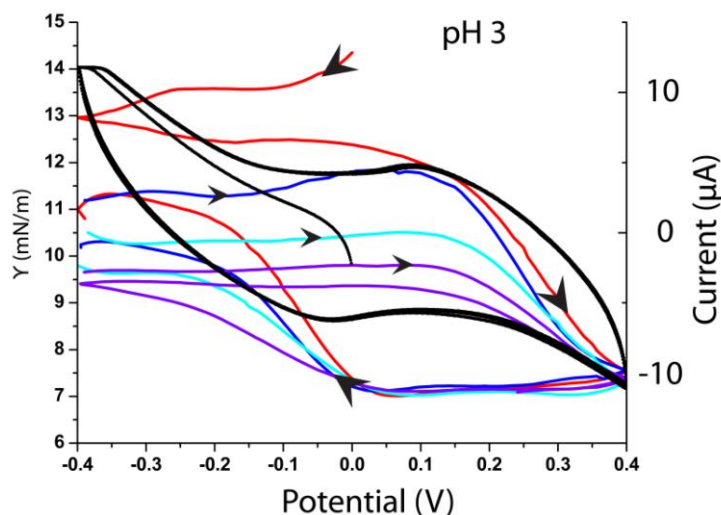


Figure 5.15 An γ /CV diagram with an aqueous phase containing 1 mg catalase and 3 % (w/v) NaCl (pH 3). The oil phase contained 10 mM TBATPB. Coloured lines indicate different potential sweep cycles with respect to the cyclic voltammogram component inherent in the diagram. The first cycle (in red), changes to the second cycle (navy blue) at -0.4V. Navy blue changes to light blue and light blue changes to magenta. Arrows indicate cycle direction. Solid black line indicates a conventional cyclic voltammogram for corresponding γ -data. Data has been smoothed using a Savitsky-Golay algorithm for clarity and is not represented by a solid fitting line.

The diagram (Figure 5.15) for catalase (1 mg/ml) at pH 3 obtained by simultaneously plotting interfacial surface tension versus applied potential and obtained currents versus applied potentials on the same graph, indicates difference in

suggested potential-dependent adsorption/desorption behaviour between positively charged catalase (Figure 5.15) and negatively charged catalase (Figure 5.17) .

The potential-dependent γ behaviour is also different between the low (0.05 mg/ml) and the high concentration conditions (1 mg/ml).

At pH 3 (Figure 5.15), the potential at which catalase (1 mg/ml) initially appears to adsorb, trends towards more negative potentials as evidenced in Figure 5.16. This behaviour is somewhat expected and concomitant with the adsorption of positively charged catalase to the oil/water interface¹⁴ . At $\approx + 0.15$ V, ion transfer (TPB⁻ from oil to water) begins, thus the reduction in interfacial tension may be due to coupled effects of both ion transfer¹⁰ and suggested potential-dependent protein adsorption.

The extent of the decrease in interfacial tension due to ion transfer alone should be approximately 3-5 mN/m (as has been seen on the blank condition), this suggests that the rest of the reduction in γ may be attributable to potential-dependent protein adsorption phenomena. γ reaches a minimum at + 0.4 V. The suggested interfacially potential-adsorbed catalase appears to remain on the interface until at approximately 0 V, at which time it appears to undergo a desorption process¹¹ , evidenced by a sudden increase in γ . The potential at which desorption appears to occur shows a shift toward more negative potentials (Figure 5.16). This behaviour would be consistent with a negatively shifted pzc by virtue of the adsorption of a positively charged protein¹⁴ to the aqueous side of the ITIES.

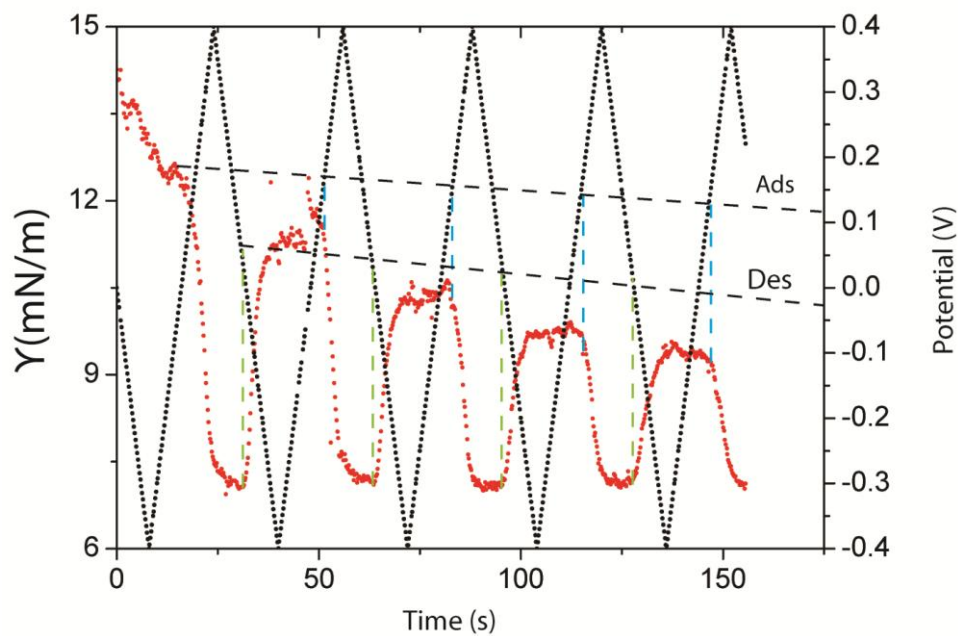


Figure 5.16 Shifts in postulated adsorption (Ads) and desorption (Des) potentials with increasing cycle number for catalase at pH 3. Cell 1 with an aqueous phase containing 1 mg/ml catalase with 3% NaCl (at pH 3). The adsorption and desorption potentials trend toward more negative potentials

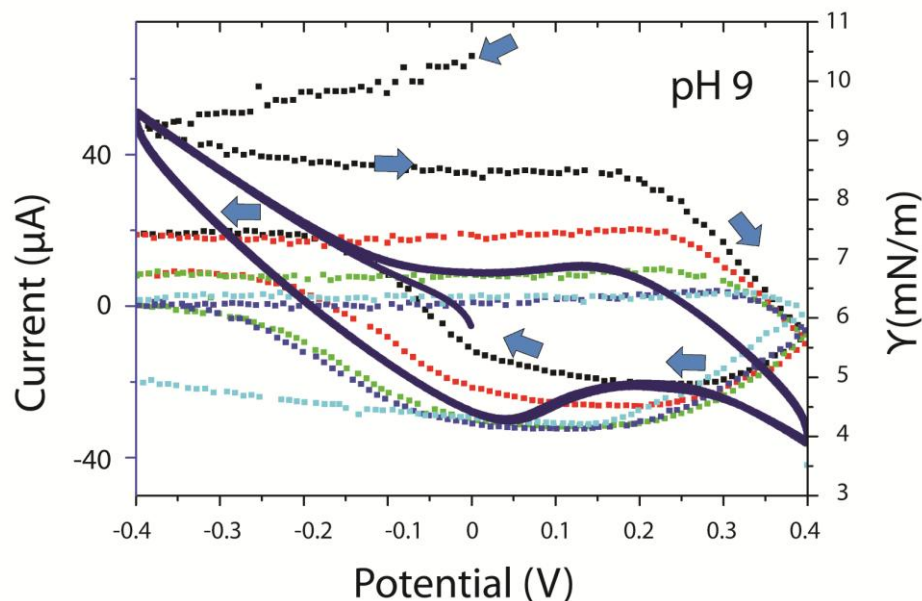


Figure 5.17 γ -potential diagram with aqueous phase containing 1 mg catalase and 3 % (w/v) NaCl (pH 9). The oil phase contained 10 mM TBATPB. Coloured lines indicate different cycles with respect to the cyclic voltammogram component inherent in the diagram. The first cycle (in black), changes to the second cycle (in red) at -0.4 V. Red changes to green, green changes to dark blue and dark blue changes to light blue. Arrows indicate cycle direction. Solid blue line indicates a conventional cyclic voltammetry curve.

At pH 9 (Figure 5.17) postulated initial catalase adsorption occurs at ≈ 0.2 V as evidenced by a rapid decrease in γ . This apparent initial adsorption trend is towards more positive potential with increasing cycle number. This behaviour suggests a positively shifted pzc with the interfacial adsorption of negatively charged protein¹⁴. The potential at which TPB^- ion transfer occurs remains largely independent on cycle number.

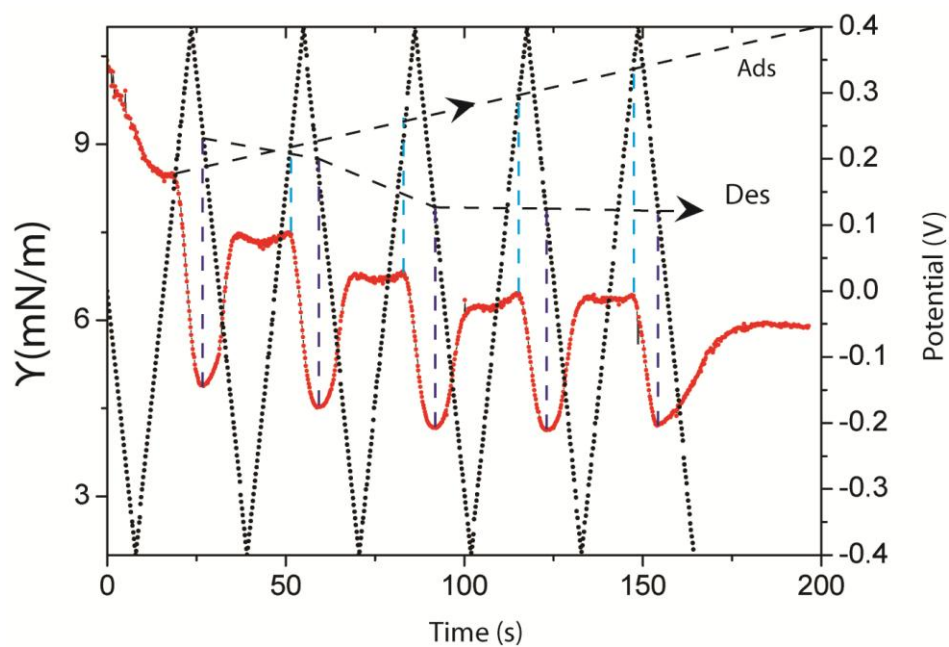


Figure 5.18 Shifts in apparent adsorption (Abs) and desorption (Des) potentials with cycle number for catalase at pH 9. Cell 1 with an aqueous phase containing 1 mg/ml catalase and 3% (w/v) NaCl. Note the opposite trending between the Ads and the Des. The Abs trends as expected from the adsorption of negatively charged protein to the interface but the Des trends opposite to that which was expected.

5.C.4. Myoglobin

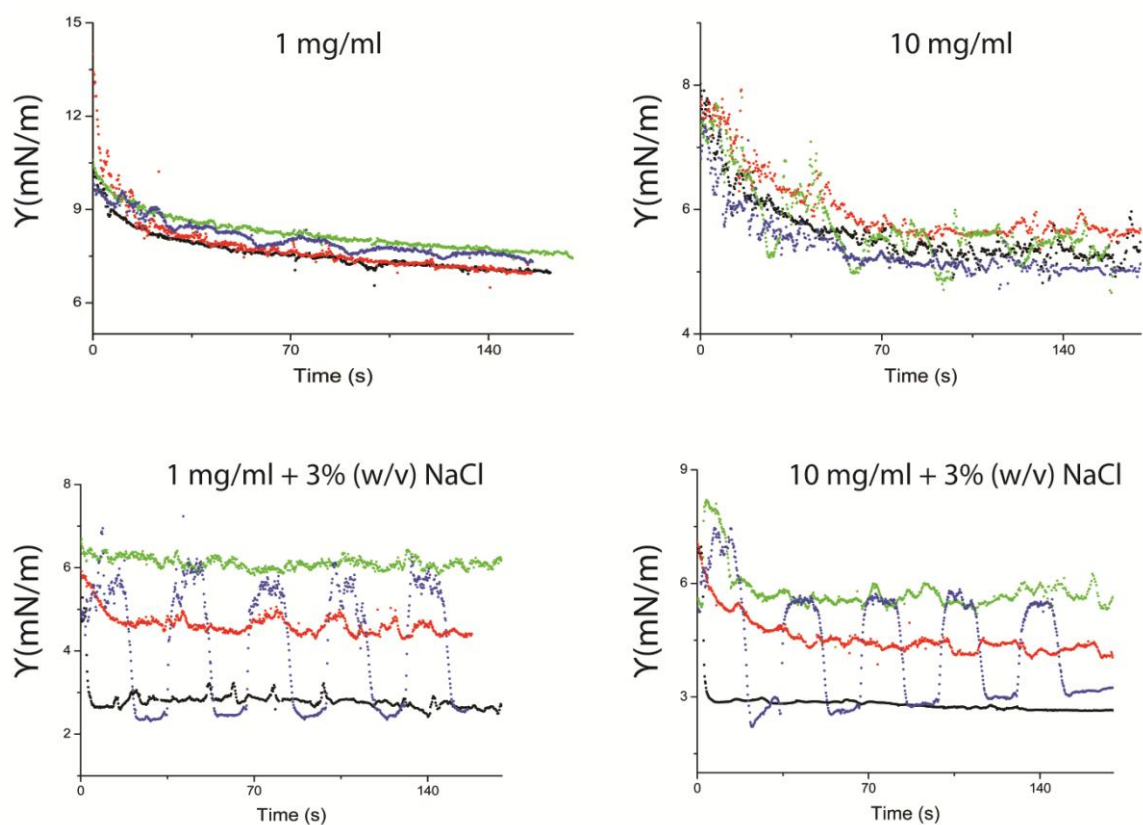


Figure 5.19 Dynamic interfacial tension data for aqueous pendant droplets containing 1 and 10 mg/ml myoglobin with (bottom panels) and without (top panels) 3% (w/v) NaCl. Oil phase contained 10 mM TBATPB in 1,2-DCE. Key for panels in **Table 5-3**.

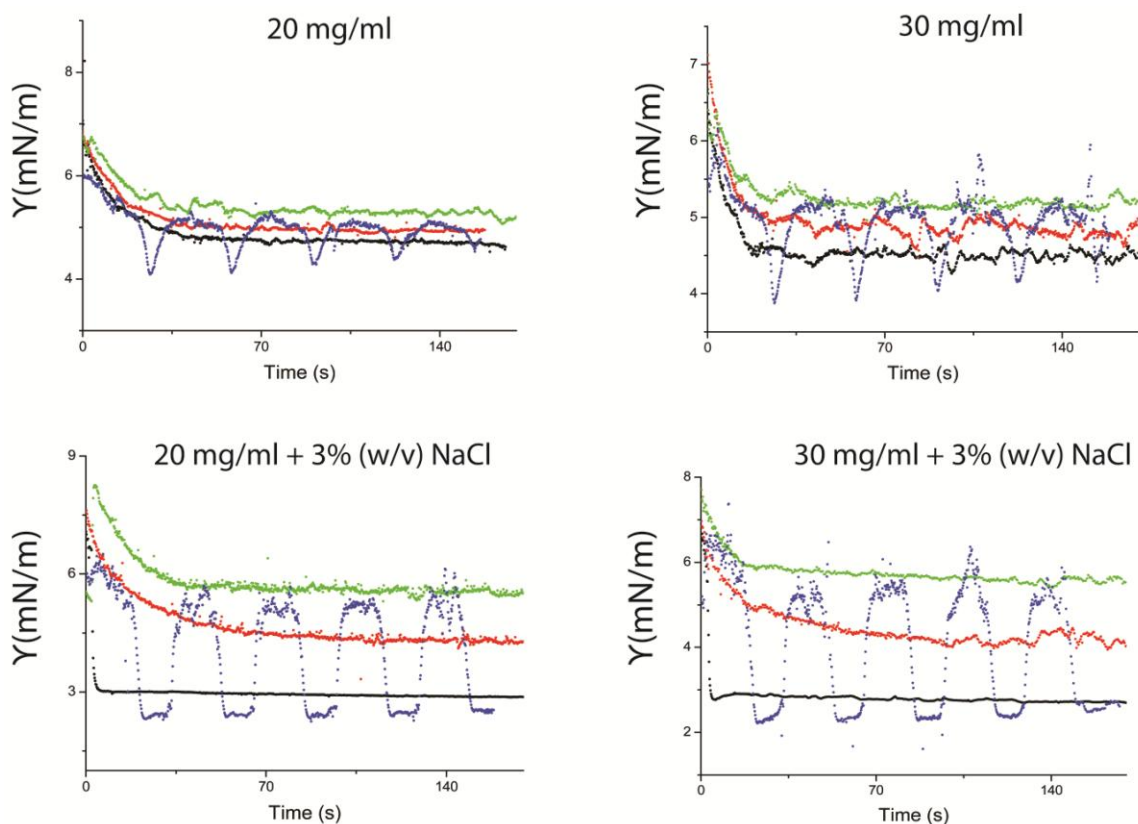


Figure 5.20 Dynamic interfacial tension data for aqueous droplets containing 20 and 30 mg/ml myoglobin with (bottom panels) and without (top panels) 3% (w/v) NaCl. Oil phase contained 10 mM TBATPB in 1,2-DCE. Key for all panels in **Table 5-3**.

Table 5-3 Key for figures **Figure 5.19** and **Figure 5.20**

Protein	Figure	CV	OCP	" $+0.2V$ "	" $-0.2V$ "
Myoglobin	5.19	blue	red	black	green
Myoglobin	5.2	blue	red	black	green

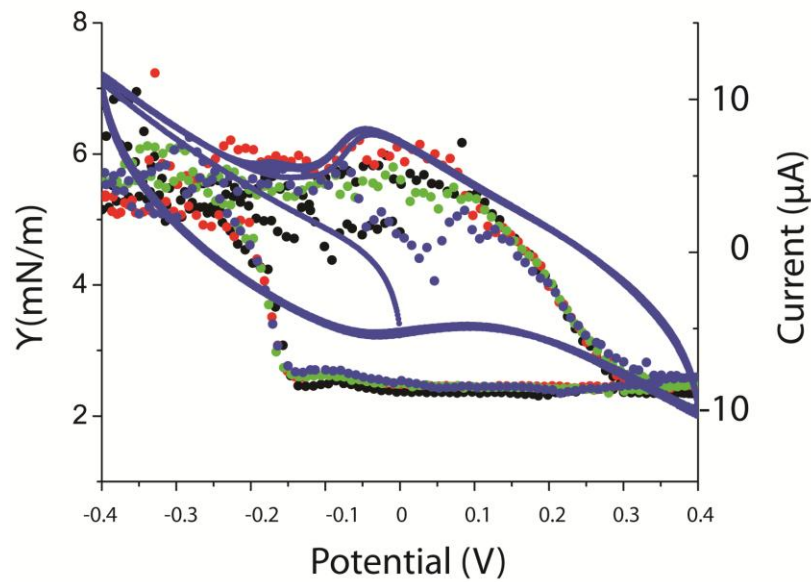


Figure 5.21 An γ /CV diagram for 1 mg myoglobin and 3% (w/v) in the aqueous phase and 10 mM TBATPB (in 1,2-dichloroethane) in the oil phase. Different coloured lines indicate different sweep segments. Due to the reversible nature of protein adsorption indicated within this figure, all segments overlap. Arrows indicate cycle direction. Solid blue line indicates a conventional cyclic voltammetry curve. 1st cycle in black, 2nd cycle in red, 3rd cycle in green and 4th cycle in blue.

Myoglobin (Figure 5.19, Figure 5.20 and Figure 5.21), appears more surface active than the other proteins, as low surface tensions are immediately achieved at protein concentrations of 1 mg/ml. It is hard to delineate processes which sought to lower γ , as γ values are immediately low.

5.C.5. Cytochrome C

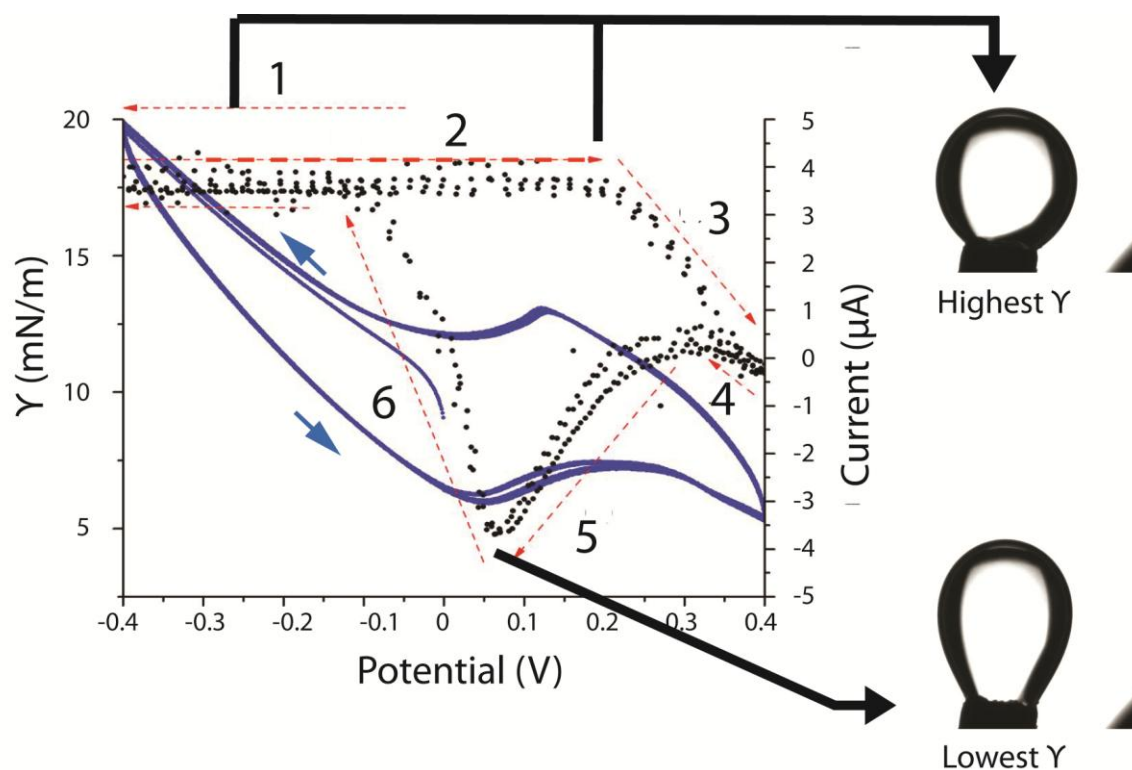


Figure 5.22 A plot of current and interfacial surface tension against applied potential for an aqueous pendant droplet containing 0.05 mg/ml cytochrome c and 3 % (w/v) NaCl at pH 3. The organic phase was 1, 2-dichloroethane. The potential was cycled between 0.4 and -0.4 V (scan rate was 50 mV/s, starting at 0V, initial direction negative).

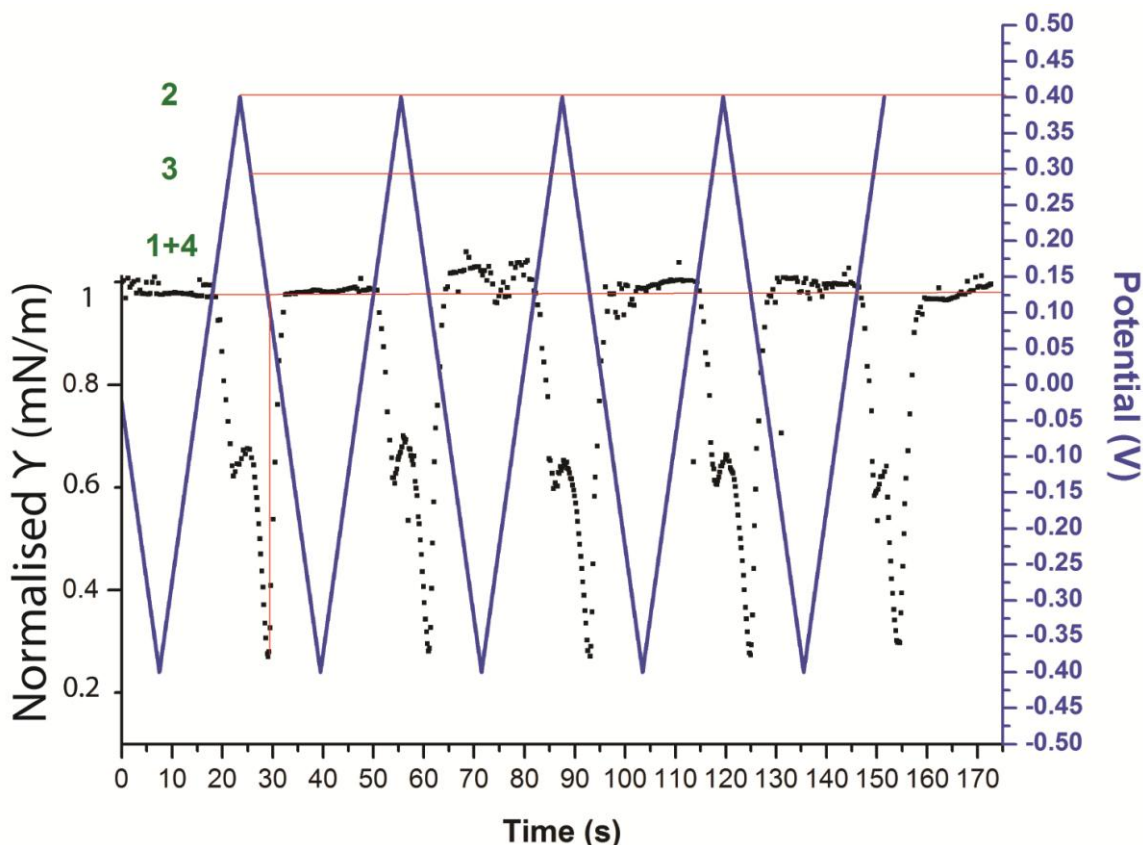


Figure 5.23 A plot of potential and normalised (against maximum) interfacial surface tension against time for an aqueous pendant droplet containing 0.05 mg/ml cytochrome c and 3 % (w/v) NaCl at pH 3.

The data is from Figure 5.22. The organic phase was 1, 2-dichloroethane. The potential was cycled between 0.4 and -0.4 V (scan rate was 50 mV/s, starting at 0V, initial scan rate negative). Conditions were the same as that represented in Figure 5.22. Numbers in green indicate different stages of potential dependent surface tension change. Red horizontal lines indicate potentials at which each stage begins. Note the lack of shift in adsorption and desorption potentials. The normalised data (γ) only extends to a value of 1.

The most striking effect was seen with Cyt-c. Figure 5.22 and Figure 5.23 demonstrates suggested electroadsorption/ desorption of positively charged Cyt-c (at pH 3) to the ITIES that is almost entirely reversible and characterised by large potential-dependent changes in γ (> 12 mN/m).

Stage 1 on Figure 5.22 indicates that γ attained a maximum value between 0 V and -0.4 V even though TBA^+ transfer occurs in this potential range (as indicated by the simultaneously recorded CV). γ does not decrease until ≈ 0.12 V (Cycle 1, Figure 5.23. End of stage 2, into stage 3 on Figure 5.22) which corresponds to the onset of TPB^- transfer.

As is also seen with catalase, γ values continue to decline on the reverse sweep (TPB^- transfer also occurs), resulting in a particularly large decline from ≈ 0.3 V (Figure 5.23, and Figure 5.22, stage 3). Suggesting that both protein adsorption and ion transfer occur in this potential region causing the large decrease in γ during segments 3,4 and 5, which are only slightly arrested during the brief period at the end of stage 4. The steep decrease in γ during stage 5 suggests the significant build up of material, initially formed during segment 3. Nonetheless, the decrease in γ halts and switches at $\approx +50$ mV, attributed to Cyt-c desorption, and maximum γ values are recovered at ≈ -0.1 V during segment 6. The cycle begins again almost reversibly.

We noticed some deterioration in reversibility but only after about 10 cycles, which was accompanied by precipitation at the ITIES. This is further diagnostic of a significant accumulation of material at the interface during potential cycling which may be responsible for the rapid and dramatic shifts in IFT. It is notable that Cyt-c is a known facilitator of TPB^- transfer³⁷, and an interaction between Cyt-c and TPB^- ³⁸ is likely to play an important role in the dramatic γ behaviour observed.

5.C.6. Dodecylbenzenesulfonic acid sodium salt

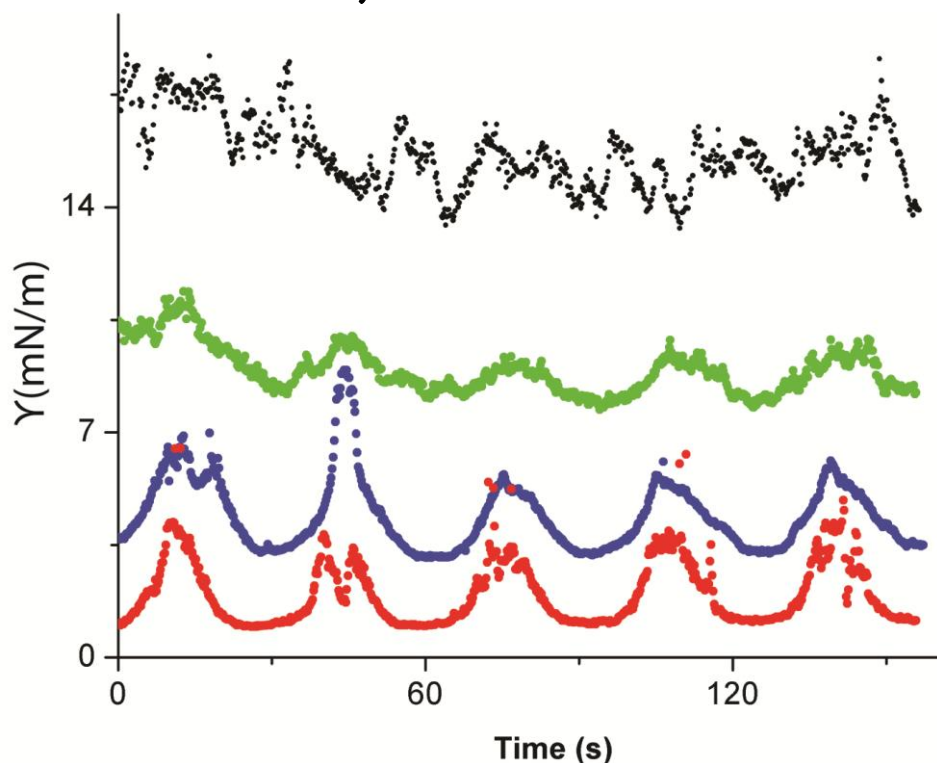


Figure 5.24 Interfacial surface tension data with aqueous phase containing 20 mM LiCl and 0.125 mM (black), 0.25 mM (green), 0.5 mM (blue) and 1 mM (red) dodecylbenzenesulfonic acid sodium salt. Oil phase contained 10 mM TBATPB in 1,2-DCE. Potential was cycled between 0.4 and -0.4 V at 50 mV/s. Initial scan was negative. Anionic surfactant. The pH of solution was approximately 6.5.

Sodium dodecylbenzenesulfonate (SDBS) (Figure 5.24) is an anionic surfactant with a CMC of 963 mg/ml³⁹. The concentrations used herein are below the CMC, but that is not to say some micellization may occur by virtue of potential-induced adsorption or surface excess.

We would consider small changes in surface tension, or droplet geometry, between ‘highs’ and ‘lows’ as an undesirable component within an electrowetting system, despite the fact that both surfactant molecules trialled herein display

considerable surface activity in their own right. In contrast to previous studies⁹, which have suggested the use of surfactant molecules with low dipole moment to enhance electrowetting systems, we have shown herein that high dipole moment molecules (such as proteins) are very effective too.

5.C.7. Gold nanoparticles

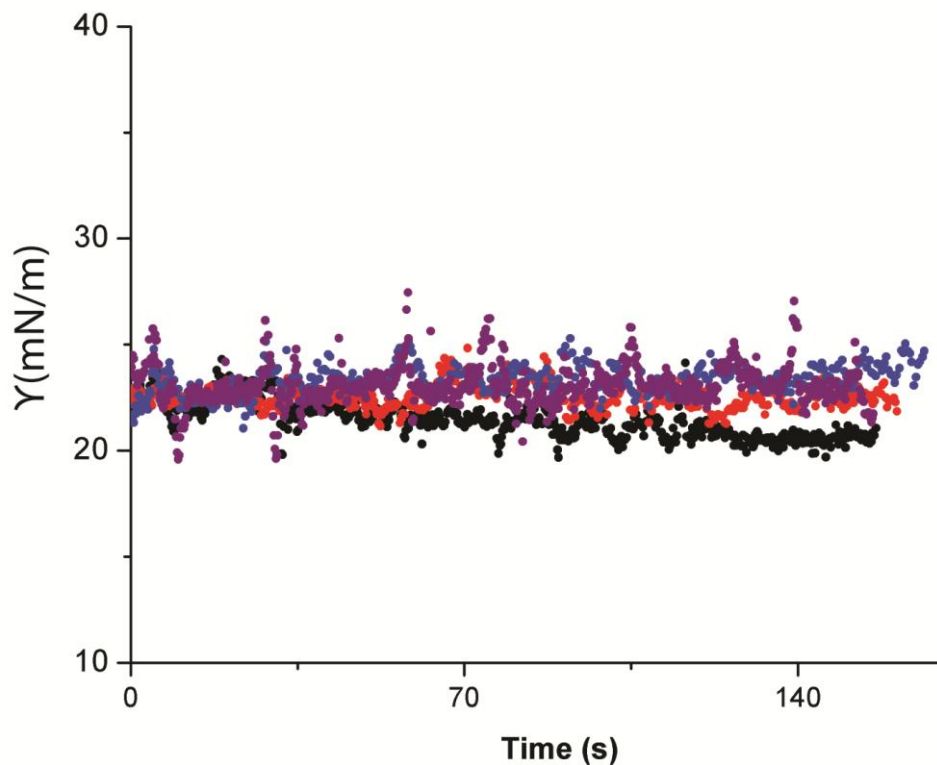


Figure 5.25 Gold nanoparticles in 20 mM LiCl (aqueous phase). The oil phase consisted of 10 mM TBATPB in 1,2-dichloroethane in all cases. Purple = gold full (no dilution), blue= 0.5, red= 0.25, black = 0.125 (0.875 water + 0.125 gold stock). Potential was cycled between 0.8 and -0.8V at 50 mV/s. Initial scan direction was negative.

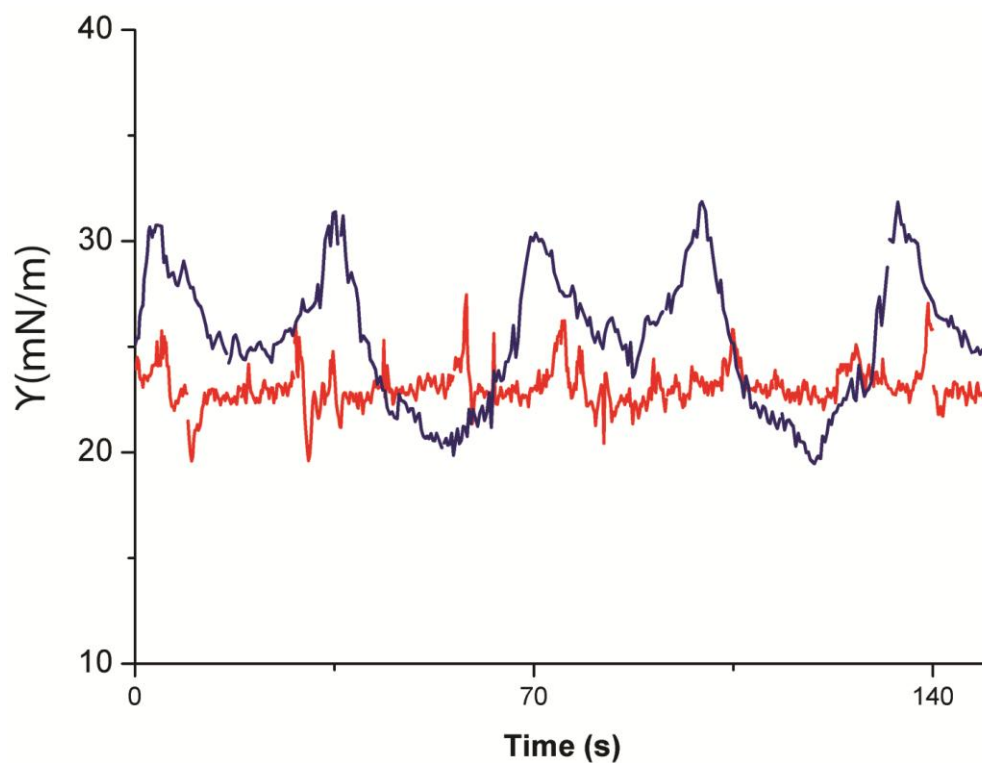


Figure 5.26 Gold nanoparticles (no dilution) with no salt (except 20 mM LiCl-red) and gold nanoparticles with salt (960 mM NaCl-blue). Potential was scanned between 0.8 and -0.8 V at 50 mV/s. Initial scan direction negative from 0V.

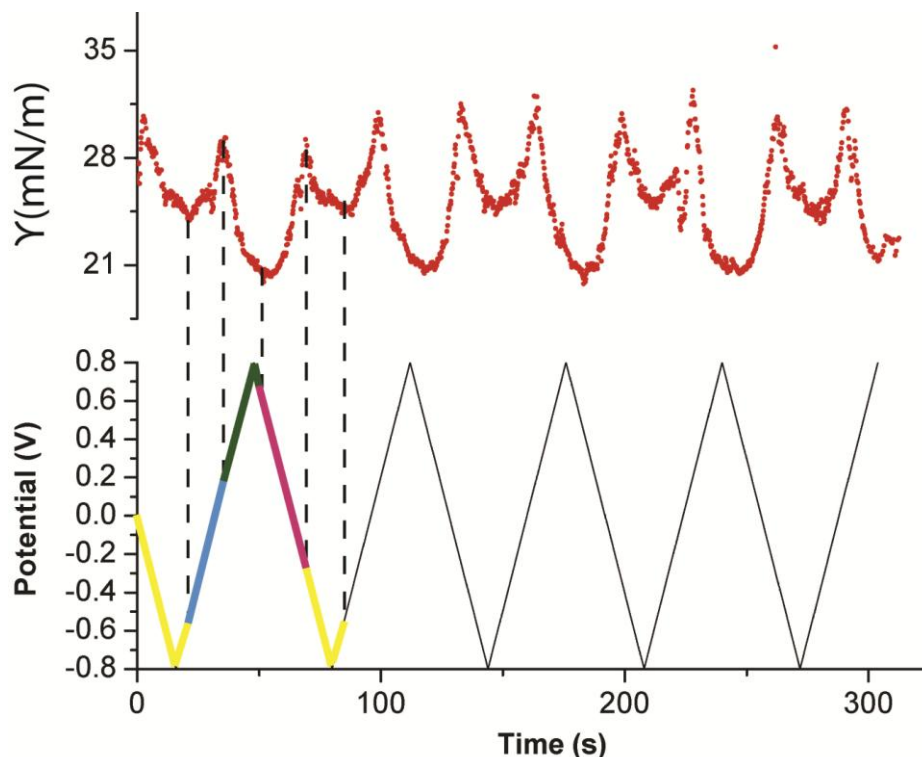


Figure 5.27 Potential-dependent adsorption of gold nanoparticles (no dilution) and 960 mM NaCl. Potential sweep between -0.8 and 0.8V at 50 mV/s . The initial scan was negative from 0V. Different stages of the reversible adsorption process are featured as coloured lines on the potential versus time curve. Yellow line indicates a decrease in surface tension, accumulation of nanoparticles⁴⁰ and ion transfer¹⁰ (-0.2 V to -0.8 V), blue line and pink line indicates an area within and either side of the potential window which sees a return to γ values at ca. $t=0^{10}$, green line indicates positive potential nanoparticle accumulation and ion transfer¹⁰.

Gold nanoparticles (Figure 5.25, Figure 5.26 and Figure 5.27) used herein are in the size range of 8-12 nm in diameter and possess negative charge (manufacturers material sheet, see experimental). There is little change between ‘highs’ and ‘lows’ in interfacial tension, in comparison to say Cyt-c (Figure 5.25 and Figure 5.26) between -0.4 V and 0.4 V. However, large potential-dependent γ changes are realised at much higher potentials (-0.8 V to 0.8 V), which are in the range of almost 10 mN/m.

The nanoparticles did however appear to possess some potential-dependent reversible adsorption, very much in accordance with previous work⁴¹⁻⁴². Previous

work⁴¹ also noted that an increase in Au particle density occurs at negative potentials with a concomitant decrease in surface tension, which was consistent with results reported here.

Considering this, one may say that an increase in nanoparticle density also took place at high positive potentials as the surface tension is in decline here too (Figure 5.27). However, the effects of charge transfer¹⁰ on the surface tension at high positive and negative potentials (+0.8V and -0.8V) may be considerable and of a similar magnitude seen herein (with other molecules). One therefore cannot ignore the effects of ion transfer in this case. Despite the potential-dependent reversibility of adsorption of the gold nanoparticles noted here and elsewhere^{41, 43-44}, surface activity upon interfacial adsorption was extremely low and therefore gold nanoparticles are not desirable for use as ‘electrowetting particles’ without surface functionalization.

Table 5-4 Summary of main physical properties of proteins used within this chapter

Protein	No. of AA⁴⁵	MW⁴⁵	PI⁴⁵	Instability index⁴⁵	Aliphatic Index⁴⁵	Dipole Moment⁴⁶	Quad. Moment⁴⁶	R⁴⁶	PDB Code
Lysozyme	129	14313	9.3	16.09	65.02	212	1137	166	liee
Myoglobin	154	17082	7.2	10.11	88.77	339	657	176	1wla
Catalase	527	59915	6.8	26.32	67.72	63	10140	1508	1tgu
Cytochrome c	105	11832	9.6	15.51	58.57	252	1217	132	1giw ¹

¹ No. of AA = number of amino acids, MW = molecular weight in Daltons, PI is theoretical isoelectric point, Instability index and aliphatic index from (ref. in table), overall dipole moments, quadrapole moments (in Debyes) and R= means radius of protein from web based server by Felder and co-workers(as referenced Table 5-4).

We have introduced a number of different particles and molecules for possible use within ITIES-based electrowetting systems and the results are interesting from a number of different perspectives, which include traditional electrocapillary studies and potential-dependent protein adsorption studies at liquid-liquid interfaces¹¹, for example

Cyt-c was found to be the 'best performing' particle, mostly due to the apparent reversibility of its suggested potential-dependent adsorption/desorption characteristics at the DCE/water interface. Although, it should be remembered that what appears to be favourable potential-dependent adsorption/desorption behaviour demonstrated by Cyt-c may be linked in addition to other processes, such as a possible interaction between the anion of the organic phase electrolyte and Cyt-c, of the type previously seen for lysozyme¹⁴ and TPB⁻.

Cyt-c is a protein and we have shown that not all proteins can be used for this purpose, as some experiments appear to show that some proteins are adsorbed in an irreversible manner (in a potential-dependent way) to the oil-water interface. Moreover, we have also shown in Chapter 3, that proteins can possess different interfacial behaviours at different oil/water interfaces^{17, 47} and have suggested that some proteins may also be denatured at some oil/water interfaces but not at others.

We have also demonstrated that the use of a conventional surfactant as ‘electrowetting enhancers’ may be undesirable as these surfactants possessed very high surface activity, but no apparent potential-dependent reversibility of adsorption. The reversibility of ‘surfactant’ adsorption seems to be a key attribute in this regard, as it is clear that one may use a plethora of molecules to lower interfacial tension but only a handful may be reversibly adsorbed via the application of potential, and hence will be useful for their ‘electrowetting’ abilities.

Low dipole moment surfactant molecules (such as those trialled herein) have been previously suggested for use within electrowetting systems⁹, as these molecules were considered to be less deleterious to the ‘electrowetting field’. We have, however, shown that this notion may be misleading and that the use of surfactant molecules, such as proteins, which possess high dipole moment may also be effectively used to possibly lower driving voltages. We are unsure about the origin of this discrepancy.

As ‘natural surfactants’, proteins possess both hydrophobic and hydrophilic patches on their solvent accessible surface areas⁴⁸. When adsorbed to the ITIES the surface tension is lowered by varying amounts depending on the concentration of protein, the nature of the protein and the nature of the oil/water interface to which the protein adsorbs (Chapter 3)²². Some of the apparent potential-dependent reversibility of Cyt-c may be due to the well known hydrophilicity of this protein, coupled with the fact that this protein may be stable at the water/DCE interface (it seems able to undergo electron-transfer reasonably well at such interfaces⁴⁹). In other words, we suggest that Cyt-c may not be easily wetted by the oil phase, and hence the energy required to detach such a protein may be greatly reduced in comparison to a ‘wetted’ particle.

. A major limitation of this study was the fact that relatively high protein concentrations were used. This, in some cases, may have given the impression that changes in γ were mostly due to standard ion-transfer processes superimposed on a background of slow protein adsorption. Potential-dependent adsorption and desorption of lysozyme from oil- water interfaces has been recently demonstrated¹¹. We would argue that in this study we have also convincingly demonstrated the potential-dependent adsorption/desorption of cytochrome-c at the oil-water interface. It is therefore entirely reasonable to assume that these potential-dependent adsorption/desorption processes can occur for other proteins systems such as those featured herein (myoglobin and for example, Table 5-4).

As this presents a 'new area' for future investigation, future experiments should be conducted using vastly reduced protein concentration. This is to enable the effects of various processes on γ to be more clearly seen.

Because of the relatively large interfacial surface areas used within this Chapter, cyclic voltammograms were distorted somewhat by large resistances and charging currents⁵⁵. The voltammetry presented herein did not have the benefit of IR compensation and thus quoted potentials will undoubtedly be influenced by ohmic effects.

Light scattering techniques in conjunction with 4-electrode potentiostats (with IR compensation) of the type used by Su and co-workers⁴¹ would be useful here as small interfacial areas could be used in conjunction with the light scattering which would allow the accurate measurement of current, voltage and interfacial tension simultaneously without distortion and error due resistance/capacitance.

This coupled with experiments conducted with low protein concentration should prove interesting work for future study.

One may now perhaps envisage the use of ‘manufactured’ synthetic nanoparticles which possess ‘electrowetting’ characteristics much akin to that exhibited by Cyt-c, but without the problem of deterioration after a low number of reversible cycles. Most certainly, one could begin to consider synthetic nanoparticles within the size range of 10-20 nm minimum (the approximate diameter of Cyt-c). However, as we have shown with gold nanoparticles, these ‘manufactured’ particles should possess considerable surface activity for potential-dependent reversible adsorption behaviour at low potential to become useful. Additionally, most inorganic nanoparticles would possibly be stable at the ITIES, in other words, not become ‘denatured’⁵⁶ as proteins do.

The use of irregularly shaped, amphiphilic, Janus-type nanoparticles are therefore suggested and should be a topic for future research. Another possible avenue for future research may be the functionalization of conventional metallic nanoparticles with synthetic amino acid sequences.

5.D References

1. S. A. Morton, D. J. Keffer, R. M. Counce and D. W. DePaoli, *Langmuir*, 2005, **21**, 1758-1765.
2. F. Mugele, *Soft Matter*, 2009, **5**, 3377-3384.
3. S. Berry, J. Kedzierski and B. Abedian, *J. Colloid Interface Sci.*, 2006, **303**, 517-524.
4. H. H. Girault, *Nat. Mater.*, 2006, **5**, 851-852.
5. C. W. Monroe, M. Urbakh and A. A. Kornyshev, *J. Electrochem. Soc.*, 2009, **156**, P21-P28.
6. C. W. Monroe and et al., *J. Phys.: Condens. Matter*, 2007, **19**, 375113.
7. C. W. Monroe, L. I. Daikhin, M. Urbakh and A. A. Kornyshev, *Phys. Rev. Lett.*, 2006, **97**, 136102.
8. O. Raccurt and et al., *Journal of Micromechanics and Microengineering*, 2007, **17**, 2217.
9. T. Roques-Carmes, A. Gigante, J.-M. Commenge and S. Corbel, *Langmuir*, 2009, **25**, 12771-12779.
10. S. E. C. Dale and P. R. Unwin, *Electrochem. Commun.*, 2008, **10**, 723-726.
11. E. Alvarez de Eulate and D. W. M. Arrigan, *Anal. Chem.*, 2012.
12. P. Vanysek, ed., *Electrochemistry on Liquid/Liquid Interfaces*, Springer-Verlag, Berlin, Germany, 1985.
13. D. J. Clarke, D. J. Schiffrin and M. C. Wiles, *Electrochim. Acta*, 1989, **34**, 767-769.
14. R. A. Hartvig, M. A. Méndez, M. v. d. Weert, L. Jorgensen, J. Østergaard, H. H. Girault and H. Jensen, *Anal. Chem.*, 2010, **82**, 7699-7705.
15. R. G. Barradas, P. G. Hamilton and B. E. Conway, *The Journal of Physical Chemistry*, 1965, **69**, 3411-3417.
16. H. Jensen, D. J. Fermin, J. E. Moser and H. H. Girault, *J. Phys. Chem. B*, 2002, **106**, 10908-10914.
17. T. Sengupta and S. Damodaran, *J. Colloid Interface Sci.*, 1998, **206**, 407-415.
18. J. T. Chin, S. L. Wheeler and A. M. Klibanov, *Biotechnol. Bioeng.*, 1994, **44**, 140-145.
19. T. Sengupta, L. Razumovsky and S. Damodaran, *Langmuir*, 1999, **15**, 6991-7001.
20. E. J. F. Dickinson, J. G. Limon-Petersen, N. V. Rees and R. G. Compton, *The Journal of Physical Chemistry C*, 2009, **113**, 11157-11171.

21. V. Le Brun, W. Friess, T. Schultz-Fademrecht, S. Muehlau and P. Garidel, *Biotechnol. J.*, 2009, **4**, 1305-1319.
22. É. Kiss and R. Borbás, *Colloids Surf., B*, 2003, **31**, 169-176.
23. M. A. Bos and T. van Vliet, *Adv. Colloid Interface Sci.*, 2001, **91**, 437-471.
24. E. M. Freer, K. S. Yim, G. G. Fuller and C. J. Radke, *The Journal of Physical Chemistry B*, 2004, **108**, 3835-3844.
25. P. A. Wierenga, H. Kusters, M. R. Egmond, A. G. J. Voragen and H. H. J. de Jongh, *Adv. Colloid Interface Sci.*, 2006, **119**, 131-139.
26. S. G. Baldursdottir, M. S. Fullerton, S. H. Nielsen and L. Jorgensen, *Colloids and Surfaces B: Biointerfaces*, 2010, **79**, 41-46.
27. A. Watanabe, M. Matsumoto, H. Tamai and R. Gotoh, *Colloid Polym. Sci.*, 1967, **220**, 152-159.
28. V. S. Markin and A. G. Volkov, *Electrochim. Acta*, 1990, **35**, 715-724.
29. T. Samejima, M. Kamata and K. Shibata, *J. Biochem. (Tokyo)*, 1962, **51**, 181-187.
30. D. J. Fermin, H. Jensen, J. E. Moser and H. H. Girault, *ChemPhysChem*, 2003, **4**, 85-89.
31. D. J. Fermín, H. Jensen, J. E. Moser and H. H. Girault, *ChemPhysChem*, 2003, **4**, 85-89.
32. A. Watanabe, M. Matsumoto, R. Gotoh and H. Tamai, *Colloid Polym. Sci.*, 1967, **221**, 47-52.
33. J. R. Lu, T. J. Su, P. N. Thirtle, R. K. Thomas, A. R. Rennie and R. Cubitt, *J. Colloid Interface Sci.*, 1998, **206**, 212-223.
34. C. Postel, O. Abillon and B. Desbat, *J. Colloid Interface Sci.*, 2003, **266**, 74-81.
35. T. Lefèvre and M. Subirade, *J. Colloid Interface Sci.*, 2003, **263**, 59-67.
36. M. van der Veen, W. Norde and M. C. Stuart, *Colloids and Surfaces B: Biointerfaces*, 2004, **35**, 33-40.
37. M. Shinshi, T. Sugihara, T. Osakai and M. Goto, *Langmuir*, 2006, **22**, 5937-5944.
38. G. Herzog, V. Kam and D. W. M. Arrigan, *Electrochim. Acta*, 2008, **53**, 7204-7209.
39. K. Yang, L. Zhu and B. Xing, *Environ. Pollut.*, 2007, **145**, 571-576.
40. B. Su, J.-P. Abid, D. J. Fermín, H. H. Girault, H. Hoffmannová, P. Krtíl and Z. Samec, *J. Am. Chem. Soc.*, 2003, **126**, 915-919.
41. B. Su, J.-P. Abid, D. J. Fermín, H. H. Girault, H. Hoffmannová, P. Krtíl and Z. Samec, *J. Am. Chem. Soc.*, 2003, **126**, 915-919.
42. J.-P. Abid, M. Abid, C. Bauer, H. H. Girault and P.-F. Brevet, *The Journal of Physical Chemistry C*, 2007, **111**, 8849-8855.
43. B. Su, J.-P. Abid, D. J. Fermín, H. H. Girault, H. Hoffmannová, P. Krtíl and Z. Samec, *J. Am. Chem. Soc.*, 2004, **126**, 915-919.

44. N. Younan, M. Hojeij, L. Ribeaucourt and H. H. Girault, *Electrochem. Commun.*, 2010, **12**, 912-915.
45. E. Gasteiger, C. Hoogland, A. Gattiker, S. Duvaud, M. R. Wilkins, R. D. Appel and A. Bairoch, in *The Proteomics Protocols Handbook*, Humana Press, ed. J. M. Walker, Humana Press., 2005, pp. 571-607.
46. C. E. Felder, J. Prilusky, I. Silman and J. L. Sussman, *Nucl. Acids Res.*, 2007, **35**, W512-521.
47. T. Sengupta and S. Damodaran, *Langmuir*, 1998, **14**, 6457-6469.
48. B. Halle, *Philosophical Transactions of the Royal Society of London. Series B: Biological Sciences*, 2004, **359**, 1207-1224.
49. G. C. Lillie, S. M. Holmes and R. A. W. Dryfe, *The Journal of Physical Chemistry B*, 2002, **106**, 12101-12103.
50. T. Asakura, K. Adachi and E. Schwartz, *J. Biol. Chem.*, 1978, **253**, 6423-6425.
51. L. A. S. Gorman and J. S. Dordick, *Biotechnol. Bioeng.*, 1992, **39**, 392-397.
52. M. C. Parker, B. D. Moore and A. J. Blacker, *Biotechnol. Bioeng.*, 1995, **46**, 452-458.
53. E. Liepinsh and G. Otting, *Nat Biotech*, 1997, **15**, 264-268.
54. C. Mattos and D. Ringe, *Curr. Opin. Struct. Biol.*, 2001, **11**, 761-764.
55. Y. Shao and M. V. Mirkin, *J. Am. Chem. Soc.*, 1997, **119**, 8103-8104.
56. D. E. Graham and M. C. Phillips, *J. Colloid Interface Sci.*, 1979, **70**, 427-439.

6. The rapid crystallization of tetrabutylammonium tetraphenylborate (TBATPB) at the ITIES.

The rapid crystallization of TBATPB at the ITIES is reported. Results suggest that the nucleation of TBATPB crystals may be heterogeneous in nature and may be initiated by the formation of a water insoluble interfacial ion-pair. This work is of importance to theory and experiment regarding ion transfer mechanisms at the ITIES. Additionally, this work may point towards a new type of crystallization technology grounded in methodologies developed for liquid/liquid electrochemistry.

6.A Introduction

It has been known for some time that by passing high currents through the oil/water interface of some conductive biphasic systems, an interfacial “precipitate” would sometimes be observed¹⁻⁵. It was also reported that the precipitate was accompanied by a concomitant reduction in the usable width of the polarisable potential window³⁻⁴ of the ITIES. Reductions in the width of the potential window were reported as being a product of ion-pair formation between the anion of the organic phase (particularly tetraphenylborate (TPB^-)) and the aqueous phase cation. The formation of the ion-pair lowered the formal ion transfer potential of a variety of monovalent cations (such as K^+ , Rb^+ and H^+ for example)^{1,6}.

Herein, we show that by using simple two electrode liquid/liquid electrochemical cells, the rapid crystallization of an organic phase electrolyte (TBATPB) was initiated via ion transfer, probable ion association and probable formation of an insoluble ion-pair at the ITIES. The results have wide ranging implications for theory and experiment regarding ion transfer mechanisms at the ITIES. In addition, this crystallization mechanism points toward a new type of crystallization technology based upon methodologies developed for liquid/liquid electrochemistry.

6.B Experimental

All ITIES-based experiments employed a CHI 800b potentiostat (CHI instruments)

The following two-electrode cells (Cell 1 and Cell 2 *vide infra*) were used throughout, and all potentials quoted are that of the aqueous phase electrode with respect to the oil phase electrode.

Cell 1:



where ‘x’ M refers to the molarity of KCl in the aqueous phase, typically between 22 mM and 0.8 M. ‘y’ refers to the molarity of TBATPB (86897, Sigma-Aldrich) in the organic phase, typically between 0.1 mM and 50 mM. Actual concentrations are indicated within the text. AgTPB electrodes were prepared in accordance with previous work ⁷.

Two types of experimental arrangement were used in conjunction with Cell 1. Interfacial crystal growth was monitored (*in-situ*) using a Krüss DSA 100 drop shape analysis system (as in previous Chapters), which allowed low magnification optical microscopy of oil/water interfaces produced by extruding small pendant droplets containing aqueous phase into a reservoir containing a conductive organic phase (DCE). The second arrangement comprised a micro-ITIES formed at the tip of a silanized micropipette (53 μm in inner diameter) containing aqueous solution in contact with the organic phase. Micro-pipette manufacture and subsequent silanization procedures were the same as described elsewhere ⁸.

Cell 2:

Due to the use of concentrated NH_4OH in the aqueous phase (in some of the experiments which is known to dissolve AgCl from Ag wire) a tungsten (W) based electrode system was employed (Cell 2). The tungsten-based electrode system was used solely as a means to pass current through the ITIES and to enable the application of a potential difference across the ITIES without interference and/or contamination from Ag^+ . No voltammetry is presented for Cell 2 arrangements herein.



The oil phase in Cell 2 contained either 10 mM TBATPB (86897, Sigma-Aldrich) in 1, 2-dichloroethane or 10 mM TBAPF_6 (86879, Sigma-Aldrich) in 1, 2 - dichloroethane. A variety of compounds were used in the aqueous phase, namely solutions of KCl , CsCl , NH_4OH and NaCl . Aqueous phase solutions were chosen to purposefully enable the possible formation of so-called ‘water insoluble ion-pairs’ between ions from the aqueous phase and ions from the oil phase (upon ion transfer across the ITIES). Oil/water interfaces were produced by extrusion of an aqueous droplet into the oil phase within a Krüss drop shape analysis system. Potentials quoted were that of the aqueous phase electrode with respect to the electrode in the oil phase.

For example, it was presumed that the following cell, given by



might produce water insoluble KTPB after ion transfer at high positive potentials (high enough for K^+ transfer from water to oil).

In some experiments, various metal chlorides and nitrates (in 1 mM amounts) were added to solutions containing NH_4OH namely $AuCl_3$, $CoCl_2$, $AgCl$, $PdCl_2$ and $AgNO_3$. Compositions of aqueous solutions containing metal chlorides are detailed in figure captions.

Crystals from both cell arrangements (Cell 1 and Cell 2) were hand-harvested from the interface with the aid of a Pasteur pipette. The crystals were placed into a volume of isopropyl alcohol (IP) and centrifuged at 13 000 rpm on a standard bench-top centrifuge for 10 min. The supernatant was discarded and the pellet resuspended in IP. This was repeated three times, each time discarding the supernatant. Remaining solvent was removed under vacuum at 20 °C. The white crystalline material was then dispersed in 2 ml of DMSO and transferred into an NMR tube. Proton NMR (1H -NMR) spectra were collected on a Bruker DPX 400MHz spectrometer against a standard of tetramethylsilane at $\delta=0$.

Crystals harvested (as above) were spotted onto silicon wafers, and examined with a ZEISS SUPRA55VP scanning electron microscope incorporating a Genesis EDAX analytical system. In some cases crystals were also examined using TEM (Jeol 2011 STEM with a Gatan Ultrascan 1000 camera), after being placed/spotted onto a Lacey carbon grid (Agar Scientific). A stain containing tin (II) chloride were prepared as described elsewhere⁹ (*vide infra*)

Harvested crystals were additionally sent for CHN elemental analysis. CHN analysis was conducted by an analytical service allied with Warwick University.

6.C Results and Discussion

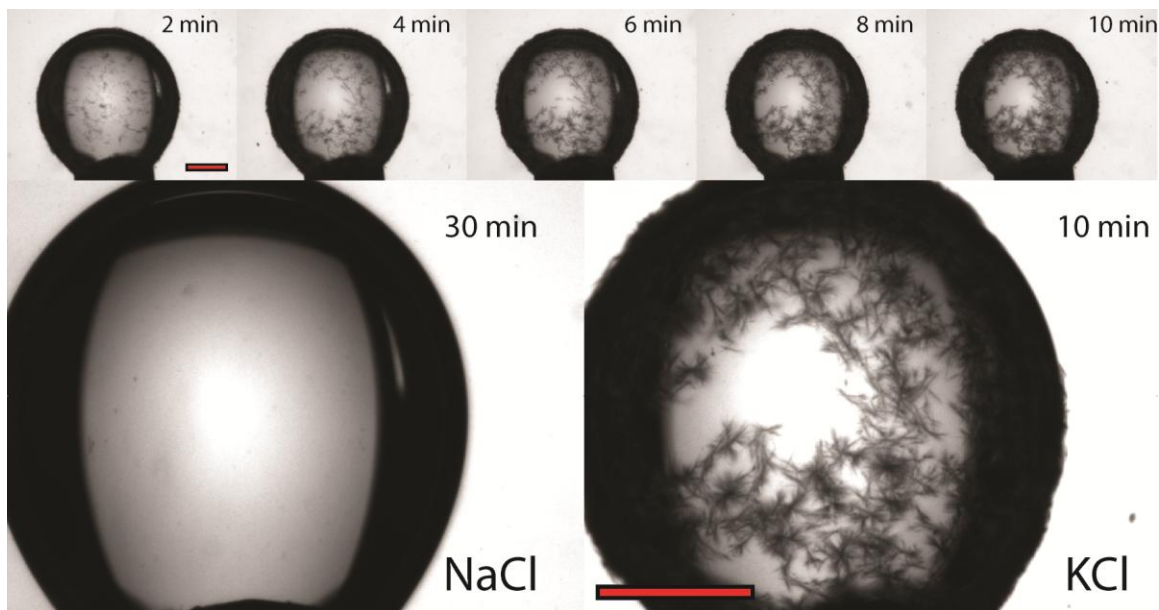


Figure 6.1 Rapid interfacial crystallization promoted by KCl but not NaCl over the experimental time frame. Panels top were a Cell 1 arrangement with 0.1 M KCl (aqueous phase) and 20 mM TBATPB (organic phase). A constant potential of +0.6 V was applied. Individual panels (top) indicate the amount of time after application of the potential. Big panel bottom right: a magnified view of the last panel at top left. Big panel bottom left was the Cell 1 arrangement with 0.1 M NaCl (aqueous phase) and 20 mM TBATPB (organic phase) and demonstrates an absence of interfacial crystals after 30 minutes at a constant potential of +0.7 V. Scale bars indicated are 700 μm . The ‘whisker-like’ crystals formed as above were observed after about 25 s (after the potential was applied).

The formation of a water-insoluble solid phases (precipitate or nuclei for example) by the association of ions from the aqueous phase and ions from the organic phase (Figure 6.1 to Figure 6.5) might be a prerequisite for the crystallization of TBATPB (*vide infra*). Cations K^+ , NH_4^+ and Ag^+ are known to form water insoluble interfacial ion-pairs with TPB^- ^{1, 4-6, 10}.

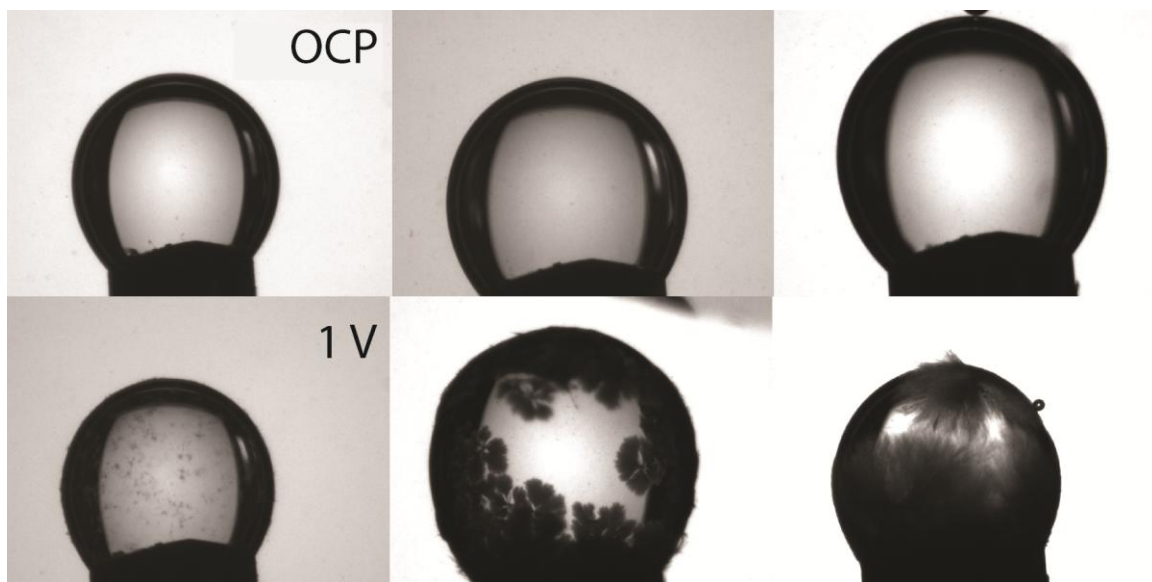


Figure 6.2 Top panels (left to right): an open-circuit condition with no applied potential (OCP). Bottom panels (left to right): a constant +1 V potential. The oil phase contained 10 mM TBATPB in 1, 2-DCE in all cases. Aqueous phase (droplets) contain from left to right (top and bottom): 3% (w/v) NaCl, 3% (w/v) NaCl + 10% (v/v) NH_4OH (conc.) and 3% (w/v) NaCl + 10 % (v/v) NH_4OH + 15 mM hydrazine. Potential was applied for about 15 minutes in all cases. The black object supporting the pendant droplet was 1.47 mm in diameter. All experiments were conducted within the Cell 2 arrangement. Some light crystallization is evident on the 3% (w/v) NaCl condition.

NaTPB and KTPB show marked differences in water solubility (water solubility (S_w) = 0.67 M^{11} and $1.8 \times 10^{-4} \text{ M}^{12}$ respectively), thus comparatively little K^+ or TPB^- might be need to be transferred into the interfacial region in order to exceed the solubility limit for KTPB at that locale (in comparison to an association between Na^+ and TPB^- for example). Data for the solubility of KTPB and NaTPB in 1,2 –dichloroethane was not available at the time of writing.

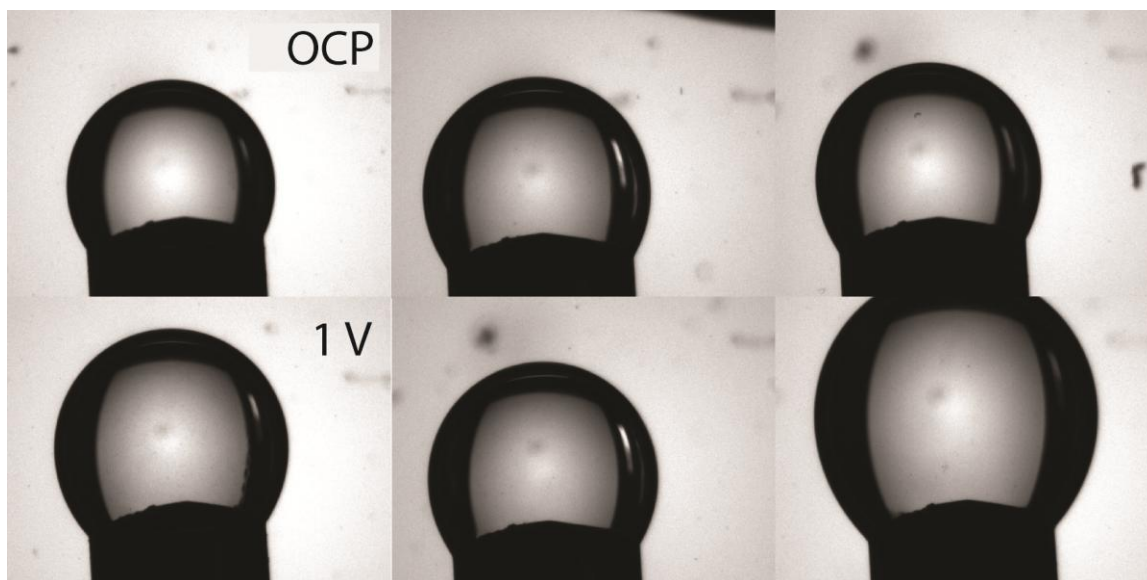


Figure 6.3 Top panels (left to right): an open-circuit condition with no applied potential (OCP). Bottom panels (left to right): a constant +1 V potential was applied. The oil phase contained 10 mM TBAPF₆ in 1, 2-DCE in all cases. Aqueous phases contain from left to right: 3% (w/v) NaCl, 3% (w/v) NaCl + 10% (v/v) NH₄OH (conc.) and 3% (w/v) NaCl + 10% (v/v) NH₄OH + 15 mM hydrazine. Potential was applied for about 15 minutes in all cases. The black object supporting the pendant droplet was 1.471 mm in diameter. All experiments were conducted within the Cell 2 arrangement. No crystallization was evident under any condition over the experimental time frame.

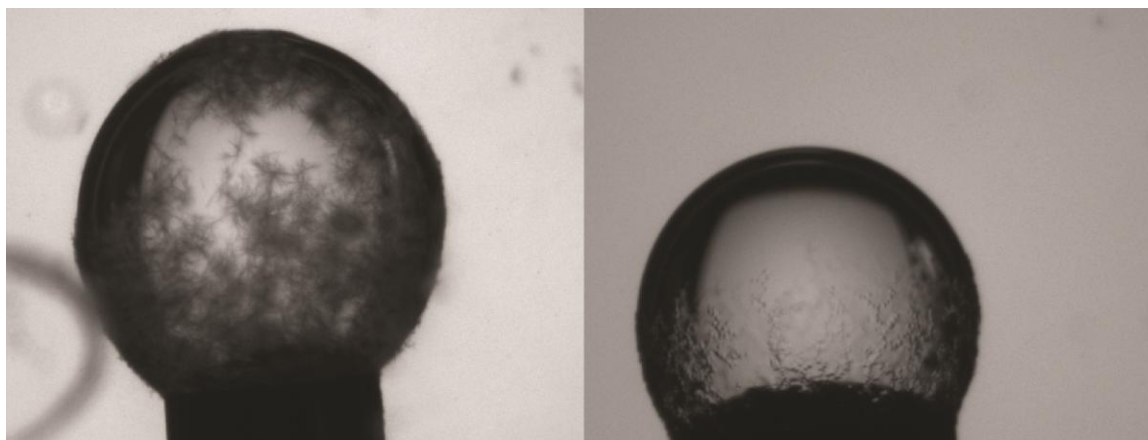


Figure 6.4 Needle-like (left) and cube-like (right) crystals grown on the ITIES using pendant droplets with different aqueous and oil phase ion combinations. Left panel: aqueous phase contained 6% (w/v) KCl and the oil phase contained 10 mM TBATPB (in 1,2-DCE). Potential was applied for 5 minutes at +1 V. Right panel: the aqueous phase contained 6% (w/v) CsCl and the oil phase contained 10 mM TBAPF₆ (in 1,2-DCE). Potential was applied for 10 minutes at +2 V. Small cubes (right) appear to be growing in a chain-like manner. All experiments conducted within the Cell 2 arrangement.



Figure 6.5 Interfacial crystals resulting from an applied potential of + 1 V using an aqueous phase containing 1 mM AgNO_3 + 10 % (v/v) NH_4OH . The oil phase contained 10 mM TBATPB in 1, 2-DCE. Crystals appeared after approximately 10 minutes. Black region at the bottom of the pendant droplet is 1.47 mm across. Experiments conducted within the Cell 2 arrangement.

The polarity of the interfacial region may be given by an arithmetic average of the polarities of both liquid phases ¹³ (approximate dielectric constant ≈ 45). This suggests that the extent of ion association between TPB^- and cations Na^+ and K^+ at the ITIES might be more extensive than ion association which occurs in the bulk of the aqueous phase. The force between two oppositely charged ions is inversely proportional to the dielectric constant of the medium¹⁴ (dielectric constant of water ≈ 80)¹⁵.

We have observed (via low magnification optical microscopy) that the time for the appearance of interfacial ‘whiskers’ may be related to the water solubility of known tetraphenylborate ion-pairs⁶. The solubility of these ion-pairs in water are given for NH_4TPB ($S_w = 2.88 \times 10^{-4} \text{ M}$ ¹⁶); CsTPB , ($S_w = 2.8 \times 10^{-5} \text{ M}$ ¹⁷), AgTPB ($S_w = 2.81 \times 10^{-6} \text{ M}$ ¹⁸) and KTPB ($S_w = 1.8 \times 10^{-4} \text{ M}$ ¹²). The fastest formation of crystals was seen for cases where the aqueous phase contained NH_4^+ and K^+ (the fastest). We have not however fully investigated this important aspect, which should be a topic for future work.

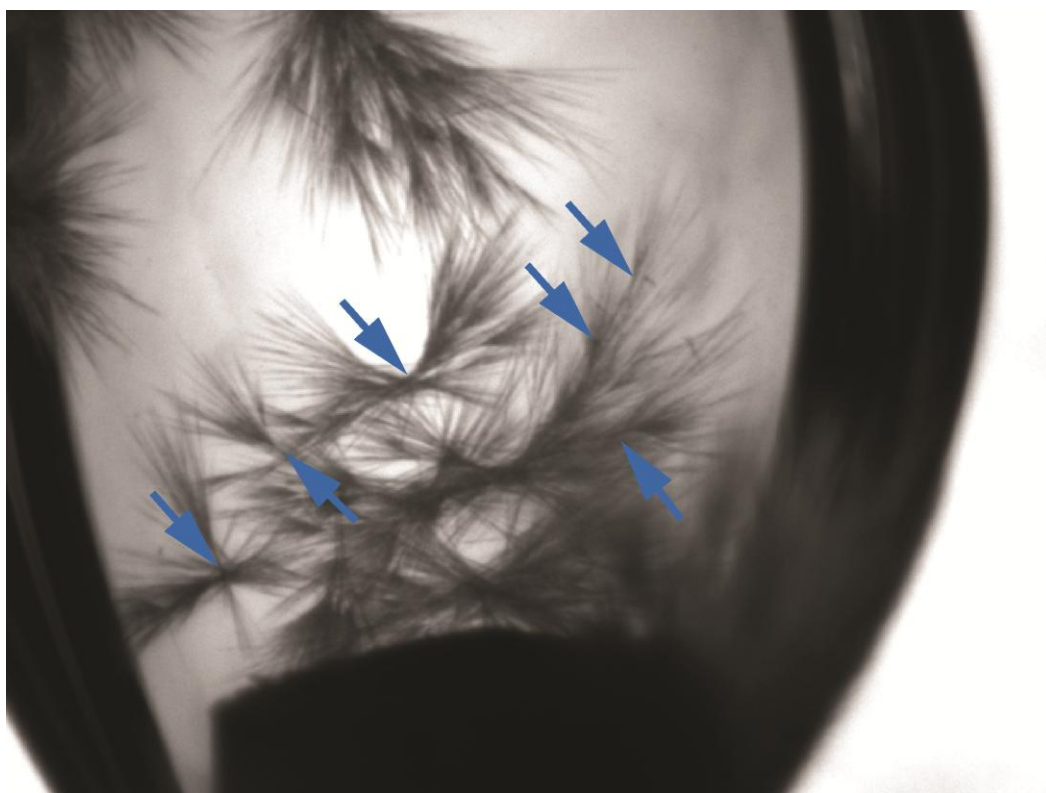


Figure 6.6 Branching “fern” growth with bunches of needle-like crystals which appear to originate and branch from single points. The aqueous phase contained 3% NaCl + 10% (v/v) NH_4OH . A potential of +0.8 V was applied for a few minutes. Blue arrows indicate apparent origin of branching points. Experiments conducted within the Cell 2 arrangement.

Figure 6.3 suggests that the possible formation of salts (with high water solubility) such as NH_4PF_6 ($S_w = 4.5 \text{ M}$)¹⁹ and NaPF_6 at the ITIES (via ion transfer) does not initiate electrolyte crystallization on the experimental time scales/potential ranges used herein. The organic phase electrolyte in experiments featured in Figure 6.3 was TBAPF_6 and we have found no evidence of its interfacial crystallization via low magnification optical microscopy. However, when using CsCl (in the aqueous phase) a presumed ion association between Cs^+ and PF_6^- , with the possible formation of water insoluble CsPF_6 ²⁰ may have led some TBAPF_6 crystallization (evident as semi-transparent ‘cubes’ in Figure 6.4).

TBATPB crystallization may be initiated by what may be the association of Na^+ and TPB^- (giving very water soluble NaTPB ¹²), given that a high enough potentials are applied for sufficient periods of time (Figure 6.2). At lower potentials this was not evident (Figure 6.1).

‘Whiskers’ (Figure 6.1 and Figure 6.6) often appear to originate from single points on the ITIES. This behaviour suggests that some nuclei/precipitate/solid phase may template or ‘seed’ TBATPB crystallization. Moreover, we have observed marked differences in ‘whisker’ morphology when different metal cations are used in the aqueous phase (Figure 6.1, Figure 6.2, Figure 6.5 and Figure 6.6). This suggests that crystals formed at the ITIES may have a cation-dependent growth mechanism.

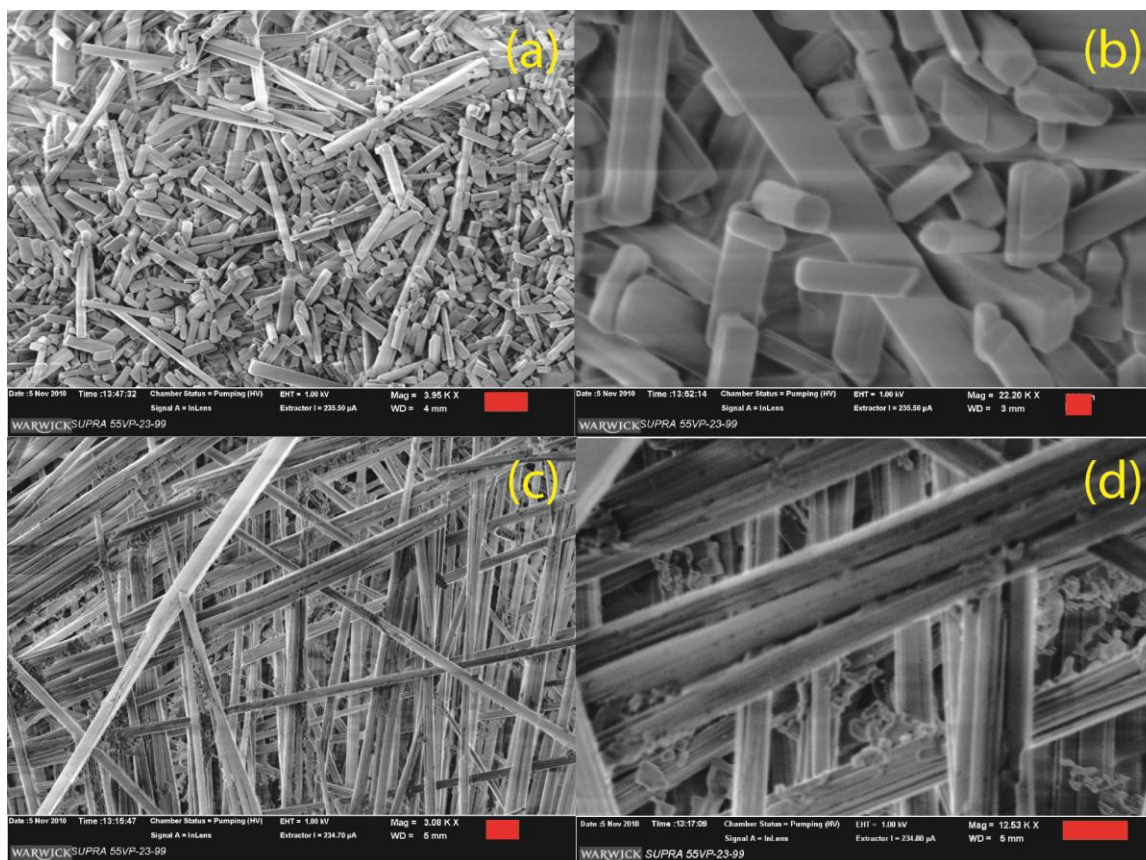


Figure 6.7 A comparison between the TBATPB morphology straight from the bottle [(a) and (b)] and TBATPB grown on the ITIES via the application of + 1 V potential [(c) and (d)]. For (c) and (d) the Cell 2 arrangement was used and 0.8 M KCl was present in the aqueous phase with 50 mM TBATPB present in the organic phase. Scale bars represent 2 μm in (a) and (c), 200 nm in (b) and 1 μm in (d). Crystals were imaged using SEM. Crystals grown at the ITIES are considerably longer along the c-axis than those from the 'bottle'. No gold sputtering was used and extensive charging effects are evident.

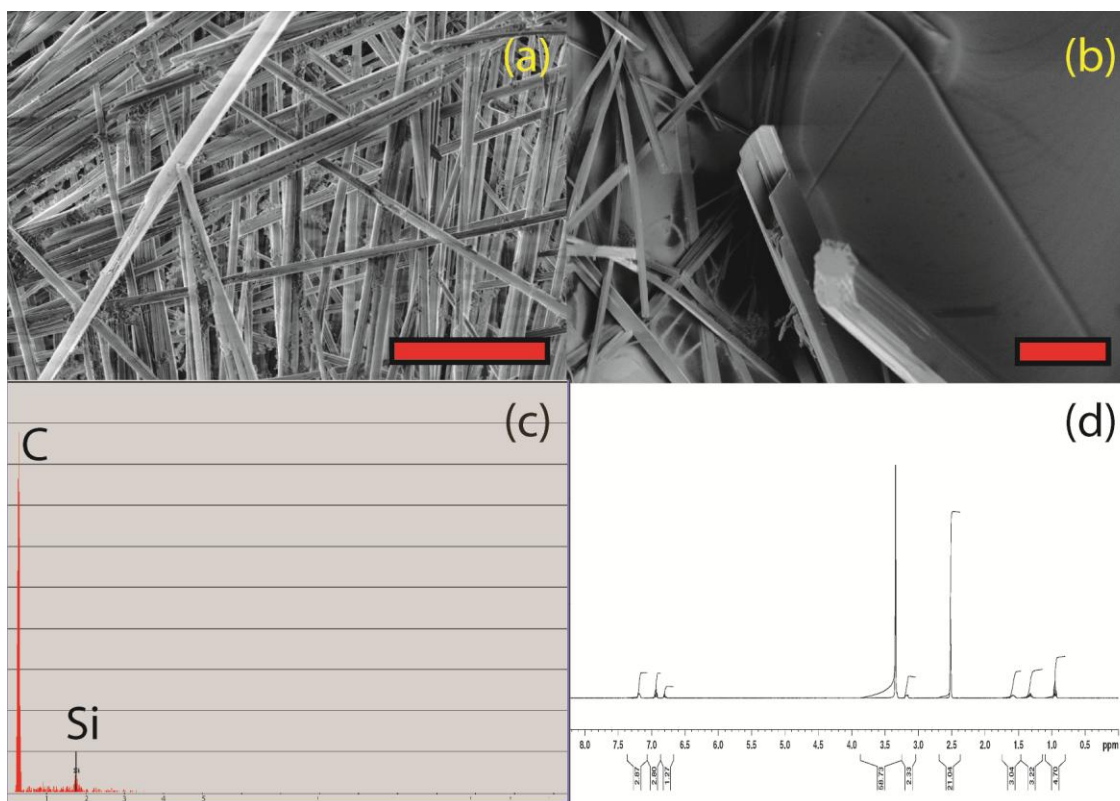


Figure 6.8 (a) and (b) Scanning electron micrographs of crystals ‘harvested’ from the interface (Cell 1). (a) Crystals, not gold sputtered, and extensive ‘charging’ is evident. (b) Crystals which were gold sputtered allowing examination at high magnification without deterioration under the electron beam. The geometric cross section and the elongated morphology was typical for crystals produced at oil/water interface (c) Typical SEM-EDAX analysis of the ‘whiskers’, the silicon peak is due to the silicon wafer substrate. (d) ¹H-NMR spectrum of needles harvested from the interface, indicating TBATPB. Scale bar on (a) is 10 μm and scale bar on (b) is 20 μm.

Crystals grown in the presence of Au^{3+} were collected for CHN analysis and were examined using SEM. CHN analysis revealed the crystals (of the type featured in Figure 6.9) were composed 63% C, 7.33% H, and 1.85 % N. The CHN analysis for pure TBATPB is 85% C, 10 % H, and N 2.49% (from the supplier’s analysis – see experimental section). The reason for this discrepancy is unclear.

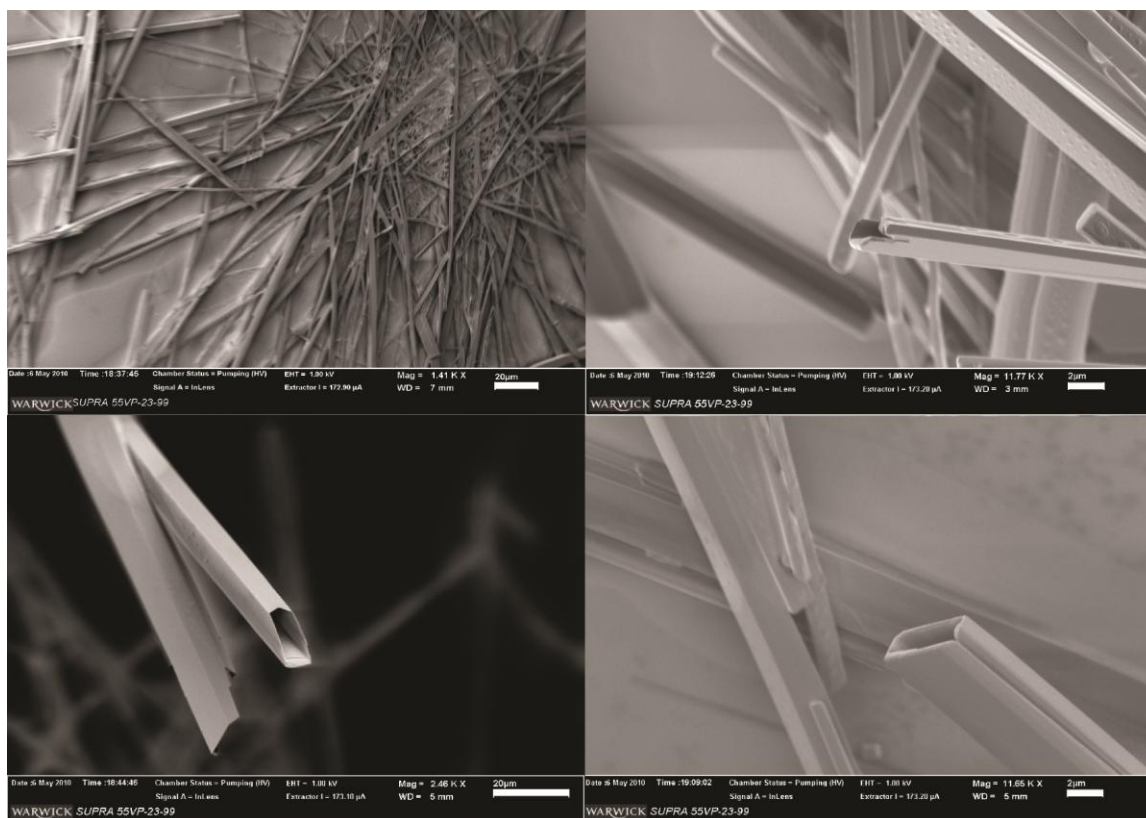


Figure 6.9 SEM micrographs of structures grown using 10% (v/v) NH_4OH (conc) + 1 mM AuCl_3 + 3 % (w/v) NaCl in the aqueous phase and 10 mM TBATPB in 1,2-dichloroethane in the organic phase. The applied potential was +1 V. Top left: typical crystal morphology. Top right: 'rod-like' tubular structures. Bottom left: hollow structure with geometric cross section. Bottom right: hollow structure with rectangular cross section. Crystals were formed using the Cell 2 arrangement.

No crystallography was conducted, which could have unequivocally confirmed the presence of any Au that could have been incorporated within the crystal lattice. The binding of Au to hydrophobic anions in the organic phase and the formation of AgTPB is known², although it appears that metallic gold was found mostly on the crystal surface. SEM-EDX analysis revealed the crystals to be organic in nature (high carbon peaks, Figure 6.8c). Additionally crystals were seen to 'melt' and 'distort' under low accelerating voltages (on the SEM) without gold coating, further suggesting the presence of a low melting point organic phase.

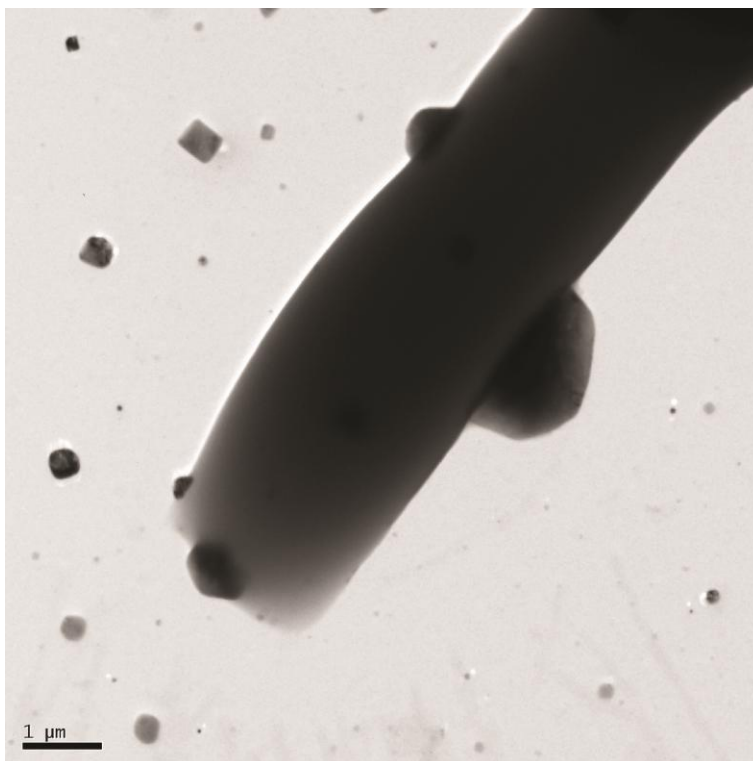


Figure 6.10 TEM micrograph of crystals of the type shown in Figure 6.9. The tube-like structures are the ‘whiskers’ and the geometric dark patches are electron-dense and could be metal particles.

Crystals grown in the absence of metallic cations (as in Figure 6.7) in the aqueous phase (without Au and Ag for example with the aqueous phase containing only KCl) were collected from the ITIES and subjected to H-NMR analysis. H-NMR analysis confirms that crystals/whiskers were composed of TBATPB, a result which was supported by SEM-EDX analysis which further reveals the ‘whiskers’ grown in the absence of metallic cations were solely organic in nature (Figure 6.8). SEM-EDX analysis of ‘whiskers’ (grown in the absence of metallic cation) did not reveal the presence of any K^+ or Cl^- on the whisker surface.

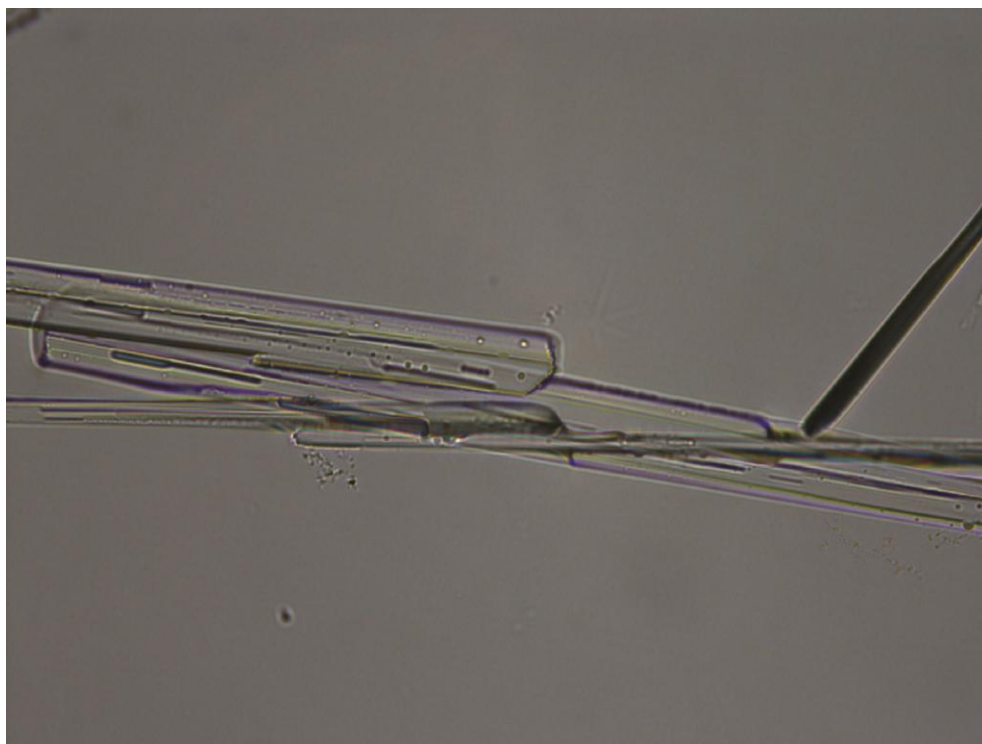


Figure 6.11 Optical micrograph of crystals harvested from the interface and spot stained with SnCl_2 . Note the purple stain around the periphery of the ‘whisker’, indicating the presence of gold. The crystals were grown within the Cell 2 arrangement and contained 10% (v/v) NH_4OH (conc) + 1 mM AuCl_3 + 3 % (w/v) NaCl in the aqueous phase and 10 mM TBATPB in 1,2-dichloroethane in the organic phase. Magnification was x 500.

The reader will note that in some experiments (Figure 6.2 and Figure 6.3), the aqueous phase contained small additions of hydrazine. Preliminary investigation, involving aqueous solutions containing millimolar amounts of various transition metal cations (such as those indicated in Figure 6.5, for example) gave the impression that some of these transition metal ions may have undergone reduction on the ‘whisker’ surface (Figure 6.10 and Figure 6.11, for example).

As no clear explanation could be given for the proposed appearance of the reduced metals on the ‘whisker’ surface, it was thought that ammonium hydroxide may have undergone electrochemical oxidation to hydrazine²¹ at the electrode surface. Hydrazine is a well known reducing agent²¹.

Experimentation, immediately preceding these preliminary investigations, demonstrated that it was not necessary for transition metal cations to be present in the aqueous phase order to initiate the interfacial crystallization process (Figure 6.1). We have, however, still chosen to use those experiments which contain hydrazine in order to demonstrate important effects of the organic phase electrolyte anion on the interfacial crystallization process.

As the interfacial crystallization of TBATPB was extremely rapid when the aqueous phase contained KCl. We further probed this system using voltammetry with the aqueous phase contained within micropipettes²² (Figure 6.12).

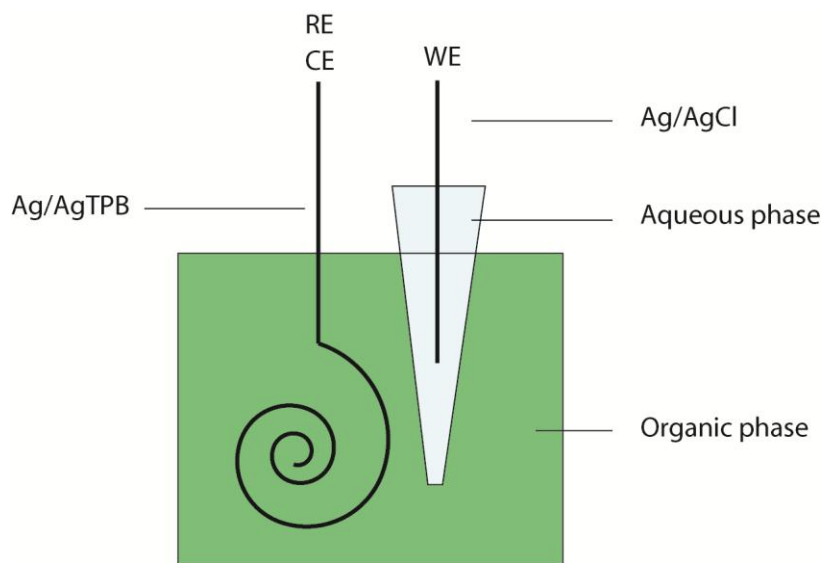


Figure 6.12 Typical experimental arrangement used for Cell 1. A micropipette of 53 μm inner diameter containing aqueous solution and a Ag/AgCl electrode was immersed into a reservoir containing a conductive organic phase and a Ag/AgTPB electrode. 'WE' is the 'working electrode', 'CE' is the counter-electrode and 'RE' is the reference electrode. The reference and counter electrodes were shorted together. The arrangement was viewed optically from a sideways aspect within a Krüss DSA 100 apparatus, as has been done in previous chapters.

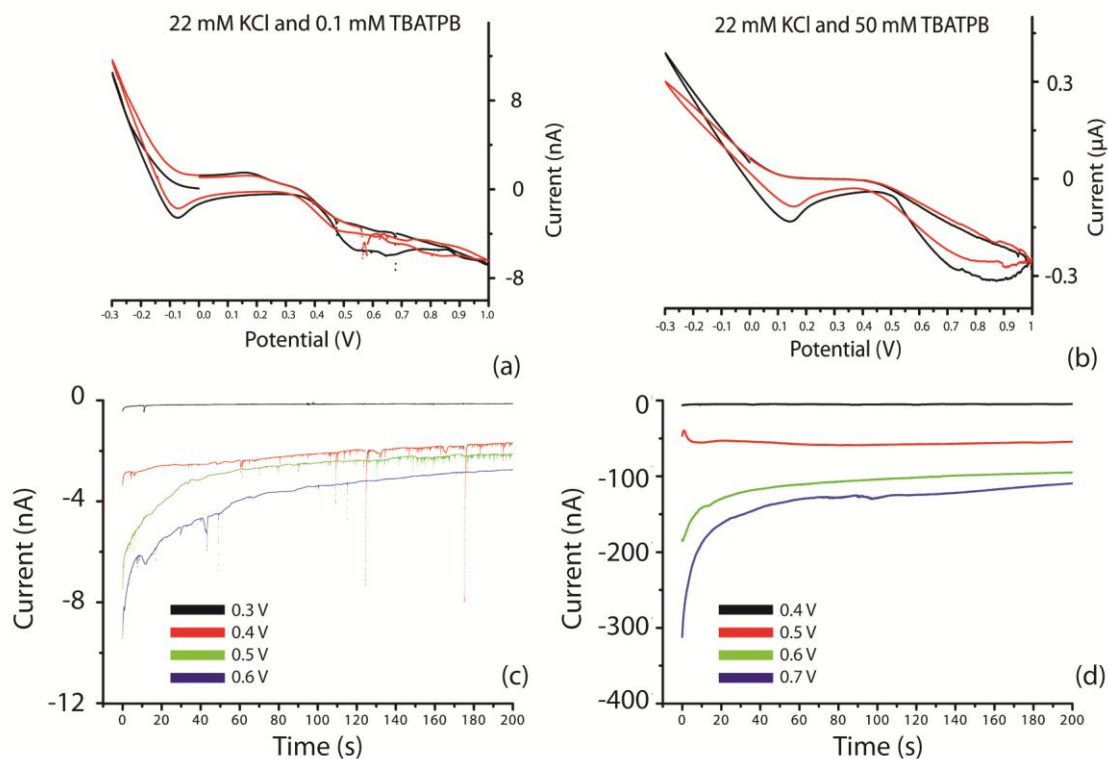


Figure 6.13 Cyclic voltammograms (CVs) (a and b) and corresponding potentiostatic current transients (c and d) for micro-ITIES arrangement (Cell 1). Concentration of electrolyte in aqueous and organic phase are indicated on figures. First potential sweep cycle on (a) and (b) is indicated in black, with the second indicated in red. Coloured lines in (c) and (d) correspond to applied anodic potentials. Scan rates for CV's were (a) = 0.025 V/s and (b) = 0.02 V/s.

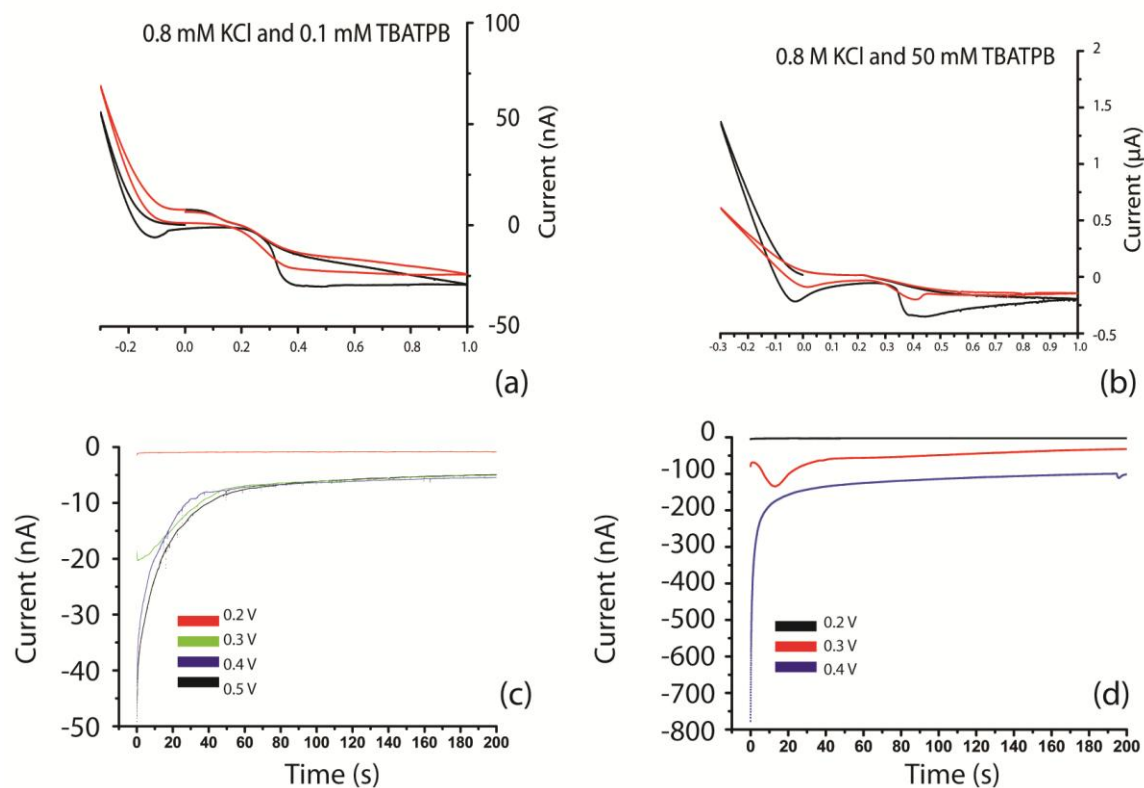


Figure 6.14 Cyclic voltammograms (CV) (a and b) and corresponding potentiostatic current transients (c and d) for the micro-ITIES arrangement (Cell 1). Concentrations in both aqueous and organic phases are indicated on figures. First potential sweep cycle is indicated in black on (a) and (b), with the second indicated in red. Coloured lines in (c) and (d) refer to applied anodic potentials. Scan rates for CV's were (a) = 0.025 V/s and (b) = 0.025 V/s.

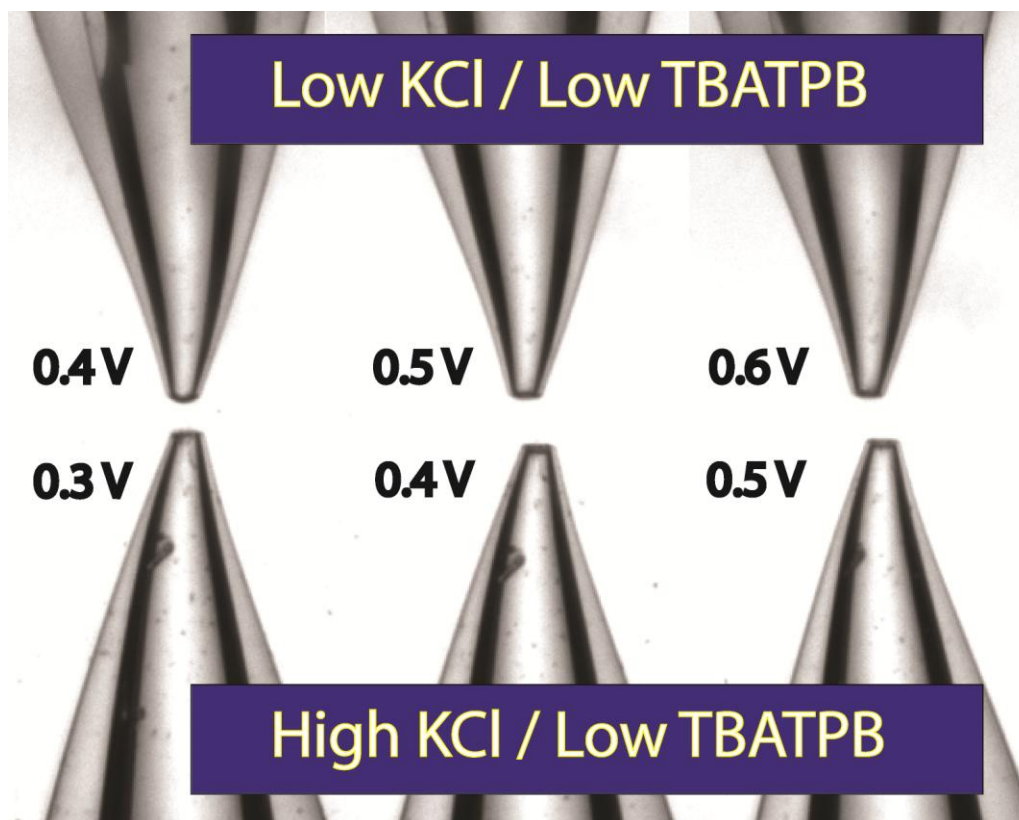


Figure 6.15 Optical micrograph indicating the extent of crystallization at the mouth of the micropipettes at varied potential. “High” and “Low” KCl refer to an aqueous phase containing 0.8 M KCl and 22 mM respectively which was contained within the micropipette. Low TBATPB refers to an oil phase (outside the pipette) containing 0.1 mM TBATPB. Each micropipette represented in the micrograph was the same micropipette. The micropipette was however used in different experiments. Applied potentials were as indicated and were applied for a period of 400 s using Cell 1. This figure corresponds directly to the end result of potentiostatic current transients in Figure 6.13 (c) and Figure 6.14 (c). The internal diameter of the micropipette was 53 μm .

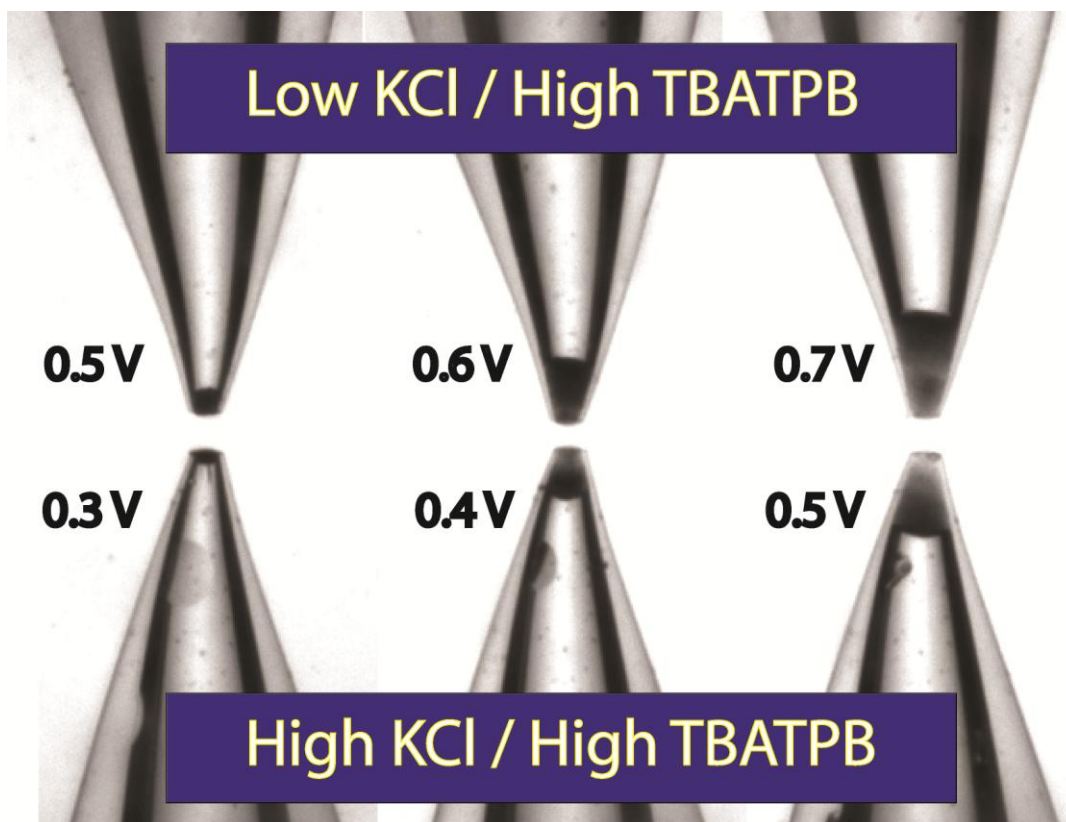


Figure 6.16 Optical micrograph indicating the extent of crystallization at the mouth of the micropipettes at varied potential. “High” KCl and “Low” KCl refer to an aqueous phase containing 0.8 M KCl and 22 mM KCl respectively (within the pipette). High TBATPB refers to an oil phase containing 50 mM TBATPB (outside the pipette). Each micropipette represented in the micrograph was the same micropipette. The micropipette was however used in different experiments. Applied potentials are as indicated and were applied for a period of 400 s using Cell 1. This figure corresponds directly to the end result of potentiostatic current transients in Figure 6.13 (d) and Figure 6.14 (d). The internal diameter of the micropipette was 53 μm .

Using a simple argument based on solubility

$$K_{sp}(\text{TBATPB in DCE}) = [\text{TBA}^+]_{bulk} [\text{TPB}^-] = 0.0501 \text{ mol}^2/\text{dm}^6 \quad (6.1)$$

an estimate can be made of the concentration of TPB^- required at the interface in order to exceed the solubility product (K_{sp}) of TBATPB in DCE ²³. We find that for 0.1 mM TBATPB ($[\text{TBA}^+]_{bulk} = 0.1 \text{ mM}$), the surface excess of $[\text{TPB}^-]$ must equal 501 M. This value is extraordinarily high; we must therefore assume that TBATPB crystallization, at these low TBATPB concentrations is unlikely.

This behaviour could be reflected in the CV's (Figure 6.13 (a) and Figure 6.14 (a)), where at cathodic potentials the peak height on the first potential sweep is lower than that of the second, which suggests an increase in the local TBA^+ concentration. The lack of TBATPB crystallization at low TBA^+ concentration is further evidenced in Figure 6.15, where in contrast to Figure 6.16; a very thin layer of 'material' was evident at the opening of the micropipette after the conclusion of a 400 s potentiostatic current transient.

Similarly, for 50 mM bulk concentrations of TBATPB, we find only 1 M TPB^- is required to exceed $K_{sp}(\text{TBATPB in DCE})$. This magnitude of surface ion excess is easily achieved upon polarization of the ITIES ²⁴. The crystallization of TBATPB may be reflected in CV's (Figure 6.13 (b) and Figure 6.14(b)) with peak heights at cathodic potential limits (on the second sweep) showing marked decreases, suggesting decreases in the interfacial concentration of TBA^+ due to the proposed crystallization of TBATPB. This type of behaviour has been reported in previous work^{1,5} but was interpreted there only as an association of the aqueous phase cation with TPB^- .

The CV's reveal that most of the current at large positive potential was due to TPB^- transfer, as large differences in current at positive potential can be seen for large increases in TBATPB (Figure 6.13 'a' and 'b') but not for large increases in KCl (Figure 6.14 'a' and 'b'). The reason as to why this is, is currently unclear. The CV's indicate that the extent of the decrease in TBA^+ peak heights could be KCl concentration dependent which is suggestive of a propensity for higher TBATPB crystallization at higher KCl concentrations.

We have considered low bulk TBATPB concentrations unfavourable for interfacial TBATPB crystallization. One could argue that current transients at low TBATPB concentration may therefore reflect the proposed KTPB nuclei/precipitant formation (as current spikes²⁵), without 'interference' from the crystallization of TBATPB at short times.

At the lowest KCl and TBATPB concentrations (Figure 6.13 (a)), the extent of the potential window is the widest. Potentiostatic current transients (Figure 6.13 (c)) were recorded across and beyond this window and reveal that nucleation⁸ events take place when TPB^- (standard Gibbs energy of transfer ($\Delta G_{tr}^{0,w \rightarrow o}$) = -33 kJ/mol²⁶) transfers solely from oil to water (0.4 V) and when both K^+ ($\Delta G_{tr}^{0,w \rightarrow o}$ = 49 kJ/mol²⁷) and TPB^- are provided enough energy to transfer across the ITIES simultaneously.

Recent work²⁵, which studied nanoprecipitation reactions within the confines of nanopipettes, noticed similar current spikes. These authors found that the origin of the current spikes were due to the precipitation of insoluble salts within the capillary²⁵. The origin of these current peaks (Figure 6.13) (in our case) are currently unclear and may also be due precipitation or crystallization reactions. It may be that the initial (proposed) KTPB nuclei/precipitate event could be too rapid for detection on our equipment (with millisecond time resolution). We were also unable to go below the nA current range due to noise related issues.

Most of the nucleation-type behaviour^{8, 28} evident on potentiostatic current transients on Figure 6.13 and Figure 6.14 could be related to the process of TBATPB crystallization or a mixture of the two processes (proposed KTPB formation and TBATPB crystallization).

The use of small currents, such as that achieved by using a nanopipette-based approach, would be more advantageous. As the suggested initial association between K^+ and TPB^- , may comprise a greater proportion of the total current and therefore be more easily detected.

Concentration-dependent changes in the extent of the potential window are in accordance with previous work⁴. However, in the case of 22 mM KCl, an increased TBATPB concentration resulted in the potential window being narrowed from negative potentials towards more positive potentials.

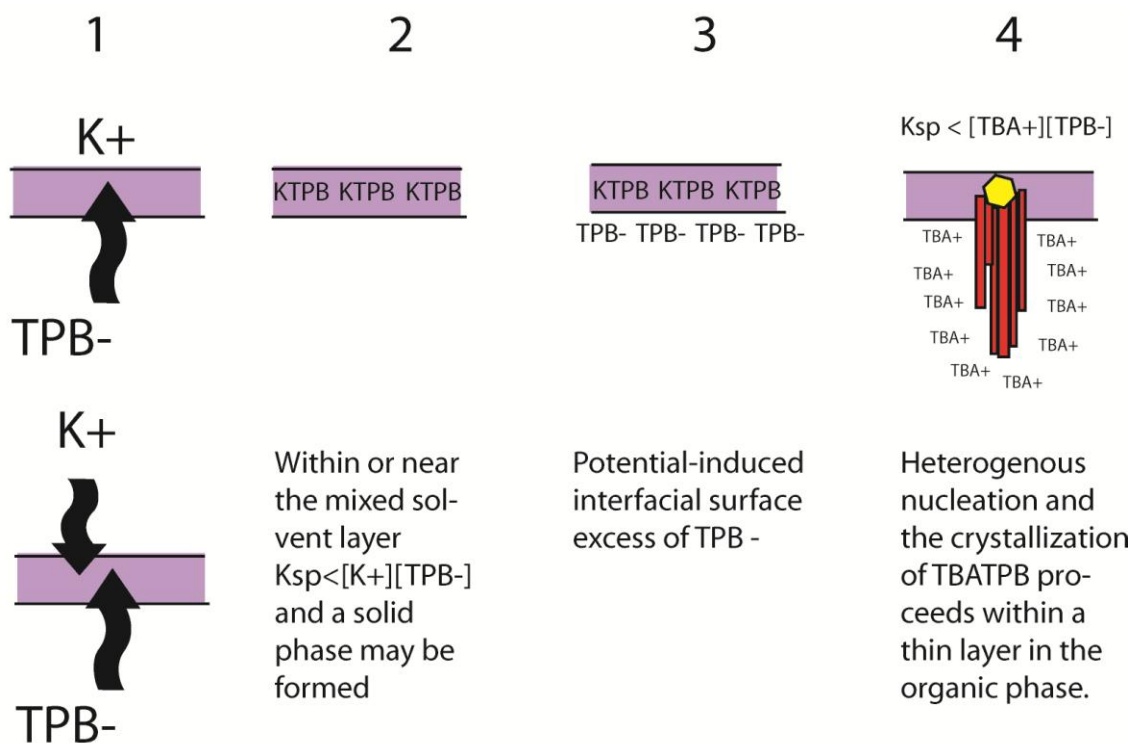


Figure 6.17 A cartoon of the suggested TBATPB crystallization mechanism, which may be initiated by the association of K^+ and TPB^- . Each stage of the process is numbered and we have divided the process into 4 stages.

TBATPB crystals, grown on the ITIES in most cases, were found to display a rectangular cross-section and were highly elongated along the c-axis. SEM images reveal a sometimes hollow morphology (Figure 6.7 to Figure 6.9). Also evident on micrographs are solid rectangular cross-sections made up of what seems to be elongated 'whiskers'. This crystal growth mechanism is active in a number of different inorganic (such as $Sb_8O_{10}(OH)_2I_2$ ²⁹ and ZnO ³⁰ for example) and organic crystals (caffeine and aspirin³¹ for example). The crystal morphology is suggestive of rapid growth³¹. This crystal growth mechanism should be explored in more detail in future research efforts.

The proposed “ion association” mechanism and subsequent crystallization process is featured in cartoon form in Figure 6.17 and are discussed below.

At positive potentials, which are too low for K^+ transfer (from water to oil) but high enough for TPB^- transfer (from oil to water), the transfer of TPB^- from oil to water begins⁴. Possible ion-pairing between K^+ and TPB^- may take place at some as yet undetermined interfacial location⁴. At positive potentials high enough for both K^+ transfer (from water to oil) and TPB^- transfer (from oil to water), both ions will transfer simultaneously⁴ and may have more opportunity to form an insoluble ion-pair within the interfacial region.

KTPB is very insoluble in water¹⁷ but more soluble in water-solvent mixtures¹⁷. It is therefore reasonable to assume that in cases where positive potentials are high enough for both K^+ and TPB^- transfer to occur, ion association and the ability to over-exceed the solubility limit are more favourable (for ion-pair formation) than situations in which potentials are high enough only for TPB^- transfer from oil to water to occur (Figure 6.13 and Figure 6.14).

It is assumed in both cases the solubility product of KTPB will eventually be overcome (albeit at different times). Due to the insoluble nature of KTPB (approximately 6.2 wt% in 100 % acetone and 0.0063 wt% in water⁴) an insoluble solid phase is formed.

As the liquid-liquid interface is polarised, and potentials are high enough to transfer TPB^- from oil to water, we expect large excesses of TPB^- to be present on the

oil side of the liquid-liquid interface^{24, 32}. These presumed surface excess coupled with 'ambient' organic phase concentrations of TBA^+ may be large enough to initiate a solid TBATPB²³ phase which subsequently grows in a crystalline manner.

We propose that the formation of the KTPB solid phase which precedes the crystallization of TBATPB for the following reasons:

- 1) KTPB is water insoluble and has limited solubility in water-solvent mixes¹⁷ and the crystallization process is seen to occur in a matter of seconds (Figure 6.1). If KTPB were not involved in the crystallization process then it could be argued that crystals would also have formed in cases where the aqueous phase contained NaCl (Figure 6.1).
- 2) In cases where TBATPB crystallization was not favoured (Figure 6.13 and Figure 6.14), current spikes were still evident on current transients. These spikes have been shown to be indicative of the formation of a solid phase²⁵.
- 3) Crystals appear to originate from a single point, and grow out in a 'star-like'/ radial fashion. This type of growth suggests a solid phase which may have acted as a heterogeneous nucleant.

This proposed crystallization of methodology may be applicable to other organic and inorganic materials. Of special mention here are the organic pharmaceutical compounds (benzoic acid and acetaminophen) which initial work suggests may provide interesting focal points for future study. Preliminary results in this regard indicate that it is not necessary for the subject of crystallization to be localised exclusively within the organic phase.

6.D References

1. B. Hundhammer, T. Solomon, S. K. Dhawan, T. Zerihun and M. Tessema, *Journal of Electroanalytical Chemistry*, 1994, **369**, 275-277.
2. A. Sherburn, D. Arrigan, R. Dryfe and N. Boag, *Electroanalysis*, 2004, **16**, 1227-1231.
3. P. Vanysek, ed., *Electrochemistry on Liquid/Liquid Interfaces*, Springer-Verlag, Berlin, Germany, 1985.
4. G. Geblewicz, A. K. Kontturi, K. Kontturi and D. J. Schiffrin, *Journal of Electroanalytical Chemistry*, 1987, **217**, 261-269.
5. M. H. M. Caçote, C. M. Pereira, L. Tomaszewski, H. H. Girault and F. Silva, *Electrochim. Acta*, 2004, **49**, 263-270.
6. A. K. Kontturi, K. Kontturi, L. Murtomäki and B. Quinn, *Acta Chem. Scand.*, 1996, **50**, 640-642.
7. D. J. Clarke, D. J. Schiffrin and M. C. Wiles, *Electrochim. Acta*, 1989, **34**, 767-769.
8. P. V. Dudin, P. R. Unwin and J. V. Macpherson, *The Journal of Physical Chemistry C*, 2010, **114**, 13241-13248.
9. H. Elftman, A. G. Elftman and R. L. Zwemer, *The Anatomical Record*, 1946, **96**, 341-353.
10. A. K. Kontturi, K. Kontturi and D. J. Schiffrin, *J. Electroanal. Chem.*, 1988, **255**, 331-336.
11. S. M. Ponder, R. Helkowski and T. E. Mallouk, *Ind. Eng. Chem. Res.*, 2001, **40**, 3384-3389.
12. A. K. Gupta, R. J. Hanrahan and D. D. Walker, *The Journal of Physical Chemistry*, 1991, **95**, 3590-3594.
13. H. Wang, E. Borguet and K. B. Eisenthal, *The Journal of Physical Chemistry B*, 1998, **102**, 4927-4932.
14. P. W. Atkins, *Physical Chemistry*, Oxford University Press, Oxford, 1990.
15. K. Izutsu, *Electrochemistry in Nonaqueous Solutions*, Wiley-VCH Verlag GmbH & Co. KGaA, 2002.
16. S. M. Ponder and T. E. Mallouk, *Ind. Eng. Chem. Res.*, 1999, **38**, 4007-4010.
17. A. N. Kirgintsev and V. P. Kozitskii, *Russ. Chem. Bull.*, 1968, **17**, 1116-1118.
18. A. Sherburn, M. Platt, D. W. M. Arrigan, N. M. Boag and R. A. W. Dryfe, *Analyst*, 2003, **128**, 1187-1192.
19. W. L. F. Armarego and C. L. Lin Chai, *Purification of Laboratory Chemicals (Sixth Edition)* Butterworth-Heinemann, 2009.

20. M. A. Ilies, W. A. Seitz, I. Ghiviriga, B. H. Johnson, A. Miller, E. B. Thompson and A. T. Balaban, *J. Med. Chem.*, 2004, **47**, 3744-3754.
21. V. Rosca and M. T. M. Koper, *Electrochim. Acta*, 2008, **53**, 5199-5205.
22. G. Taylor and H. H. J. Girault, *J. Electroanal. Chem.*, 1986, **208**, 179-183.
23. M. H. Abraham and A. F. D. de Namor, *Journal of the Chemical Society, Faraday Transactions 1: Physical Chemistry in Condensed Phases*, 1976, **72**, 955-962.
24. N. Laanait, J. Yoon, B. Hou, P. Vanysek, M. Meron, B. Lin, G. Luo, I. Benjamin and M. L. Schlossman, *The Journal of Chemical Physics*, 2010, **132**, 171101.
25. B. Vilozy, P. Actis, R. A. Seger and N. Pourmand, *ACS Nano*, 2011, **5**, 3191-3197.
26. A. J. Olaya, M. A. Méndez, F. Cortes-Salazar and H. H. Girault, *J. Electroanal. Chem.*, 2010, **644**, 60-66.
27. Z. Samec, V. Marecek and M. P. Colombini, *J. Electroanal. Chem.*, 1988, **257**, 147-154.
28. J. Guo, T. Tokimoto, R. Othman and P. R. Unwin, *Electrochem. Commun.*, 2003, **5**, 1005-1010.
29. Q. Yang, K. Tang, C. Wang, F. Li, B. Hai, G. Shen, C. An, W. Yu and Y. Qian, *J. Cryst. Growth*, 2001, **233**, 287-291.
30. H. Iwanaga and N. Shibata, *J. Cryst. Growth*, 1974, **24-25**, 357-361.
31. M. D. Eddleston and W. Jones, *Cryst. Growth Des.*, 2009, **10**, 365-370.
32. G. Luo, S. Malkova, J. Yoon, D. G. Schultz, B. Lin, M. Meron, I. Benjamin, P. Vanysek and M. L. Schlossman, *Science*, 2006, **311**, 216-218.

7. Conclusions

7.A Chapter 2

In Chapter 2, we set-out to investigate if simple DC electrochemical systems could be used to influence a model protein crystallization system. It is clearly shown that an electrochemically-based approach can have a vast influence on both the extent of nucleation and growth of lysozyme crystals. In addition, we have developed a new and simple conceptual framework which may help to explain the effect of DC electrolysis on lysozyme crystallization. The kind of approach outlined in Chapter 2 may be generic for other protein crystallizing systems.

The proposed conceptual framework in Chapter 2 is able to provide a reasonable explanation for and rationalise the extent of electrochemically assisted lysozyme crystallization under a wide range of initial solution conditions and applied currents.

Experimental platforms suggested and presented in Chapter 2 are immediately amenable to fundamental *in-situ* protein crystal growth studies using scanned probe techniques and may prove additionally useful in order to grow large crystals for neutron crystallography studies, for example. This is corroborated by very recent work by other researchers (published just after thesis submission) which details the use of similar experimental platforms for *in-situ* protein crystallization study, in the manner in which we have suggested within this thesis.

Basic finite element modelling methodologies used in Chapter 2 to place the electrochemically-assisted protein crystal growth process on more quantitative grounds, although useful for an initial approximation; need to be vastly improved in terms of 'realism' and complexity. Such modelling methodologies could be improved by an experimental investigation into the nature of the protein film and the rates of electrochemical reactions taking place at the electrode surface. An improved modelling methodology will presumably save a great deal of tangible resource and may lead to new process insights via *in-silico* simulation.

The proposed conceptual framework and methodology proposed in Chapter 2, relies specifically and purposefully on navigating phase space on a protein/precipitant phase diagram via DC electrolysis. The phase diagram would therefore be an essential requirement for this purpose and needs accurate compilation for each protein/precipitant combination under consideration. It is also necessarily required that a crystallization protocol be in existence before phase diagram compilation has begun. This is necessary as one may need to determine the location of the borders between the three zones of undersaturation, metastability and nucleation on a protein/precipitant phase diagram in order to successfully 'navigate' phase space using electrolysis.

In order to provide a more balanced/nuanced interpretation of the results, an alternative hypothesis has been presented in order to explain the results. This is based on migration effects within solution. We however show that an explanation based on electrolysis is much more probable and future work should aimed in this direction.

Atypical electrochemical systems, as presented in Chapter 2, may thwart attempts at absolute quantification and therefore direct temporal measurement of precipitant ion concentrations and pH, at a range of heights above the electrode surface, using microelectrodes, has been strongly recommended. A possible experimental arrangement for this purpose was suggested and may lead to new insights regarding pH and ion concentration gradients above electrodes in the presence of proteins undergoing phase change.

7.B. Chapter 3

In Chapter 3, we have discovered that by crystallizing lysozyme on variety of oil/water interfaces, radical increases in the amount of nucleation and sometimes growth of lysozyme crystals can be realised. This effect is seen with some but not all oil/water interfaces. The enhancement in the extent of nucleation has been proposed as being caused by organic solvent-dependent dehydration of protein hydration waters around crystal contact areas.

Protein films formed at such oil/water interfaces (via irreversible protein adsorption) may afford large increases in crystal growth, in effect supplying amorphous precursor to growing crystals, as per a recently proposed and popular mechanism within the literature.

The extent of lysozyme crystallization at most 'active' oil/water interfaces is far in excess of that found at corresponding air/water interfaces under identical crystallizing conditions. This observation is very significant, as a large number of high

throughput, costly protein crystallization trials are currently conducted at the air/water interface.

The results reported within Chapter 3 seem to hold some future promise and are important. This is mostly because they could result in success rate increases for a large variety of large scale protein crystallization trials. Due to the inherent difficulty and large expense of such crystallization trials, it is thought that this particular new approach to protein crystallization may be of great interest to industry as well as academia. Much work is however needed and we would suggest the use of high-throughput batch-type techniques in order to flesh out the various details of this potentially important effect.

A particularly important aspect of future work is to elucidate a series of specific trends that be used to predict whether oil-water interfaces would be 'active' or 'inactive' for a particular protein crystallization system. It is thought that a combination of physicochemical properties (of the oil-water interface) may lead to such an interface being defined as 'active' or 'inactive'.

Additionally, within Chapter 3, it was found that when lysozyme was crystallised at water immiscible ionic-liquid (BMIM-PF6)/water interfaces the resulting crystal morphologies appear different to lysozyme crystals found on other 'conventional' oil/water interfaces. This proposed morphological change at the (water immiscible ionic liquid) oil/water interface has not been previously reported within the literature. Future work has also been suggested in this regard within Chapter 3.

We therefore suggest that the current practice of using ‘under oil’ microbatch-type experimental arrangements within high throughput protein crystallization trials needs reconsideration, as it appears that current methodology could possibly and unnecessarily retard the crystallization process of some protein crystallization systems. Additionally, within Chapter 3, we have demonstrated that oil/water interfaces provide both an alternative and an attractive platform upon which to study protein crystallization processes via various physical and chemical means.

7.C Chapter 4

In Chapter 4, we presented initial findings and proof of concept studies concerning a novel lysozyme crystal growth methodology. The methodology is based upon the use of the electrified oil/water interface. This protein crystal growth methodology featured within Chapter 4 appears to be based on potential-induced increases and decreases in protein concentration in the vicinity of growing protein crystals at the oil/water interface. In addition, the crystallization process may further be affected by disturbances in the electric double layer. However, the actual cause of this effect is at the time of writing unclear and much further work using more sophisticated techniques is strongly recommended. The methodology may be extendable to other protein/precipitant systems and further work in this regards is also strongly suggested.

7.D Summary Chapters 2,3 and 4

In summary, within Chapters 2, 3 and 4 we have presented 3 new and interesting approaches to protein crystallization, with many avenues for future work suggested and recommended. It is thought that these experimental Chapters represent significant and original contributions to the field of protein crystallization. This is further evidenced by much of the work within these Chapters receiving publication and suggestions contained within these Chapters being published by other research groups.

7.E Chapter 5

Outside the field of protein crystallization, and within Chapter 5, we have demonstrated that by using an appropriate type of 'particle' at the ITIES, large, reversible, potential-dependent changes in γ (interfacial surface tension) can be realised.

In this regard, we have further suggested that the desirable physical properties to be exhibited by the proposed 'designer particles' should be based on physical properties exhibited by the protein cytochrome c. These physical properties could include the possession of a large electrical dipole moment, irregular surface geometry, reversibility of adsorption at the ITIES (with an applied potential), amphiphilicity and low surface activity under non-potential and non adsorbing conditions. These suggestions are contrary to suggestions from previous work.

We also find, within Chapter 5, that although conventional surfactants do indeed lower γ , they appear to be not reversibly adsorbed from the interface at low potential and hence their use within conventional and unconventional electrowetting systems may be limited. The suggested manufacture of new ‘electrowetting’ particles may serve to enhance the performance of both conventional EWOD systems as well as ultra-low voltage ITIES-based electrowetting systems.

Additionally, in Chapter 5, we introduced the γ /CV diagram which enables useful depiction of potential-dependent interfacial properties in conjunction with associated cyclic voltammetry data. As these graphical representations of simultaneously acquired multidimensional data are ‘new’, further work is suggested in order to extract more accurate, fully quantitative and useful surface property/electrochemical data from them using more sophisticated equipment.

7.F Chapter 6

In Chapter 6, we report, for the first time, initial studies into the rapid interfacial crystallization of TBATPB at the ITIES, initiated by what appears to be the formation of an insoluble interfacial KTPB solid phase. TBATPB crystallization, of the type reported herein, has been previously and erroneously reported within the literature as precipitation and/or insoluble ion-pair complex formation. The results are therefore of importance to theory and experiment regarding ion-transfer mechanisms at the ITIES, where conclusions from fundamental work have been drawn using experimental systems of the type used herein, but without knowledge of the crystallization phenomenon.

A further, more extensive analytical effort is needed to further the understanding of 'materials' produced at the ITIES using experimental systems of the type described herein. We suggest that there may still be some compounds (KTPB for example) which may be formed on time scales and in amounts that would evade our current attempts at analysis. In this regard better 'resolution' in terms of voltammetry is required for future work; in particular the use of nanopipette voltammetry with fast sampling rates was suggested.

Future work, with regard Chapter 6, should also be aimed at adapting this novel crystallization method for the crystallization of other compounds of academic and commercial interest. We suggest that this novel liquid/liquid crystallization technology could be adapted to other experimental systems which contain valuable/relevant components contained in either the organic phase or the aqueous phase. As such this methodology may be of interest to both various sectors in both industry and academia.